NANOSTRUCTURED ELECTRODES FOR PHOTOELECTROCHEMICAL WATER SPLITTING

HENRY ARTHUR BURCH

A thesis submitted to the University of Birmingham for the degree of DOCTOR OF PHILOSOPHY

School of Chemical Engineering

College of Engineering and Physical Sciences

University of Birmingham

March 2016

Abstract

Nanostructured MoS_2 and $ZnFe_2O_4$ were synthesised and tested as catalytic water splitting photoelectrodes. MoS_2 was nanopatterned from a bulk crystal using a combination of nanosphere lithography and plasma etching. Three morphologies were produced: nanospheres deposited with interstices between them produced nanopillars, nanospheres squashed into hexagons imprinted a nanowell pattern, and linked nanopillars resulted from parts of each. The MoS_2 was tested as a photocathode and morphologies with linkages between features had improved catalysis than those without. This was attributed to the layered structure of MoS_2. These samples degraded in air to $MoS_xO_{(2-x)}$, and an electrochemical technique utilising $Na_2S_2O_3$ was used to re-sulfidate the $MoS_xO_{(2-x)}$. The technique decreased the onset potential from -0.27 V SHE to -0.17 V SHE, and the Tafel slope from 282 mV dec^{-1} to 87 mV dec^{-1}.

$ZnFe_2O_4$ electrodes were deposited by AACVD from a precursor molecule. The deposition solvent composition was systematically altered between methanol and ethanol to examine its effect on the nanostructure. $ZnFe_2O_4$ electrodes deposited from predominantely methanol solvent had compact morphologies due to heterogenous nucleation, while the electrodes deposited from predominantly ethanol solvent had high surface area structures due to homogeneous nucleation. The more exothermic enthalpy of combustion of ethanol was deemed responsible.

“We imagine that when we are thrown out of our usual ruts all is lost, but it is only then that what is good and new begins. While there is life there is happiness.”

Leo Tolstoy

Acknowledgements

Thank you to my supervisors Upul Wijayantha, Richard Palmer and Neil Rees for all your help and guidance. I learnt many things from each of you. I'm also so grateful for all the support I received and the friends I made at the Energy Research Laboratory at Loughborough, and the hydrogen CDT and NPRL at Birmingham. Thank you to the EPSRC for generously funding my research.

Thank you to my parents, Pauline and David for supporting me through this process and always being interested in whatever breakthrough or breakdown I was having that week. And to my sisters Lucy and Hazel for being there for me.

Finally thank you to all the old friends who have stuck with me, and the new friends I made along the way. The People and Planeteers plus crowd, Jeju sarams, and the Horsell crew. I couldn't have finished without your distractions to give me perspective. Love to you all.

Publications

A. A. Tahir, H. A. Burch, K. G. U. Wijayantha, B. Pollet, A new route to control texture of materials: Nanostructured $ZnFe_2O_4$ photoelectrodes, *Int. J. Hydrogen Energy*, 2013, **38,** 4315 - 4323

H. A. Burch, M. Isaacs, K. Wilson, R. E. Palmer and N. V. Rees, Electrocatalytic regeneration of atmospherically aged MoS_2 nanostructures via solution-phase sulfidation, *RSC Adv.*, 2016, **6**, 26689 – 26695.

Contents

1.0 Introduction 1

1.1 Solar Power 1

1.1.1 The Photovoltaic Effect 1

1.1.2 Semiconductors 2

1.1.3 Sunlight to Electricity 4

1.2 Photoelectrochemical Water Splitting 6

1.2.1 The Energetics of Water Splitting 6

1.2.2 Photoelectrochemical Cells 10

1.2.3 Charge Carrier Recombination 11

1.2.4 Oxygen Evolution Reaction 13

1.2.5 Hydrogen Evolution Reaction 14

1.3 Nanostructuring 18

1.3.1 Nanosphere Lithography and Plasma Etching 19

1.3.2 Aerosol Assisted Chemical Vapour Deposition 22

1.3.3 Mass Transport to Nanoelectrode Arrays 23

1.4 $ZnFe_2O_4$ as an Oxygen Evolution Photocatalyst 25

1.4.1 $ZnFe_2O_4$ Structure and Properties 26

1.5 MoS_2 as a Hydrogen Evolution Photocatalyst 28

1.5.1 The Structure of MoS_2 29

1.5.2 MoS_2 Photocathodic Properties 33

1.5.3 Current State of the Art of MoS_2 HER 33

1.6 Thesis layout 37

2.0 Materials and Methods 39

2.1 Fabrication Techniques 40

2.1.1 MoS_2 Electrode Assembly 40

2.1.2 Nanosphere Lithography 41

2.1.3 Plasma Etching 44

2.1.4 $ZnFe_2O_4$ Electrode Assembly 47

2.1.5 $ZnFe_2O_4$ Precursor Synthesis 48

2.1.6 Aerosol Assisted Chemical Vapour Deposition 49

2.2 Sulfidation of Air Degraded MoS_2 50

2.3 Characterisation Techniques 51

2.3.1 Electrochemistry of MoS_2 52

2.3.2 Photoelectrochemistry of MoS_2 53

2.3.3 Photoelectrochemistry of $ZnFe_2O_4$ 54

2.3.4 Incident Photon Conversion Efficiency (IPCE) 54

2.3.5 Scanning Electron Microscopy 55

2.3.6 X-ray Photoelectron Spectroscopy 58

2.3.7 X-ray Diffraction 60

2.3.8 Electrode Size Calculations 61

2.3.9 Density Flask 61

2.3.10 Du Nouy Tensiometer 62

3.0 Nanopatterning of MoS_2 by Nanosphere Lithography and Plasma Etching 65

3.1 Electrode Assembly 66

3.2 Electrode Geometric Area 68

3.3 Nanosphere Lithography 69

3.3.1 Solution Concentration 70

3.4 Nanopatterning 71

3.4.1 Blank MoS_2 74

3.4.2 O_2 Etch Length 80

3.4.3 SF_6 Etch Length 84

3.4.4 C_4F_8 Flow Rate 87

3.4.5 SF_6 Flow Rate 90

3.4.6 O_2 Flow Rate 92

3.4.7 Relationship Between Nanosphere Deposition Conditions and HER Catalysis 95

3.5 Morphology 102

3.5.1 Nanopillars 104

3.5.2 Nanowells 105

3.5.3 Linked Pillars 113

3.5.4 Relationship Between Nanosphere Deposition Conditions and Morphology 114

3.6 Electrochemistry of the Three Morphologies 115

3.6.1 Electrochemical Modelling 122

3.7 Freshly Nanostructured Measurements 124

4.0 Sulfidation of Air Degraded MoS_2 128

4.1 $Na_2S_2O_3$ as the Sulfur Source 129

4.1.1 $Na_2S_2O_3$ Sulfur Deposition Methodology 130

4.1.2 Acid Concentration Optimisation 135

4.1.3 Deposition Potential Optimisation 138

4.2 XPS Determination of Surface Composition 144

4.3 Electrochemistry 148

4.3.1 Proton Reduction 149

4.3.2 Degradation 154

4.3.3 Photoelectrochemistry 158

4.4 Homogenisation of the Surface Morphology 161

5.0 Deposition Solvent Composition Effect on the PEC Properties of $ZnFe_2O_4$ 164

5.1 Electrode Deposition 165

5.2 XRD Identification 167

5.3 Aerosol Physical Properties 168

5.3.1 Aerosol Droplet Size 169

5.3.2 Solvent Enthalpy of Combustion 173

5.4 The Influence of Solvent on Surface Morphology..... 175

5.5 Influence of Solvent Composition on PEC Properties 183

6.0 Conclusion..... 191

7.0 References 195

List of Illustrations

Figure 1.1. The relative energy levels of the conduction band (E_C), valence band (E_V), and Fermi level (E_F) of n-type and p-type semiconductors. The potential difference between the E_C and E_V is the band gap (E_g) of the semiconductor[7]. 3

Figure 1.2. Electrons promoted by photons in a two band photoconverter. Photons with energy $E < E_g$ cannot promote electrons to an excited state. Photons with energy $E > E_g$ can promote electrons but any excess energy is lost as heat as the electron relaxes to the conduction band. As such photons with $E >> E_g$ produce the same effect as photons with $E = E_g$[7]. 5

Figure 1.3. The band positions of a selection of candidate photoelectrode materials shown against the reduction potential of hydrogen and the oxidation potential of water. E_{VAC} and E_{NHE} correspond to the absolute vacuum level, and standard (normal) hydrogen electrode respectively[21,24,25,26,27]. 9

Figure 1.4. Configurations of one photoelectrode water splitting PEC cells. a. comprises of a n-type photoanode and a metal cathode, and b. of a p-type photocathode and a metal anode. 10

Figure 1.5. The five major types of recombination that can occur to photogenerated charge carriers in a PEC cell. (1) Recombination at defect sites at the semiconductor / liquid interface (J_{ss}). (2) Recombination in the semiconductor bulk (J_{br}). (3) Recombination in the space charge region (J_{dr}). (4) Thermal promotion over the interfacial potential barrier (J_{et}).

(5) Tunnelling through the interfacial potential barrier (J_t). (6) Represents the desired charge transfer process[17,32,33,34] 12

Figure 1.6. A Sabatier plot of exchange current density against energy of adsorbed hydrogen (ΔG_H) used to help identify potential new HER catalysts[59]. 17

Figure 1.7. Bottom-up and top-down nanosphere lithography. (a) Orange nanospheres hexagonally close packed on a blue substrate. (b) Material deposited over the top of the nanospheres and substrate. (c) Following removal of the nanospheres the material deposited in the interstices remains. (d) A selective etchant is used to remove material from the interstices of the nanospheres. (e) After removal of nanospheres pillars remain under the nanospheres' positions[66,70] 20

Figure 1.8. The four categories of diffusion regime observed on micro- and nano-electrodes defined by whether the feature size and peak separation are longer or shorter than the diffusion length of the analyte[87]. 24

Figure 1.9. The layered structure of MoS_2 showing the (1010) edge. Each layer consists of covalently bonded molybdenum and sulfur atoms, and the layers are connected by van der Waals forces. 29

Figure 1.10. The Volmer-Heyrovský mechanism of H^+ reduction on a MoS_2 (1010) edge site. The proton is adsorbed to the MoS_2 (1010) edge site during the Volmer reaction, and the Heyrovský reaction follows in which a second proton from solution binds to an adsorbed proton to produce H_2 gas[50]. 32

Figure 2.1. MoS_2 electrode assembly showing the 5mm diameter GC disk, silver paint, and the MoS_2 in the centre. Epoxy resin covers the GC and silver, but is transparent. 41

Figure 2.2. The set-up for modified Langmuir-Blodgett nanosphere deposition. Showing the MoS_2 adhered to GC submerged in the dish, and the syringe assembly by which the water level is lowered. 42

Figure 2.3. A nanosphere monolayer being deposited onto the water-air interface. (a) Lid to block air currents while lowering the water level. (b) Glass dish. (c) Si wafer coated with nanospheres. (d) Nanospheres on the water-air interface. (e) Glass dish to hold sample steady. (f) MoS_2 adhered to GC. (g) Ultrapure water. (h) Syringe – the needle is connected to the barrel by flexible tubing so as to be able to pass between the dish and lid. 44

Figure 2.4. A schematic of an Oxford Instruments PlasmaPro NGP80 etcher. (a) gas inlet. (b) Induction coil. (c) plasma. (d) temperature controlled base. (e) vacuum chamber. (f) RF generator[135]. 45

Figure 2.5. $ZnFe_2O_4$ electrode assembly with the blank FTO strip (white) and the deposited $ZnFe_2O_4$ (red). 48

Figure 2.6. AACVD deposition apparatus. (a) Direction of precursor solution flow. (b) Deposition chamber. (c) Deposition nozzle. (d) FTO substrate. (e) Second piece of FTO supporting a piece of glass with a ≈ 2 mm overlap on the first piece to prevent the entire substrate from being deposited upon. 50

Figure 2.7. A diagram of a scanning electron microscope equipped with a secondary electron detector[146]. 57

Figure 2.8. Constructively interfering X-rays being emitted following excitation. By measuring θ d may be determined, and hence the material composition identified. 61

Figure 3.1. A SEM image of the finished electrode assembly. The light gray rectangle in the middle is the patterned MoS_2, and the darker, shiny substance surrounding it is the epoxy resin. The silver adhesive cannot be seen under SEM. 68

Figure 3.2. Exposed MoS_2 geometric size measurements. The measurements were obtained by taking an image of the sample surface using an optical microscope, and then defining the area using image measurement software 69

Figure 3.3. Nanospheres deposited onto MoS_2 at different solution concentrations. (a) 0.75:1 NS:EtOH. (b) 1:1 NS:EtOH. (c) 1.25:1 NS:EtOH. (d) 2:1 NS:EtOH. 71

Figure 3.4. SEM images of the formation of nanopillars by NSL. (a) Nanospheres deposited on the surface of MoS_2, showing small gaps between the spheres. (b) Nanospheres that have shrunk due to be subjected to a 35 second O_2 plasma etch. (c) MoS_2 nanopillars formed from exposing the etch mask in (b) to 30 seconds of SF_6 and C_4F_8 plasma. (d) Side view of the nanopillars..... 73

Figure 3.5. Randomly patterned surface resulting from subjecting the MoS_2 to all three plasma etch steps without first depositing nanospheres onto the surface. 76

Figure 3.6. Proton reduction on bulk and randomly patterned MoS_2. The bulk sample is an unetched piece of MoS_2, and the randomly etched is the result of plasma etching without nanosphere lithography. 77

Figure 3.7. Experimental and predicted peak currents for the cleaved blank MoS_2 78

Figure 3.8. Experimental and predicted peak currents for the glassy carbon blank as per the Randles-Ševčík equation. 79

Figure 3.9. Four MoS_2 sample morphologies resulting from a 30 second O_2 nanosphere shrinking etch. Samples (a), (b), and (c) had a pillar morphology with spacings between features of 122nm, 162nm, and 158nm respectively. (d) had a mixed morphology comprising of pillars, and nanowells. 81

Figure 3.10. Four MoS_2 sample morphologies resulting from a 35 second O_2 nanosphere shrinking etch. All four displayed pillar morphology, however (b) and (c) had larger clumps resulting from the nanospheres not separating. The feature spacings were 171 nm, 160 nm, 116 nm, and 130 nm for (a), (b), (c), and (d) respectively. 82

Figure 3.11. Four MoS_2 sample morphologies resulting from a 40 second O_2 nanosphere shrinking etch. These all displayed a pillar morphology, with (a) 109 nm, (b) 136 nm, (c) 174 nm, and (d) 196 nm spacings. 83

Figure 3.12. Four MoS_2 sample morphologies resulting from a 25 second SF_6 nanosphere shrinking etch. Each formed pillars, although the spacing of the pillars varied between

samples with (a) having 149 nm spacings between samples, and (b) having 164 nm, (c) was 147 nm and (d) 161 nm.....84

Figure 3.13. Four MoS_2 sample morphologies resulting from a 35 second SF_6 nanosphere shrinking etch. Each formed pillars with spacings of 146 nm, 134 nm, 118 nm, and 152 nm, for (a), (b), (c) and (d), respectively. 85

Figure 3.14. Four MoS_2 sample morphologies resulting from a 40 second SF_6 nanosphere shrinking etch. Pillar morphologies were formed with some clumping from where the nanosphere resist didn't separate in (a), (c) and (d). The pillar spacings were 147 nm for (a), 127 nm for (b) and (c), and 131 nm for (d). 86

Figure 3.15. Four MoS_2 sample morphologies resulting from a flow rate of 10 SCCM C_4F_8 during the SF_6 etch. (a) was predominantly pillars, with some linkages in between and spacings of 145 nm between nanopillars. (b) was mostly comprised of linked pillars, with some nanowells. (c) and (d) had a nanowell morphology.....87

Figure 3.16. Four MoS_2 sample morphologies resulting from a flow rate of 30 SCCM C_4F_8 during the SF_6 etch. (a) was comprised of anisotropic pillars with variable spacings between features. (b), (c), and (d) were nanowells with a central pillar remaining within the well. ...88

Figure 3.17. Three MoS_2 sample morphologies resulting from a flow rate of 40 SCCM C_4F_8 during the SF_6 etch step. (a) was comprised of anisotropic pillars with 126 nm between features. (b) was unformed nanowells with the central well remaining closed. (c) was

comprised of anistropic pillars with some proto-nanowells. The pillars had 118 nm spacings. 89

Figure 3.18. Two MoS_2 samples morphologies resulting from a flow rate of 15 SCCM SF_6 during the final etch. (a) was comprised of linked pillars with some nanowells. (b) had a nanowell morphology. In this image the nanomesh formed from the nanospheres is visible over some parts of the MoS_2. 90

Figure 3.19. Three MoS_2 sample morphologies resulting from a flow rate of 35 SCCM SF_6 during the final etch. (a) was comprised of anisotropic pillars, with linkages, (b) was nanowells with a central pillar, and (c) was comprised entirely of nanowells.....91

Figure 3.20. Two MoS_2 sample morphologies resulting from a flow rate of 40 SCCM SF_6 during the final etch. (a) was mostly unformed nanowells, although in some the centre has opened. (b) had a nanopillar morphology. 92

Figure 3.21. Three MoS_2 sample morphologies resulting from a 90 SCCM O_2 flow rate during the nanosphere shrinking etch. (a) and (b) had pillar morphologies with separations of 96 nm and 142 nm, respectively. (c) was comprised of poorly defined nanowells. 94

Figure 3.22. Two MoS_2 sample morphologies resulting from a flow rate of 80 SCCM O_2 during the nanosphere shrinking etch. Both (a) and (b) were comprised of pillars with spacings of 130 nm and 87 nm respectively, although in (b) some of the pillars had aggregated. 94

Figure 3.23. Proton reduction on nanostructured MoS_2. The sample subjected to a 25 second SF_6 etch had an earlier onset potential but no clearly defined proton reduction peak. The 35 second SF_6 etch had a peak, but at a high overpotential of -0.93 V SHE. 96

Figure 3.24. Proton reduction on two samples of each set of the C_4F_8 variable flow rate experiment. Blue is 10 SCCM, red is 30 SCCM, and green is 40 SCCM C_4F_8 flow rate.....97

Figure 3.25. HER on two samples of each MoS_2 set resulting from variable SF_6 flow rates. Blue was 15 SCCM, red was 35 SCCM and green was 40 SCCM SF_6 flow rate. 100

Figure 3.26. Proton reduction on four MoS_2 nanostructures resulting from varying the O_2 flow rate during the nanosphere shrinking etch. Blue is 90 SCCM, and red is 80 SCCM O_2 flow rate.....102

Figure 3.27 (a) pillar morphology. (b) linked pillar morphology. (c) nanowell morphology.103

Figure 3.28. SEM images of the formation of nanopillars by NSL. (a) Nanospheres deposited on the surface of MoS_2, showing small gaps between the spheres. (b) Nanospheres that have shrunk due to being subjected to a 35 second O_2 plasma etch. (c) MoS_2 nanopillars formed from exposing the etch mask in (b) to 30 seconds of SF_6 and C_4F_8 plasma. (d) Side view of the nanopillars.....104

Figure 3.29. SEM images of the formation of nanowells by NSL and plasma etching. (a) Nanospheres deposited on the surface in such close proximity as to squash into tessellating hexagons. (b) Nanomesh formed by exposure of (a) to O_2 plasma. (c) Nanowells formed from etching (b) With SF_6 and C_4F_8 plasma. (d) A side view of the nanowells. 106

Figure 3.30. SEM images of nanomesh formation from nanospheres exposed to O_2 plasma. The sample was removed from the chamber and imaged at regular intervals such that each image was exposed to O_2 plasma approximately 4 seconds longer than the previous image. (a) is prior to O_2 etching, and (s) is the result of 67 seconds total etch time. 109

Figure 3.31. SEM images of nanowell formation and structure. (a) Polystyrene nanomesh formed by the exposure of closed packed nanospheres to O_2 plasma. (b) Nanomesh on top of a nanowell patterned MoS_2 surface. (c) MoS_2 nanowells. (d) Damaged nanowells showing the layered structure of MoS_2. 112

Figure 3.32. (a) Nanospheres deposited partially with small gaps, partially with no gaps. (b) Nanospheres shrunk by O_2 plasma with some linkages between the individual spheres. (c) the linked pillar morphology. 113

Figure 3.33. The voltammograms for the best performing samples of each morphology as determined by Tafel slope. All the morphologies displayed enhanced catalytic properties as compared to the MoS_2 blank and randomly patterned samples. 116

Figure 3.34. The surface morphologies corresponding to the voltammograms presented in Figure 3.33. (a) and (b) are nanowells (a) and (b) respectively. (c) and (d) are nanopillars (a) and (b) respectively. (e) and (f) are linked pillars (a) and (b) respectively. 117

Figure 3.35. Tafel slopes derived from the voltammograms in Figure 3.33. The graph is plotted with the dependent variable on the x-axis as in this configuration the gradient is the Tafel slope. 120

Figure 3.36. An attempt at modelling the voltammogram of Figure 3.33 – Linked pillars (a). It was considered inaccurate as to achieve a fit the modelled area needed to be greater than the geometric area, and all parameters required iterative calculations. 123

Figure 3.37. Voltammograms obtained from performing H^+ reduction on nanostructured MoS_2 electrodes in 2 mM $HClO_4$ electrolyte at 25 mV s^{-1}. 125

Figure 3.38. Tafel slopes for the nanostructured MoS_2 tested shortly after patterning. The slopes are derived from Figure 3.37. 126

Figure 4.1. Initial sulfur deposition test from 10mM $Na_2S_2O_3$, different deposition potentials were applied with a H^+ reduction test in-between. Deposition 1 applied a cathodic potential from 0 V to -1.6 V Ag/AgCl. Deposition 2 applied an anodic potential from 0 V to +1.6 V Ag/AgCl. Deposition 3 was cycled from 0 V to +1.6 V to -1.6V to 0V Ag/AgCl. Deposition 4 was swept from 0 V to +1.6 V to -1.6V Ag/AgCl. 131

Figure 4.2. H^+ reduction on the MoS_2 treated with $Na_2S_2O_3$ in Figure 4.1. Depositions 1, 2, and 3 lowered the current and increased the onset potential as compared to the before measurement. However deposition 4 showed a beneficial effect to onset potential, and also a more defined peak. 132

Figure 4.3. The voltammogram of an air-exposed MoS_2 electrode in 10 mM $Na_2S_2O_3$, 1 mM H_2SO_4, and 0.1 M Na_2SO_4 with the potential swept from 0 V to +1.6 V to -1.6 V Ag/AgCl. .133

Figure 4.4. H^+ reduction on MoS_2 before and after sulfidation as per Figure 4.3. The sulfidation resulted in an earlier onset potential and higher peak current. These metrics

degraded between the 1st and 2nd measurements, but were stable between the 2nd and 3rd. 134

Figure 4.5. The voltammogram for sulfidation using both 1 mM and 10 mM H_2SO_4 in conjunction with 10 mM $Na_2S_2O_3$. 136

Figure 4.6. H^+ reduction measurements taken before and after sulfidation depicted in Figure 4.5. Both post-sulfidation results were superior to the before measurement, and the 1 mM displayed an earlier onset potential and a higher peak current. 137

Figure 4.7. Four sulfidations were undertaken to determine whether the oxidative sweep alone is necessary, and what the optimum reductive potential was. Before and between each sulfidation the H^+ reduction ability was tested. Each sulfidation started at 0 V Ag/AgCl and was taken to +1.6 V Ag/AgCl. The linear oxidation was halted at +1.6 V Ag/AgCl while the cyclic swept back to 0V Ag/AgCl. The reductive sweeps had the full cyclic oxidation performed first each time before being swept to -0.6 V Ag/AgCl, and -1.6 V Ag/AgCl. 139

Figure 4.8. In between the sulifidations presented in Figure 4.7 the MoS_2 electrode was tested for H^+ reduction catalysis. The full potential window where the sulfidation was taken from 0 V to +1.6 V to -1.6 V Ag/AgCl yielded the best results. Both cyclic and linear oxidations were shown to have a beneficial effect on the electrodes ability to reduce protons. Although the reduction to -0.6 V Ag/AgCl was superior to the before measurement it was detrimental compared to a just oxidative deposition.....140

Figure 4.9. Determination of the optimum oxidative potential for sulfidation. The maximum potential was increased in 0.1 V increments to +1.2 V Ag/AgCl, and in 0.2 V increments thereafter. The peaks at ≈+0.8 V Ag/AgCl on the forward scan, and ≈+0.2 V Ag/AgCl on the back scan were common features. 142

Figure 4.10. H^+ reduction test results produced from incrementally increasing the oxidative potential window during sulfidation. The MoS_2 electrode was cyclically oxidised to the stated potential, then reduced to -1.6 V Ag/AgCl. In between sulfidations these H^+ reduction measurements were taken. 143

Figure 4.11. The freshly nanostructured material produced molybdenum species corresponding to MoS_2 (B.E. Mo $3d_{5/2}$ = 229 eV), MoO_2 (B.E. Mo $3d_{5/2}$ = 229.7 eV) and MoO_3 (B.E. Mo $3d_{5/2}$ = 232.5 eV), alongside a strong signal at 227 eV corresponding to sulfur in the metal sulfide form. The degraded sample produced a broadened peak at 229.5 eV, shifted to slightly higher binding energy, indicative of a shift towards a more oxidic Mo species, as well as a decrease in surface sulfur species. Decrease in MoO_3 is clearly evident due to the diminished Mo $3d_{3/2}$ species at 235.6 eV, indicating the sample consists of largely MoO_2. After sulfidation, the major Mo photoelectron peak narrows and returns to a lower binding energy, consistent with the reformation of surface MoS_2 species. The $Mo(O_3)$ 3d peak at 235.6 eV remains in a diminished form, suggesting the sample has returned to a majorly MoS_2 composition[173]. 147

Figure 4.12. Two atmospherically-aged $MoS_xO_{(2-x)}$ electrodes were H^+ reduction tested before and after sulfidation. The results are compared against two freshly fabricated nanostructured MoS_2 samples and bulk MoS_2.....150

Figure 4.13. Tafel slopes derived from Figure 4.12 as a means of comparison of reaction kinetics between freshly prepared, atmospherically-aged, and sulfidated MoS_2.....152

Figure 4.14. To determine the stability of the sulfidated MoS_2 in the acidic electrolyte used for H^+ reduction measurements the catalytic ability was tested prior to sulfidation and 20 times following[173].....154

Figure 4.15. As a measurement of the stability of the sulfidated MoS_2 in air a sample H^+ reduction measurements were performed before and after sulfidation and then three times over the next three weeks. The sample was then re-sulfidated[173].....156

Figure 4.16. Tafel slopes derived from the degradation measurements presented in Figure 4.15[173].....157

Figure 4.17. H^+ reduction performed on air-exposed $MoS_xO_{(2-x)}$ under dark, light, and interrupted conditions[173].....159

Figure 4.18. H^+ reduction performed on sulfidated MoS_2 under dark, light, and interrupted conditions[173].....160

Figure 4.19. SEM images showing the effect of sulfidation on the surface of nanopatterned MoS_2. (a) Sample 1 before sulfidation: the features are individual and distinct, and (b) after

2 sulfidations: the features remain distinct. (c) Sample 2 before sulfidation: the features are individual and distinct, and (d) after 8 sulfidations: the surface has homogenised though some features remain visible[173].....162

Figure 5.1. An XRD spectra of the thin film deposited by AACVD from a $[Fe_2(acac)_4(dmaeH)_2][ZnCl_4]$ precursor. The spectra confirmed that the film was comprised of $ZnFe_2O_4$, although it showed that α-Fe_2O_3 was also present in the film. 168

Figure 5.2. The density of the deposition solution vs percentage of ethanol. The solution was pure ethanol and methanol and so the percentage methanol was the inverse of the percentage ethanol[68]. 170

Figure 5.3. The surface tension of the deposition solution vs percentage of ethanol. The solution was pure ethanol and methanol and so the percentage methanol was the inverse of the percentage ethanol[68]. 171

Figure 5.4. The aerosol droplet diameter against percentage ethanol of the deposition solvent used for the AACVD of $ZnFe_2O_4$. The diameter differed by only 0.04 µm between the pure solutions[68].....172

Figure 5.5. The calculated enthalpies of combustion for pure ethanol, pure methanol, and the mixtures of the two which were used as deposition solvents for the AACVD of $ZnFe_2O_4$. The enthalpy of combustion of pure ethanol is nearly twice as exothermic as that of pure methanol[68]. 175

Figure 5.6. SEM images of $ZnFe_2O_4$ deposited by AACVD with the solvent composition changing from 0 % ethanol to 100 % ethanol in 10 % (by volume) increments. The increase in ethanol corresponds to a morphology shift from relatively compact to more textured[68]. 176

Figure 5.7. Average feature size of the deposited films against the enthalpy of combustion of the solvent used during deposition. The decrease in average feature size corresponds to a more exothermic enthalpy of combustion of solvent, which was the result of a higher volume of ethanol[68]. 178

Figure 5.8. A schematic representation of the conditions that resulted in homogeneous or heterogeneous reaction pathways during the deposition of ZnFe2O4 electrodes by AACVD[68]. 180

Figure 5.9. A photocurrent density comparison of the films deposited using pure ethanol and pure methanol as the deposition solvents. The light was interrupted during measurement to observe the difference between light and dark current[68].....185

Figure 5.10. The photocurrent density of the $ZnFe_2O_4$ electrodes at 1.27 V SHE against the potential ethanol in the deposition solvent. It has been established that an increase in percentage ethanol corresponds to a decrease feature size in the nanostructure[68]. 187

Figure 5.11. IPCE measurements for five electrodes deposited with solvent systematically altered between pure methanol and pure ethanol. A higher proportion ethanol in the deposition solvent correlated to a higher conversion efficiency. 189

List of Tables

Table 2-1. The etch parameters used to increase the hydrophilicity of the MoS_2 prior to nanosphere deposition. To initially ignite the plasma a strike step was used with higher power and pressure than the main etch. 47

Table 3-1. Standard O_2 etch parameters used for the nanosphere shrink step of the plasma etching process. These conditions were used unless stated otherwise..... 74

Table 3-2. The SF_6 and C_4F_8 etch parameters used to etch the surface of MoS_2 following the shrinking of the nanospheres. These parameters were used for all SF_6 and C_4F_8 etch steps unless stated otherwise. 75

Table 4-1. The molar percentages of MoS_2, MoO_3, and MoO_2 in the electrodes immediately following fabrication, in their air-exposed state, and after sulfidation as determined by XPS analysis. 148

Table 5-1. The enthalpies of formation used to calculate the enthalpies of combustion of methanol and ethanol. 174

List of Abbreviations

α	–	Transfer coefficient
β	–	Correction factor for the Du Nouy tensiometer
ΔG (kJ mol^{-1})	–	Gibbs free energy
ΔH (kJ mol^{-1})	–	Enthalpy change
ΔH_C (kJ mol^{-1})	–	Enthalpy change of combustion
ΔH_f (kJ mol^{-1})	–	Enthalpy change of formation
ΔS (J K^{-1})	–	Change in entropy
η_{coll}	–	Electron collection efficiency
θ	–	The angle at which constructively interfering X-rays leave a crystal
λ (nm)	–	Wavelength
µA	–	Microamps
υ (Hz)	–	Frequency of a light wave
π	–	Pi
ρ (kg m^{-3})	–	Density
σ (N m^{-1})	–	Surface tension
Σ	–	Sum
φ (J)	–	Work function
ϕ_{inj}	–	Quantum yield for electron injection
Ω	–	Ohm
Ø	–	Diameter
A	–	Area

AACVD	–	Aerosol assisted chemical vapour deposition
Ag/AgCl	–	Silver / silver chloride reference electrode
AM 1.5	–	Air mass 1.5 (1000 W m^{-2})
B.E	–	Binding energy
c	–	Lightspeed (3×10^8 m s^{-1})
C (mol cm^{-3})	–	Concentration
°C	–	Degrees centigrade
d (Å)	–	Distance between crystal lattice planes
d_a (m)	–	Aerosol droplet diameter
D (cm^2 s^{-1})	–	Diffusion coefficient
DC	–	Direct current
e^-	–	Electron
eV (J)	–	Electronvolt
E (J)	–	Energy
E^0 (V)	–	Standard reduction potential
E_b (eV)	–	Electron binding energy
E_c (eV)	–	Energy of the conduction band
E_F (eV)	–	Energy of the Fermi level
E_g (eV)	–	Band gap of a semiconductor
E_k (eV)	–	Kinetic energy of a photoelectron
E_{Red} (V)	–	Adjusted reduction potential
E_{rev} (V)	–	Reversible potential
EtOH	–	Ethanol

E_{tn} (V) – Thermoneutral potential

E_V (eV) – Energy of the valence band

E_{VAC} (V) – Absolute vacuum potential

f (Hz) – Frequency of the ultrasonic oscillator

F – Faradays constant (96485 C mol^{-1})

F_a (N) – Force applied by the Du Nouy tensiometer loop

FEGSEM – Field emission gun scanning electron microscopy

FTO – Fluorinated tin oxide

g – Acceleration due to gravity (9.81 m s^{-2})

GC – Glassy carbon

h – Planck constant (6.63 × 10^{-34} m^2 kg s^{-1})

h^+ – Mobile hole

Hz (s^{-1}) – Hertz

HER – Hydrogen evolution reaction

i_0 (A) – Exchange current

i_P (A) – Peak current

i-V – Current-voltage measurements

ICP – Inductively coupled plasma

IPA – Isopropyl alcohol

IPCE – Incident photon conversion efficiency

j_0 – Exchange current density

j-V – Current density-voltage measurements

J – Joules

J_{br}	–	Recombination in the semiconductor bulk
J_{dr}	–	Recombination in the space charge region
J_{et}	–	Thermal promotion over the interfacial potential barrier
J_{ss}	–	Recombination at defect sites at the semiconductor / liquid interface
J_t	–	Tunnelling through the interfacial potential barrier
K	–	Degrees Kelvin
LHE	–	Light harvesting efficiency
m (kg)	–	Mass
M	–	Moles
Mol	–	Moles
Mol. %	–	Molar percent
mV dec^{-1}	–	Tafel slope
n	–	Number of electrons
n-type	–	Negative type semiconductor
NHE	–	Normal hydrogen reference electrode
NS	–	Nanospheres
NSL	–	Nanosphere lithography
OER	–	Oxygen evolution reaction
p-type	–	Positive type semiconductor
PEC	–	Photoelectrochemical
R	–	Gas constant (8.315 J mol^{-1} K^{-1})
R_l	–	Radius of the Du Nouy tensiometer loop
RDE	–	Rotating disk electrode

RF	–	Radio frequency
Sat.	–	Saturated
SCCM	–	Standard cubic centimetres per minute
SE	–	Secondary electron
SEM	–	Scanning electron microscopy
SHE	–	Standard hydrogen reference electrode
SSR	–	Solid state reaction
t (s)	–	Time
T (K)	–	Temperature
TLD	–	Through the lens detector
v (V s^{-1})	–	Potential scan rate
v_0	–	Volume of the liquid suspended in the Du Nouy tensiometer ring
V	–	Volts
V (m^3)	–	Volume
W	–	Watts
XPS	–	X-ray photoelectron spectroscopy
XRD	–	X-ray diffraction spectroscopy

1.0 Introduction

1.1 Solar Power

The surest way to avoid future energy shortages is a gradual transition from the current fossil-fuel heavy energy mix to alternative power sources. This requires that in the interim the diverse range of renewable energies, nuclear, and fossil fuels that constitutes the current energy mix be maintained, but the proportion produced by renewable energies and nuclear power be gradually increased at the expense of fossil fuels[1]. Solar power has several strengths that make it an attractive addition to this energy mix. The sun provides the earth's surface a prodigious $3x10^{24}$ J per year, which amounts to 5,000 times the total global energy production during 2013[2,3]. It is also available over the entire Earth's surface, although sunnier climes are more amenable to utilisation[4]. High costs and low efficiencies currently inhibit solar power from being fully exploited however, and more research and development is required for the full potential of solar power to be realised[5].

1.1.1 The Photovoltaic Effect

Solar harvesting technology began with the photoelectric effect. This was the observation that photons which exceed a threshold energy excite electrons from the surface of a metal, causing an emission of electrons[6]. This work provided evidence that photons exist as

discrete packets of energy, the exact energy of which depends on the frequency of the wave as per Eq. 1.1[7].

$$E = h\upsilon \qquad \text{(Eq. 1.1)}$$

Where E is the energy of the photon, h is the Planck constant, and υ is the frequency of the wave.

The photovoltaic effect is the result of capturing photo-promoted electrons within an electrical circuit to create an electrical current. To obtain this efficiently from the sun it is necessary that the light absorbent material captures the incident light with the greatest spectral irradiance at the surface of Earth[7]. This region of the electromagnetic spectrum ranges from ≈320 – 1100 nm in wavelength[8]. Capturing electrons promoted from photons of this energy requires a material with an equivalent band gap (forbidden zone) between its conduction and valence bands. Materials which have band gaps of 0.5 - 3.0 eV are capable of absorbing and converting all or part of this spectrum and are termed semiconductors[7].

1.1.2 Semiconductors

Semiconductors are the materials used to exploit the photovoltaic effect to generate electrical current. Semiconductors have a small band gap (0.5 - 3.0 eV) between the conduction and valence bands, as opposed to conductors in which the conduction and valence bands overlap, and insulators which have band gaps >3.0 eV. The band gap in semiconductors is of a size that incident photons from the visible spectrum are able to

promote an electron from the filled valence band to the empty conduction band. The promoted electron leaves a mobile positive charge in the valence band termed a hole (h^+). In a photovoltaic device a potential difference arising from an in-built asymmetry mobilises these charge carriers and thereby produces an electrical current[7].

The in-built asymmetry can be achieved by pairing negative (n-type) semiconductors with positive (p-type) semiconductors. In n-type semiconductors electrons are the majority charge carriers, and holes are the minority charge carriers, whilst in p-type the charges are reversed. The type is determined by the position of the Fermi level within the band gap of the semiconductor[7].

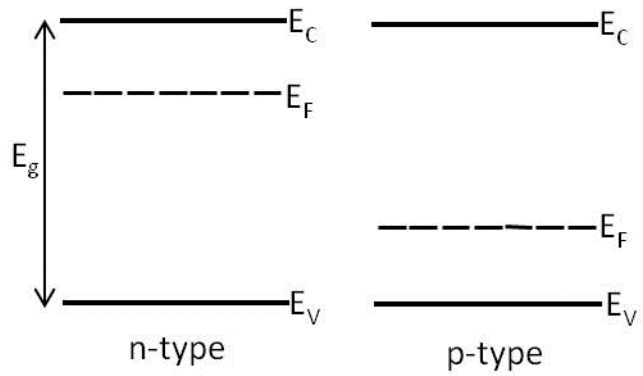

Figure 1.1. The relative energy levels of the conduction band (E_C), valence band (E_V), and Fermi level (E_F) of n-type and p-type semiconductors. The potential difference between the E_C and E_V is the band gap (E_g) of the semiconductor[7].

The Fermi level is the highest energy level within a semiconductor that is full of electrons at 0 K. Electron and hole densities vary exponentially with the position of the Fermi level within the band gap. As such semiconductors with a Fermi level closer to the conduction

band have high electron densities and are n-type, while semiconductors with a Fermi level closer to the valence band have high hole densities and are p-type[7,9].

1.1.3 Sunlight to Electricity

A material with a band gap of 3.88 eV will be able to convert the highest energy 320 nm light, but any photons with a longer wavelength will not be able to promote an electron fully to the conduction band. These electrons decay back to the valence band without being drawn into the external circuit. Similarly a semiconductor with a bandgap of 1.13 eV will be able to absorb and convert all light in the range of 320 – 1100 nm, however photons with wavelengths <1100 nm will overpromote electrons. These then decay back to the conduction band, losing energy in the process. The net energy of each converted electron by this hypothetical semiconductor is therefore capped at 1.13 eV.

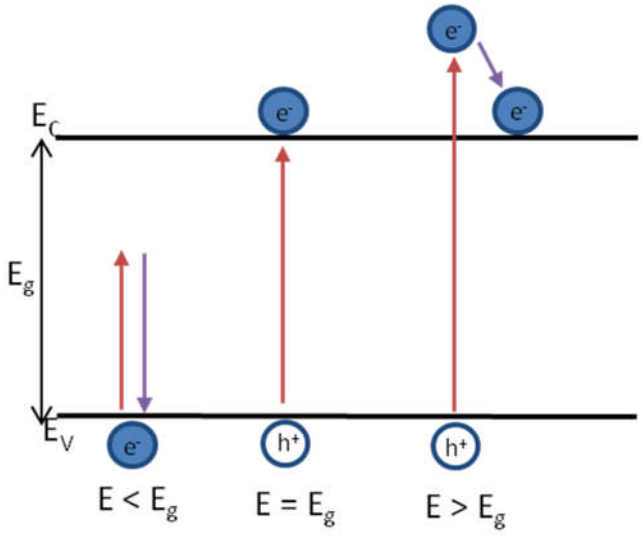

Figure 1.2. Electrons promoted by photons in a two band photoconverter. Photons with energy $E < E_g$ cannot promote electrons to an excited state. Photons with energy $E > E_g$ can promote electrons but any excess energy is lost as heat as the electron relaxes to the conduction band. As such photons with $E >> E_g$ produce the same effect as photons with $E = E_g$[7].

As the incident spectrum is fixed the efficacy of a photoconverter depends on the band gap of the semiconductor. To design an efficient photovoltaic system it is necessary to use a material with a band gap that is optimised between absorbing a significant part of the incident light, whilst not wasting too much energy through overpromotion[10,11]. The selection of appropriate materials to construct a photovoltaic system is therefore a key and complex concern.

An additional problem with contemporary photovoltaics is that charge carriers, once photogenerated, must be utilised immediately or they will relax back to their unexcited

state[12]. One way to store solar energy for a prolonged period is to use the photogenerated charge carriers in a redox reaction to synthesise a chemical energy store. A device capable of this is called a photoelectrochemical (PEC) cell[13].

1.2 Photoelectrochemical Water Splitting

PEC cells operate in a similar way to the photosynthesis of glucose by plants[14]. In theory a wide variety of compounds could be photosynthesised, however designing an efficient PEC cell is a complex endeavour. As such to date most research efforts have focussed on the comparatively simple photoelectrolysis of water to produce H_2 and O_2 gases[13,15,16].

A PEC cell consists of an anode and a cathode separated by an electrolyte. Either one or both electrodes could be a semiconductor photoelectrode. If only one is a photoelectrode a metal, typically Pt, is used as the other electrode[17].

1.2.1 The Energetics of Water Splitting

PEC water splitting utilises semiconductors as both the light absorber and energy converter to store chemical energy in the H_2 chemical bond. H_2 gas is generated in the hydrogen evolution reaction (HER) (Eq. 1.2)[17].

$$2H^+_{(aq)} + 2e^- \rightleftharpoons H_{2(g)} \qquad \text{(Eq. 1.2)}$$

The corresponding half-reaction is the oxygen evolution reaction (OER) (Eq. 1.3)[17].

$$H_2O_{(l)} + 2h^+ \rightleftharpoons {}^1/_2O_{2(g)} + 2H^+_{(aq)} \qquad \text{(Eq. 1.3)}$$

Together these comprise water splitting. The electrical energy is stored due to the Gibbs free energy (ΔG) of H_2 being elevated 237.2 kJ mol^{-1} at 298 K and 1 bar with respect to water. The reversible potential (E_{rev}) can be calculated as 1.23 V per electron transferred by (Eq. 1.4)[17].

$$E_{rev} = \frac{-\Delta G}{nF} \qquad \text{(Eq. 1.4)}$$

Where n is the number of electrons transferred, and F is the Faraday constant.

For light driven water splitting to be achieved the semiconductor materials must therefore have a bandgap >1.23 eV, which corresponds to wavelengths shorter than 1008 nm[17]. In practice there are several inhibiting factors such as recombination and the relatively slow rate of the OER, and an overpotential is required to drive the reaction. As the overall reaction is endothermic additional energy is required to account for the increase in entropy (ΔS). The potential at which this is exactly accounted for is the thermoneutral potential (E_{tn}) (Eq. 1.5). The overall enthalpy change (ΔH) in the system is 283.93 kJ mol^{-1}, and the thermoneutral potential is therefore 1.47 V[18].

$$E_{tn} = \frac{-\Delta H}{nF} \qquad \text{(Eq. 1.5)}$$

Additional overpotential is required to account for the sluggish reaction kinetics of the OER and the HER which is discussed in greater detail in Sections 1.2.4 and 1.2.5. Taking into account of all losses the potential required to drive water splitting is 1.6 – 2.4 eV per electron/hole pair[19,20].

Having generated sufficient potential it would be possible to split water using an electrolyser, however a PEC device can theoretically be more efficient[21]. This increase in efficiency comes at a price of additional complexity as the band edges must also match the redox potentials of water. The reduction potential of hydrogen (Eq. 1.2) is by definition 0 V against a standard hydrogen electrode (SHE) on a Pt electrode, from the reversible potential (Eq. 1.4) the oxidation potential of water is therefore +1.23 V SHE[22,23]. The ideal material would have a valence band at a potential more positive than 1.23 V, and a conduction band more negative than 0 V[17]. The band positions of several photoelectrode candidate semiconductors are shown in comparison to the redox potentials of water in Figure 1.3[21,24,25,26,27].

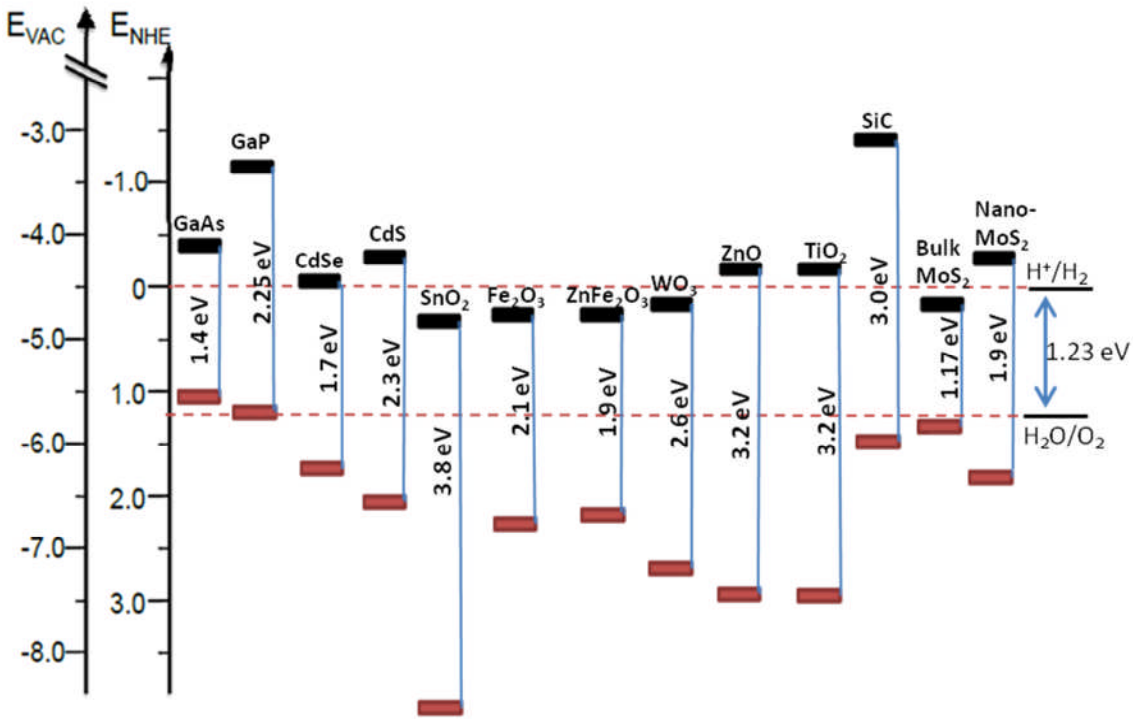

Figure 1.3. The band positions of a selection of candidate photoelectrode materials shown against the reduction potential of hydrogen and the oxidation potential of water. E_{VAC} and E_{NHE} correspond to the absolute vacuum level, and standard (normal) hydrogen electrode respectively[21,24,25,26,27].

On Figure 1.3 CdSe and CdS best match the requirement of the photoelectrode to straddle the redox potentials of water. It is possible to tune the suitability of other semiconductors by altering the band gap and band edges of semiconductors through techniques such as nanostructuring[28,29]. In addition to the conduction and valence band positioning the photoelectrode must possess strong light absorption, high chemical stability, and efficient charge transport[21]. Hence far no material has been found that can used in an economically viable PEC cell[21].

1.2.2 Photoelectrochemical Cells

In Figure 1.4 idealised PEC cells are shown where one photoelectrode material with a conduction band negative of the proton reduction potential, and a valence band positive of the water oxidation potential are presented[13].

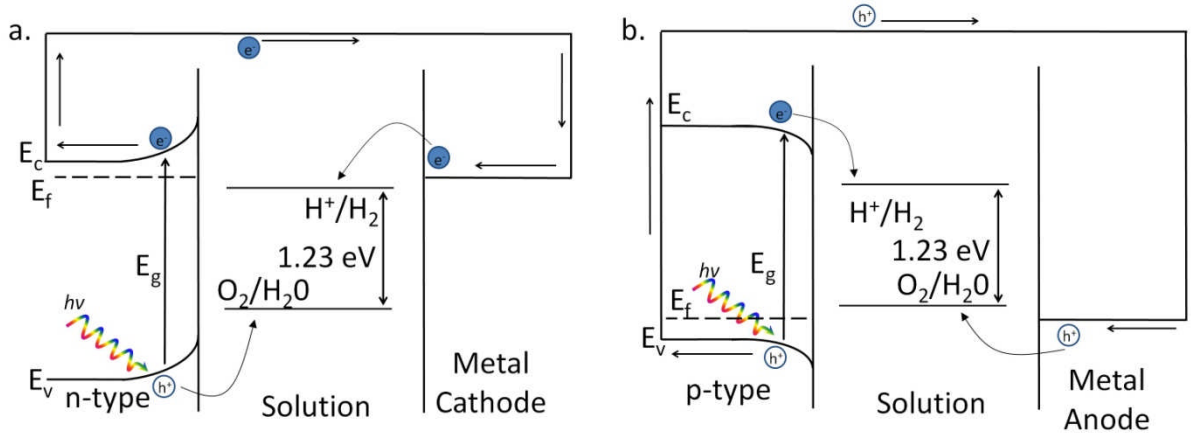

Figure 1.4. Configurations of one photoelectrode water splitting PEC cells. a. comprises of a n-type photoanode and a metal cathode, and b. of a p-type photocathode and a metal anode.

The band bending at the semiconductor / electrolyte interface in Figure 1.4 is the result of equilibrium being established between the Fermi level of the semiconductor and the electrochemical potential of the electrolyte. This produces a space-charge layer on both sides of the junction in which the charge distribution differs from the bulk material[13]. In n-type semiconductors electrons flow from the semiconductor to the electrolyte resulting in a positive space charge layer in the semiconductor, and a negative double layer (Helmholtz plane) at the photoanode / electrolyte interface. The negative charge repulses additional electrons and hence the bands of the semiconductor bend to negative potentials due to

this additional energy requirement. Upon illumination the minority charge carrier (h^+) is attracted by the negative double layer and thus oxidation occurs at the surface of the n-type electrode. The majority charge carrier (e^-) is driven by the electrical asymmetry through an external circuit to the metal cathode where it reduces protons to H_2 gas. A p-type photocathode behaves analogously although with the charges reversed. The equilibrium established between the semiconductor and electrolyte results in a positive Helmholtz layer, causing the bands bend to more positive potentials. Therefore electrons are drawn to the photocathode / electrolyte interface, while holes are driven to the metal anode[7,13,24,30,31,32]. In practice however, many photogenerated charge carriers are lost to competing processes collectively termed recombination.

1.2.3 Charge Carrier Recombination

The five dominant processes competing with the desired charge transfer are: recombination at defect sites at the semiconductor / liquid interface (J_{ss}), recombination in the semiconductor bulk (J_{br}), recombination in the space charge region (J_{dr}), thermal promotion over the interfacial potential barrier (J_{et}), and tunnelling through the interfacial potential barrier (J_t) (Figure 1.5)[17,32,33,34].

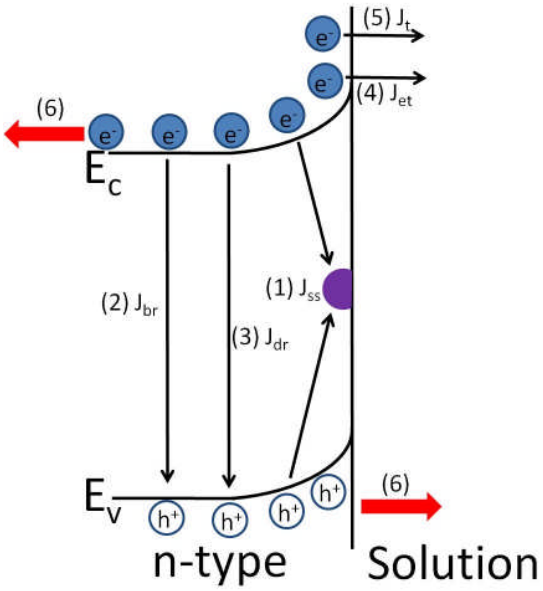

Figure 1.5. The five major types of recombination that can occur to photogenerated charge carriers in a PEC cell. (1) Recombination at defect sites at the semiconductor / liquid interface (J_{ss}). (2) Recombination in the semiconductor bulk (J_{br}). (3) Recombination in the space charge region (J_{dr}). (4) Thermal promotion over the interfacial potential barrier (J_{et}). (5) Tunnelling through the interfacial potential barrier (J_t). (6) Represents the desired charge transfer process[17,32,33,34].

Recombination processes inhibit the efficiency of PEC devices as photogenerated charge carriers are lost before they can be participate in the redox reaction[35]. These losses can be mitigated against through nanostructuring the photoelectrode, however. Nanostructuring reduces the mean path length of the charge carriers thereby reducing the time between generation and use, and limiting the chance of encountering an particle of opposing charge[36,37]. Increased light absorption is an additional advantage of nanostructuring[36].

1.2.4 Oxygen Evolution Reaction

To liberate the protons necessary for the HER (Eq. 1.2) it is first necessary to oxidise water as per (Eq. 1.3). Oxides are preferred as the anode material as these are resistant to further oxidation by either adsorbed oxygen or the generated O_2 gas[38,39]. In particular transition metal oxides such as TiO_2, WO_3 and ferrites (MFe_2O_3) have been attempted, although no fully capable material has emerged[40,41,42,43]. The sluggish reaction kinetics due to the complex four h^+ reaction are one of the key difficulties to identifying an appropriate material[44].

The exact mechanism of water oxidation remains a matter of some debate, however it is posited that it follows a four-step mechanism[45].

$$OH^-_{(aq)} + h^+ \rightleftharpoons OH_{(ads)} \qquad \text{(Eq. 1.6)}$$

$$OH_{(ads)} + h^+ \rightleftharpoons O_{(ads)} + H^+_{(aq)} \qquad \text{(Eq. 1.7)}$$

$$O_{(ads)} + OH^- + h^+ \rightleftharpoons OOH_{(ads)} \qquad \text{(Eq. 1.8)}$$

$$O_{(ads)} + OH_{(ads)} + h^+ \rightleftharpoons O_{2(g)} + H^+_{(aq)} \qquad \text{(Eq. 1.9)}$$

$$OOH_{(ads)} + h^+ \rightleftharpoons O_{2(g)} + H^+_{(aq)} \qquad \text{(Eq. 1.10)}$$

A OH^- ion is adsorbed to a catalytic site by a hole in step 1 (Eq. 1.6). Step 2 consists of a second hole oxidising the $OH_{(ads)}$ to $O_{(ads)}$ (Eq. 1.7), with the $O_{(ads)}$ therefore having a double bond to the catalytic site. Following this step 3 is either a repeat of step 1, or a OH^- ion is oxidised by a third hole directly onto the $O_{(ads)}$, resulting in $OOH_{(ads)}$ (Eq. 1.8). If step 3 was a

repeat of step 1 a fourth hole oxidises an $O_{(ads)}$ and a nearby $OH_{(ads)}$ causing them to desorb from the surface as O_2 (Eq. 1.9). Alternatively if step 3 generated $OOH_{(ads)}$ the fourth hole deprotonates the compound and it desorbs as O_2 (Eq. 1.10). Deviations along the same basic scheme have been proposed and mostly differ as to when, or indeed whether, the $OH_{(ads)}$ deprotonates prior to the final desorption step[45].

α-Fe_2O_3 is a well studied photoanode material due to its well positioned and sized bandgap (≈2.1 eV), its chemical stability, non-toxicity, abundance, and low cost. However, its use is hindered by a short hole diffusion length (2 – 4 nm), and brief excited state lifetime (10^{-12} s)[46,47]. The rate constant of water oxidation is ≈ 10 – 0.1 s^{-1}, and is thus far slower than the charge carrier lifetime[48]. Further, 500 nm wavelength light penetrates ≈118 nm into α-Fe_2O_3, and as the hole-diffusion length is considerably shorter high rates of recombination are a major source of inefficiency[49]. Nanostructuring the morphology to make the feature size on the same scale as the transport length can be used to increase the probability of charge carriers reaching the electrode / electrolyte interface, however[49]. α-Fe_2O_3 has been well studied as a photoanode material, but still remains unsuitable[43]. As a result the suitability of bi-metallic ferrites such as $ZnFe_2O_4$ have been researched as photoanodes[43].

1.2.5 Hydrogen Evolution Reaction

The protons liberated by the OER (Eq. 1.3) are reduced in the HER (Eq. 1.2) to H_2 gas in order to store the incident solar energy. The HER in acidic media is known to proceed via two pathways, each composed of two reaction steps. The first step is the Volmer reaction

(Eq. 1.11), this is common to both pathways and is otherwise known as the primary discharge step. In this step a proton is adsorbed to the surface of the cathode[50]. The subsequent step is either the Heyrovský reaction (Eq. 1.12), or the Tafel reaction (Eq. 1.13). The Heyrovský reaction is an electrochemical desorption step in which a second proton from solution binds to an adsorbed proton to produce H_2 gas[50]. The alternative is recombination / desorption step termed the Tafel reaction. This consists of the H_2 gas being formed from two protons adsorbed during the Volmer reaction[50].

$$H_3O^+ + e^- \rightleftharpoons H_{ads} + H_2O \qquad b = \frac{2.3RT}{\alpha F} \approx 120\ mV \qquad \text{(Eq. 1.11)}$$

$$H_{ads} + H_3O^+ + e^- \rightleftharpoons H_2 + H_2O \qquad b = \frac{2.3RT}{(1+\alpha)F} \approx 40mV \qquad \text{(Eq. 1.12)}$$

$$H_{ads} + H_{ads} \rightleftharpoons H_2 \qquad b = \frac{2.3RT}{2F} \approx 30mV \qquad \text{(Eq. 1.13)}$$

Where b is the Tafel slope, R is the gas constant, T is the absolute temperature, and α is the transfer coefficient[50,51,52,53].

The reaction pathway and rate determining step may be elucidated by calculating the Tafel slope. The Tafel slope is obtained by a plot of applied overpotential against $\log_{10}|j|$ in the Tafel region[54]. As the Tafel region can be ambiguous in this work it was taken as being 20 % to 80 % of the proton reduction wave. For internal consistency the slope was the average gradient over this region.

As R, T and F are constants the Tafel slope gives an estimation of the transfer coefficient, which is classically interpreted to indicate the transition state of the reaction coordinate[55].

Due to the fast kinetics of the HER on Pt it is considered a benchmark catalyst. As the Tafel slope of HER on Pt is 30 mV dec^{-1} the reaction is known to proceed through the Volmer-Tafel reaction (Eq. 1.11) followed by (Eq. 1.13)[51,52,53]. Pt is a high cost material however, leading to a search for other highly active HER catalysts[52].

An optimal HER catalyst requires that the free energy of adsorbed hydrogen (ΔG_H) be as close to zero as possible, as such the protons are bound neither too strongly or too weakly to the electrode surface[50,56,57]. The reagents and intermediates must bind strongly to the catalyst so that they are likely to adsorb to the surface, and thus the reaction can proceed. However, if the intermediates or products bind too strongly to the catalyst desorption is inhibited and the products cannot be obtained[58]. A well used technique to identify promising new catalysts is a Sabatier plot of exchange current density (j_0) against ΔG_H (Figure 1.6)[58].

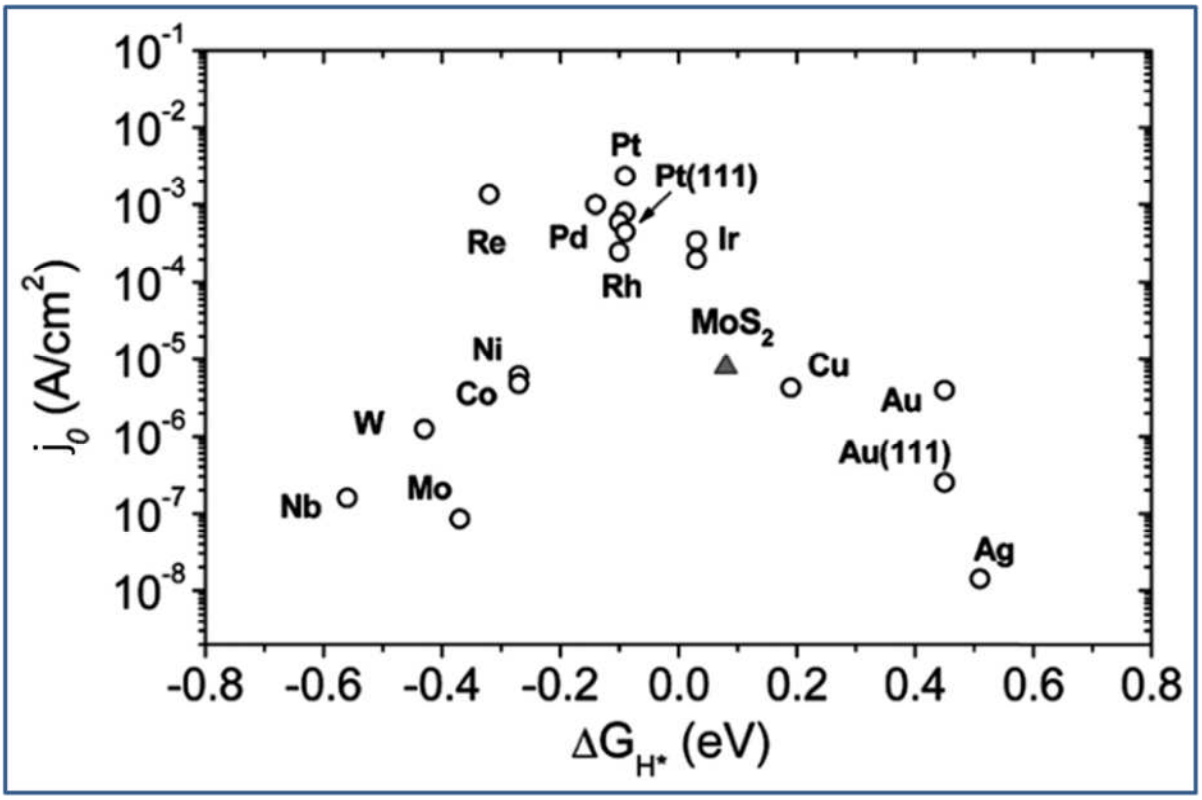

Figure 1.6. A Sabatier plot of exchange current density against energy of adsorbed hydrogen (ΔG_H) used to help identify potential new HER catalysts[59].

Figure 1.6 shows that the exchange current density increases as ΔG approaches zero. On the left side of the graph (-ΔG) the proton adsorption (Eq. 1.11) is the rate determining step, and j_0 increases as the proton binds more strongly to the electrode. At the peak the rate determining step transitions to the desorption step (Eq. 1.12) or (Eq. 1.13), and the increasing strength of adsorption progressively slows the reaction by hindering the desorption mechanism[60].

Sabetier analysis has led to interest in MoS_2 for the HER as the MoS_2 $(10\bar{1}0)$ edge sites have a ΔG_H of +0.08 eV and j_0 of 7.9 μA cm^{-2} which places it superior to the common metals, and

slightly inferior to the high cost Pt-group metals[59]. These edge sites are scarce in bulk MoS_2, however, their number may be increased by nanostructuring[59].

1.3 Nanostructuring

The promise of reduced material requirements, higher surface area, improved charge transport and refined catalysis has insured that nanostructuring is one of the most common approaches to PEC research[27,61]. Many different nanostructuring techniques have been applied including: electrodeposition[62], cluster deposition[63], sonochemical synthesis[64], chemical exfoliation[54], and sol-gel synthesis[65]. In this work a combination of nanosphere lithography (NSL) and plasma etching was used to nanopattern MoS_2, and aerosol assisted chemical vapour deposition (AACVD) was used to deposit nanostructured $ZnFe_2O_4$.

Nanostructuring techniques can be defined as either top-down or bottom up. In top-down techniques bulk materials are reduced in size down to nanoscale though techniques such as plasma etching or chemical exfoliation[66]. Bottom-up on the other hand uses small building blocks that self-assemble into larger, more complex structures[66]. Self-assembly is defined as the spontaneous organisation of larger structures from two or more components[67]. AACVD and sol-gel synthesis are examples of a bottom-up approach[68,69].

1.3.1 Nanosphere Lithography and Plasma Etching

Nanosphere lithography (NSL) can be used for either top-down or bottom-up nanostructuring techniques. Either method begins with the deposition of monodisperse spherical colloids (nanospheres) onto the materials surface[66]. The suspension fluid is then allowed to evaporate leaving a monolayer of nanospheres on the surface termed a resist. The top-down approach then etches away the interstices between nanospheres, leaving a pillar beneath each individual nanosphere[70]. The bottom-up approach deposits a material, usually metal, over the top of the nanospheres and substrate. When the nanospheres are subsequently removed accumulated material is left in the interstices of the nanospheres[66]. These are depicted in Figure 1.7.

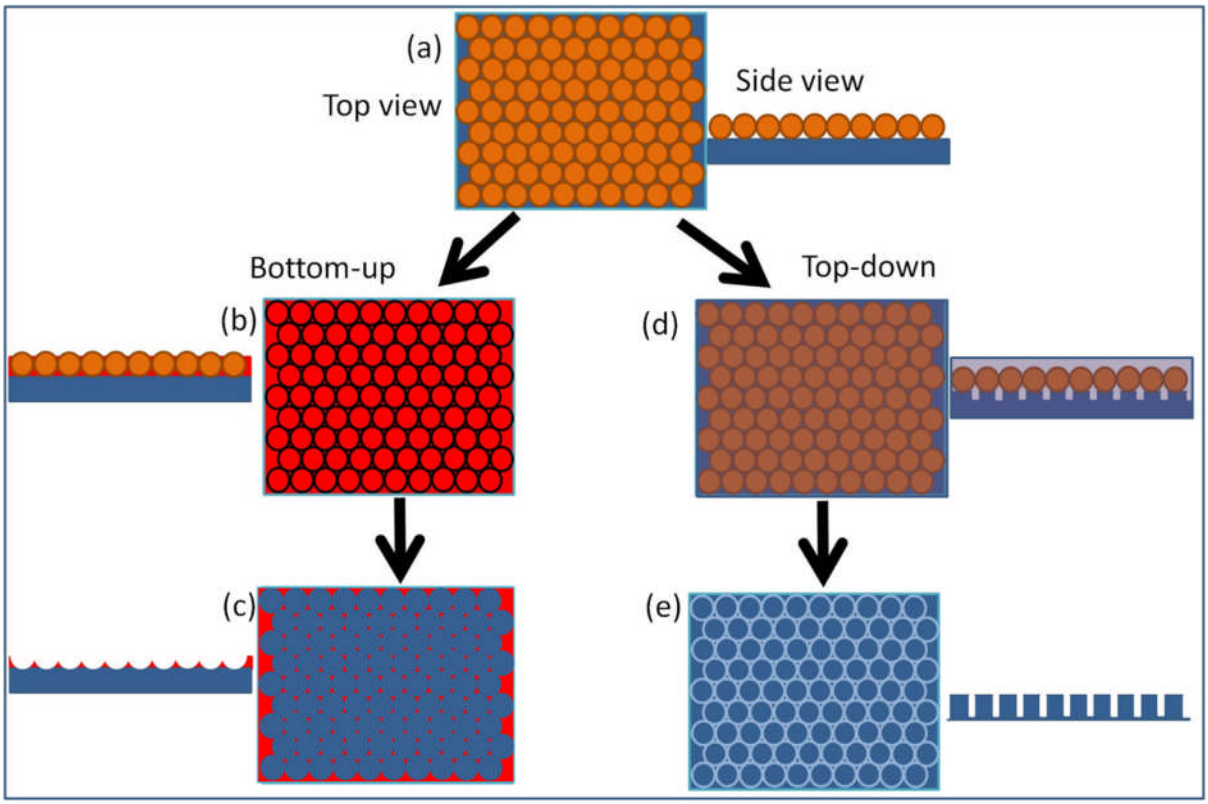

Figure 1.7. Bottom-up and top-down nanosphere lithography. (a) Orange nanospheres hexagonally close packed on a blue substrate. (b) Material deposited over the top of the nanospheres and substrate. (c) Following removal of the nanospheres the material deposited in the interstices remains. (d) A selective etchant is used to remove material from the interstices of the nanospheres. (e) After removal of nanospheres pillars remain under the nanospheres' positions[66,70].

NSL has been used to create a variety of nanopatterns such as nanodots, nanowells, and nanopillars[71–73]. In this work a top-down technique was applied to create MoS_2 nanopillars and nanowells. A modified Langmuir-Blodgett method was used to deposit the nanospheres on the surface of the MoS_2, and plasma was used to etch the surface. The Langmuir-Blodgett method is a commonly used NSL technique whereby nanospheres are deposited

on a water-air interface and compressed into a self-assembled monolayer either by reducing the water surface area or by the addition of more nanospheres[74–76]. The process used to formulate the nanowell pattern is the first time nanowells have been fabricated by NSL without an additional step to deposit materials into the interstices.

A versatile etchant for top down NSL is plasma. Through the use of different etchant gases the nanospheres or surface may be selectively etched, or the aspect ratio of the features may be controlled[77]. Oxygen plasma selectively etches polystyrene nanospheres, leaving metal surfaces unetched. Oxygen plasma shrinks the individual nanospheres symmetrically, and can therefore be used to adjust the final morphology by reducing the surface area covered by each nanosphere[77]. SF_6 plasma, on the other hand, selectively etched the MoS_2 surface but could not reach an area covered by a nanosphere[78,79]. A problem with this is the top of the feature is exposed to SF_6 plasma for the entire etch length while the remainder of the feature is only exposed after it has been etched from the bulk. As a result without a passivating agent the features will be isotropic with wide bottoms and narrow tops. A passivation agent, such as C_4F_8, is used in conjunction with the etchant to inhibit over etching. It covers the exposed surfaces and slows the rate of etching. As the exposed features are subjected to the same length of time of etchant and passivation layer this presents an elegant way to promote anisotropy[78,79]. A combination of these three plasmas in conjunction with NSL is able to provide a diverse range of nano-morphologies.

1.3.2 Aerosol Assisted Chemical Vapour Deposition

AACVD is a solution based variant of chemical vapour deposition, and a bottom-up nanostructuring technique[80]. A precursor solution is mixed with a volatile solvent and vaporised in order to be transported to the deposition chamber by a carrier gas[68,81]. The deposition chamber is heated from the bottom providing a temperature gradient. This increase in temperature causes the precursor to decompose to the desired product. Two decomposition pathways are possible, and the morphology of the deposited film is in part determined by which one occurred[68,82]. The difference in decomposition pathways is whether the precursor nucleates in the vapour phase, or on the target substrate[68].

Nucleation on the target substrate is termed heterogeneous deposition and is similar in practice to flame pyrolysis[83,84]. The film is produced by adsorption and decomposition of material onto the heated substrate. As the material decomposes it draws energy from the substrate generating a cooling effect, and subsequent adsorbed materials therefore have less energy available to decompose. The practical upshot is a compact film without fine nanoscale features[68,82]. Alternatively, if the temperature in the deposition chamber is sufficient, the precursor nucleates in the vapour phase and is termed homogeneous nucleation. Homogeneous nucleation can be encouraged by the use of a combustible solvent with a highly exothermic enthalpy of combustion. Solvent combustion creates a steep local temperature gradient leading to vapourisation and condensation of nanoscale particles within the thermal boundary region of the reacting droplets[68,82]. In the case of homogeneous nucleation the precursor is already decomposed to nanoscale particles prior to impacting the substrate. As such there is less of a cooling effect on the substrate and the

particles are nanoscale before striking the substrate homogenous nucleation. This process typically creates porous, high surface energy films of the sort typically suitable for PEC applications[68,82,83].

1.3.3 Mass Transport to Nanoelectrode Arrays

In practice the rate of each reaction is determined partially by the rate of the electron transfer reaction, and partially by the rate of transport of the reactant species to the electrode surface. The rate of transport of a species in an electrochemical cell is a function of migration, convection, and diffusion[85]. In this work convection was not used, and the effects of migration were limited through the use of a large excess of supporting electrolyte. Therefore diffusion was the only significant mechanism of mass transport. The length of diffusion in one dimension can be calculated by Einstein's relation (Eq 1.14)[86].

$$\langle x \rangle = \sqrt{2Dt} \qquad \text{(Eq 1.14)}$$

Where $\langle x \rangle$ is the length of diffusion, D is the diffusion coefficient, and t is the time taken to complete the voltammetric sweep. When considering nanoelectrode arrays of the type fabricated in Section 3.0 it is necessary to consider the diffusion length relative to the radius of the features and peak separation distance[87]. Four categories of diffusion regime have been identified[87].

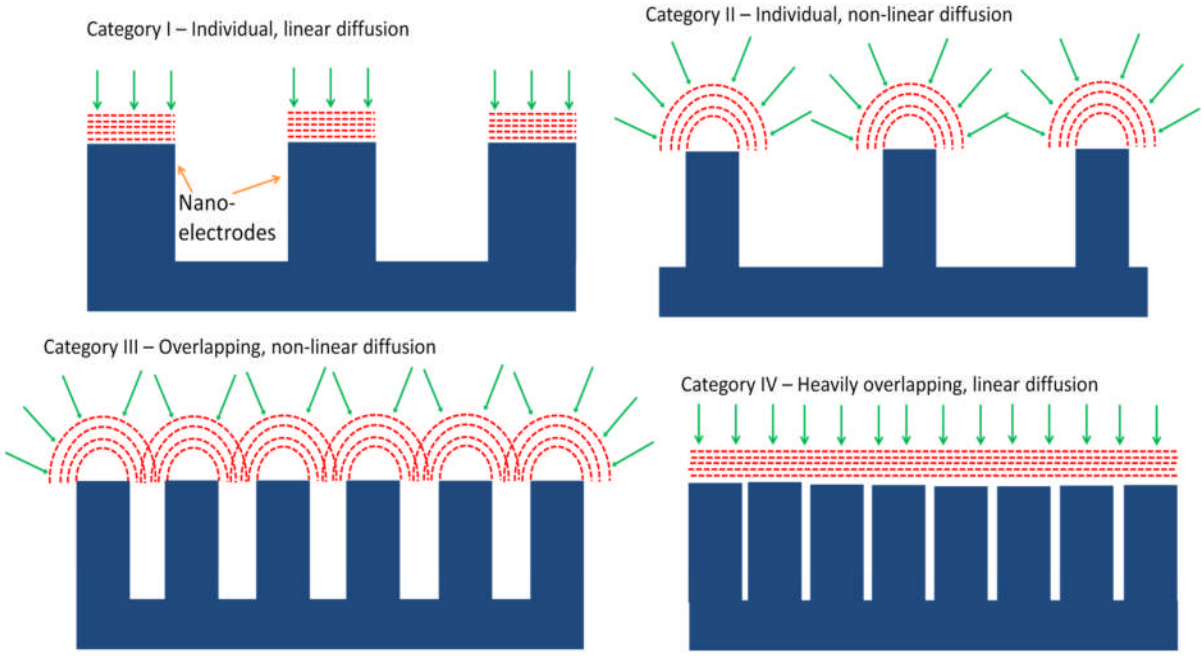

Figure 1.8. The four categories of diffusion regime observed on micro- and nano-electrodes defined by whether the feature size and peak separation are longer or shorter than the diffusion length of the analyte[87].

In category I the diffusion length is smaller than both the radius of the features and peak separation length, and individual, linear diffusion dominates leading to a voltammetric response similar to a scaled down macroelectrode[87]. Category II is defined as having the diffusion length shorter than peak separation but greater than the microdisk radius. In this case the diffusion to the features is individual and non-linear[87]. In category III the diffusion length is greater than both the radius of the features and peak separation length, leading to overlapping, non-linear diffusion layers. Due to this overlap the microelectrodes deplete the same volume of electrolyte resulting in reduced current compared to category II[87]. Finally, category IV consists of microelectrodes with feature radii and peak separations far smaller than the diffusion length. This causes the diffusion layers to heavily overlap, and the

diffusion to become linear across the entire array[87]. The microelectrodes in conjunction behave as a single macroelectrode of the same size as microelectrode array[86].

Since the diffusion length was orders of magnitude greater than the difference between feature separation and electrode radius (ca. 100 nm) in any of the morphologies produced the electrodes were treated as class IV systems. Thus as discussed in Section 1.2.5 the Tafel slope and onset potential were used as a relative measure to compare the catalytic performance between MoS_2 morphologies.

1.4 $ZnFe_2O_4$ as an Oxygen Evolution Photocatalyst

$ZnFe_2O_4$ has many of the desired properties of a prospective photoanodic material[88,89]. The band gap of $ZnFe_2O_4$ is 1.9 eV, slightly smaller than the 2.1 eV band gap of the widely studied α-Fe_2O_3[90,91]. 1.9 eV is wide enough to power PEC water splitting and provide the necessary overpotential, and the 0.2 eV smaller band gap allows $ZnFe_2O_4$ to harvest more sunlight than α-Fe_2O_3[68]. This is offset by the additional complexity in synthesising a bi-metallic oxide[68]. The band positions are, however, too positive to be ideal for PEC water splitting (Figure 1.3)[92]. $ZnFe_2O_4$ also possesses the necessary PEC photoelectrode properties of being stable to prolonged exposure to sunlight, resistive to undesirable processes such as dissolution, photocorrosion, and oxidation, and is earth abundant[68,93].

In this work $ZnFe_2O_4$ was used to prove that precursor decomposition pathways in AACVD can be controlled by shifting the deposition solvent composition systematically between

ethanol and methanol. $ZnFe_2O_4$ was chosen because metal ferrites are an emerging class of photoelectrode materials and it was possible to assess the changes of texture by measuring the photocurrent in a standard PEC cell[68].

1.4.1 $ZnFe_2O_4$ Structure and Properties

Bulk $ZnFe_2O_4$ has a spinel structure which contains two different cationic sites. These are eight tetrahedral A sites and 16 octahedral B sites. Fe^{3+} ions occupy both A and B sites, but Zn^{2+} ions exclusively occupy the tetrahedral A sites[94]. The lattice parameter is ≈ 0.85 nm[95].

While the band gap of $ZnFe_2O_4$ is better suited to PEC water oxidation than that of α-Fe_2O_3 it shares the short hole diffusion length and excited state lifetime of α-Fe_2O_3[96]. This combination causes many photogenerated charge carriers to be lost via recombination[97,98]. Due to this weakness much research has gone into structuring the shape, morphology and size of the α-Fe_2O_3 to be more suitable for PEC water splitting, and similar efforts have been applied to $ZnFe_2O_4$[88].

Recombination is an issue because of the disparity between the timescales of the OER and charge carrier lifetimes. The OER happens on a timeframe of ≈ 0.1 – 10 s^{-1}, while the lifetime of holes has been measured as 10 ps in hematite electrodes[48,49]. As the complex oxygen evolution reaction is considerably slower than the average hole lifetime recombination is a likely outcome for photogenerated charge carriers. However, the hole collection can be improved by nanostructuring the individual feature size to be comparable

to the space charge width[68]. This has the additional benefit of increasing the surface area available for light harvesting[99] . When the electrode texture is altered in such a way it has been found that the bulk recombination is reduced and the hole collection efficiency under illumination is increased[99].

A variety of synthesis and nanostructuring techniques have been used to reduce the path length of $ZnFe_2O_4$. A solid state reaction (SSR) between ZnO and Fe_2O_3 ground into methanol and calcined produced crystalline $ZnFe_2O_4$ with a crystallite size of ≈51 nm. These were tested for the photodegradation of isopropanol (IPA) to CO_2 and found to generate 50 % more gas than the $TiO_{2-x}N_x$ nanoparticles which were used as a benchmark[100]. Another technique used $Zn(NO_3)_2{\cdot}6H_2O$ and $Fe(NO_3)_3{\cdot}9H_2O$ and made a polymer complex with ethylene glycol and citric acid. The complex was heated and dried leaving $ZnFe_2O_4$ nanocrystalline pellets. This was measured for photocatalytic water splitting using a water-methanol mixture, again using $TiO_{2-x}N_x$ nanoparticles as a comparison. The $ZnFe_2O_4$ nanocrystalline pellets produced 15 times the amount of gas as the $TiO_{2-x}N_x$ nanoparticles, with the smaller band gap and hence greater light absorption being cited as the reason[101].

Hydrothermal synthesis has been used frequently to generate $ZnFe_2O_4$ nanostructures with beneficial catalytic effects[102–104]. This technique has achieved structures down to 5 nm, although the morphology was irregular[102]. Co-precipitation has also been applied to synthesise $ZnFe_2O_4$ along with imbedded Ag and $SrTiO_3$. The nanostructuring and pairing of materials was once again found to enhance the natural photocatalytic properties of $ZnFe_2O_4$[105,106].

Pairing narrow band gap photoanodic materials with established wide band gap photoanodic materials has been a common strategy to date. For $ZnFe_2O_4$ pairing with TiO_2 in particular was the focus of considerable early research. TiO_2 was an early mainstay of PEC research due to its stability and relative abundance, however, its large 3.2 eV band gap makes TiO_2 unable to absorb all but UV region of the solar spectrum[107]. By pairing with a smaller band gap semiconductor with aligned bandgaps so that charge carriers can traverse the semiconductor-semiconductor junction[93].

1.5 MoS_2 as a Hydrogen Evolution Photocatalyst

As discussed in Section 1.2.5 MoS_2 has attracted attention for the HER due to its combination of low ΔG_H and high exchange current density. MoS_2 is an attractive alternative to Pt as it is non-toxic, environmentally friendly and earth-abundant. As such it could offer a low-cost alternative provided several photocatalytic HER compatibility issues are addressed[27].

Currently MoS_2 has found widespread use in hydrodesulfurisation catalysis[108,109], electrocatalysis[62,110], solid lubrication[111], and transistor manufacture[112]. The variety of uses is in part attributable to the anistropic properties of MoS_2 arising from the layered structure with strong covalent intralayer bonds, and weak Van der Waals interlayer bonds[113].

1.5.1 The Structure of MoS_2

MoS_2 has a layered structure similar to graphene with the bulk comprised of a stack of 0.65 nm thick individual layers[113]. The stacks are held in place by relatively weak Van der Waals forces enabling MoS_2 to be cleaved into a monolayer[114]. Each monolayer of MoS_2 has a plane of hexagonally arranged molybdenum atoms sandwiched between two planes of hexagonally arranged sulfur atoms. The covalently bonded S-Mo-S atoms in a trigonal prismatic arrangement form a hexagonal crystal structure[113]. The bond length of the Mo-S is 0.24 nm, and the crystal lattice constant is 0.32 nm[115].

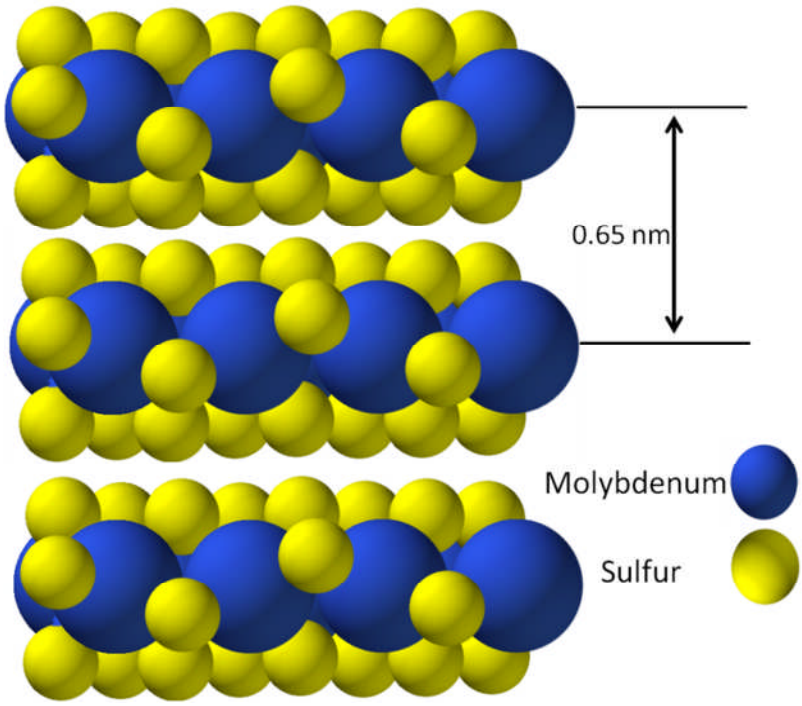

Figure 1.9. The layered structure of MoS_2 showing the $(10\bar{1}0)$ edge. Each layer consists of covalently bonded molybdenum and sulfur atoms, and the layers are connected by van der Waals forces.

The layered structure presents a problem for efficient HER as good electrical conductivity between the catalytically active sites and the substrate is necessary for efficient charge transport[116]. Charge carriers travel 2200 times faster along the covalently bonded layer than between layers held by Van der Waals forces[117]. This hindered vertical charge transport is critical to the successful application of HER on MoS_2 as the energy transfer between the substrate and the edge sites must be faster than the electron-hole recombination time or charge carriers will be lost[118]. High conductivity between the substrate and surface is also necessary for a kinetically fast HER[52].

Layered TMD materials, such as MoS_2, are comprised of two different polymorph structures depending on the metal coordination by the six chalcogen atoms. If the metal atom coordination is trigonal prismatic the material is semiconducting, and the structure is referred to as 2H. The 1T structure, on the other hand, is comprised of trigonal antiprismatic metal coordination and gives a metallic character[119]. Naturally occurring MoS_2 has a 2H phase crystal structure with a monolayer bandgap of ~1.9 eV, which renders it semiconducting[120]. This is appropriate for a PEC electrode, however charge-carrier recombination leading from the poor conduction can inhibit the performance (Section 1.2.3)[121]. Nanostructuring the bulk material has been found to create a blend of the metallic 1T phase, and the semiconducting 2H phases of MoS_2[119]. The 1T MoS2 phase is 107 times more conductive than the semiconducting 2H phase, and by mixing the two properties MoS_2 has displayed superior catalytic properties in comparison to the bulk material[121].

An additional issue with the natural state of MoS_2 is the basal plane being inert for HER. In order to be a viable HER catalyst the hydrogen adsorption Gibbs free energy (ΔG_H) must be

low; ideally 0 eV. The ΔG_H of the MoS_2 $(10\bar{1}0)$ edge sites is 0.08 eV; close to ideal for HER[56,57,122]. However, in bulk the MoS_2 $(10\bar{1}0)$ edge sites are relatively small in surface area as compared to the inactive basal plane. The ratio of edge sites can be increased without altering their catalytic properties through careful structuring[59]. In practice it has been identified that the HER current directly correlates with the number of exposed $(10\bar{1}0)$ edge sites[59].

The lowest MoS_2 Tafel slopes to date are ≈41 mV dec^{-1} and were achieved by combination with reduced-graphene oxide (RGO), as well as single-walled carbon nanotubes[52,123]. This slope indicates the HER in aqueous, acidic media proceeds on MoS_2 through the Volmer-Heyrovský reaction, beginning with a proton from H_3O^+ adsorbing to an active MoS_2 $(10\bar{1}0)$ edge site. This adsorbed proton then binds to a second proton, again from H_3O^+, resulting in H_2 gas (Figure 1.10)[50]. In order for this reaction to proceed it is necessary to input energy sufficient to promote an electron to the conduction band. The semiconducting nature of MoS_2 enables this energy to be obtained from an incident photon[50].

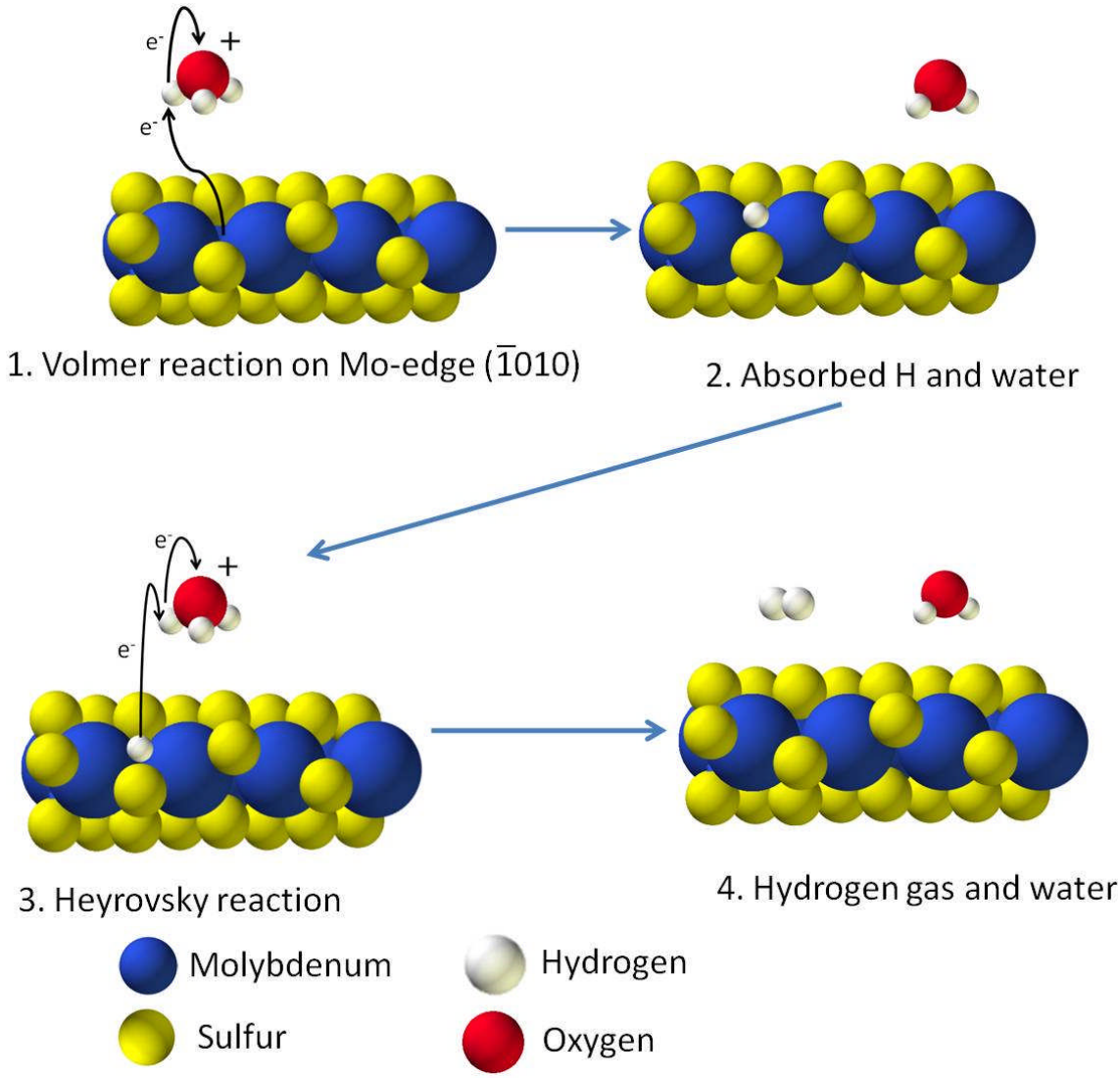

Figure 1.10. The Volmer-Heyrovský mechanism of H^+ reduction on a MoS_2 ($10\bar{1}0$) edge site. The proton is adsorbed to the MoS_2 ($10\bar{1}0$) edge site during the Volmer reaction, and the Heyrovský reaction follows in which a second proton from solution binds to an adsorbed proton to produce H_2 gas[50].

1.5.2 MoS_2 Photocathodic Properties

The bulk band gap of MoS_2 is 1.17 eV, which is too small to provide enough potential for PEC HER[124]. However, structuring on a nanoscale has been found to increase the band gap to 1.9 eV, which is close to ideal for providing the necessary overpotential required to drive PEC water splitting (Figure 1.3)[27,113]. Further, the band position is close to ideal with the conduction band negative of the H^+/H_2 reduction potential, and the valence band positive of the H_2O/O_2 oxidation potential (Figure 1.3)[125,126]. Together with the catalytic $(10\bar{1}0)$ edge sites these traits enable MoS_2 to function both as semiconductor light absorber and catalyst material[50].

1.5.3 Current State of the Art of MoS_2 HER

The primary metrics applied in this work to measure the efficacy of the nanostructured MoS_2 for the HER are onset potential, and Tafel slope. Onset potential provides a measure of the overpotential required to initiate the HER, as such it is a measure of the catalytic effect. An onset potential close to E^0 was preferred. The consensus of other studies on nanostructured MoS_2 HER are an onset potential of ≈ -0.20 V SHE[59,60,110,120,124,125]. The Tafel slope was taken as a measure of catalytic efficacy as discussed in section 1.2.5, this was the preferred metric for comparison as, unlike the onset potential and peak current, it is independent of experimental variables such as electrolyte concentration, electrode area, and scan rate. Bulk MoS_2 has been found to have a slope of ≈ 120 mV dec^{-1}, suggesting the Volmer reaction is rate limiting[127,128,129]. A lower value was considered favourable as this

indicates improved catalysis as a smaller overpotential is required to increase the current tenfold[130].

Various approaches have been attempted to improve the suitability of MoS_2 for the PEC HER. These are substrate choice, doping, intercalation between the layers, nanostructuring, or a combination of the preceding techniques. The lowest Tafel slopes achieved to date are ≈ 41 mV dec^{-1} [52,123]. The first of these was achieved by synthesising MoS_2 / reduced-graphene oxide (RGO) hybrids from $(NH_4)_2MoS_4$ and hydrazine in a solution of graphene oxide[52]. This resulted in MoS_2 nanoparticles evenly distributed on the RGO supports. The supported MoS_2 had a low onset potential of -1.1 V SHE, by comparison MoS_2 synthesised by the same method without the RGO had an onset potential of -0.21 V SHE and a Tafel slope of 94 mV dec^{-1} [52].

The other was also achieved by using a carbon support, in this case single-walled carbon nanotubes were used as a 3D support to increase the active surface area of MoS_2[123]. Oxygen incorporated MoS_2 was deposited on these supports by chemical vapour deposition (CVD) from a mixture of $(NH_4)_6Mo_7O_{24}{\cdot}4H_2O$ and thiourea[131]. The onset potential for these samples was -0.2 V SHE.

A variety of other supports have been used for MoS_2 which yielded Tafel slopes higher than 41 mV dec^{-1}, but lower than 120 mV dec^{-1}. Au was used as a backbone for physical vapour deposition from Mo and H_2S, giving a low onset potential of -1.1 V SHE, and a Tafel slope of 55 mV dec^{-1} [59]. Ag has also been used as a support in conjunction with mechanical strain as tensile-strain-induced Mo atoms had an increased number of electron states near the

Fermi-level and facilitated charge transfer from the substrate to the active sites[132]. However, in practice this technique had results worse than bulk MoS_2; with an onset potential of -0.35 V SHE and a Tafel slope of 135 mV dec^{-1} [132].

Doping is another commonly applied technique. This is used often in semiconductors for photovoltaic purposes to tune their properties by altering the Fermi level, improving charge transport, or imbuing catalytic properties[133]. A variety of chemicals have been incorporated into MoS_2 to enhance its catalytic ability for PEC HER. For example, it has been calculated through density functional theory (DFT) that the addition of cobalt to MoS_2 greatly improved the activity by reducing the hydrogen binding energy from 0.18 eV to 0.1 eV on the normally catalytically inert S-edge of MoS_2, thus endowing a greatly improved number of HER catalytically active sites[134]. This was tested experimentally by doping edge-terminated MoS_2 electrodes that were deposited by CVD[127]. Fe, Co, Ni, and Cu were used as dopants, and it was found that while transition metal doping does indeed lower the ΔG_H of the usually inactive S-edge, the ΔG_H of the Mo-edge is detrimentally increased. The net effect on catalysis was positive, although the improvement was lessened by the impedance of catalysis on the Mo-edge. The Tafel slopes were between 109 and 117 mV dec^{-1} and onset potentials were 0.2 V SHE[127]. Although the improvements to catalysis were minor, there was an increase in current due to the higher availability of active sites[127]. Transition metals dopants have been successfully used to increase catalysis, however. MoS_2 was doped with Ni at a ratio of 1 : 15 Ni : Mo by drop coating a slurry onto a glassy carbon (GC) substrate. This engendered a reduction in the Tafel slope to 47 mV dec^{-1}, although the onset potential was slightly high at -0.25 V SHE[135].

Due to the layered structure of MoS_2 it is also possible to incorporate additional chemicals by intercalation between the layers. This has the advantage of improving the conduction between layers due to a shift from the semiconducting 2H phase to the metallic 1T phase[54]. This technique has been used to reduce the Tafel slope to among the best reported at 43 mV dec^{-1} [128].

As discussed in Section 1.3 catalytic performance can be improved by structuring on a nanoscale. Several structuring techniques have been applied to optimise the performance of MoS_2 in the HER. However, most MoS_2 nanostructuring research has been focussed on using structural supports or monolayers, rather than synthesising MoS_2 into a nanostructure or nanopatterning bulk MoS_2. The lowest measured Tafel slope for MoS_2 without a structural framework is 49 mV dec^{-1}. This also had a low onset potential of -0.1 V SHE, and was achieved through edge termination and layer expansion[136]. Edge-termination greatly increases the proportion of active edge sites by synthesising the MoS_2 in effect rotated 90° so that the active edge sites occupy the position usually held by the basal plane. This was synthesised by reacting $(NH_4)_2MoS_4$ with *N,N*-dimethylformamide (DMF) at high temperature. The layer expansion was caused by intercalation of oxidised DMF species between the layers[136]. As with AACVD (Section 1.3.2) higher temperatures were associated with higher surface area structures. An alternative structure with edge termination, but without the layer expansion was made by heating elemental S and Mo in a tube furnace[110]. This achieved a Tafel slope of 86 mV dec^{-1}, and an onset potential of 0.2 V SHE[110].

Other groups have structured MoS_2 by synthesising or depositing the semiconductor onto a disposable framework that when removed leaves a porous, high surface area structure. A Si

substrate was successfully used for the electrodeposition of Mo followed by sulfidation by H_2S. The Si substrate was then etched away by HF leaving a porous MoS_2 electrode with a Tafel slope of 50 mV dec^{-1} and an onset potential of 0.19 V SHE[62].

1.6 Thesis layout

This thesis explores MoS_2 as a HER photoelectrode, and $ZnFe_2O_4$ as an OER photoelectrode. The aim was to investigate new ways of nanopatterning the electrodes, and assessing the changes effect on the catalytic properties. The nanostructuring of MoS_2 by NSL and plasma etching is presented in Section 3.0, this consisted of unsuccessful attempts to control the nanostructure through altering the etching parameters. Nevertheless, a nanowell morphology was achieved for the first time without an additional material deposition step. The plasma etching process caused damaging oxidation to the MoS_2 however, reversing this was the content of Section 4.0.

Section 4.0 details the creation of a new way to sulfidise air oxidised MoS_2 while avoiding toxic chemicals. $Na_2S_2O_4$ was chosen as the source of sulfur, and the sulfidation was achieved through a solution phase technique. The efficacy of the method was proven, and the deposition parameters optimised. It was found that the sulfidation resulted in improved catalytic and photocatalytic properties.

Finally Section 5.0 investigates the choice of solvent selection on morphology produced by AACVD. The solvent was systematically altered between methanol and ethanol and the samples were tested for OER catalysis and imaged. It was found that ethanol results in more porous films that had superior OER properties. Methanol on the other hand produced

compact films with relative poor catalysis. This was attributed to the more exothermic enthalpy of combustion of ethanol enabling heterogeneous nucleation to take place.

2.0 Materials and Methods

The focus of this work is the fabrication of nanostructured materials, followed by the characterisation of their properties, with an emphasis on the electrodes' performance as PEC water decomposition catalysts. MoS_2 was examined as a photocathode for the HER, and $ZnFe_2O_4$ as a photoanode for the OER.

MoS_2 was nanopatterned using NSL and plasma etching. The catalytic properties of MoS_2 were measured using electrochemistry, and the surface morphology and chemical composition were observed using Scanning Electron Microscopy (SEM) and X-ray Photoelectron Spectroscopy (XPS), respectively. Following prolonged (≈1 month) exposure to air the catalytic properties of the MoS_2 degraded. The air-degraded MoS_2 was then rejuvenated by solution phase sulfidation. Two different sulfidation techniques were attempted. The catalytic properties of the sulfidated MoS_2 were measured using electrochemistry and photoelectrochemistry, and the surface morphology and chemical composition were characterised using SEM and XPS, respectively.

Nanostructured $ZnFe_2O_4$ was synthesised in-situ from a precursor solution by AACVD. The solvent used to make the precursor solution was systematically altered between methanol and ethanol to elucidate the effect of the solvent on the final morphology. The surface morphology was imaged using SEM, and the chemical composition determined by XRD. The aerosol droplet size and enthalpies of combustion of the $ZnFe_2O_4$ precursor solutions were measured to account for the changes in morphology. This required that the density and surface tension of the deposition solutions were measured. A density flask and a Du Nouy

tensiometer were used, respectively. The catalytic properties of the electrodes were measured using photoelectrochemistry and incident photon conversion efficiency (IPCE). The methodology of established techniques used are found in this chapter, as well as details on the chemicals and instrumentation employed.

2.1 Fabrication Techniques

As discussed in Section 1.3 there are numerous advantages to nanostructuring electrodes for PEC. The main goals were to increase surface area, increase the number of catalytic sites, and improve charge carrier mobility. In this work the photocathodic MoS_2 was nanopatterned by a combination of NSL and plasma etching, while the photoanodic $ZnFe_2O_4$ was deposited into a nanostructure by AACVD from a precursor solution. In order to have their performance accurately assessed by electrochemical testing it was necessary to perform these fabrication techniques so as the nanostructured product forms part of an electrode assembly designed to have good conductivity, and has only the electrode material exposed to the electrolyte solution.

2.1.1 MoS_2 Electrode Assembly

Naturally occurring MoS_2 (99% purity, SPI Supplies Ltd) was adhered to a glassy carbon (GC) substrate (Alfa Aesar Ltd, 5mm dia., type 2) using conductive double sided carbon adhesive tape (SPI Supplies Ltd). Glassy carbon was chosen as it is highly conductive, hard wearing,

and resistant to chemical attack[137]. The MoS_2 crystal was then nanopatterned. Following nanopatterning silver conductive adhesive (RS components) was painted on the sides of the crystal to increase conductivity between the surface and substrate. The GC and silver were then coated with epoxy resin (Permatex quick set epoxy glue) leaving only the MoS_2 exposed for use as the working electrode (Figure 2.1). A syringe needle was used to apply the silver paint and epoxy resin. In order to ensure the silver and epoxy was coated in a way that left most of the MoS_2 crystal exposed to the electrolyte, and prevented exposure of the silver and GC the painting was performed under an optical microscope.

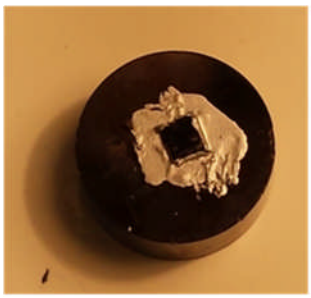

Figure 2.1. MoS_2 electrode assembly showing the 5mm diameter GC disk, silver paint, and the MoS_2 in the centre. Epoxy resin covers the GC and silver, but is transparent.

2.1.2 Nanosphere Lithography

A modified Langmuir-Blodgett technique was used to deposit nanospheres onto the surface of the MoS_2 crystal[74,75]. The technique was simplified by generating a close packed monolayer through the control of vibrations at the water-air interface, instead of restricting the surface area as in the original Langmuir-Blodgett technique (Figure 2.2).

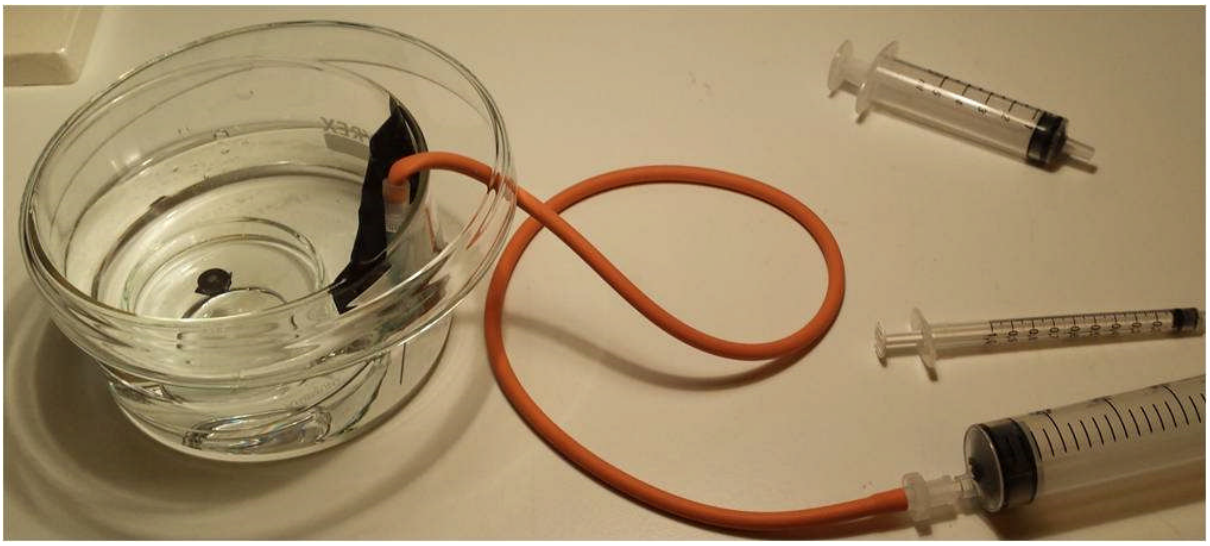

Figure 2.2. The set-up for modified Langmuir-Blodgett nanosphere deposition. Showing the MoS_2 adhered to GC submerged in the dish, and the syringe assembly by which the water level is lowered.

To conduct the deposition a 10 cm diameter dish had a syringe needle taped to the side with the tip close to the bottom of the dish. The syringe needle was connected to the barrel with flexible tubing so as to permit the use of a lid during deposition. The dish was then filled half way with ultra pure water (MilliQ by Millipore, with resistivity ≥18 MΩ cm). The MoS_2 was made hydrophilic by exposure to O_2 plasma as described in (2.1.3). The electrode assembly was adhered to a glass petri dish with carbon tape (SPI Supplies Ltd) for the purpose of holding the electrode steady during the deposition. The petri dish and electrode were placed at the bottom of the dish. A Si wafer was used to deposit the nanospheres on the water-air interface.

The piece of Si wafer (SEMI Std flats, IDM Technologies Ltd) was cleaned with piranha solution (2-parts H_2SO_4 98%, Sigma-Aldrich), 1-part H_2O_2 30%, Sigma-Aldrich). Piranha

solution is highly corrosive and a strong oxidising agent used to remove organic compounds. Si wafers soaked in piranha solutions become hydrophilic, which is necessary to achieve an even spread of nanosphere solution on the surface.

The nanosphere suspension was made from stock polystyrene nanosphere solution (0.22 µm, Thermo Scientific Microparticle Technology) and ethanol (>99.5%, Sigma-Aldrich) (2:1, NS:EtOH). Before deposition it was sonicated to improve the homogeneity of the dispersion. An aliquot of 20 µl of prepared nanosphere solution was pipetted onto the hydrophilic Si wafer and gently lowered into the water, leaving the nanospheres on the water-air interface. The nanosphere cloud was positioned over the MoS_2 and a lid was placed on the dish (Figure 2.3). The water level was slowly lowered by syringe, drawing from the bottom of the dish. After the water level was beneath the MoS_2 surface the sample was removed and left to dry in air. Once dry a monolayer of nanospheres remained on the crystal surface.

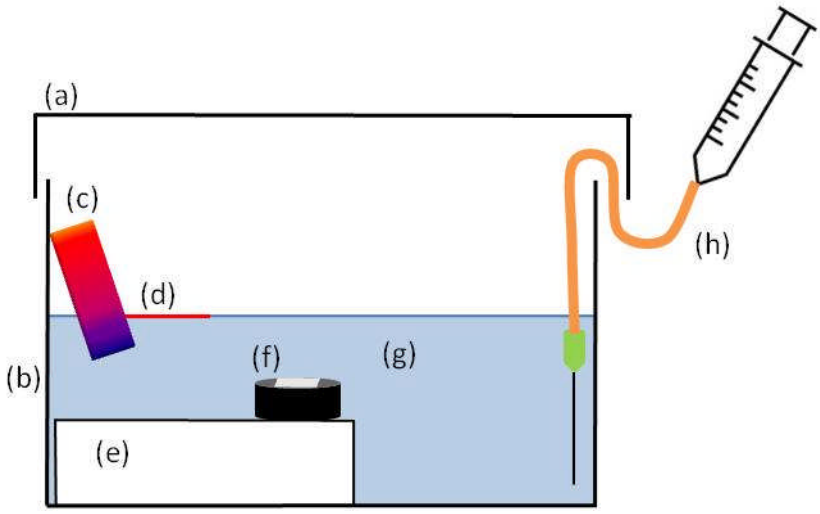

Figure 2.3. A nanosphere monolayer being deposited onto the water-air interface. (a) Lid to block air currents while lowering the water level. (b) Glass dish. (c) Si wafer coated with nanospheres. (d) Nanospheres on the water-air interface. (e) Glass dish to hold sample steady. (f) MoS_2 adhered to GC. (g) Ultrapure water. (h) Syringe – the needle is connected to the barrel by flexible tubing so as to be able to pass between the dish and lid.

2.1.3 Plasma Etching

Plasma etching is a powerful technique to be used in conjunction with NSL as different etchants can be used to selectively etch the nanospheres or the surface[77]. An Oxford Instruments PlasmaPro NGP80 etcher was used to generate O_2 plasma to shrink the nanospheres and increase the hydrophilicity of the MoS_2 prior to nanosphere deposition, as well as SF_4 and C_4F_8 plasmas to etch the surface of the MoS_2.

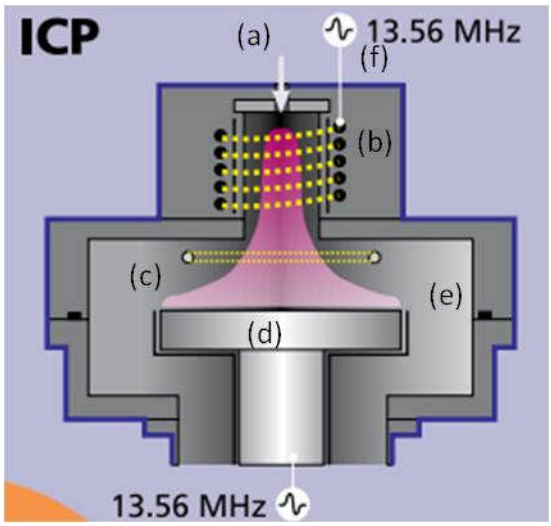

Figure 2.4. A schematic of an Oxford Instruments PlasmaPro NGP80 etcher. (a) gas inlet. (b) Induction coil. (c) plasma. (d) temperature controlled base. (e) vacuum chamber. (f) RF generator[138].

In order to generate plasma the process gas is ionised in the vacuum chamber by applying one to two radio frequency (RF) signals at 13.56 MHz. This particular frequency is commonly used in plasma etchers as it creates a uniform plasma at a flat surface over a 100 mm diameter[139]. One of these is coupled to the induction coil to produce inductively coupled plasma (ICP), while the other remains RF[79]. The ICP power was used to generate high density plasma, while the RF power provided a DC self bias. The advantage utilising both is that the ion energy at the sample is controlled independently to the ion density[79].

Polystyrene nanospheres are often size controlled using O_2 plasma as they display a linear response to etching and the individual nanospheres are etched at a similar rate. Allowing control over size whilst maintaining an evenly distributed resist[70]. In this study the O_2

plasma was also used to make the surface of the MoS_2 hydrophilic. This occurs in a similar way to the effect of piranha solution on a Si wafer; by removing organic impurities.

SF_6 plasma was used to etch the surface of the MoS_2. SF_6 plasma dissociates into a variety of subspecies, the main etchant of which has been identified as atomic fluorine. This chemically etches the surface by combining to make volatile products[140]. This was used in conjunction with C_4F_8 plasma to promote anisotropic etching. Ionisation of C_4F_8 produces a polymer passivation layer that inhibits etching by SF_6. As the etching process is top down the surface is subject to a longer etch than the bulk material that is exposed during the etch, therefore without a passivation layer the features will have narrow tops and wider bottoms. C_4F_8 helps to prevent this as it is also top down and so each part of the features will be exposed to the passivation layer for the same length of time as SF_6 plasma[70].

The etchant gas flow rate and etch time were varied as required by the experiment. However, the ICP and RF power were held steady as investigating these variables was outside the bound of this study. For the SF_6 and C_4F_8 etch the RF power used was 25 W and the ICP power was 200 W. For the O_2 etch the RF power was 100 W and ICP was not used. A strike step with higher pressure and power was employed to ignite the plasma before the main etch. The base temperature was maintained at 20°C to prevent the sample being damaged by excess heat. The O_2 etch used to increase the hydrophilicity of the MoS_2 prior to nanosphere deposition used the conditions in Table 2-1.

	Strike step	Main etch
Time (s)	1	20
APC (mTorr)	40	20
Base temp (°C)	20	20
Helium pres (Torr)	10	10
SF_6 (SCCM)	0	0
C_4F_8 (SCCM)	0	0
O_2 (SCCM)	100	20
RF (W)	100	40
ICP (W)	0	0

Table 2-1. The etch parameters used to increase the hydrophilicity of the MoS_2 prior to nanosphere deposition. To initially ignite the plasma a strike step was used with higher power and pressure than the main etch.

Specific details of the etch parameters used for each batch of samples can be found in Section 3.4.

2.1.4 $ZnFe_2O_4$ Electrode Assembly

Fluorine-doped tin oxide (FTO) coated glass was used as the conductive substrate (TEC 8 Pilkington, 8 Ω/square). The FTO was cut into rectangle pieces (ca. 1×2 cm) pieces using a diamond tipped glass cutter. The FTO substrates were ultrasonically cleaned twice, once with acetone (≥99.5%, Sigma Aldrich) and a second time with ultrapure water (≥18 MΩ cm), and finally stored in ethanol (absolute, Sigma Aldrich). The $ZnFe_2O_4$ was directly deposited onto the FTO as described in section 2.1.6. During deposition a piece of glass covered an

approximately 2 mm wide strip in order to leave a part blank for attaching the working electrode connection (Figure 2.5).

Figure 2.5. $ZnFe_2O_4$ electrode assembly with the blank FTO strip (white) and the deposited $ZnFe_2O_4$ (red).

2.1.5 $ZnFe_2O_4$ Precursor Synthesis

A single source bi-metallic precursor $[Fe_2(acac)_4(dmaeH)_2][ZnCl_4]$ was synthesised as reported by Tahir et al[89]. A solution of 12.3 mM 2,4-Pentanedione (acacH) (97% Sigma Aldrich), 6.17 mM N,N-dimethylaminoethanol (dmaeH) (98% Sigma Aldrich), and 6.15 mM anhydrous $FeCl_3$ (98%, Sigma Aldrich) was made in a known mixture of methanol and ethanol at room temperature and stirred.

After 20 min stirring, 3.07 mM of Zn acetate·$2H_2O$ was added and the mixture stirred for an additional 2 hours. The reaction mixture was filtered and evaporated to dryness under reduced pressure in a Buchner flask.

2.1.6 Aerosol Assisted Chemical Vapour Deposition

AACVD utilises a vapourisable aerosol to deliver the precursor solution into a heated reaction zone where combustion creates the desired product[83]. A FTO substrate was placed under a deposition chamber on a Corning PC-101 hot plate (Figure 2.6), with a second piece placed perpendicular in order to support the strip of glass which prevents the entire substrate from being deposited upon (Figure 2.5). The $ZnFe_2O_4$ precursor was dissolved in either methanol, ethanol, or a mix of the two to make the precursor solution. Eleven methanol/ethanol compositions were made with a change in proportion of 10 % (by volume) increments between pure ethanol and methanol to investigate the effect the deposition solvent has on the final morphology.

For each deposition 6 ml of the precursor solution was poured into a two necked round bottomed flask half submerged in an ultrasonic humidifier. One neck was attached to a gas cylinder connected to a flow meter, and the other to a three neck round bottom flask. This second flask acts a trap for large particles to prevent them reaching the deposition chamber. The second flask was also connected to a flow meter connected to a gas cylinder in order to maintain a constant flow rate between flask 1, flask 2 and the deposition chamber. In the deposition chamber the solvent was heated to combustion causing the precursor to decompose to the desired material, which finally adhered to the FTO substrate.

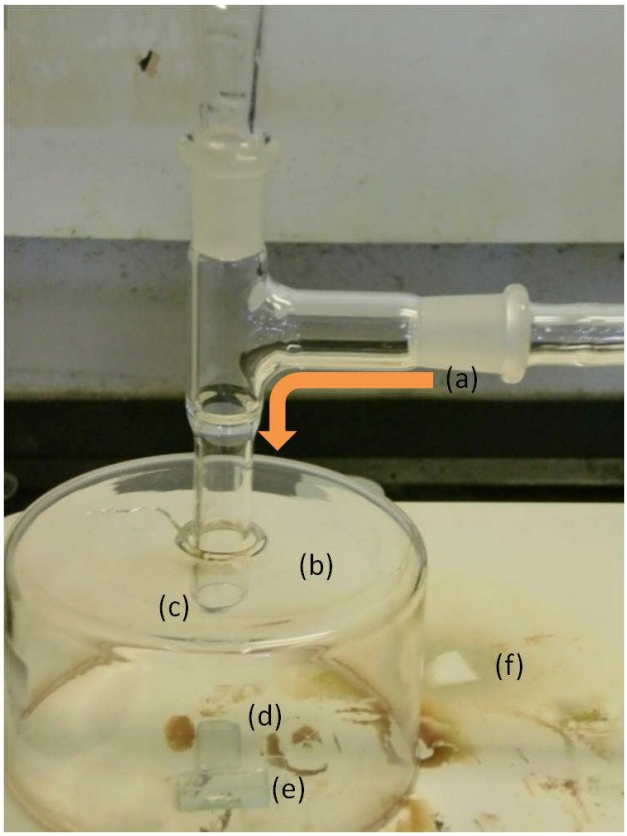

Figure 2.6. AACVD deposition apparatus. (a) Direction of precursor solution flow. (b) Deposition chamber. (c) Deposition nozzle. (d) FTO substrate. (e) Second piece of FTO supporting a piece of glass with a ≈ 2 mm overlap on the first piece to prevent the entire substrate from being deposited upon.

2.2 Sulfidation of Air Degraded MoS_2

As the HER efficiency of MoS_2 degrades over time due to atmospheric oxygen replacing the sulfur, experiments were undertaken in order to resulfidise the crystals. The sulfidation was a solution-phase reaction utilising electrochemistry apparatus and $Na_2S_2O_3$ as the sulfur source. The sulfidation was carried out in a solution of $Na_2S_2O_3$ (99%, Sigma-Aldrich), H_2SO_4

(98%, Sigma Aldrich), with 0.1 M Na_2SO_4 (99% Sigma-Aldrich) supporting electrolyte prepared in ultra pure water (MilliQ by Millipore, with resistivity ≥18 MΩ cm) purged with N_2 gas. Various concentrations of $Na_2S_2O_3$ and H_2SO_4 were experimented with, and more details can be found in Section 4.1.

The $Na_2S_2O_3$ sulfidation was carried out in a three electrode electrochemical cell connected to a PGSTAT128N potentiostat (Metrohm Autolab BV, Utrecht, NL). A double-junction Ag/AgCl (3M KCl) electrode (Sigma Aldrich) was used as a reference electrode[141]. The counter electrode was a bright Pt mesh. Various deposition conditions were attempted and details can be found in Section 4.1.

2.3 Characterisation Techniques

Electrochemistry and photoelectrochemistry were utilised to evaluate the nanostructured materials effectiveness as an electrode / photoelectrode, with the MoS_2 tested for the HER and the $ZnFe_2O_4$ tested for the OER. $ZnFe_2O_4$ was further evaluated using IPCE. The chemical composition of the materials was tested using XRD or XPS, and the surfaces were imaged by SEM. The density and surface tension of the solvent mixtures used to deposit $ZnFe_2O_4$ was tested using a density flask and a Du Nouy tensiometer, respectively.

2.3.1 Electrochemistry of MoS_2

The HER was performed on the nanopatterned MoS_2 before and after sulfidation in order to evaluate each electrodes performance as an electrocatalyst and to provide a means of comparison between samples. A three electrode set-up was used with a Ag/AgCl (Sat. KCl) reference electrode, bright Pt mesh counter electrode, and the MoS_2 electrode assembly as the working electrode. The electrochemical cell was water jacketed, and water was pumped through the jacket from a water bath held at 25°C by an immersion heater.

For testing the MoS_2 electrode assembly was placed in a cylindrical sample holder, and connected to a rotating disk electrode (RDE) (Origlys OrigaTrod). The proton reduction experiments were performed in 2 mM perchloric acid (70%, Sigma-Aldrich) electrolyte with 0.1 M sodium perchlorate (98%, Sigma-Aldrich) supporting electrolyte prepared in ultra pure water (MilliQ by Millipore, with resistivity $\geq$18 MΩ cm) and thoroughly purged with N_2 gas to remove dissolved oxygen.

A PGSTAT128N potentiostat (Metrohm Autolab BV, Utrecht, NL) was used to measure for voltammetric measurements. The MoS_2 was investigated using a variety of potential windows, further details of which can be found in section 3.6. The accuracy of the results was tested by Randles-Ševčík analysis with a range of scan rates from 5 - 1200 mV s^{-1} performed. However, all results reported for the purpose of comparison with other samples were measured at a scan rate of 25 mV s^{-1}.

Potential values quoted in the text are given against SHE for ease of comparison. 0.197 V was added for the difference in potential between a Ag/AgCl (Sat. KCl) reference electrode

and a SHE reference electrode[142]. Also 0.159 V was added for the Nernstian shift due to the 2 mM concentration of electrolyte. This was calculated using the Nernst equation (Eq. 2.1)[143].

$$E_{Red} = E^0 + \frac{RT}{nF} \ln[H^+] \qquad \text{(Eq. 2.1)}$$

Where E_{Red} is the adjusted reduction potential, E^0 is the standard potential (0 V vs SHE as definition for H^+ reduction on Pt), R is the gas constant, T is the temperature, n is the number of electrons involved in the electron transfer step, F is the Faraday constant, and $[H^+]$ is the concentration of protons.

2.3.2 Photoelectrochemistry of MoS_2

PEC measurements were made using the same electrodes, electrolyte, and potentiostat as the MoS_2 electrochemical measurements (Section 2.3.1). However, an electrochemical cell equipped with a quartz window was used so as to prevent absorption of the incident light by the glass. This cell was not water jacketed since the water would absorb some of the incident light.

A Hg-Xe lamp (Lot-Oriel) was used to provide the incident light, due to its similarity to the solar spectrum[144]. The distance between the light and the electrode was calibrated to 1000 W m^{-2} (A.M 1.5) using a pyranometer (LaserPoint Model PLUS+)[145].

2.3.3 Photoelectrochemistry of $ZnFe_2O_4$

The OER was tested on $ZnFe_2O_4$ using a similar PEC set-up as that used for testing the HER on MoS_2. The electrodes were placed in a three electrode electrochemical cell fitted with a quartz window. A Ag/AgCl (Sat. KCl) electrode was used as the reference electrode, and the counter electrode was a bright platinum mesh. The $ZnFe_2O_4$ working electrode was connected by attaching a crocodile clip to the blank strip of the electrode. All measurements were carried out in 1 M NaOH electrolyte made in ultra pure water (resistivity $\geq$18 MΩ cm).

Voltammetry was measured using a potentiostat (Micro Autolab type-III). All the $ZnFe_2O_4$ electrode measurements were recorded under illumination from a halogen lamp (Solar Light, USA) at a distance calibrated to 1000 W m^{-2} (A.M 1.5) using a pyranometer (Solar Light Co., PMA2144 Class II). All measurements were performed at a scan rate of 100 mV s^{-1} and in a potential window between -0.4 V and +0.7 V Ag/AgCl.

2.3.4 Incident Photon Conversion Efficiency (IPCE)

IPCE was used to investigate the quantum efficiency of the $ZnFe_2O_4$ electrodes for OER at wavelengths between 320 and 800 nm. IPCE refers to the number of electrons measured as photocurrent in the external circuit divided by the monochromatic photon flux incident on the semiconductor. By scanning across a range of wavelengths in 5 nm steps the IPCE is determined at specific wavelengths[2]. The IPCE can be calculated using Eq. 2.2.

$$IPCE(\lambda) = LHE(\lambda)\phi_{inj}\eta_{coll} \qquad \text{(Eq. 2.2)}$$

Where LHE is the light harvesting efficiency, ϕ_{inj} is the quantum yield for electron injection from the excited sensitizer in the conduction band of the semiconductor oxide, and η_{coll} is the electron collection efficiency[2].

The $ZnFe_2O_4$ electrodes were measured in a three electrode cell with a quartz window. The reference and counter electrodes were a Ag/AgCl (3M KCl), and a bright Pt mesh, respectively. The incident light was provided by a 75 W Xenon lamp connected to a monochromator (TMc300, Bentham Instruments Ltd.). The IPCE spectra of the $ZnFe_2O_4$ electrodes were measured at 0.25 V vs. (Ag/AgCl) / 3 M KCl. This figure was chosen as it corresponds to +1.27 V (SHE), taking into account the Nernstian shift for the pH 14 NaOH electrolyte[146], and this figure is slightly in excess of the +1.23 V required for the OER. The monochromated light was scanned between 320 to 800 nm and readings were taken at every 5 nm. The system was calibrated using a silicon diode (Bentham) from 320 nm to 1100 nm.

2.3.5 Scanning Electron Microscopy

Field Emission Gun Scanning Electron Microscopy (FEGSEM) was used to image the surface of the MoS_2 and $ZnFe_2O_4$ electrodes in order to see their surface morphology. A XL 20 FEGSEM (Phillips) was used to image the MoS_2 electrodes and a XL 30 FEGSEM (Phillips) was used for the $ZnFe_2O_4$ electrodes. Both operate under the same principles; however the XL

20 was equipped with a Through the Lens Detector (TLD) which allowed a higher resolution at high magnification than the Secondary Electron (SE) detector on the XL 30. The beam potential used on both systems was 15 kV.

FEGSEM uses electrons from a field emission cathode tip that are accelerated by the potential difference between the cathode and an anode positioned between the cathode and sample. The XL 20 and 30 FEGSEM use a LaB_6 crystal as a tip due its high current and voltage capability, low work function (2.6 eV), and low vapour pressure at high temperature[147]. It does however require a higher vacuum than the commonly used tungsten tip to operate[148].

Electrons are drawn from the LaB_6 tip by the potential difference between it and the anode. The electron beam follows a vertical path through the microscope, which is held in a vacuum to prevent the electrons interacting with air. The electron beam is then condensed and focussed onto the sample[149].

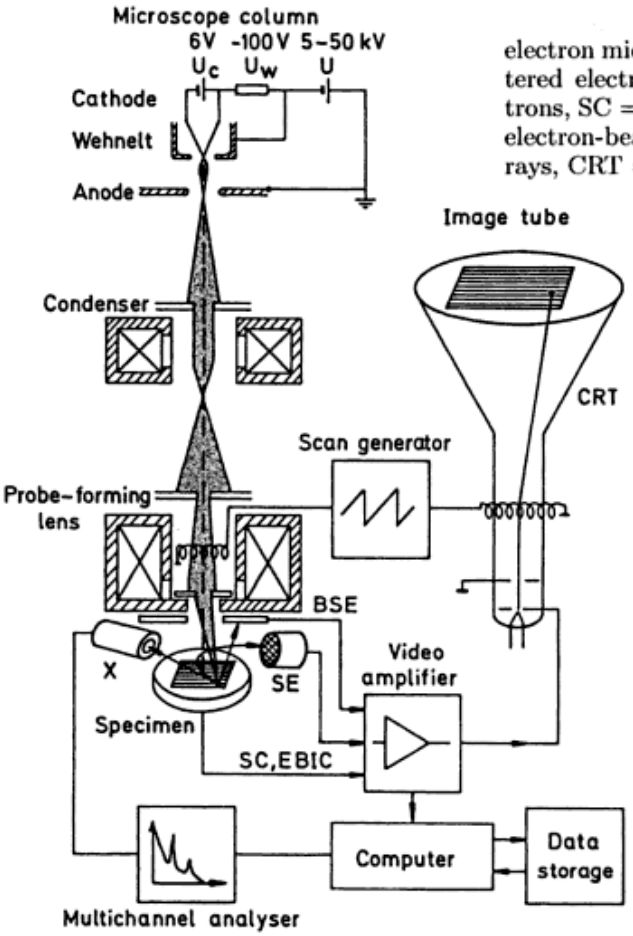

Principle of the scanning electron microscopoe (BSE = backscattered electrons, SE = secondary electrons, SC = specimen current, EBIC = electron-beam-induced current, X = x-rays, CRT = cathode-ray tube)

Figure 2.7. A diagram of a scanning electron microscope equipped with a secondary electron detector[149].

Upon contacting the sample surface a number of changes are induced by the interaction of the primary electrons with the molecules contained in the sample. The various types of signals produced from the interaction of the primary beam with the specimen include secondary electron emission, backscatter electrons, Auger electron, characteristic X-rays, and cathode luminescence. The behaviour of these particles is used to produce the SEM image[149].

The interaction most commonly used to image in SEM is the secondary electron emission[150]. Secondary electrons are generated when an incident electron collides with an electron in the sample and causes it to inelastically scatter. Secondary electrons with enough energy to overcome the work function of the sample are collected in a positively charged SE detector placed to the side of the sample. A plot of secondary electron current vs position can then be generated and used to provide a contrast based image of the surface[151].

Through the lens detectors also function in a similar manner to SE detectors, utilising the secondary electron emission to create a contrast image of the sample. However, TLDs are positioned directly above the lens and rely on the sample being positioned within the magnetic field of the lens. The scattered secondary electrons are drawn by this magnetic field to a position above the lens, and are then collected by the positively charged TLD. The advantage of having the detector directly above the sample is that it prevents directional effects as the secondary electrons travel perpendicular to the samples surface. While the positioning of SE detectors means the sample has a near side and a far side creating directional and shadowing effects[152].

2.3.6 X-ray Photoelectron Spectroscopy

XPS was used to determine the chemical composition of the surface of the MoS_2 electrodes. Samples were tested in freshly nanopatterned, air degraded, and sulfidated states in order to determine the effect exposure to air and subsequent sulfidation has on the chemical

composition. XPS was therefore a favourable choice as it provides quantification of the surface composition, which was region of interest in this study[153].

XPS is based on the principle of the photoelectric effect (Section 1.1.1). Small wavelength light is used to irradiate the sample causing photoelectrons to be emitted (Eq. 2.3)[151].

$$E_k = h\nu - E_b - \varphi \qquad \text{(Eq. 2.3)}$$

Where E_k is the kinetic energy of the photoelectron, h is Planck's constant, ν is frequency of the incident radiation, E_b is the electron binding energy, and φ is the work function of the sample[154]. Each element has a characteristic set of binding energies, and $h\nu$ and φ are known properties. An XPS determines E_k experimentally, which allows the calculation of the binding energies, and hence the identification of the material[154,155].

XPS spectra were acquired in collaboration with the European Bioenergy Research Institute (EBRI) at Aston University. The spectra were obtained using a Kratos Axis HSi XP spectrophotometer equipped with a charge neutraliser and a magnesium kα source (1,253.7 eV). Spectra were recorded at normal emission using a pass energy of 160 for survey scans and 20 for high resolution scans under a vacuum of 10^{-10} Torr. Curve fitting was performed using Casa XPS software version 2.3.16 and energy calibrated to the adventitious carbon 1s peak at 284.6 eV, employing Gaussian-Lorentz peak shapes and a Shirley background.

2.3.7 X-ray Diffraction

XRD was used to determine the bulk chemical composition of the deposited $ZnFe_2O_4$ films. As the bimetallic oxide was synthesised in-situ it was necessary to test that the correct material had been deposited onto the FTO glass.

A XRD pattern is obtained by irradiating the sample with a stationary X-ray source, and detecting the X-ray photons emitted using a movable detector. Atoms in a periodic lattice elastically scatter X-rays. The scattered X-rays that are in phase produce constructive interference, and it is these in phase X-rays that are collected by the movable detector[151]. The angle of the detector relative to the sample when constructively interfering X-rays scatter is used to determine the chemical composition of the sample.

The angle at which the constructive interfering X-rays leave the crystal can be used to calculate the lattice parameters of the crystal by applying the Bragg relationship (Eq. 2.4).

$$n\lambda = 2d \sin\theta \qquad \text{(Eq. 2.4)}$$

Where n is the order of reflection, λ is the wavelength of the incident radiation, d is the distance between two lattice planes, and θ is the angle at which the constructively interfering X-rays leave the crystal[151].

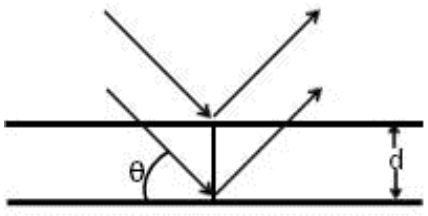

Figure 2.8. Constructively interfering X-rays being emitted following excitation. By measuring θ d may be determined, and hence the material composition identified.

By experimentally determining θ the lattice spacings of a crystal can be calculated. Lattice spacings are characteristic for a certain compound and hence the material composition is elucidated[151].

The $ZnFe_2O_4$ films compositions were determined using a Bruker D8 X-ray diffractometer operating with monochromatic high intensity Cu Kα (λ = 0.1548 nm) radiation, a scan rate of 0.008° s^{-1}, and a position sensitive detector.

2.3.8 Electrode Size Calculations

It was necessary to know the exact size of the exposed MoS_2 for comparison of the electro- and photoelectrochemical data to be meaningful, and for the application of equations such as Randles-Ševčík and Tafel. The geometric area of the MoS_2 was measured using a Zeiss Lab A1 optical microscope. Images were recorded using a MicroPublisher 3.3 RTV camera. The geometric area of the MoS_2 was calculated by Klonk image measurement software.

2.3.9 Density Flask

In order to calculate the aerosol droplet size of the ethanol / methanol $ZnFe_2O_4$ precursor solutions during AACVD it was necessary to measure the density of the precursor solutions.

The densities of pure ethanol and pure methanol precursor solutions were measured experimentally, and the mixed solutions densities were estimated from a straight line plot between the pure solutions values.

A density flask consists of a bottle of known mass and volume, and a capillary of uniform diameter which slots into the top of the bottle. The density flask was filled with $ZnFe_2O_4$ precursor solution and placed in a water bath at 25°C. Once thermal equilibrium was established the capillary tube placed on top of the flask, sealing the vessel. The precursor solution rose up the capillary tube and overflowed slightly, so that the density flask was completely filled. Therefore a known volume of precursor solution was in the density flask. The filled density flask was then weighed, and the empty mass was subtracted from that value giving the mass of precursor solution[156].

The density of the precursor solution was calculated using Eq. 2.5.

$$\rho = \frac{m}{V} \qquad \text{(Eq. 2.5)}$$

Where ρ is the density, m is the mass, and V is the volume.

2.3.10 Du Nouy Tensiometer

The surface tension of the precursor solutions was also required in order to calculate the liquid droplet size. The surface tensions of the $ZnFe_2O_4$ solution in pure methanol and pure ethanol were measured, and the surface tensions for the mixed methanol / ethanol

solutions were estimated by a straight line plot between the pure precursor solution surface tension values.

A Du Nouy tensiometer consists of a metal ring of known radius attached to a pulley connected to a Newton meter. The ring was lowered onto the surface of the $ZnFe_2O_4$ precursor solutions and slowly withdrawn until it was clear of the liquid. The Newton meter recorded the force that was necessary to remove the ring from the solution.

The surface tension was then calculated using Eq. 2.6.

$$\sigma = \frac{\beta F_a}{4\pi R_l} \qquad \text{(Eq. 2.6)}$$

Where σ is the surface tension, β is a correction factor, F_a is the force applied by the loop, and R_l is the radius of the loop[157].

β was calculated using Eq. 2.7.

$$\beta = \frac{R^3}{v_0} \qquad \text{(Eq. 2.7)}$$

Where v_0 is the volume of the liquid suspended in the ring[157].

v_0 was calculated using Eq. 2.8.

$$v_0 = \frac{F_a}{\rho g} \qquad \text{(Eq. 2.8)}$$

Where F_a is the force measured using the Du Nouy Tensiometer, ρ is the density, and g is the acceleration due to gravity.

Hence by measuring the force required to remove a ring from the surface of the precursor solutions the surface tension was calculated.

3.0 Nanopatterning of MoS_2 by Nanosphere Lithography and Plasma Etching

The natural state of MoS_2 has a small proportion of catalytic edge sites and poor conduction between layers hindering its usefulness as a HER catalyst[52,59,117,118]. To address these issues a combination of NSL and plasma etching were used to nanostructure the surface of MoS_2 electrodes. Attempts were made to control the surface morphology using the gas flow rates during plasma etching, but these were unsuccessful. However, three distinct nanopatterns were identified, and the degree of closeness in the packing of the nanospheres was found to be the key parameter determining which nanopattern was formed. Nanospheres deposited with small gaps between them shrink symmetrically when exposed to O_2 plasma, and subsequent etching of the MoS_2 surface by SF_6 plasma formed nanopillars. Control over the vibrations on the water-air interface during deposition resulted in nanospheres close-packing into a tessellating hexagonal arrangement. When these were O_2 etched the nanospheres shrank in the same way as previously, however a wall of debris was left where the hexagons conjoined, resulting in a nanomesh. The SF_6 plasma etch onto this nanomesh resulted in nanowells being etched into the MoS_2. This is the first time nanowells have been made by NSL without an additional step to deposit metal into interstices of the nanowells[66,158]. A third morphology was also identified that was a hybrid of the other two nanosphere formations, resembling in nanopillars with links between them.

All three structures were found to have an apparent catalytic effect on proton reduction as compared to a pristine MoS_2 blank. The onset potential shifted from -0.68 V SHE, to ca. -

0.24 V SHE, and there was a greater than four-fold increase in current density. The nanopillars had the highest current density, and earliest onset potential but the highest Tafel slopes, requiring an additional 66 mV to achieve a tenfold increase in current. This was attributed to the linkages between the nanowells and linked pillars as charge carriers could travel further along the covalently bonded layers to reach the point of least resistance between the edge sites and substrate, resulting in fewer charge carriers lost to recombination.

An issue with the methodology was that the batches of samples were nanopatterned one immediately after the other, and then once all the samples had been completed the electrochemical testing was performed. In between nanostructuring and testing the samples were stored in a dessicator. This did not prevent the MoS_2 oxidising from air, and due to the several weeks between fabrication and testing the electrochemical results were poorer than expected. Once this was realised the samples were tested in reverse chronological order to the order they were made so as to have some samples that had received minimal exposure to air. This excludes the blank samples, which were electrochemically tested the same day as they were made in order to provide accurate best case scenario measurements for the purposes of comparison.

3.1 Electrode Assembly

In order to achieve the nanopatterning of MoS_2 and to be able to make accurate electrochemical measurements it was necessary to design an electrode assembly. Details of

the materials used can be found in Section 2.1.1. In order to be suitable for this work four requirements had to be filled. The first consideration was to prevent the flexible MoS_2 from being damaged during handling, the second to ensure that all materials used were suitable to undergo NSL and plasma etching, the third was that there must be good conductivity between the surface of the MoS_2 and the substrate, and finally that only the MoS_2 is exposed to the electrolyte solution during electrochemical measurements. GC disks were chosen as the substrate as they are conductive and durable[137], and fitted into an available rotation disk electrode (RDE) tip for use in electrochemical experiments. Double sided conductive carbon tape (SPI supplies) was used to adhere the MoS_2 to the GC, but due to its potentially high resistivity, and so the sides of the crystal were painted with silver adhesive to increase the conductivity between the top of MoS_2 and the substrate.

When assembling the electrode using carbon tape the MoS_2 was raised above the surface of the GC as this was found to facilitate the nanosphere deposition, since an even nanosphere deposition was necessary to achieve a close-packed resist. Using carbon tape and silver adhesive also meant that the silver could be applied after the plasma etching steps are complete, removing the risk of silver being exposed to the plasma and damaging the etching chamber.

Finally it was necessary to cover the silver and GC with an electrical insulator in order to ensure that the current produced during electrochemical testing was solely due to the MoS_2 (Figure 3.1). Epoxy resin was chosen for this as it is easy to apply, an insulator, and stable in the electrolytes used. As with the silver adhesive the epoxy resin was applied under an optical microscope for an enhanced level of control.

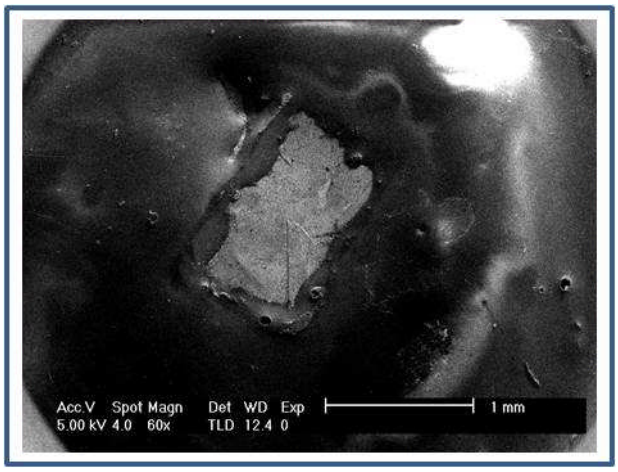

Figure 3.1. A SEM image of the finished electrode assembly. The light gray rectangle in the middle is the patterned MoS_2, and the darker, shiny substance surrounding it is the epoxy resin. The silver adhesive cannot be seen under SEM.

3.2 Electrode Geometric Area

In order for the comparison of electrochemical to be meaningful, and to apply the Randles-Ševčík and Tafel equations it was necessary to know the geometric area of the exposed MoS_2. An example of the electrode size measurements images are presented in

Figure 3.2. The size of the scale bar was defined and the outline of the exposed MoS_2 traced, the Klonk image measurement software was then able to define the area.

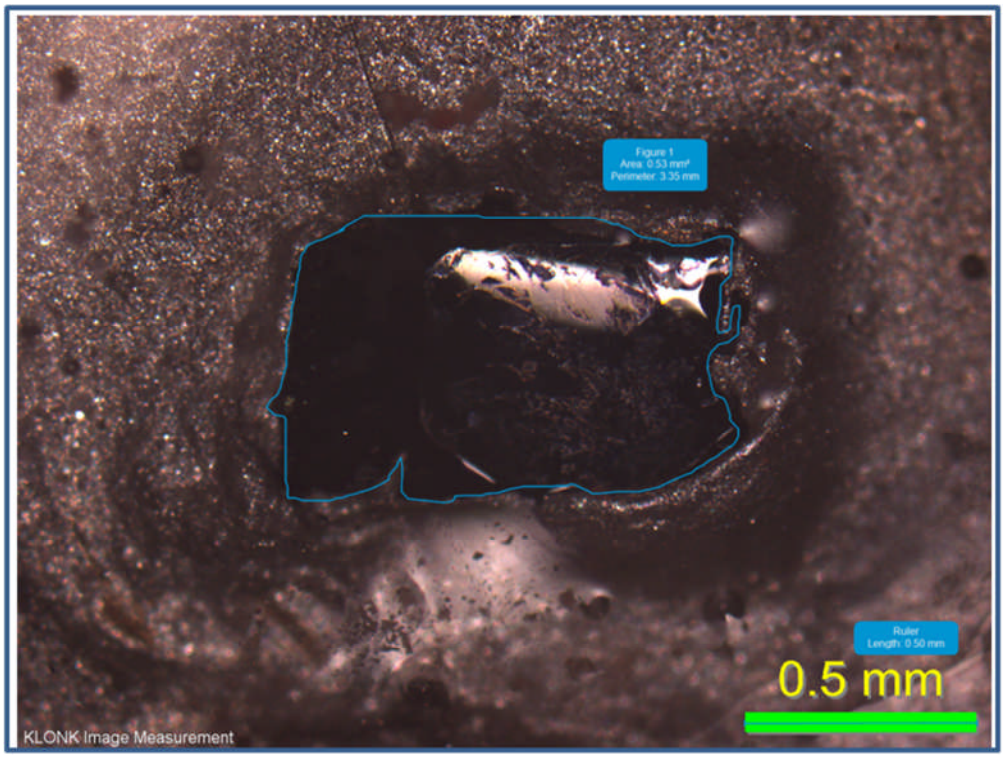

Figure 3.2. Exposed MoS_2 geometric size measurements. The measurements were obtained by taking an image of the sample surface using an optical microscope, and then defining the area using image measurement software

3.3 Nanosphere Lithography

A modified Langmuir-Blodgett technique was used for the nanosphere deposition[74–76]. This involved placing a hydrophilic MoS_2 electrode assembly at the bottom of a dish half full of water, and depositing the nanospheres on the water-air interface. The water level was then lowered until the nanospheres deposited onto the MoS_2. Complete details about the NSL set-up can be found in Section 2.1.2. The technique used here avoided compressing the nanospheres by instead taking care to minimise vibrations during the deposition to create a

close packed structure. To minimise the vibrations a lid was used to prevent air-currents were utilised, although experience and care by the operator was the best way to reduce vibrations. Control over vibrations was important because the structure of the nanospheres following deposition was found to be the greatest determining factor as to which morphology the MoS_2 was patterned into. Small changes in deposition conditions resulted in three distinct morphologies.

3.3.1 Solution Concentration

Experiments were undertaken to establish the optimum concentration of the nanosphere solution. These consisted of making different concentrations of nanosphere solution in ethanol and attempting the deposition of nanospheres on MoS_2, followed by imaging the resists with SEM to gauge the level of success. Concentrations attempted were: 0.75:1 NS:EtOH, 1:1 NS:EtOH, 1.25:1 NS:EtOH, and 2:1 NS:EtOH.

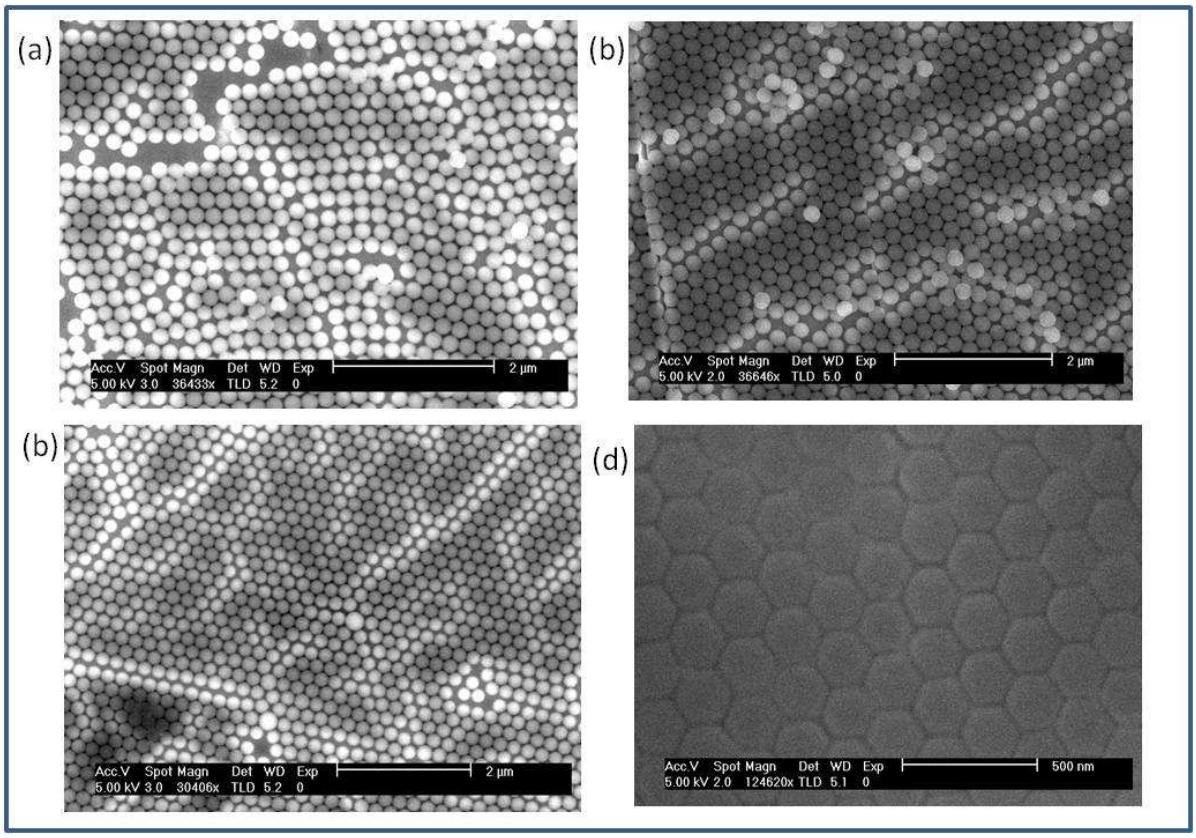

Figure 3.3. Nanospheres deposited onto MoS_2 at different solution concentrations. (a) 0.75:1 NS:EtOH. (b) 1:1 NS:EtOH. (c) 1.25:1 NS:EtOH. (d) 2:1 NS:EtOH.

In general it was found that a higher concentration of NS in solution resulted in a more close packed nanosphere resist (Figure 3.3), so 2:1 NS:EtOH was selected as the optimum concentration.

3.4 Nanopatterning

Plasma etching was used to reduce the size of the deposited nanospheres, and to etch the surface of the MoS_2. Details of the instrumentation used can be found in Section 2.1.3.

Experiments were undertaken to investigate the effect of changing the etch parameters on the final morphology. Five sets of samples were patterned, with each set containing three subsets. Each set consisted of 12 samples, and therefore each of the three subsets were 4 samples. Not every sample was completed successfully, with the painting with silver adhesive and epoxy resin being the most likely steps to fail due to the MoS_2 being inadvertently completely covered over.

Every set of samples examined the effect of altering one variable of the plasma etch parameters. The variable under investigation was systematically altered to create three distinct subsets. The variables altered were: O_2 etch length, SF_6 and C_4F_8 etch length, C_4F_8 flow rate, SF_6 flow rate, and O_2 flow rate. However, reliable control of the surface morphology through the etch parameters was never established, with the structure of the nanospheres following deposition having a far greater effect on the final surface morphology. The complete NSL and plasma etching process can be seen in Figure 3.4 with the nanospheres deposited on the surface, the shrunken nanospheres, and top and side view of the resulting nanopillars being imaged by SEM.

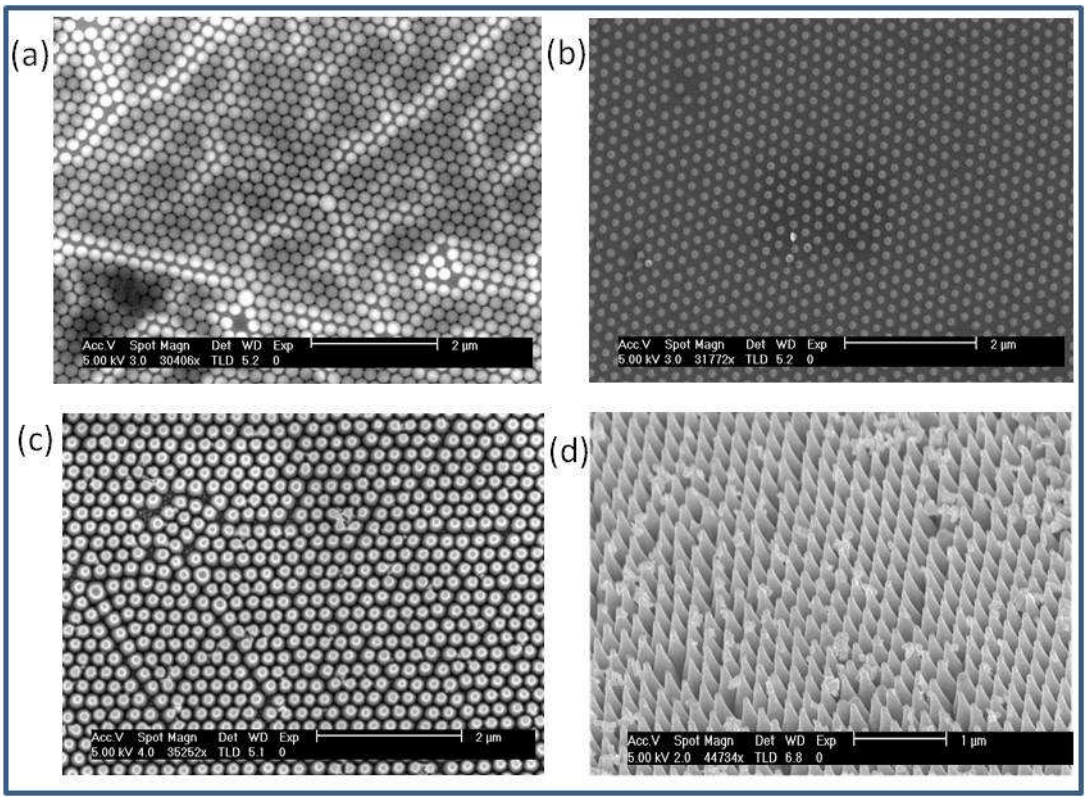

Figure 3.4. SEM images of the formation of nanopillars by NSL. (a) Nanospheres deposited on the surface of MoS_2, showing small gaps between the spheres. (b) Nanospheres that have shrunk due to be subjected to a 35 second O_2 plasma etch. (c) MoS_2 nanopillars formed from exposing the etch mask in (b) to 30 seconds of SF_6 and C_4F_8 plasma. (d) Side view of the nanopillars.

The efficacy of these MoS_2 morphologies at proton reduction was measured voltammetrically in acidic media (Section 2.3.1). The characteristics measured for comparison were the onset potential, peak current, and Tafel slope. The results were verified by Randles-Ševčík analysis.

3.4.1 Blank MoS_2

In order to establish whether the nanostructuring produced a favourable effect for the HER a series of blank samples were made. One set of these was the bulk condition, the other was randomly etched without NSL. The bulk set consisted of a piece of MoS_2 that had been cut, adhered to GC and cleaved, but had not undergone NSL or plasma etching. Following cleaving the MoS_2 had silver painted on the sides, and was coated with epoxy resin. The samples were then tested electrochemically for proton reduction.

For the randomly etched set the electrode assembly was made as described in (Section 3.1), and then was etched without depositing nanospheres on the surface. The MoS_2 was made hydrophilic using an O_2 etch as described in Section 2.1.3, and then etched further to mimic the NSL etch conditions (Table 3-1).

	Strike step	Main etch
Time (s)	1	35
APC (mTorr)	40	20
Base temp (°C)	20	20
Helium pres (Torr)	10	10
SF_6 (SCCM)	0	0
C_4F_8 (SCCM)	0	0
O_2 (SCCM)	100	100
RF (W)	100	100
ICP (W)	0	0

Table 3-1. Standard O_2 etch parameters used for the nanosphere shrink step of the plasma etching process. These conditions were used unless stated otherwise.

The SF_6 and C_4F_8 plasma etch was then performed, again without removing the MoS_2 from the etching chamber between etches. The parameters were as per Table 3-2.

	Strike step	Main etch
Time (s)	1	30
APC (mTorr)	15	15
Base temp (°C)	20	20
Helium pres (Torr)	10	10
SF_6 (SCCM)	15	25
C_4F_8 (SCCM)	50	20
O_2 (SCCM)	0	0
RF (W)	50	25
ICP (W)	300	220

Table 3-2. The SF_6 and C_4F_8 etch parameters used to etch the surface of MoS_2 following the shrinking of the nanospheres. These parameters were used for all SF_6 and C_4F_8 etch steps unless stated otherwise.

The randomly patterned samples were imaged by SEM (Figure 3.5), and silver painted with silver and epoxy resin before HER testing. The electrochemical measurements of the blanks were performed immediately after patterning.

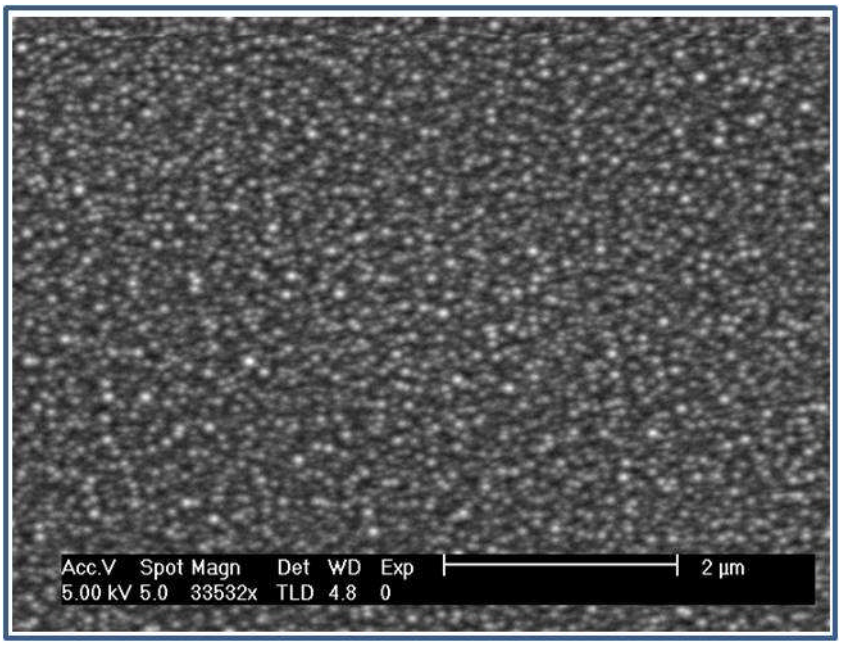

Figure 3.5. Randomly patterned surface resulting from subjecting the MoS_2 to all three plasma etch steps without first depositing nanospheres onto the surface.

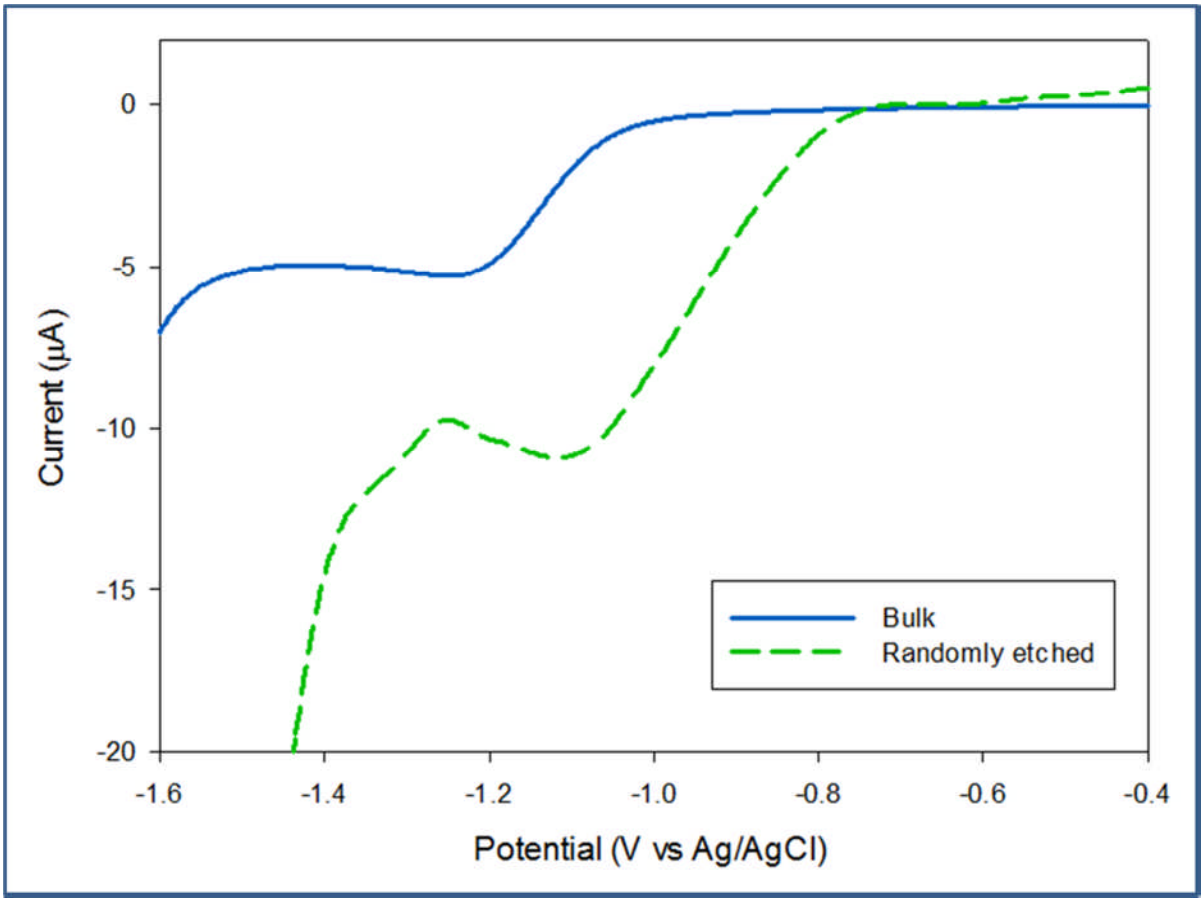

Figure 3.6. Proton reduction on bulk and randomly patterned MoS_2. The bulk sample is an unetched piece of MoS_2, and the randomly etched is the result of plasma etching without nanosphere lithography.

The randomly patterned sample showed an improvement over the bulk as it has a higher peak current and a lower onset potential (Figure 3.6). The randomly etched sample had a peak current density of -494 µA cm^{-2}, and an onset potential, identified by where the trace departed from the baseline, of -0.38 V SHE. For comparison the bulk crystal had a peak current density of -176 µA cm^{-2}, and an onset potential of -0.63 V SHE. The randomly patterned sample outperforming the bulk was expected due to the higher surface area

produced from a random orientation exposing more catalytic edge sites. The proton reduction results were verified by Randles-Ševčík analysis (Eq 3.1) (Figure 3.7).

$$i_p = 2.99 \times 10^5 \, n(\alpha n)^{0.5} \, A \, C \, D^{0.5} \, v^{0.5} \qquad \text{(Eq 3.1)}$$

Where i_p is the peak current, n is the number of electrons involved in the electron transfer step, A is the area, C is the concentration, D is the diffusion coefficient, and v is the scan rate[159]. The voltammograms were conducted in 2 mM $HClO_4$ electrolyte, at scan rates between 5 mV s^{-1} and 1200 mV s^{-1} and the areas were calculated as per Section 3.2.

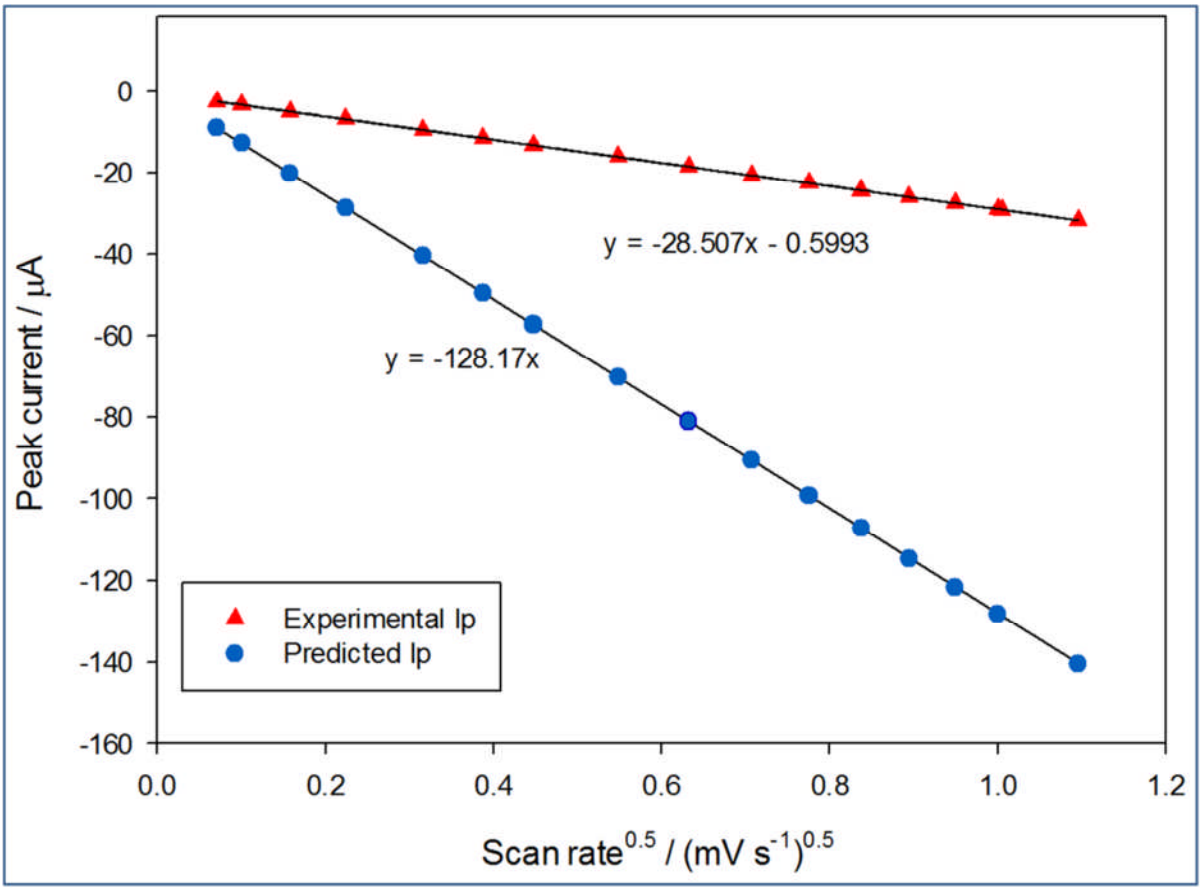

Figure 3.7. Experimental and predicted peak currents for the cleaved blank MoS_2.

The peak currents for the cleaved blank are lower than expected for an electrode of this size, presumably reflecting an active area considerably lower than the geometric area.

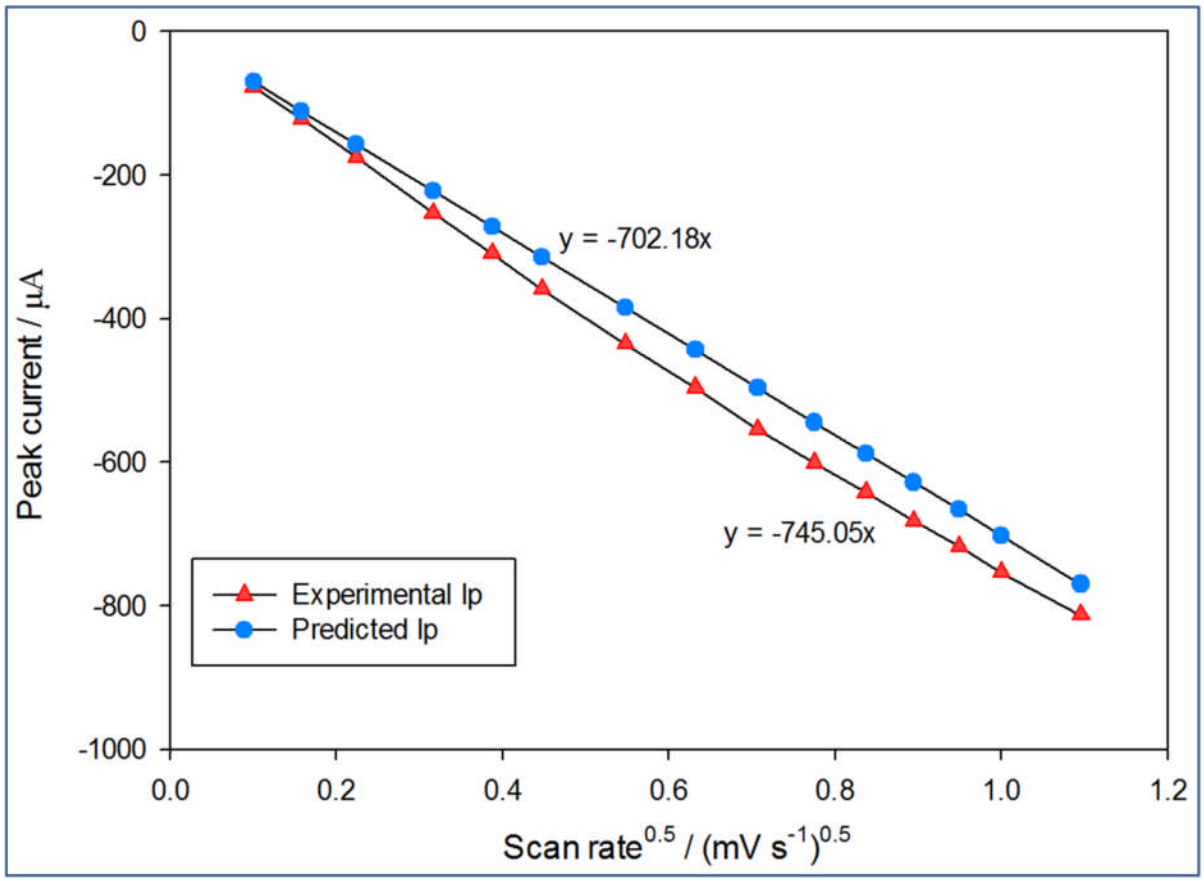

Figure 3.8. Experimental and predicted peak currents for H^+ reduction on glassy carbon blank as per the Randles-Ševčík equation.

The GC blank experimental peak currents were in agreement with the predicted results as shown in Figure 3.8. The GC blank verification was taken as proof the experimental set-up was functioning correctly, and the low gradient for MoS_2 electrodes were considered a characteristic feature. As these results were reproducible the MoS_2 electrodes were considered suitable for comparison with one another.

3.4.2 O_2 Etch Length

A set of samples were prepared to investigate the effect on O_2 etch length on the final morphology achieved, and on the catalytic effect for the HER. The samples were in three subsets with the length of time of the O_2 nanosphere shrinking etch being the variable under investigation. The first group was etched for 30 seconds (Figure 3.9), the second for 35 seconds (Figure 3.10), and the third for 40 seconds (Figure 3.11). The other variables for the O_2 etch were as Table 3-1, and the SF_6 etch was as Table 3-2.

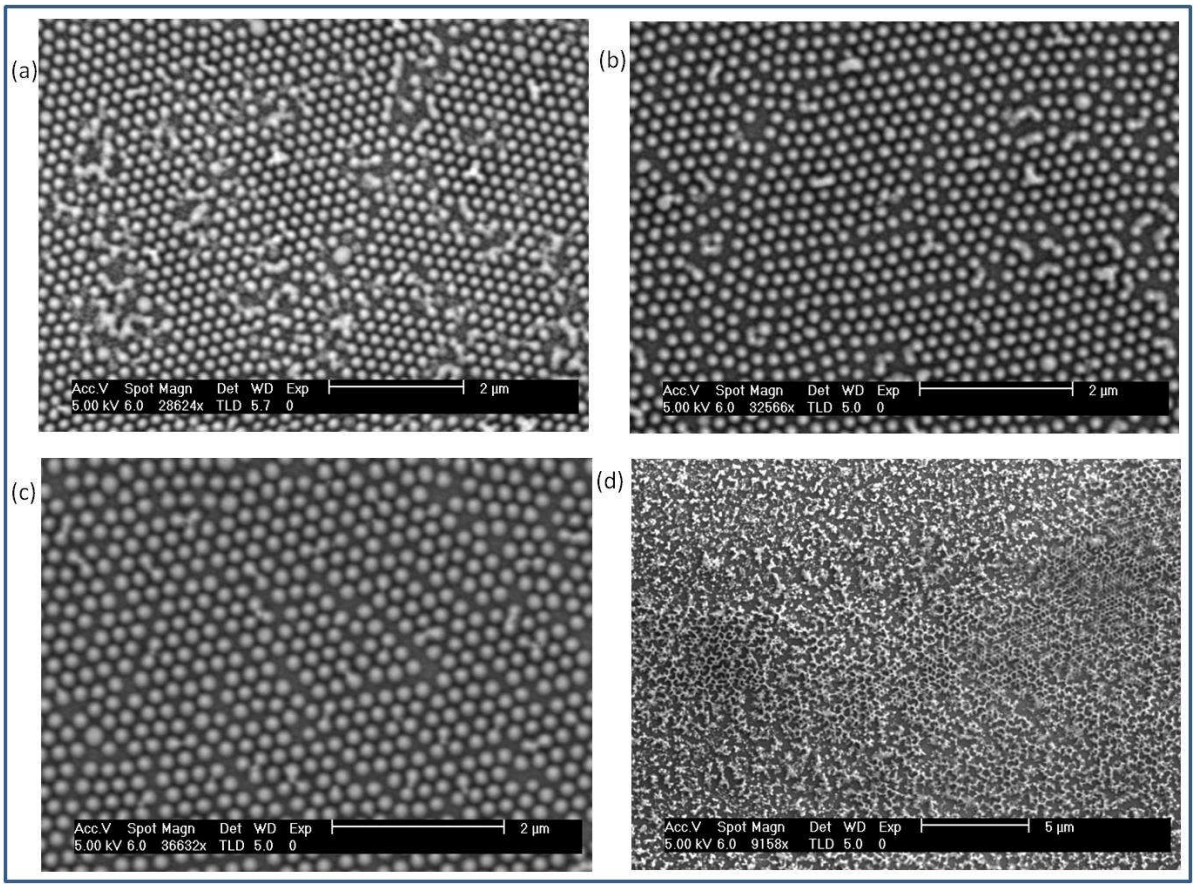

Figure 3.9. Four MoS_2 sample morphologies resulting from a 30 second O_2 nanosphere shrinking etch. Samples (a), (b), and (c) had a pillar morphology with spacings between features of 122nm, 162nm, and 158nm respectively. (d) had a mixed morphology comprising of pillars, and nanowells.

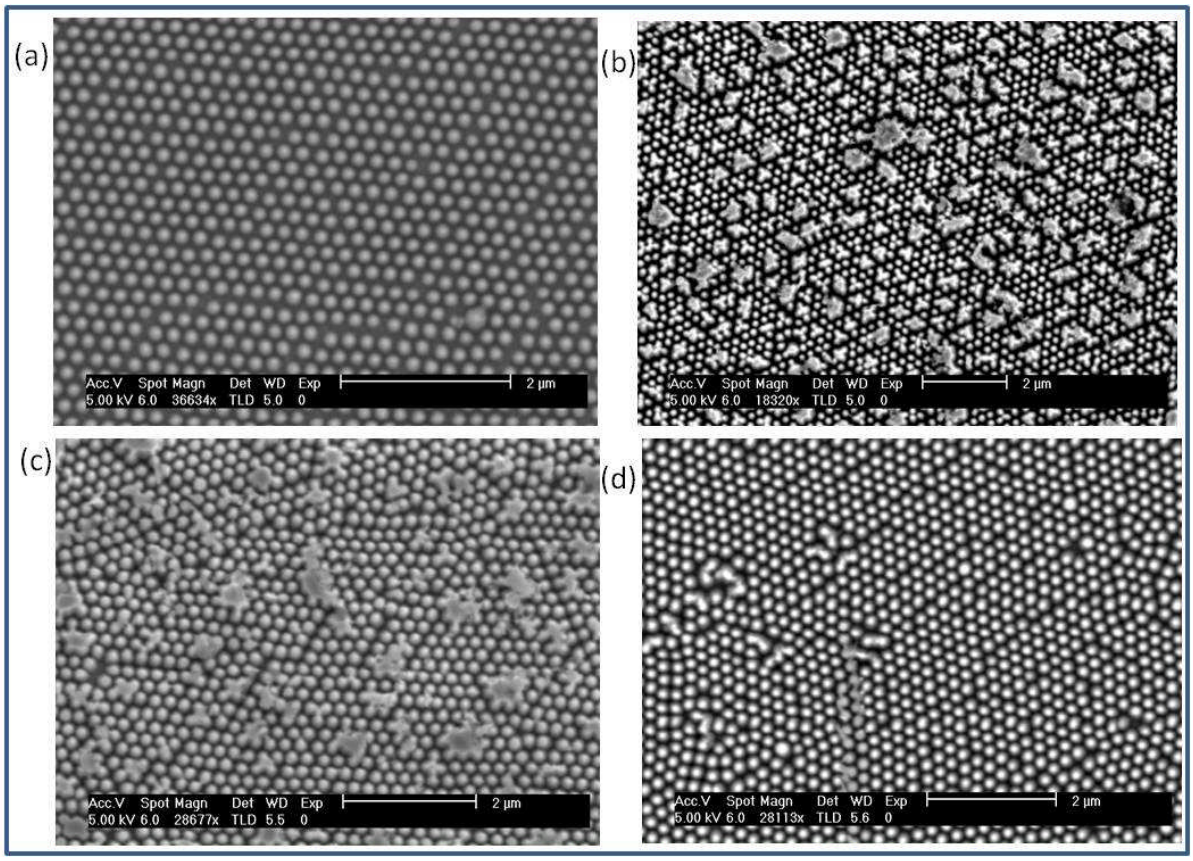

Figure 3.10. Four MoS_2 sample morphologies resulting from a 35 second O_2 nanosphere shrinking etch. All four displayed pillar morphology, however (b) and (c) had larger clumps resulting from the nanospheres not separating. The feature spacings were 171 nm, 160 nm, 116 nm, and 130 nm for (a), (b), (c), and (d) respectively.

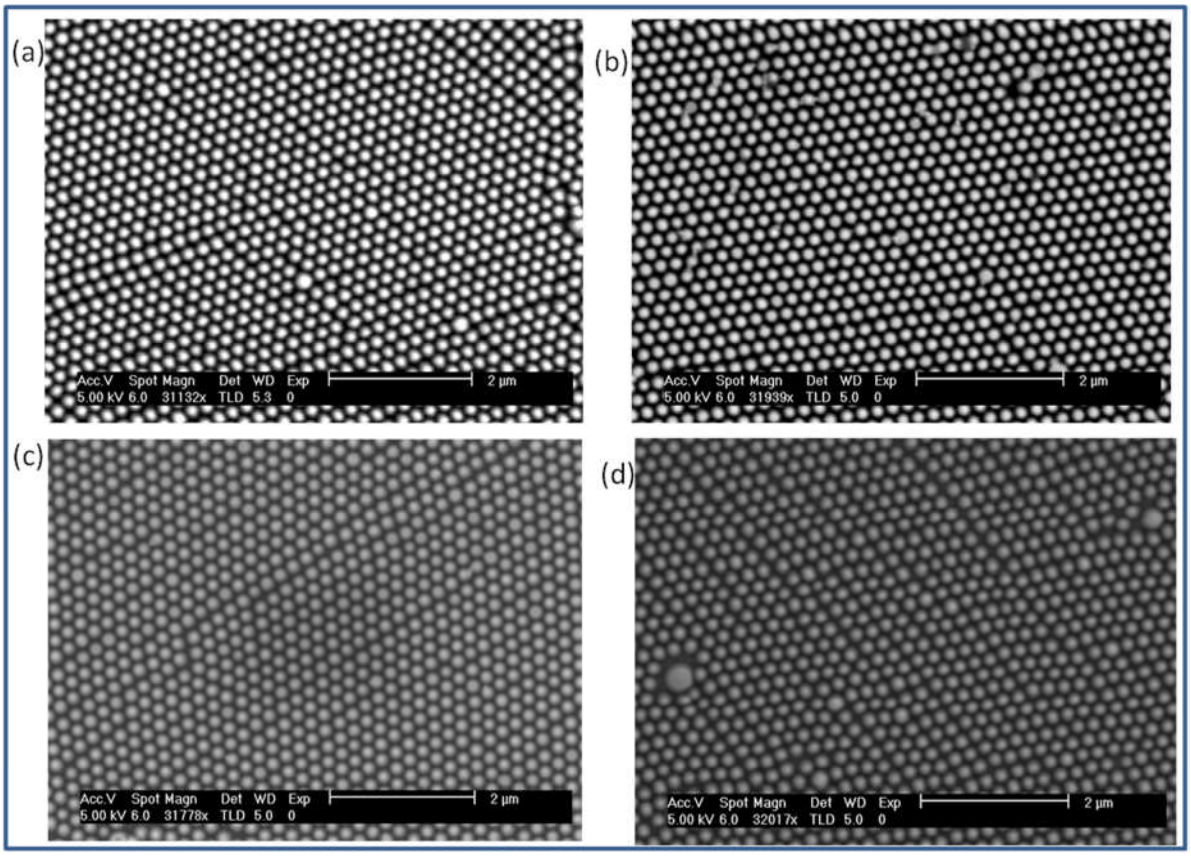

Figure 3.11. Four MoS_2 sample morphologies resulting from a 40 second O_2 nanosphere shrinking etch. These all displayed a pillar morphology, with (a) 109 nm, (b) 136 nm, (c) 174 nm, and (d) 196 nm spacings.

The O_2 exposure length did not have a controlled effect on the final morphology. These samples mostly formed nanopillars, or clumps of nanopillars. The spacing between these features varied within each set, and no trend could be drawn between O_2 etch length and pillar spacing. These samples were prepared first and HER tested last, with 28 days between nanopatterning and electrochemical testing. As such the electrochemical data was poor, and no proton reduction peak was identified for any sample.

3.4.3 SF_6 Etch Length

The effect of the length of the SF_6 and C_4F_8 was investigated by making three batches of samples and varying the time they were exposed to the relevant plasma. The first batch was exposed for 25 seconds (Figure 3.12), the second for 35 seconds (Figure 3.13), and the third for 40 seconds (Figure 3.14). The other etch parameters were as per Table 3-1 and Table 3-2.

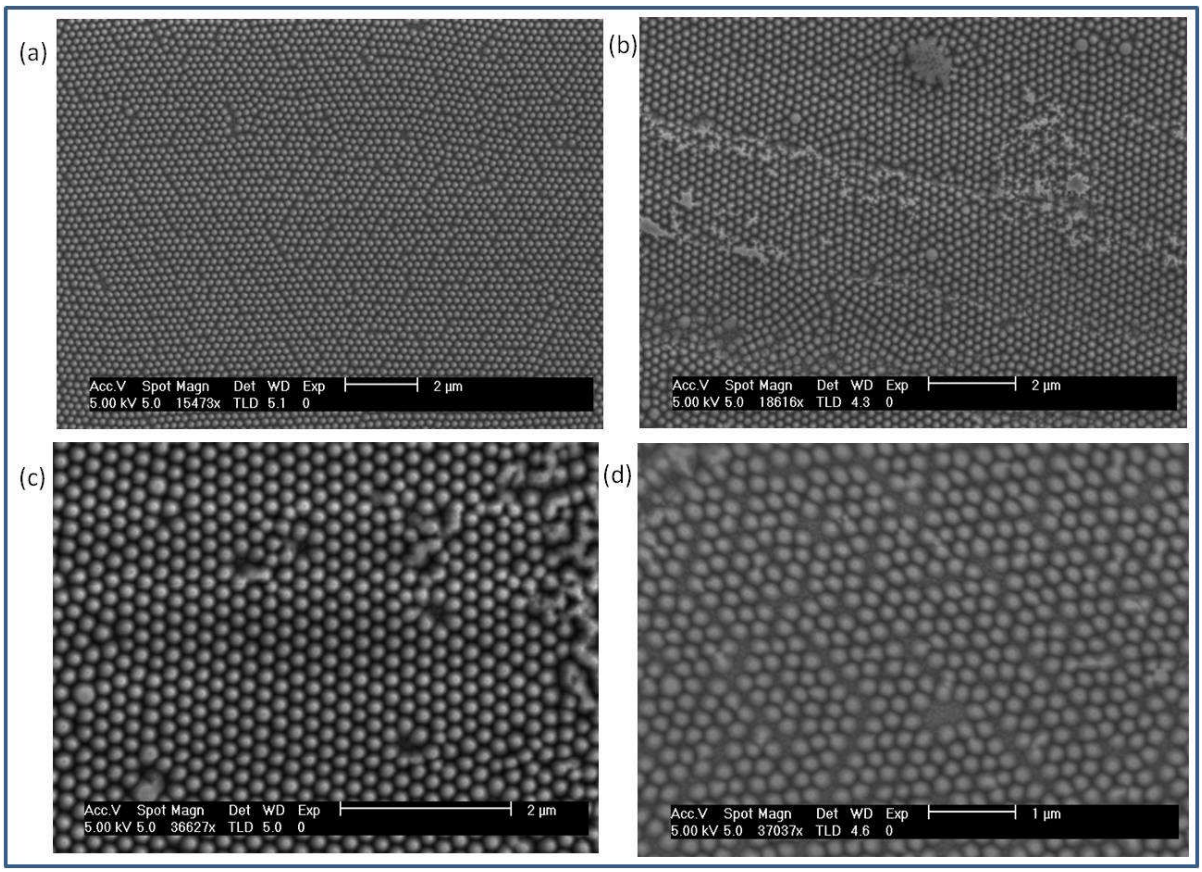

Figure 3.12. Four MoS_2 sample morphologies resulting from a 25 second SF_6 nanosphere shrinking etch. Each formed pillars, although the spacing of the pillars varied between samples with (a) having 149 nm spacings between samples, and (b) having 164 nm, (c) was 147 nm and (d) 161 nm.

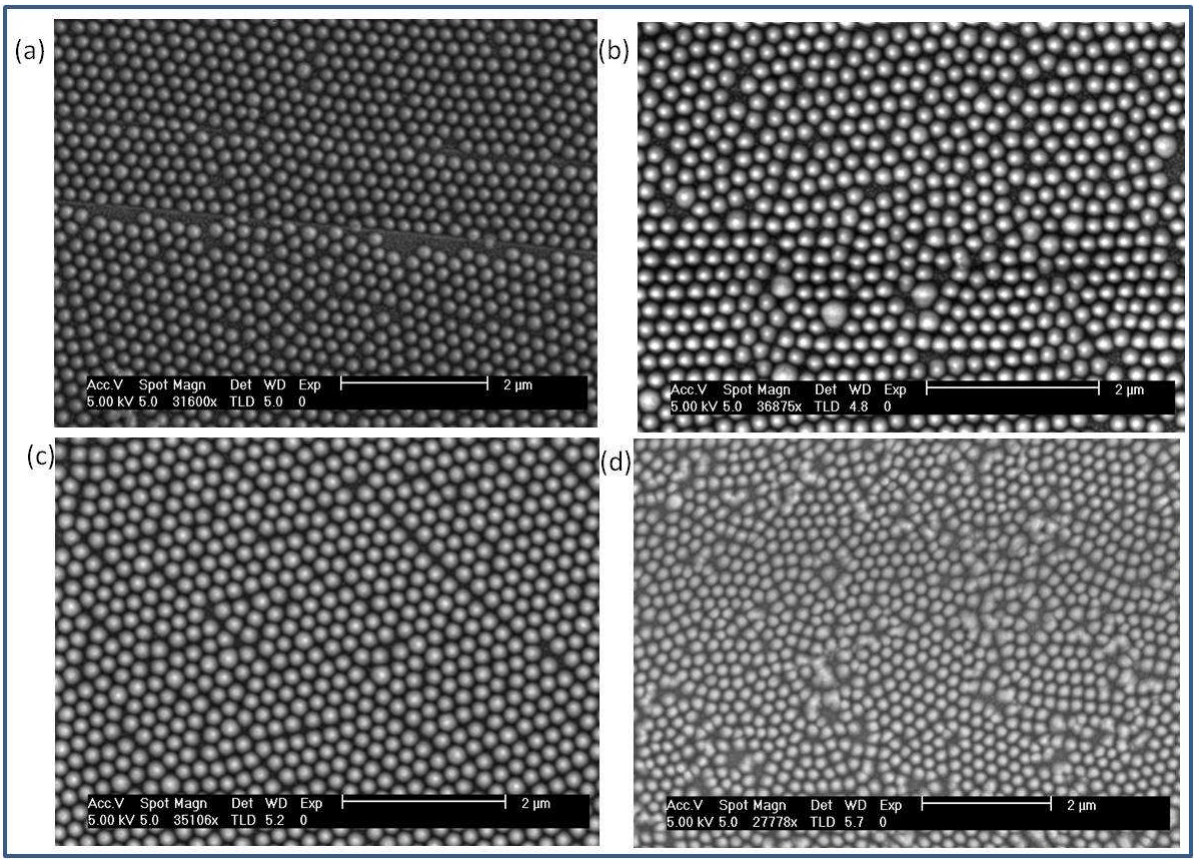

Figure 3.13. Four MoS_2 sample morphologies resulting from a 35 second SF_6 nanosphere shrinking etch. Each formed pillars with spacings of 146 nm, 134 nm, 118 nm, and 152 nm, for (a), (b), (c) and (d), respectively.

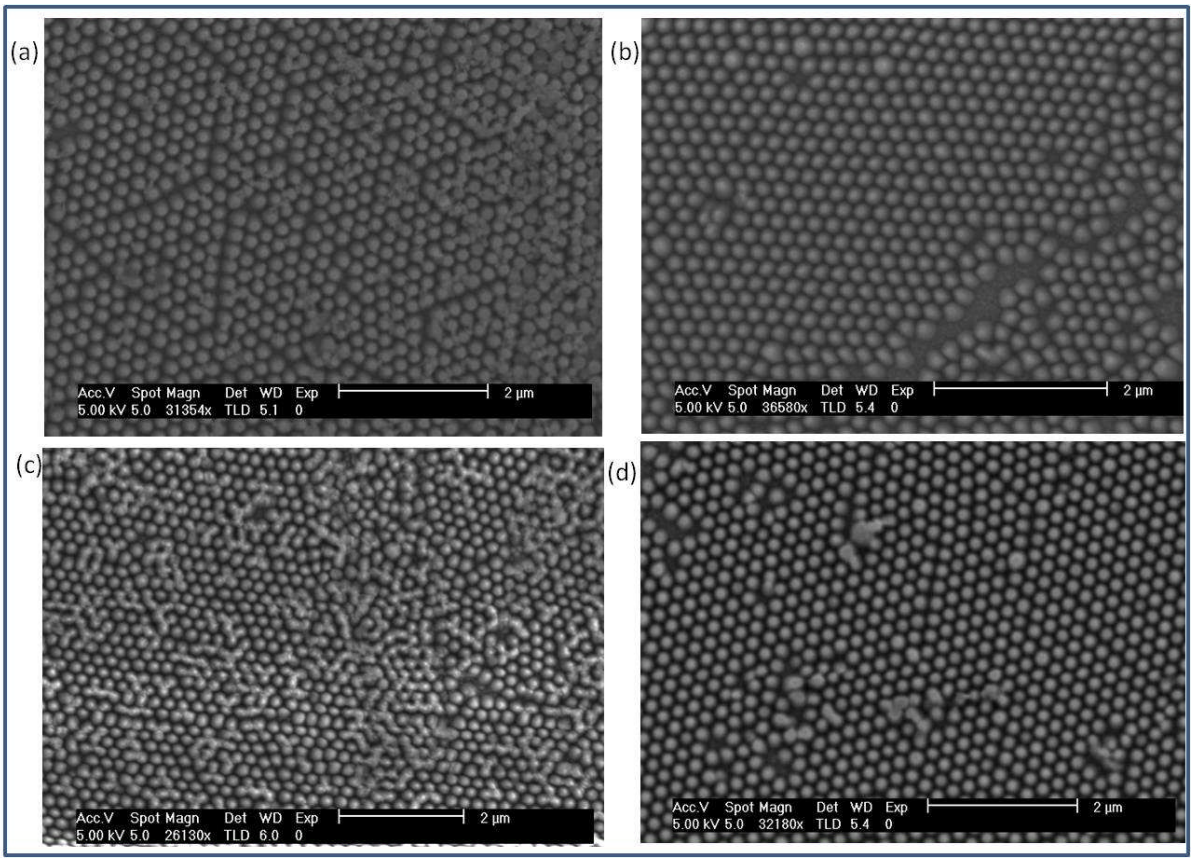

Figure 3.14. Four MoS_2 sample morphologies resulting from a 40 second SF_6 nanosphere shrinking etch. Pillar morphologies were formed with some clumping from where the nanosphere resist didn't separate in (a), (c) and (d). The pillar spacings were 147 nm for (a), 127 nm for (b) and (c), and 131 nm for (d).

It was determined that controlled reproducible morphologies could not be achieved through altering the etch length of the SF_6 and C_4F_8 etchants. These morphologies were tested for HER catalysis and the results are in Section 3.4.7.

3.4.4 C_4F_8 Flow Rate

Another batch comprised of three sets of samples was made in order to determine the effect of C_4F_8 flow rate on the morphology and HER catalysis. The first set had a C_4F_8 flow rate of 10 SCCM (Figure 3.15), the second of 30 SCCM (Figure 3.16), and the last had a flow rate of 40 SCCM (Figure 3.17). The other etch parameters were as per Table 3-1 and Table 3-2.

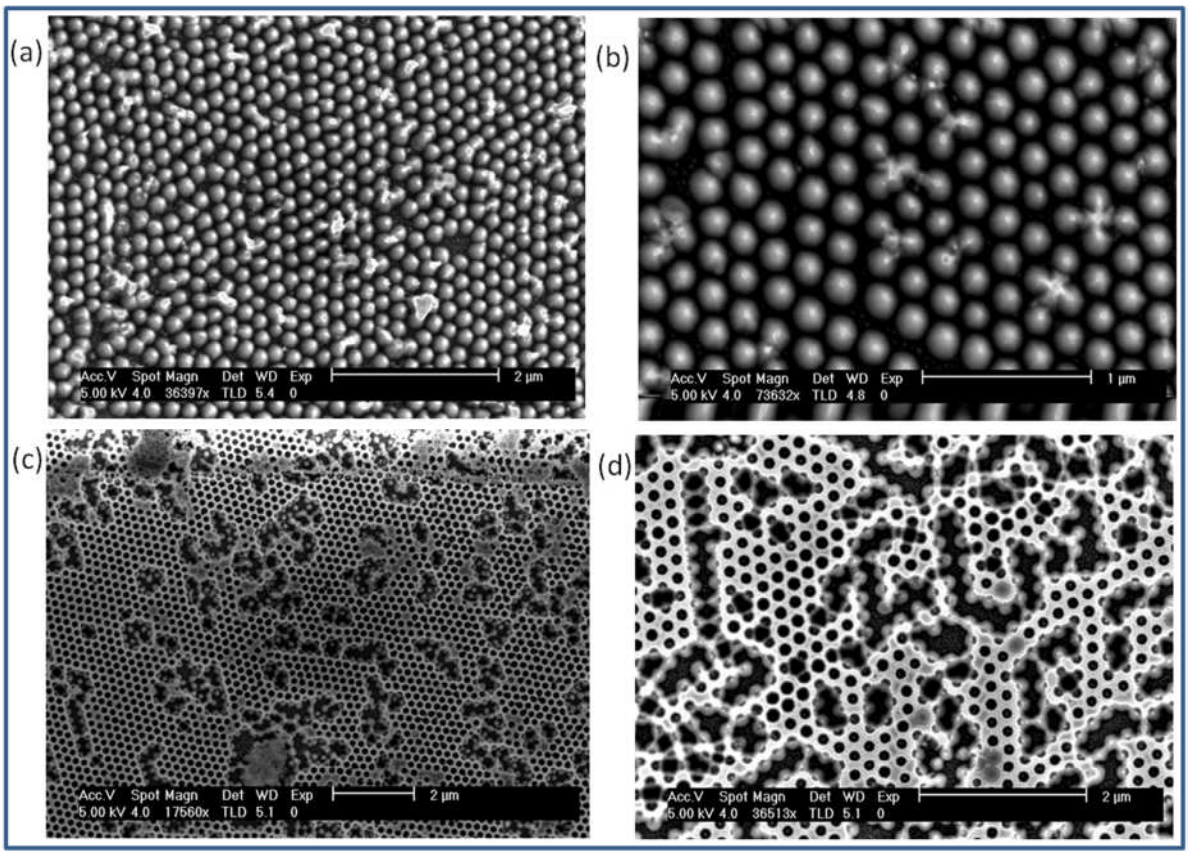

Figure 3.15. Four MoS_2 sample morphologies resulting from a flow rate of 10 SCCM C_4F_8 during the SF_6 etch. (a) Was predominantly pillars, with some linkages in between and spacings of 145 nm between nanopillars. (b) Was mostly comprised of linked pillars, with some nanowells. (c) and (d) had a nanowell morphology.

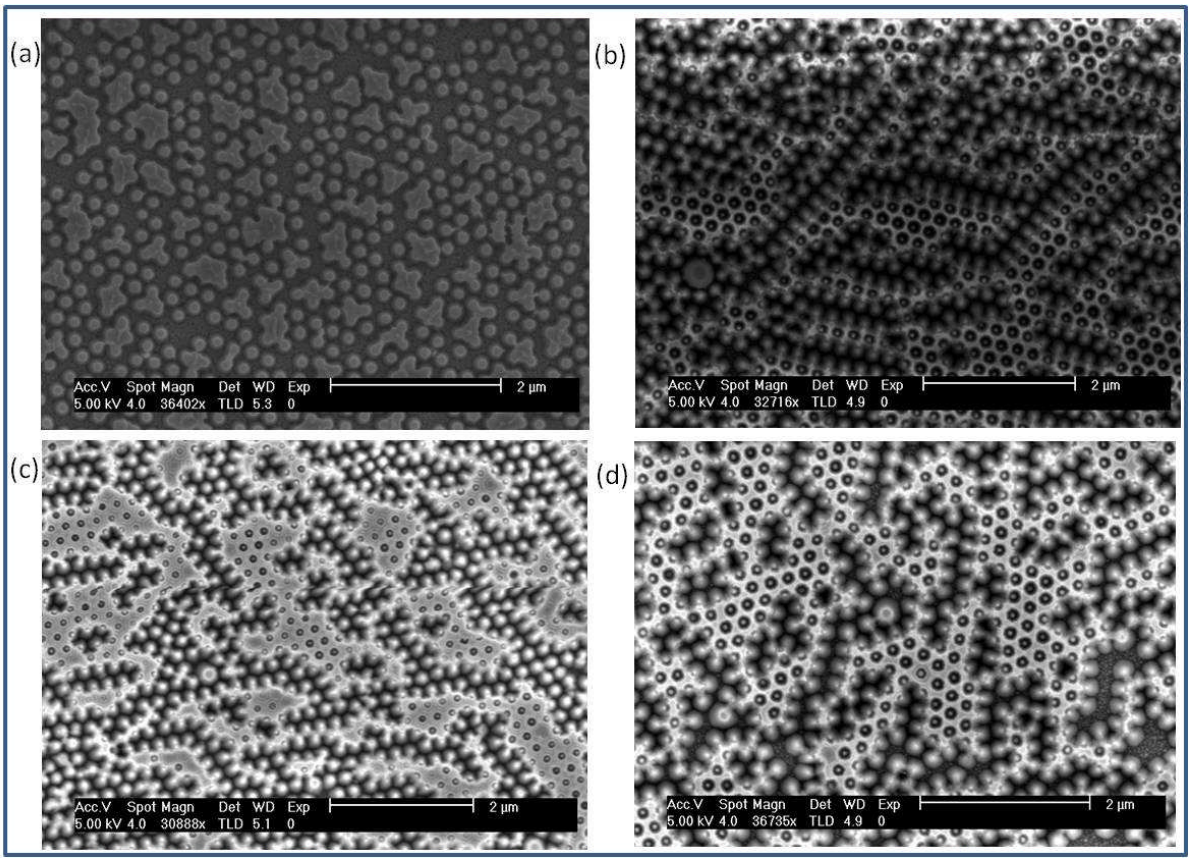

Figure 3.16. Four MoS_2 sample morphologies resulting from a flow rate of 30 SCCM C_4F_8 during the SF_6 etch. (a) Was comprised of anisotropic pillars with variable spacings between features. (b), (c), and (d) were nanowells with a central pillar remaining within the well.

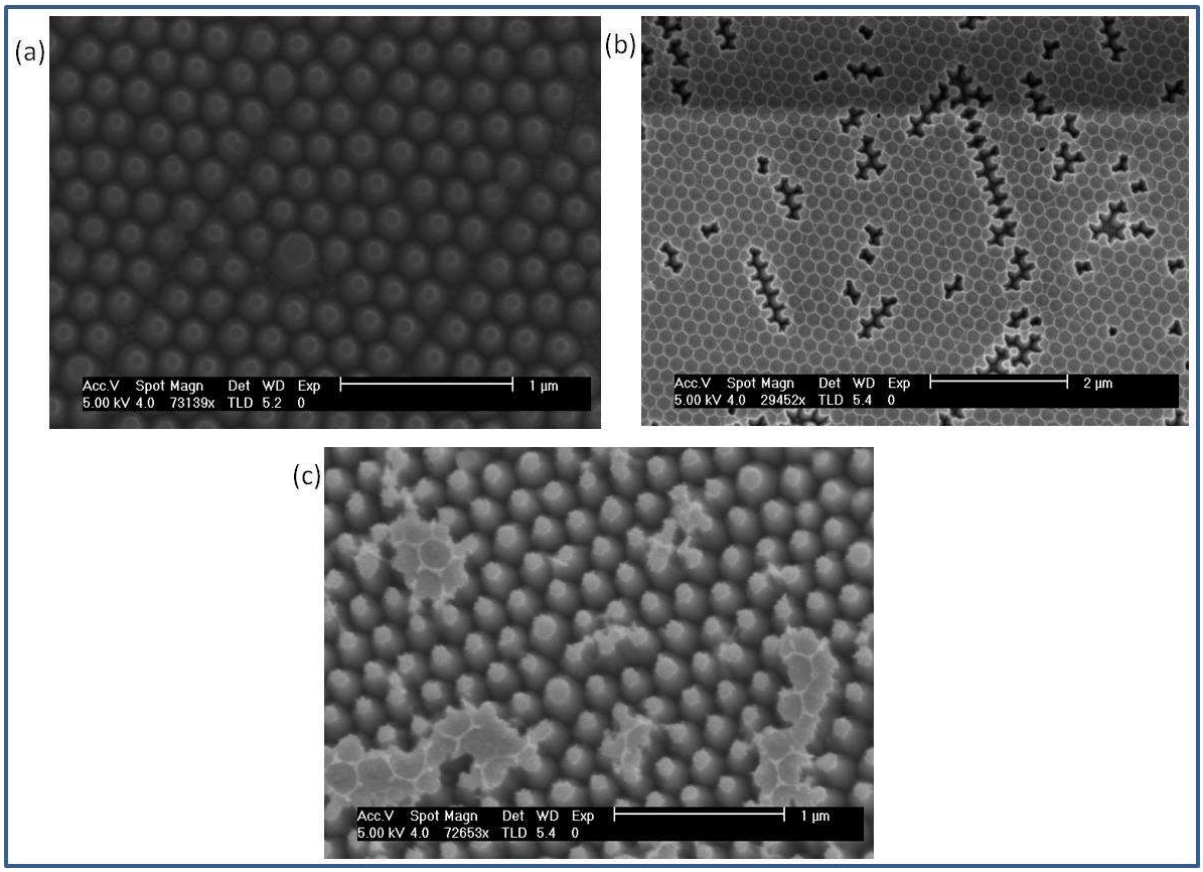

Figure 3.17. Three MoS_2 sample morphologies resulting from a flow rate of 40 SCCM C_4F_8 during the SF_6 etch step. (a) Was comprised of anisotropic pillars with 126 nm between features. (b) Was unformed nanowells with the central well remaining closed. (c) Was comprised of anistropic pillars with some proto-nanowells. The pillars had 118 nm spacings.

Similarly to the etch time experiments altering the C_4F_8 flow rate did not provide a satisfactory level of reproducibility. However, the pillars produced by a 30 and 40 SCCM C_4F_8 flow rate are more anisotropic than those made by a 10 SCCM. This is as expected as more C_4F_8 will result in a thicker passivation layer, and hence less directional etching[78].

This batch of samples resulted in a higher than usual number of nanowell morphologies, however, this is due to the nanosphere morphology following deposition rather than the etch parameters (Section 3.5).

3.4.5 SF_6 Flow Rate

The SF_6 flow rate was the next variable under investigation. As with previous experiments three sets of samples were made using the etch parameters in Table 3-1 and Table 3-2, with the exception of the SF_6 flow rate parameter. The first set of this experiment was etched using a flow rate of 15 SCCM (Figure 3.18), the second with 35 SCCM (Figure 3.19), and the final set with 45 SCCM (Figure 3.20).

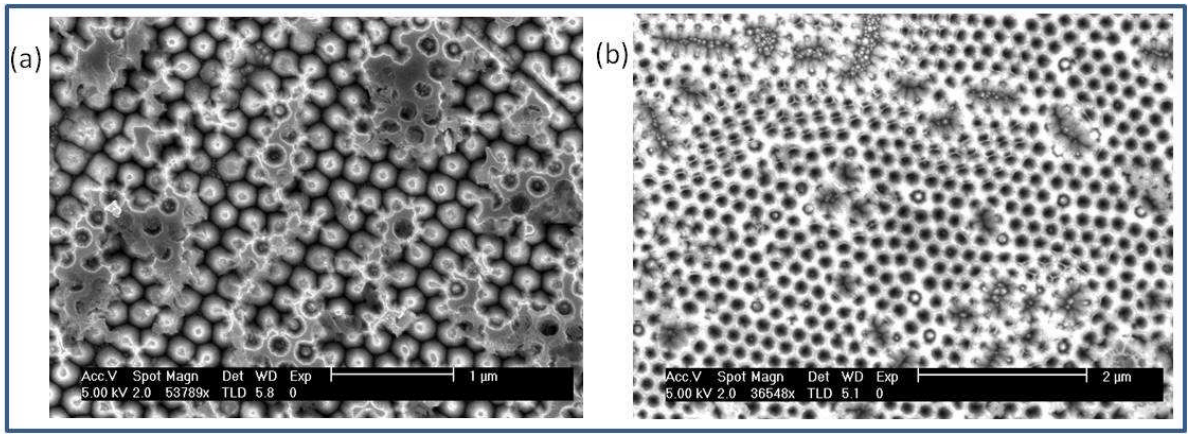

Figure 3.18. Two MoS_2 samples morphologies resulting from a flow rate of 15 SCCM SF_6 during the final etch. (a) Was comprised of linked pillars with some nanowells. (b) Had a nanowell morphology. In this image the nanomesh formed from the nanospheres is visible over some parts of the MoS_2.

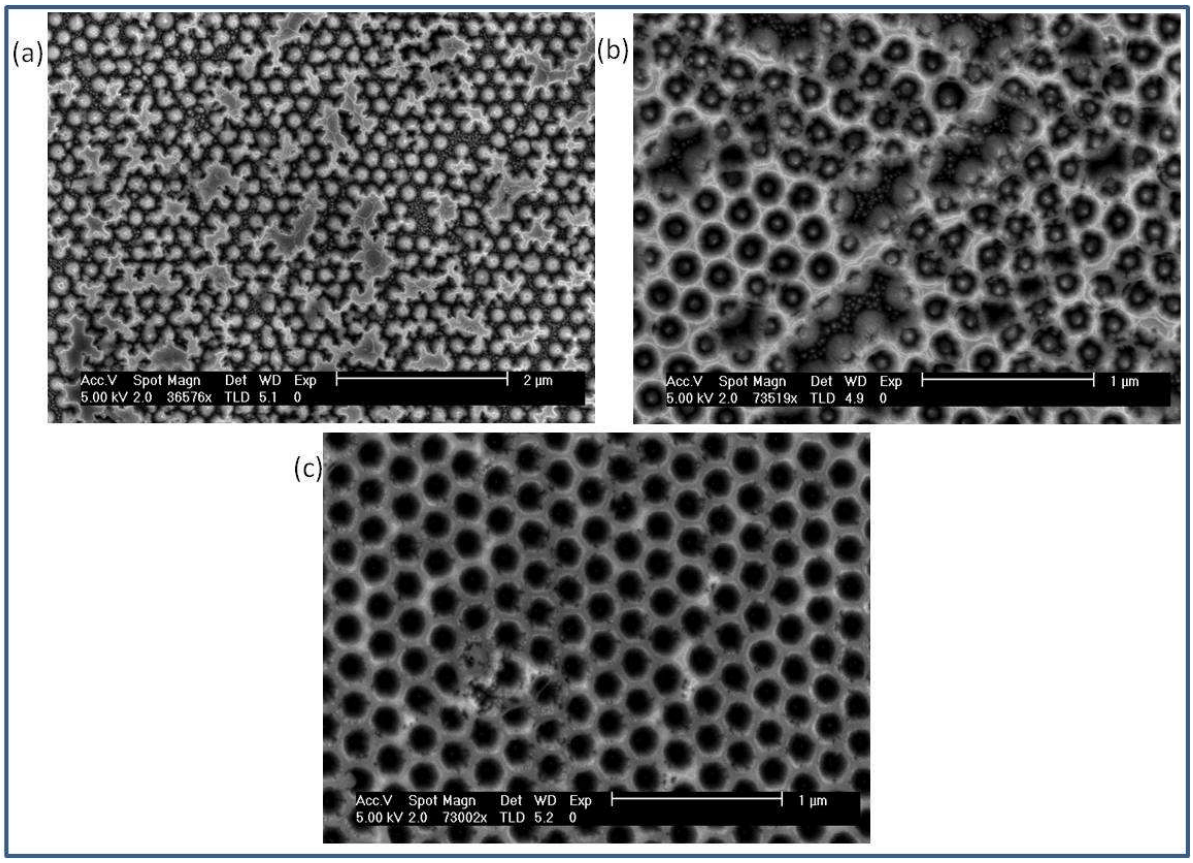

Figure 3.19. Three MoS_2 sample morphologies resulting from a flow rate of 35 SCCM SF_6 during the final etch. (a) Was comprised of anisotropic pillars, with linkages, (b) was nanowells with a central pillar, and (c) was comprised entirely of nanowells.

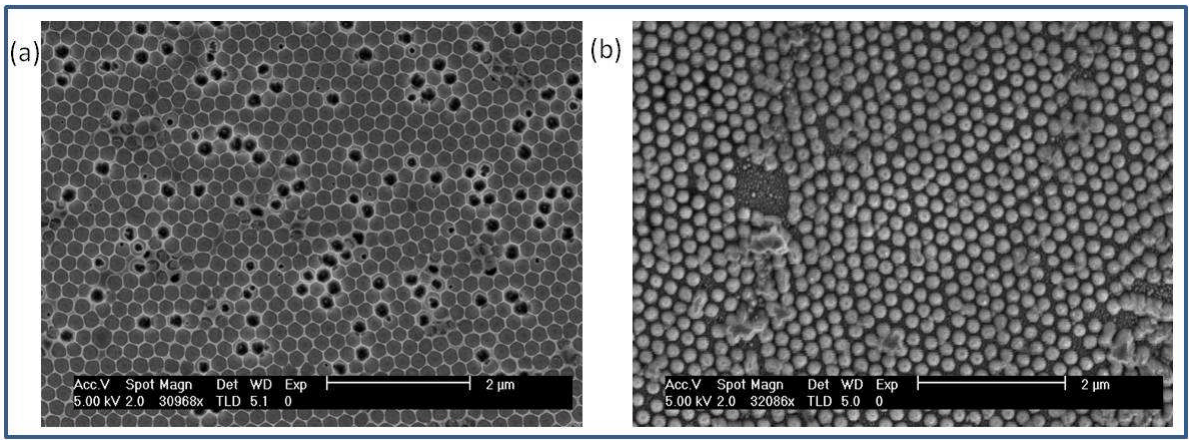

Figure 3.20. Two MoS_2 sample morphologies resulting from a flow rate of 40 SCCM SF_6 during the final etch. (a) Was mostly unformed nanowells, although in some the centre has opened. (b) Had a nanopillar morphology.

As with the other etch parameters attempted manipulating the flow rate of SF_6 did not have a reproducible effect of the final morphology. The 15 SCCM and 35 SCCM flow rates resulted in linked pillars or nanowell morphologies. The 40 SCCM flow rate had one sample that was unformed nanowells, and one with a pillar morphology.

3.4.6 O_2 Flow Rate

The final etch parameter experimented with was the O_2 flow rate. As previously the etch parameters were the same as Table 3-1 and Table 3-2 with the exception of the O_2 flow rate during the nanosphere shrinking etch. The first set was etched at a flow rate of 90 SCCM (Figure 3.21), the second 80 SCCM Figure 3.22. Two MoS_2 sample morphologies resulting from a flow rate of 80 SCCM O_2 during the nanosphere shrinking etch. Both (a) and (b) were comprised of pillars with spacings of 130 nm and 87 nm respectively, although in (b) some

of the pillars had aggregated.Figure 3.22), and the final set was etched at 70 SCCM (Figure 3.34). As with previous manipulation of the etch parameters had failed to provide control over the final morphology of the MoS_2. However, it was noticed over the course of this investigation that the nanospheres structure following deposition determined the final morphology (Section 3.5). It was considered that therefore control over the shrinking of the nanospheres could be used to reproducibly modify the final morphology.

Equipment faults with the SEM prevented imaging any of the 70 SCCM flow rate set of samples. These samples were also used for sulfidation, and repeated exposure to this technique obscured the surface features (Section 4.4). These circumstances prevented the structure of these samples from being elucidated.

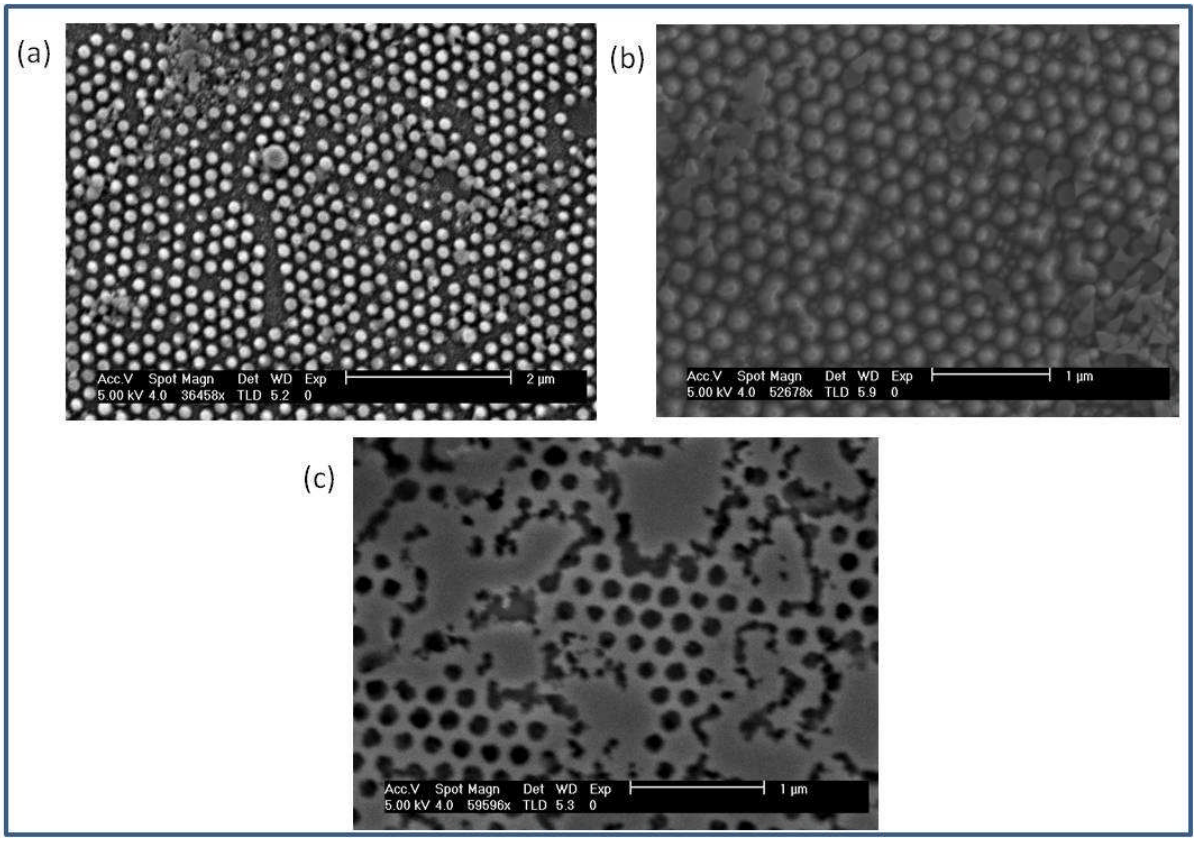

Figure 3.21. Three MoS_2 sample morphologies resulting from a 90 SCCM O_2 flow rate during the nanosphere shrinking etch. (a) and (b) had pillar morphologies with separations of 96 nm and 142 nm, respectively. (c) Was comprised of poorly defined nanowells.

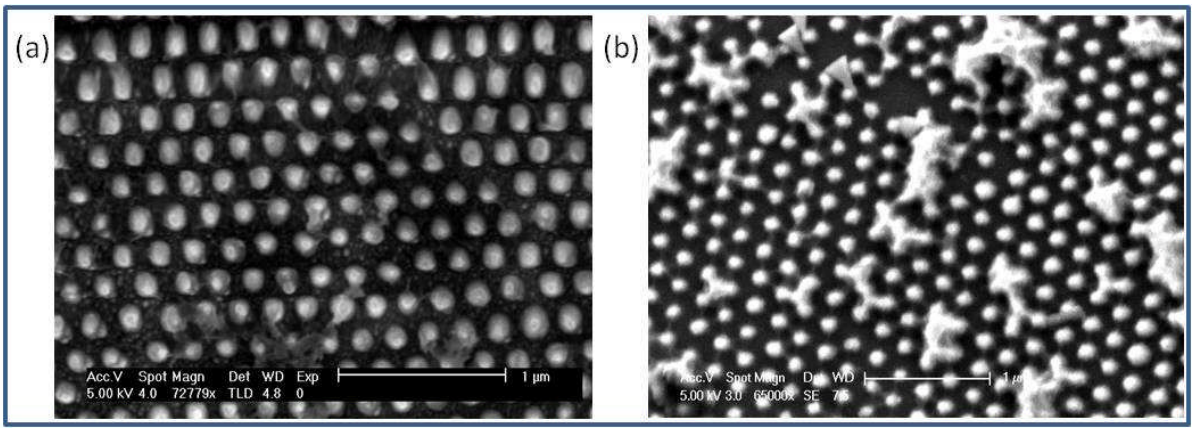

Figure 3.22. Two MoS_2 sample morphologies resulting from a flow rate of 80 SCCM O_2 during the nanosphere shrinking etch. Both (a) and (b) were comprised of pillars with spacings of 130 nm and 87 nm respectively, although in (b) some of the pillars had aggregated.

Once again this etch parameter did not yield an adequate level of control over the final morphology of the MoS_2. With the exception of Figure 3.21 (c) this experiment yielded pillar morphologies. Figure 3.21 (c) was comprised of nanowells, however in many areas these had not fully formed leaving large clumps of material.

3.4.7 Relationship Between Nanosphere Deposition Conditions and HER Catalysis

The morphologies presented above were electrochemically tested to observe the difference obtained by varying the etch parameters. The effects of diffusion regime were considered negligible for comparison between the morphologies fabricated as the length of diffusion was considerably greater than both the radius of the individual features and the distance between features. The diffusion length was calculated according to Eq 1.14 as 565 μm with a 400 mV scan window, 25 mV s^{-1} scan rate and 1×10^{-4} cm^2 s^{-1} proton diffusion coefficient[160]. The feature radius and separation for all morphologies was orders of magnitude smaller at ca. 100 nm, and therefore type IV diffusion is reasoned to be the mass transport mechanism for all samples.

The samples presented above were electrochemically tested in reverse chronological order in an attempt to mitigate against aerial oxidation. There was a delay of 29 days between construction and testing of the samples from Section 3.4.3. Two samples displayed a poorly resolved proton reduction wave when electrochemically tested (Figure 3.23).

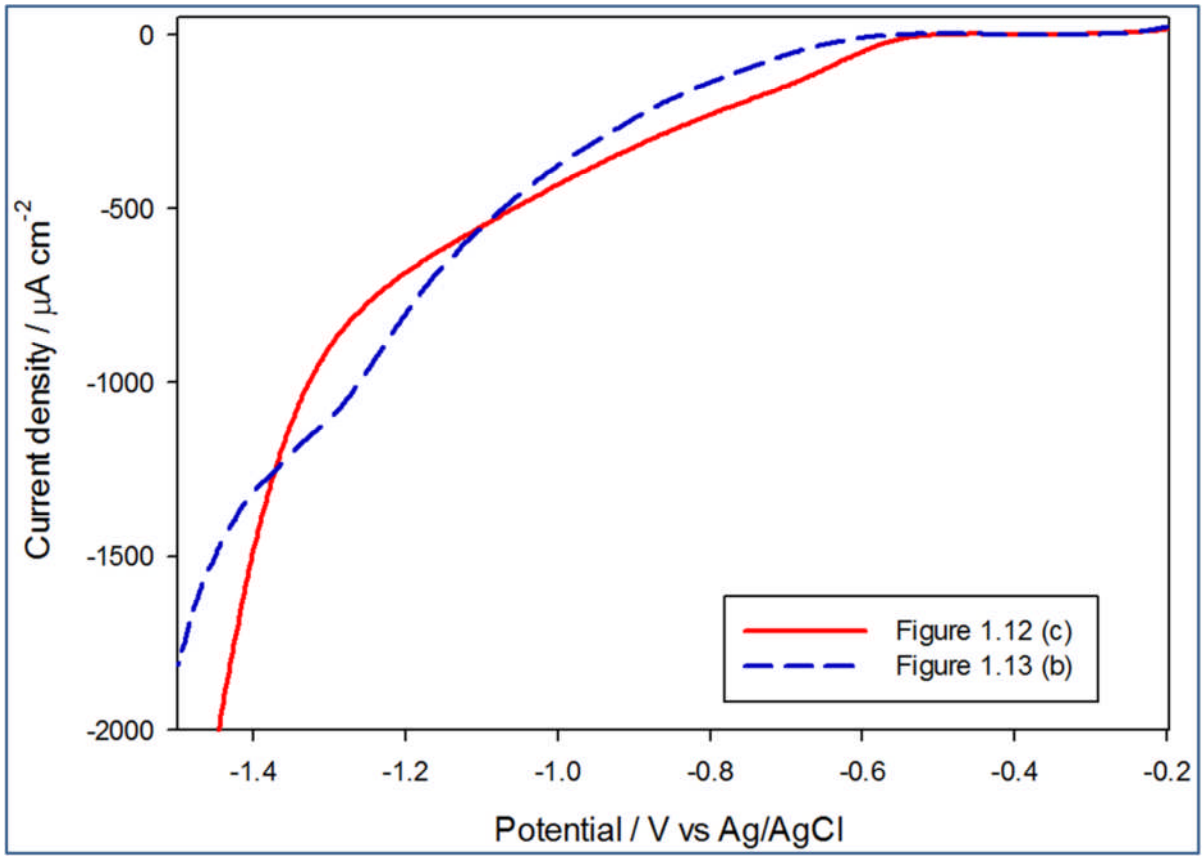

Figure 3.23. Proton reduction on nanostructured MoS_2. The sample subjected to a 25 second SF_6 etch had an earlier onset potential but no clearly defined proton reduction peak. The 35 second SF_6 etch had a peak, but at a high overpotential of -0.93 V SHE.

The 25 second SF_6 etch sample is shown in Figure 3.12 (c), and the 35 second was Figure 3.13 (b). The catalytic difference between the two samples was too small to draw conclusions from, with only the 35 second SF_6 and C_4F_8 etch length sample showing a proton reduction peak. This peak was at a high overpotential of -0.96 V SHE.

The samples from Section 3.4.4 had 23 days between nanopatterning and testing, and it appears that this 5 days shorter waiting period resulted in significantly less air degradation as every sample in this group had a clearly defined proton reduction wave (Figure 3.24).

However, every sample had a similar onset potential, and there was no correlation between C_4F_8 etchant flow rate and peak current.

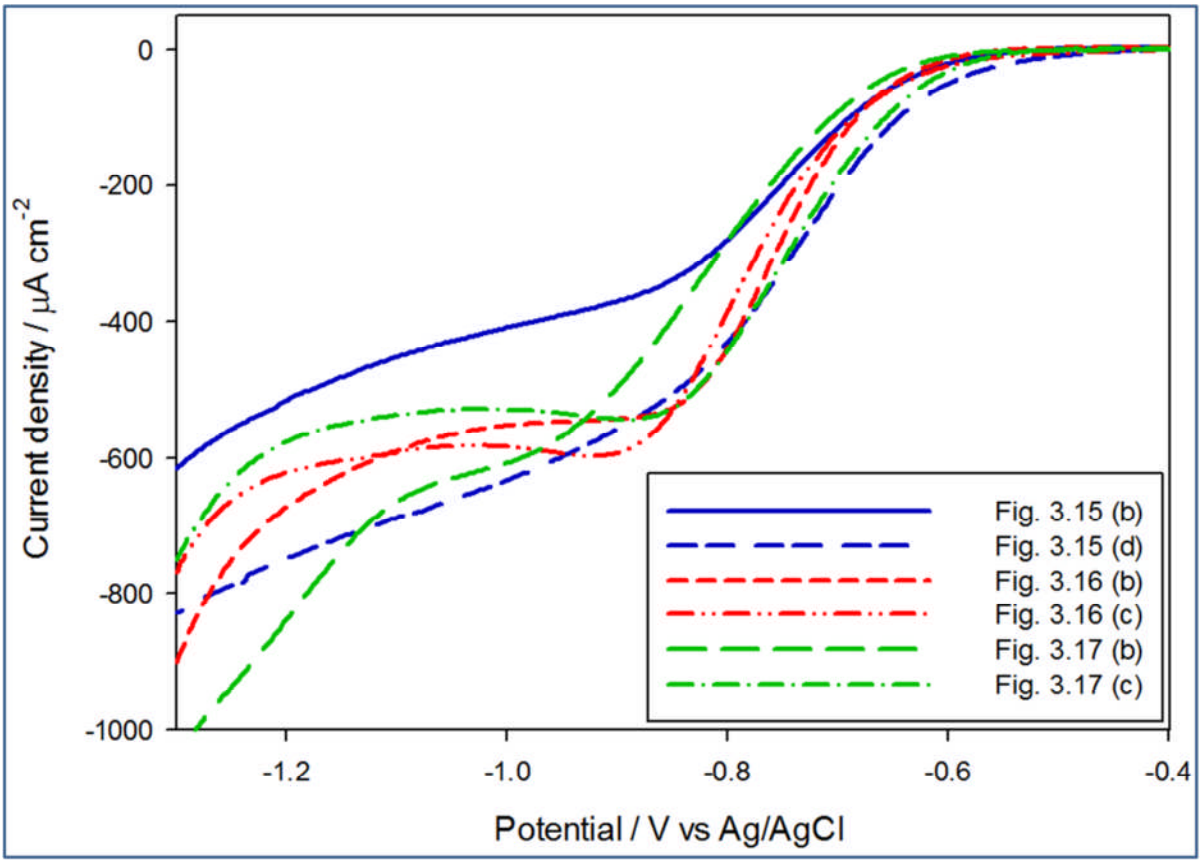

Figure 3.24. Proton reduction on two samples of each set of the C_4F_8 variable flow rate experiment. Blue is 10 SCCM, red is 30 SCCM, and green is 40 SCCM C_4F_8 flow rate.

There was however some correlation between proton catalytic ability and morphology type. It is necessary to be careful, however, when comparing porous nanoelectrode arrays with bulk morphologies[85,161]. Analyte may become trapped in pockets between features and not replenished by mass transport through diffusion. Should this occur a thin layer response is measured in which a high surface area electrode is briefly obtained before the trapped electrolyte becomes depleted. On a voltammogram this manifests itself as a shift

toward zero overpotential, and can be erroneously interpreted as an improvement in electrocatalysis[85,161]. This effect should be similar for the morphologies produced here as the feature separation does not differ greatly, though it may be more pronounced in the nanowell morphology due to the enclosed spaces.

It is also important to consider the weaknesses in using geometric surface area as the means of calculating the current density. The electrochemical surface area (ECSA) is likely smaller than the geometric as shown by the Randles-Sevcik analysis (Section 3.4.1)[159]. This indicates that the surface is heterogeneous and there are insulating areas preventing conduction between the some active sites and the substrate[162]. Capacitance is an alternative method to determine the ECSA. This method consists of measuring the capacitance in very dilute solutions (ca. 10^{-3} mol dm^{-3}) and assuming that the capacitance at the potential of zero charge is entirely due to the diffuse layer capacitance[163]. This enables the surface area to be obtained by means of the Gouy-Chapman theory. This method is dependent on the assumption that the inner layer capacitance is as low as as the case with Hg. Results for other metals such as As, Au, and Ga have shown that this is not a general case[163].

A more appriopriate method giving what is being measured would be Hydrogen adsorption from solution. This technique measures the charge under the voltammetric peaks for hydrogen adsorption or desorption and correcting for double layer capacitance. It is based on the assumption that adsorption of one hydrogen atom corresponds to one active site of the surface(Q_H)[164]. The charge associated with the one-to-one H-M correspondence per unit surface area (Q_H*) is calculated on the basis of the distribution of active sites on the

surface. This is well defined for crystals with a perfect single face whereas it is taken to be an average value between the main low-index faces for polycrystelline surfaces. The true surface area is thus easily calculated by dividing Q_H by Q_H*[165].

The validity of the method implies that the point where hydrogen adsorption is complete can be exactly identified, and that the coverage is completed before the rate of hydrogen evolution becomes significant. In addition, it is dependant on the assumption that there is a definite quantitative relation between the charge measured and the amount of substance deposited. Finally, that no alteration of the surface upon adsorption has taken place[163].

The pillars shown in Figure 3.15 (b) had the lowest current (-367.0 μA cm^{-2}). The unformed nanowells in Figure 3.17 (b) performed worse however, with the highest onset potential (-0.28 V SHE), and the highest potential for peak current density (-0.62 V SHE) indicating poor catalysis. The central well being closed in the unformed nanowells greatly reduced the number of available active sites. Samples with nanowell morphologies had higher peak current densities, with Figure 3.16 (c) having a peak current density of -602 μA cm^{-2}, and an onset potential of -0.24 V SHE. Figure 3.17 (c) performed similarly to the nanowell morphologies and this was attributed to the linkages between features. The onset potential was -0.21 V SHE, and the peak current density was -535 μA cm^{-2}. The morphologies and current varied within each subset of samples, however, and this indicated that modifying the flow rate of etchants does not offer a high degree of control over the morphology.

The batch of samples from Section 3.4.5 was stored for 14 days prior to electrochemical testing. As with previous batches the HER catalytic effect had more correlation with the surface morphology than with the etch parameters used during structuring (Figure 3.25).

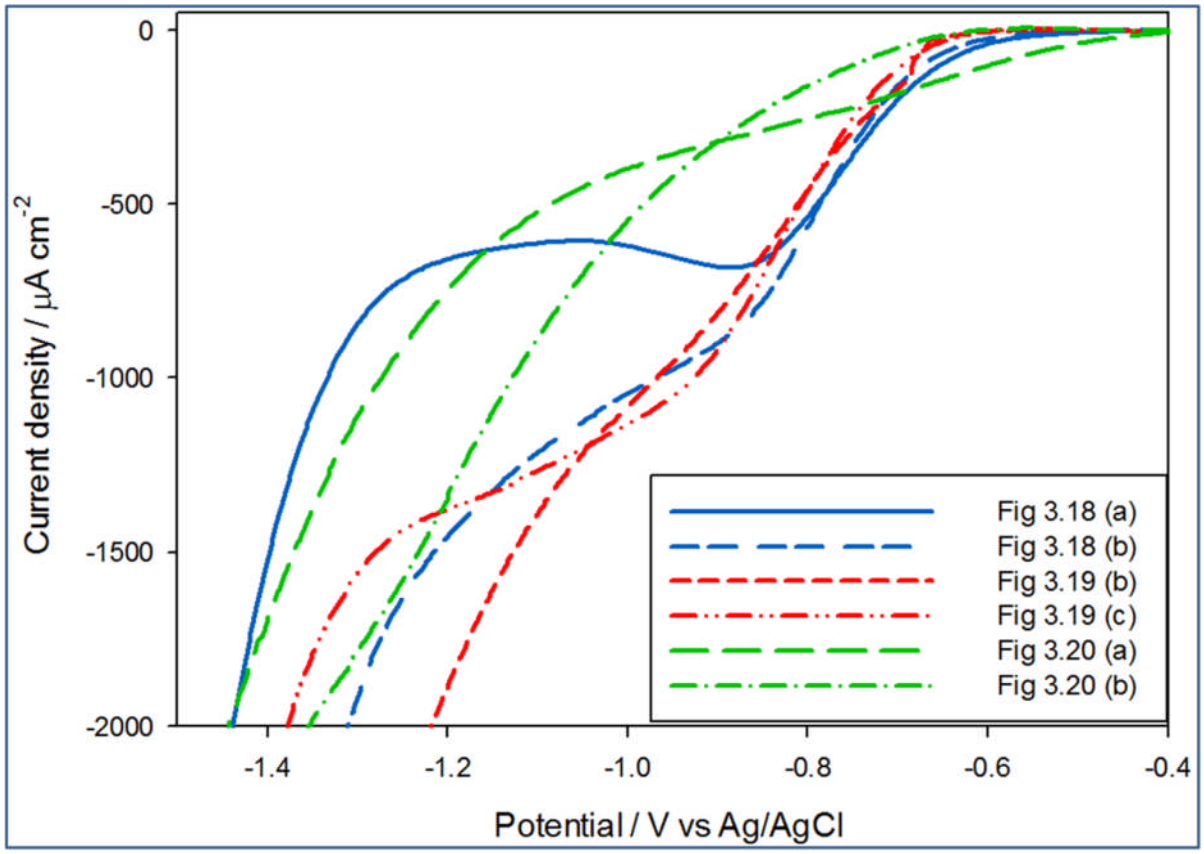

Figure 3.25. HER on two samples of each MoS_2 set resulting from variable SF_6 flow rates. Blue was 15 SCCM, red was 35 SCCM and green was 40 SCCM SF_6 flow rate.

As with the results from the C_4F_8 flow rate experiment sample morphologies that included links between features had earlier onset potentials, and higher peak currents than those without. The sample depicted in Figure 3.19 (c) had a uniform nanowell morphology and produced a peak current density higher than any other sample in this series (-1069 µA cm-

^{2}), although the onset potential was high at -0.28 V SHE. The other nanowell morphologies (Figure 3.18 (b) and Figure 3.19 (b)) had similar electrocatalytic performances.

The unformed nanowells depicted in Figure 3.20 (a) had the earliest onset potential (-0.1 V SHE), but a low and poorly defined peak current (-269 µA cm^{-2}). Again this is attributed to the lack of available edge sites. The pillar morphology shown in Figure 3.20 (b) was the worst performing sample of this set, with no clearly defined proton reduction peak. The linked pillars in Figure 3.18 (a) had intermediate performance, with a slightly earlier onset potential than the nanowells (-0.22 V SHE), but a peak current density of only -691 µA cm^{-2}.

The samples from 3.4.6 were stored for 5 days prior to electrochemical testing (Figure 3.26).

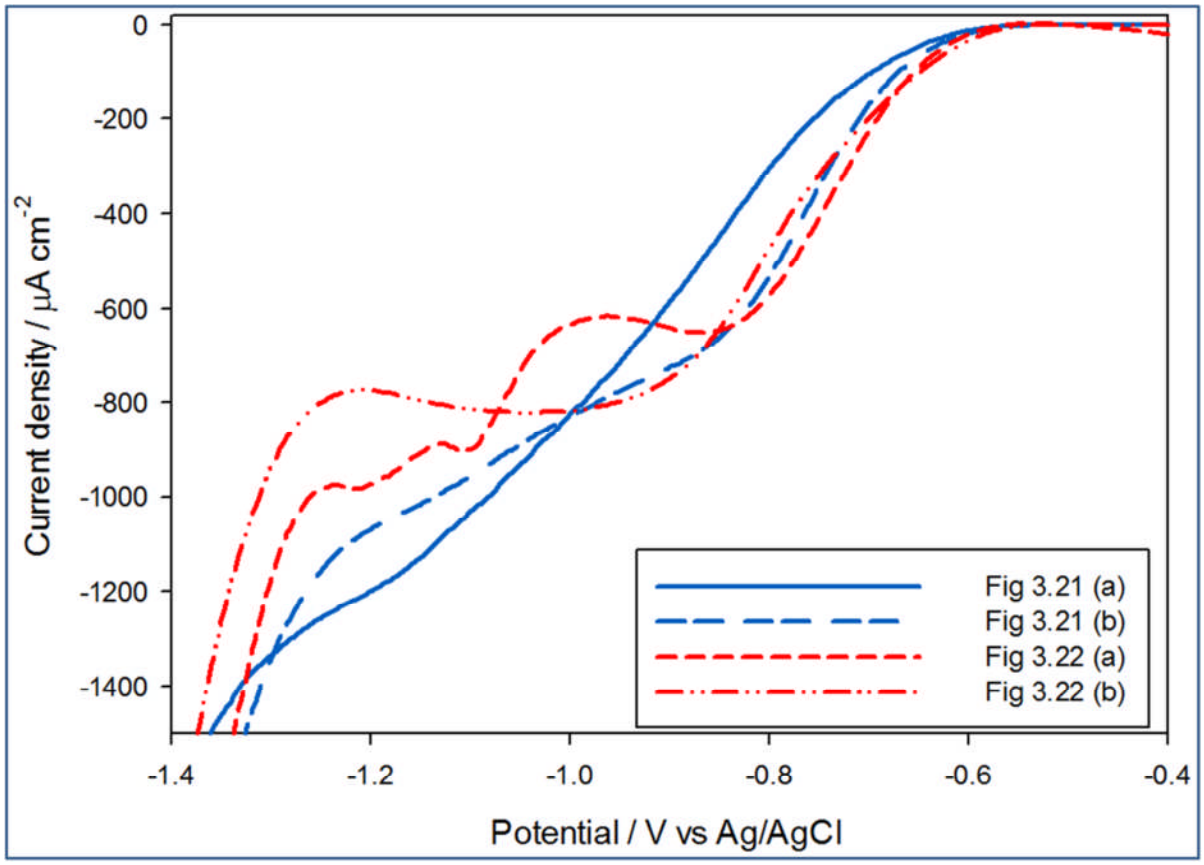

Figure 3.26. Proton reduction on four MoS_2 nanostructures resulting from varying the O_2 flow rate during the nanosphere shrinking etch. Blue is 90 SCCM, and red is 80 SCCM O_2 flow rate.

The electrochemical data revealed that the pillar structures in Figure 3.21 (b), and Figure 3.22 (a) had similar onset potentials (-0.26 V SHE) and peak currents densities of -678 μA cm^{-2} and -645 μA cm^{-2}. The pillars in Figure 3.21 (a) had poorer performance with an onset potential of -0.28 V SHE, and the peak current not occurring until -0.82 V SHE, indicating slow reaction kinetics. The linked pillars in Figure 3.22 (b) performed better which had an onset potential 50 mV less negative than the others, and also had a higher and better defined peak current at -810 μA cm^{-2}. This can be attributed to the linkages that are present between the pillars as discussed in Section 3.5.

The etch parameters were established to be a poor way to provide reproducible control over the morphology, and the electrochemical response was more attributable to the morphology than the etch parameters. The formation of the three morphologies that were identified was studied to investigate how one could be selected for during the nanostructuring process.

3.5 Morphology

In section 3.4 reproducibly manipulating the morphology of MoS_2 through the variation of plasma etching parameters was attempted. These experiments were unsuccessful in that

the etch parameters could not be used to predict the morphology that would be produced. However, a correlation between the nanosphere positioning following deposition and the final morphology was established.

Three distinct morphologies were identified in the MoS_2 patterned by nanosphere lithography and plasma etching. These were nanopillars, nanowells, and linked pillars (Figure 3.27). Linked pillars were a hybrid of the first two morphologies.

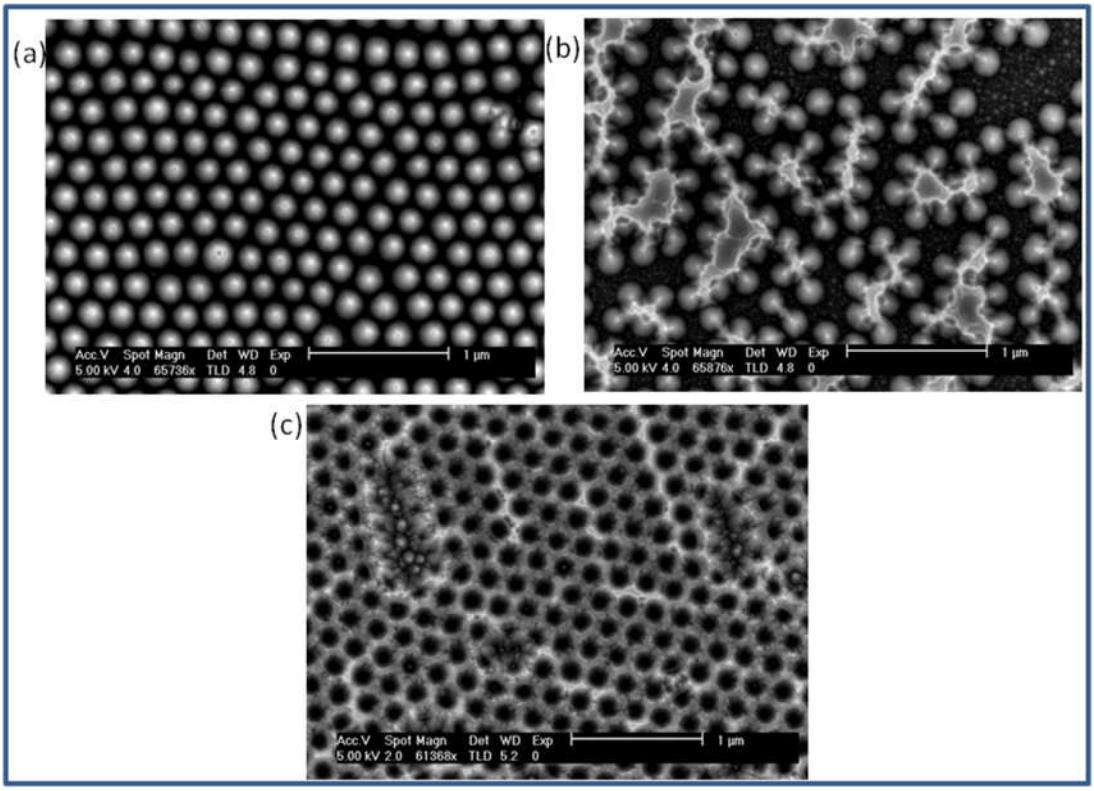

Figure 3.27 (a) pillar morphology. (b) linked pillar morphology. (c) nanowell morphology.

Each was formed depending on how close packed the nanospheres were following deposition, with very close packed nanospheres forming nanowells, and more spread out

nanospheres making nanopillars. Linked pillars were formed when there were areas of both close packed and spread out nanospheres.

3.5.1 Nanopillars

A little space between spheres meant they shrank from the outside when exposed to oxygen plasma (Figure 3.28).

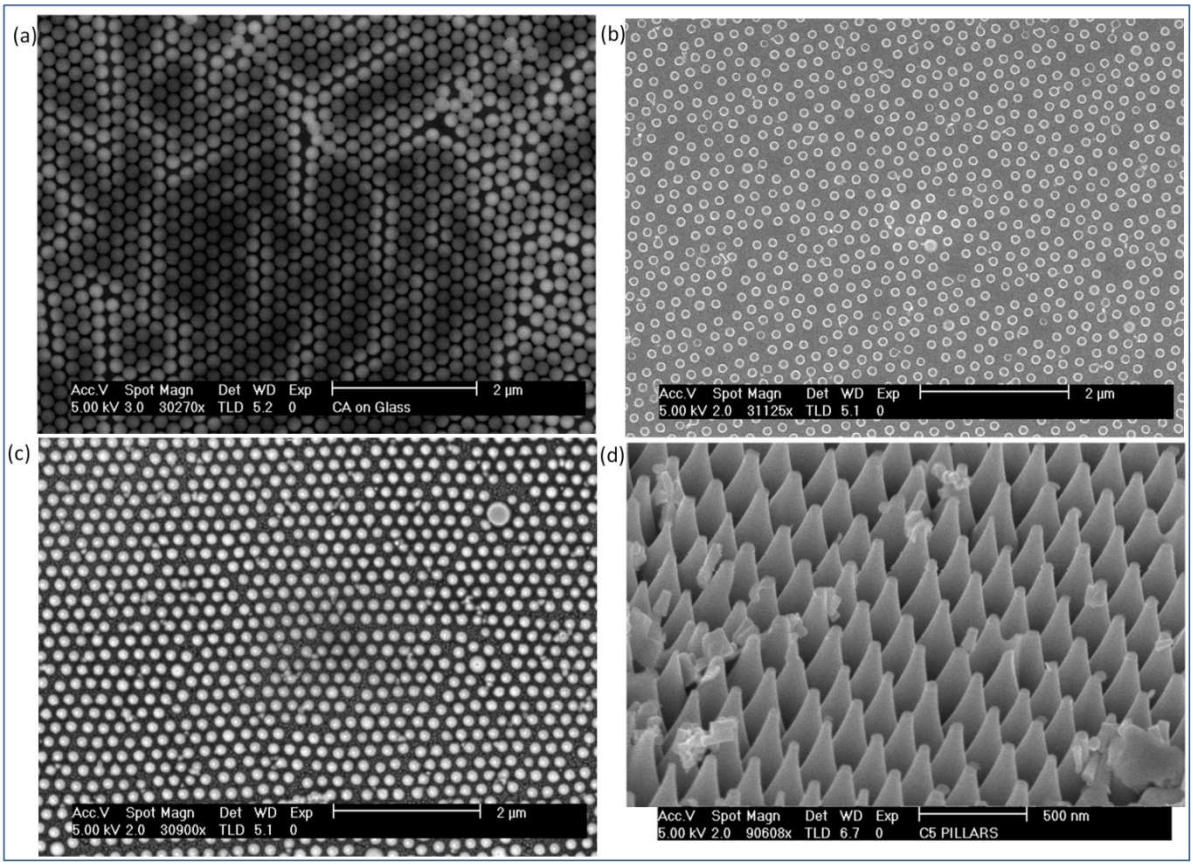

Figure 3.28. SEM images of the formation of nanopillars by NSL. (a) Nanospheres deposited on the surface of MoS_2, showing small gaps between the spheres. (b) Nanospheres that have shrunk due to being subjected to a 35 second O_2 plasma etch. (c) MoS_2 nanopillars

formed from exposing the etch mask in (b) to 30 seconds of SF_6 and C_4F_8 plasma. (d) Side view of the nanopillars.

The small gap between nanospheres caused them to shrink symmetrically from the outside in, resulting in smaller spherical nanospheres with a larger gap between the individual nanospheres. When the MoS_2 was subsequently etched by exposure to SF_6 plasma a nanopillar morphology was formed as the shrunken nanospheres prevent etching immediately beneath their positions. The example shown in Figure 3.28 (d) was isotropic (i.e the pillar bases are considerably wider than the tops), this was due to an inadequate passivation layer of C_4F_8 during the SF_6 etch[78].

3.5.2 Nanowells

When deposited close enough together the nanospheres arranged into a tessellating hexagonal morphology as shown in Figure 3.29 (a).

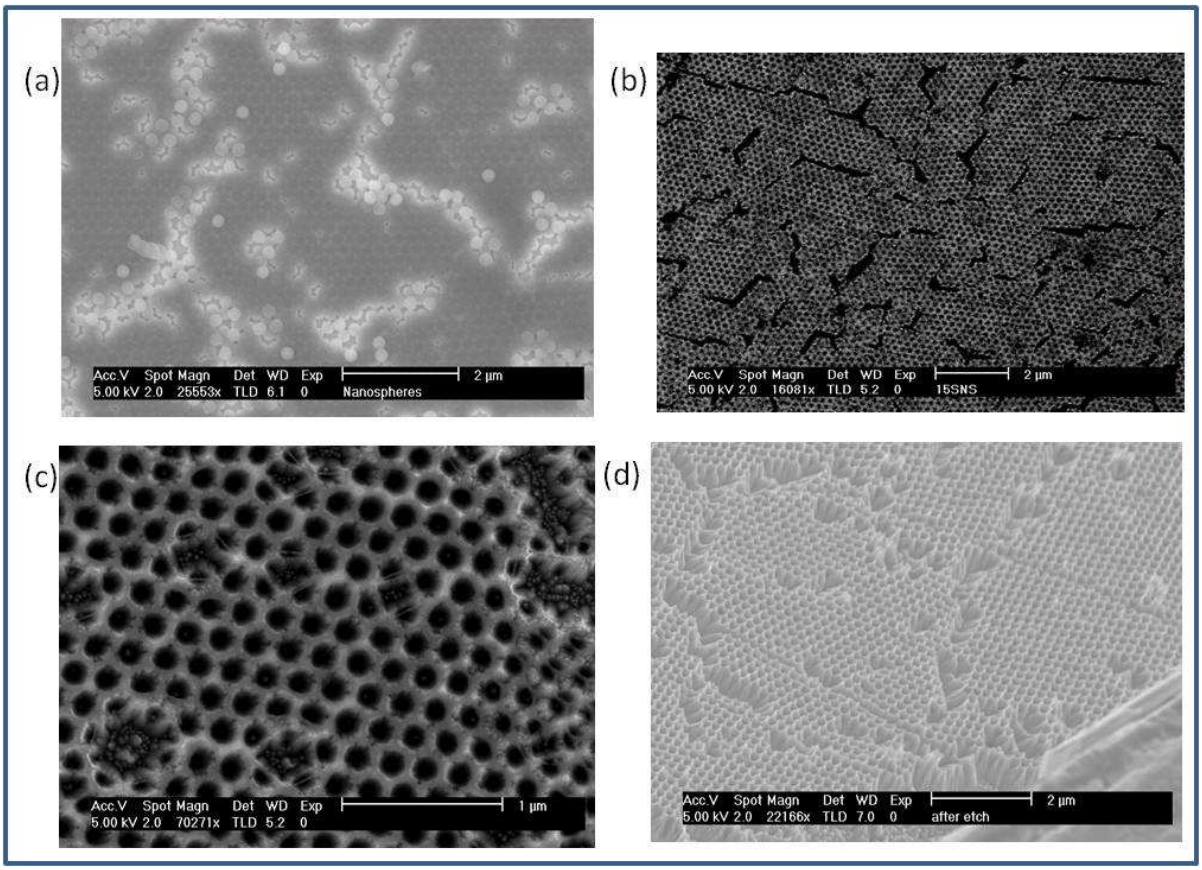

Figure 3.29. SEM images of the formation of nanowells by NSL and plasma etching. (a) Nanospheres deposited on the surface in such close proximity as to squash into tessellating hexagons. (b) Nanomesh formed by exposure of (a) to O_2 plasma. (c) Nanowells formed from etching (b) With SF_6 and C_4F_8 plasma. (d) A side view of the nanowells.

As can be seen from Figure 3.29 (a) nanospheres could be deposited hexagonally close packed to such a degree that the nanospheres squashed into one another. This deposition resulted in straight edges between the nanospheres making them symmetrical hexagons. Exposing these squashed together nanospheres to O_2 plasma caused an inversion in the resist structure. Alternatively, nanospheres with spaces shrank from the outside in, leaving nanospheres with the same shape and a smaller circumference. Hexagonal nanospheres on

the other hand instead left material where two nanospheres conjoined, and the centre was devoid of resist. When the surface of the MoS_2 was then etched this resist structure imprinted the nanowell morphology into the crystal. The side on image Figure 3.29 (d) shows that the height of the nanowells was not uniform, with the vertices being higher than the edges.

In order to investigate the change undergone by the hexagonal nanospheres when exposed to O_2 plasma hexagonal nanospheres were O_2 etched in ≈4 second periods and imaged with SEM between exposures (Figure 3.30).

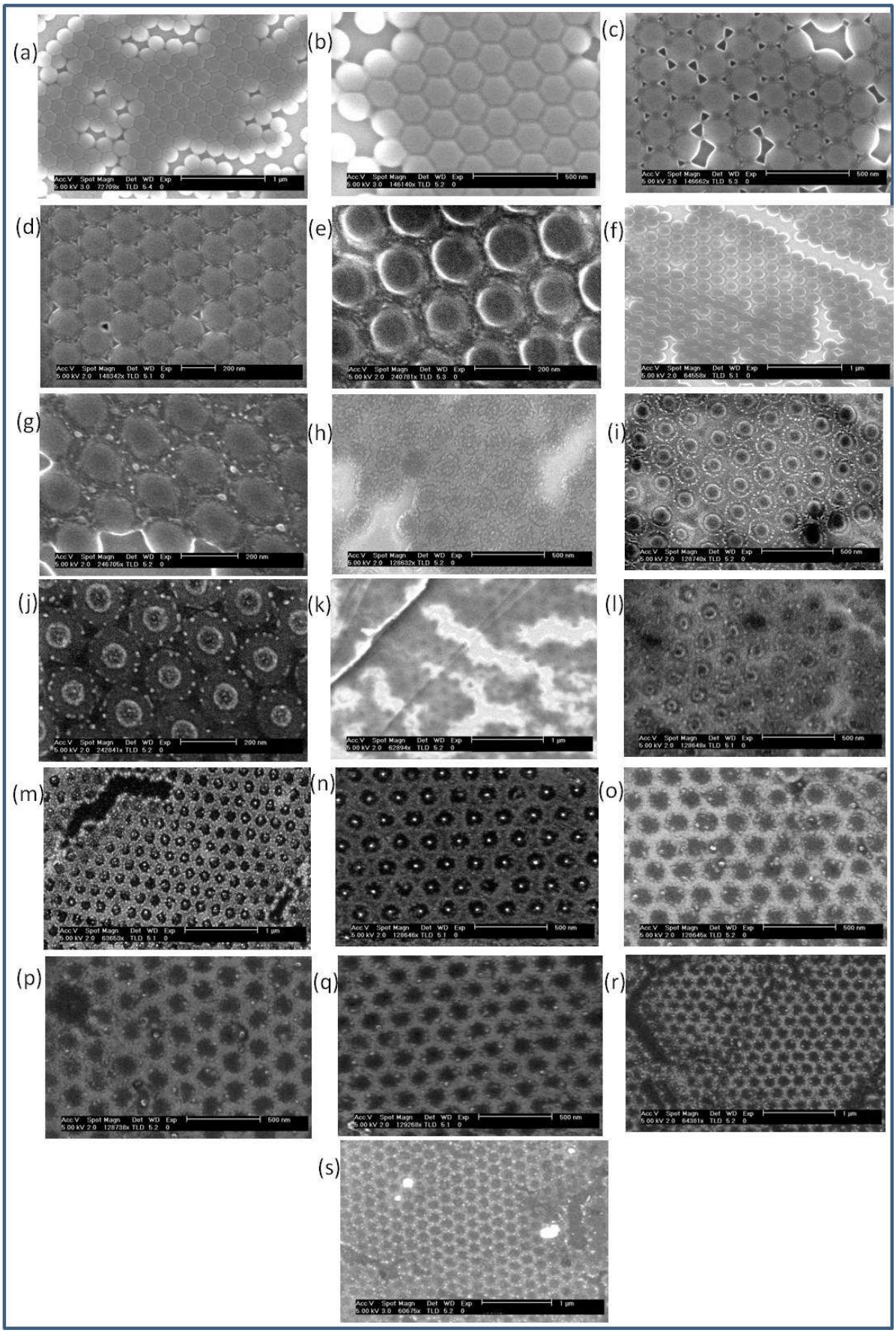
(a)
(b)
(c)
(d)
(e)
(f)
(g)
(h)
(i)
(j)
(k)
(l)
(m)
(n)
(o)
(p)
(q)
(r)
(s)

Figure 3.30. SEM images of nanomesh formation from nanospheres exposed to O_2 plasma. The sample was removed from the chamber and imaged at regular intervals such that each image was exposed to O_2 plasma approximately 4 seconds longer than the previous image. (a) is prior to O_2 etching, and (s) is the result of 67 seconds total etch time.

The forming of nanomesh from nanospheres was caused by a thickening of material at the edges and a thinning of material at the center, until the resist became homogenous, followed by inversion. In Figure 3.30 (a) the initial nanosphere deposition can be seen, with the nanospheres squashed into a tessellating hexagonal arrangement. After 4 seconds of O_2 plasma etch thinning occurred around the edges of the nanospheres. Figure 3.30 (c) reveals that after 8 seconds of O_2 plasma etch the thinning caused interstices to form at the corners of the hexagons. However, a 12 second O_2 plasma etch (Figure 3.30 (d)) caused the interstices to shrink as they began fill with debris. At 15 seconds of O_2 plasma etch the nanospheres continued shrinking with material building up along the edges of the hexagons. At this point the interstices had been filled. This trend continues in Figure 3.30 (f) and Figure 3.30 (g) where up to 22 seconds of exposure to O_2 plasma had caused the centre to continue to shrink while material built up on the edges. By Figure 3.30 (h) (29 seconds of O_2 plasma etch) the shrinking of the centre and building up of the edges resulted in a homogenous appearance.

In Figure 3.30 (i) it was revealed that a 33 second O_2 etch plasma etch is where the inversion began to take place with the continued shrinking of the nanospheres creating a gap between the centre and the material built up along the edges. This trend continued in Figure 3.30 (j), (k), and (l) with the gap between the shrinking nanosphere and the forming

nanomesh widening. These images were taken at 36 seconds, 40 seconds, and 43 seconds of O_2 plasma etch, respectively.

The nanomesh is apparent in Figure 3.30 (m) (47 seconds O_2 etch), and the nanosphere had significantly shrunk to become a separate entity. SF_6 plasma etching the MoS_2 at this point would result in nanopillars within nanowells (Figure 3.16 (d)). Figure 3.30 (n) (50 Seconds O_2 plasma etch) continued this trend with the central nanosphere now shrunk to a point, and the nanomesh gaining definition. After 54 seconds O_2 plasma etch (Figure 3.30 (o)) the central nanosphere had been completely etched away, leaving only the nanomesh. Continued exposure to O_2 plasma gradually eroded the nanomesh as can be seen that in Figure 3.30 (p) (57 seconds exposure), Figure 3.30 (q) (61 seconds exposure), and Figure 3.30 (r) (64 seconds exposure) the nanomesh had started to break up. By Figure 3.30 (s) (67 seconds O_2 etch) the nanomesh has been overexposed to O_2 plasma and only a trace remained.

It was concluded that the process of nanomesh formation began with nanospheres so closed packed as to form tessellating hexagons, and after 4 seconds of O_2 etch a thinner area 25 nm across formed on the edges of the hexagons. Interstices appeared at the corners of the hexagons after 8 seconds of etching. The interstices grew in size until at 15 seconds they were filled with debris from the etch process. At this point despite the hexagonal arrangement the nanospheres still shrank from the outside in, the same way that spaced nanospheres etch (i.e. the O_2 etch results in a sphere of decreasing diameter, however, in the case of the squashed hexagonal formation material remained where the hexagon edges were in conjunction). This process continued with the centre shrinking and

debris building up in the place of the former edges of the hexagons. The shrinking of the centre and building up of the edges happened at a similar rate until at 29 seconds the resist became homogenous in appearance. It was difficult to obtain clear images during this intermediary phase as the homogeneity of the resist lacked the contrast required for SEM. Continued etching formed a concentric circle of devoid of resist between the remaining nanosphere and the proto-nanomesh. The central nanosphere continued to diminish until at 47 seconds only a point remained. By 54 seconds this has also been etched away inverting the resist and leaving the hexagonal nanomesh. Continued etching beyond this point damaged the nanomesh until at 67 seconds only a faint trace remains. However, If the oxygen etch was timed correctly a hexagonal nanomesh resist will be formed that imprints the nanowell pattern into the MoS_2 crystal (Figure 3.31).

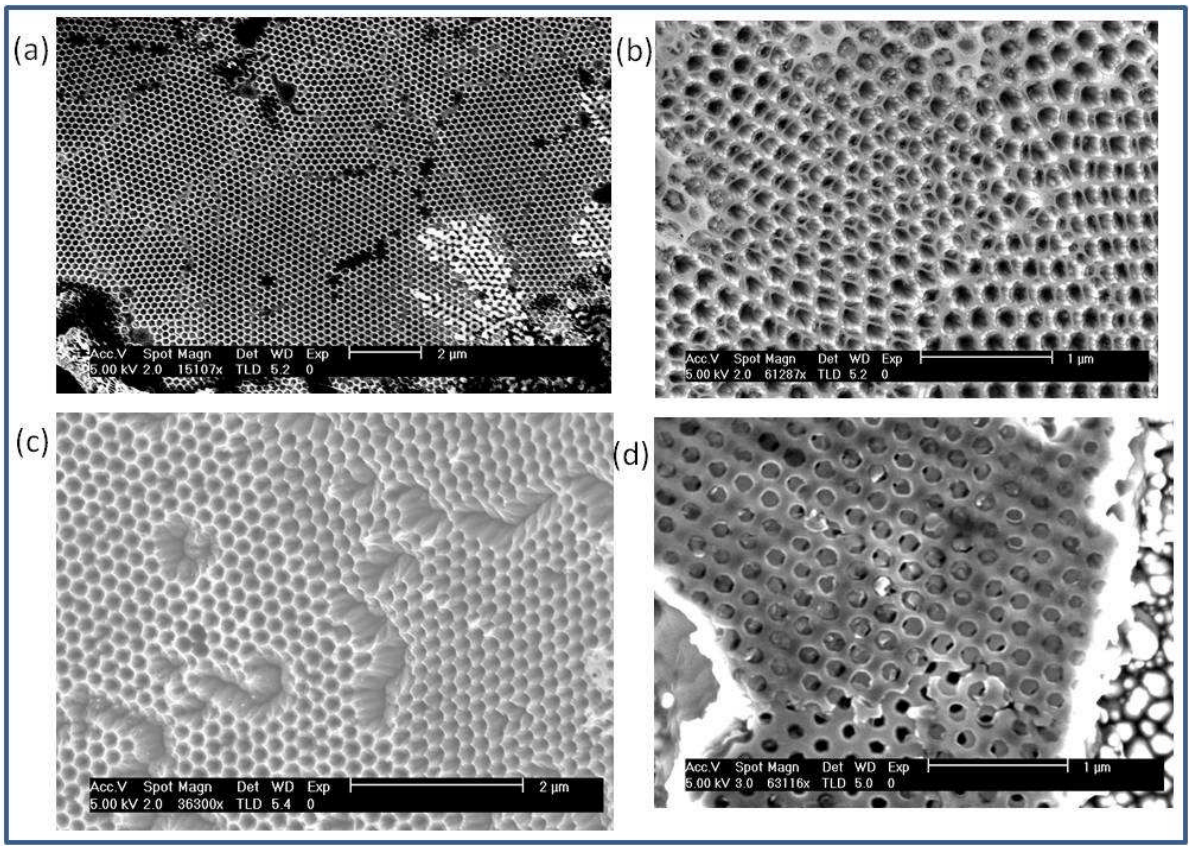

Figure 3.31. SEM images of nanowell formation and structure. (a) Polystyrene nanomesh formed by the exposure of closed packed nanospheres to O_2 plasma. (b) Nanomesh on top of a nanowell patterned MoS_2 surface. (c) MoS_2 nanowells. (d) Damaged nanowells showing the layered structure of MoS_2.

A correctly etched nanomesh can be seen in Figure 3.31 (a), and a nanomesh remaining on the surface of etched MoS_2 can be seen in Figure 3.31 (b). The nanomesh shifted slightly so that it no longer aligns with the etch pattern it imprinted and this allows the nanomesh to be clearly seen over the holes of the nanowells. Figure 3.31 (c) shows the final nanowell pattern. In Figure 3.31 (d) the MoS_2 has been damaged after etching revealing its layered structure.

3.5.3 Linked Pillars

The third structure observed was the linked pillar morphology. This is a hybrid of the nanopillar and the nanowell morphologies, and formed when some areas of nanospheres had squashed into the hexagonal arrangement, and in other areas they had the slight spacing which results in nanopillars. The process of linked pillar formation can be seen in Figure 3.32.

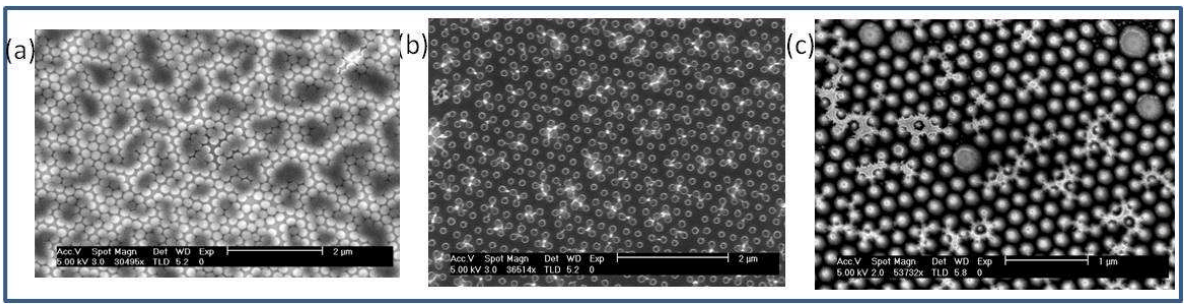

Figure 3.32. (a) Nanospheres deposited partially with small gaps, partially with no gaps. (b) Nanospheres shrunk by O_2 plasma with some linkages between the individual spheres. (c) the linked pillar morphology.

On Figure 3.32 (a) the darker areas contained nanospheres squashed into hexagons, while in the lighter areas the nanospheres had spaces separating them. Figure 3.32 (b) was the result of etching Figure 3.32 (a) with O_2 plasma. The bright white lines show where debris accumulated between the nanospheres, and it is beneath these that the linkages between the pillars would form. Figure 3.32 (c) shows MoS_2 that has been etched into a linked pillar formation. It can be seen that some nanopillars were still individual, whilst others have walls connecting them. In several places the linkages resembled incomplete nanowells.

3.5.4 Relationship Between Nanosphere Deposition Conditions and Morphology

As previously mentioned the plasma etch conditions were found to provide poor control over the reproducibility of the final morphology of MoS_2. However the positioning of nanospheres following deposition could be used to predict which morphology was produced. A precise control over the nanosphere deposition was never established; however the deposition could be made to favour nanopillars or nanowells by altering certain conditions. The key factor in determining how close packed the nanospheres deposit was the vibrational energy they were exposed to during the deposition, with more vibrations of the water-air interface resulting in additional space between nanospheres. Vibrations could be countered by covering the deposition dish with a lid to prevent air currents from disturbing the surface, an air suspended table, and care by the operator to minimise disturbances of the water during the deposition.

A lack of control over vibrations resulted in nanospheres being deposited with a small gap between them. In this arrangement the nanospheres shrank from the outside in when subjected to O_2 plasma, leaving smaller nanospheres in the same arrangements but with larger interstices. When subjected to SF_6 and C_4F_8 plasma the uncovered MoS_2 in the interstices was etched away leaving a regular array of nanopillars beneath the nanospheres. Efforts to minimise vibrations lead to the nanospheres squashing into hexagonal prisms. Nanospheres in the hexagonal arrangement initially were etched from the outside in, similarly to nanospheres deposited with gaps, however material was left at the conjoining edges resulting in nanomesh, and ultimately nanowell morphology.

As such the final morphology was determined early on during the electrode fabrication process, with simple factors such as using a lid during the NSL deposition, or how steady the operators hand was during the deposition of nanospheres on the water-air interface being the deciding factors in the final morphology of the MoS_2. This was not ideal as the reproducibility of this technique depends on the skill level of the operator, and factors that were beyond reasonable control such as the noise level of the lab. However, with practice it was possible to have some degree of control over the final morphology through the nanosphere deposition.

3.6 Electrochemistry of the Three Morphologies

The suitability of the MoS_2 morphologies as HER catalysts was tested by proton reduction measurements as described in Section 2.3.1. The patterned MoS_2 was used as the working electrode for proton reduction voltammetry in an acidic electrolyte. From these scans the characteristics used for the purposes of comparison were the peak current, onset potential and Tafel slope. The proton reduction measurements revealed that all of the morphologies produced had a catalytic effect on hydrogen production as compared to bulk or randomly orientated MoS_2 (Figure 3.33). Two examples of the three morphologies were chosen on the basis of lowest Tafel slopes and are presented in Figure 3.33. The surface morphology of each of these samples is shown by SEM images in Figure 3.34.

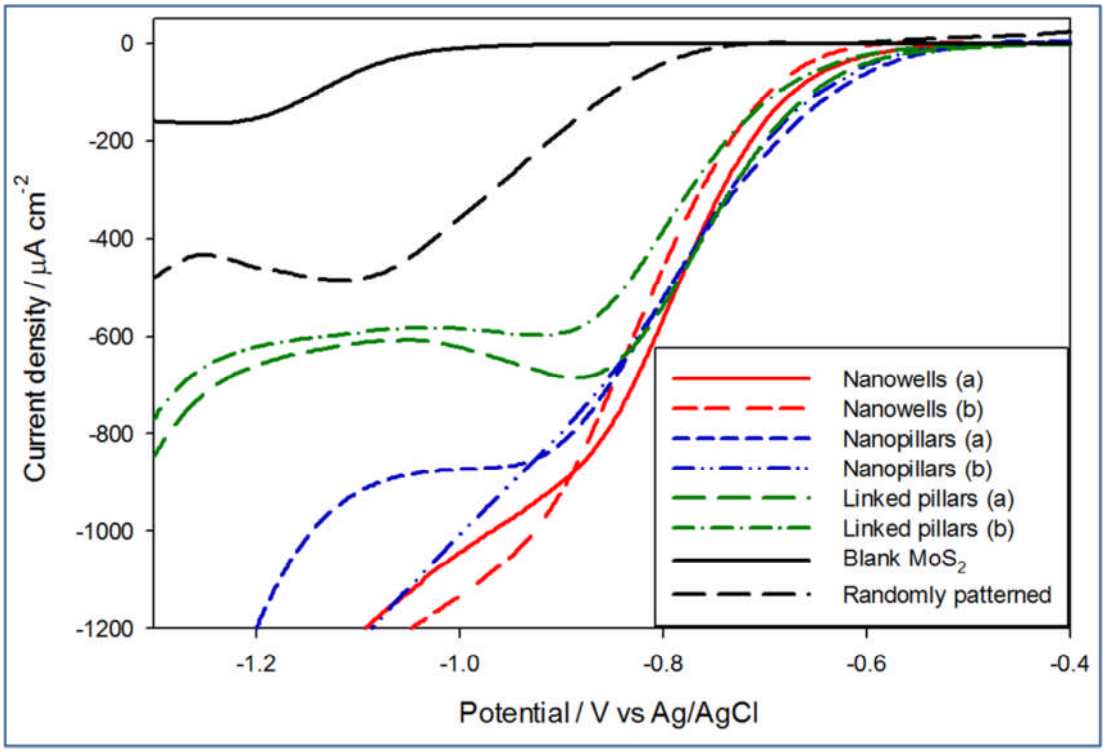

Figure 3.33. The voltammograms for the best performing samples of each morphology as determined by Tafel slope. All the morphologies displayed enhanced catalytic properties as compared to the MoS_2 blank and randomly patterned samples.

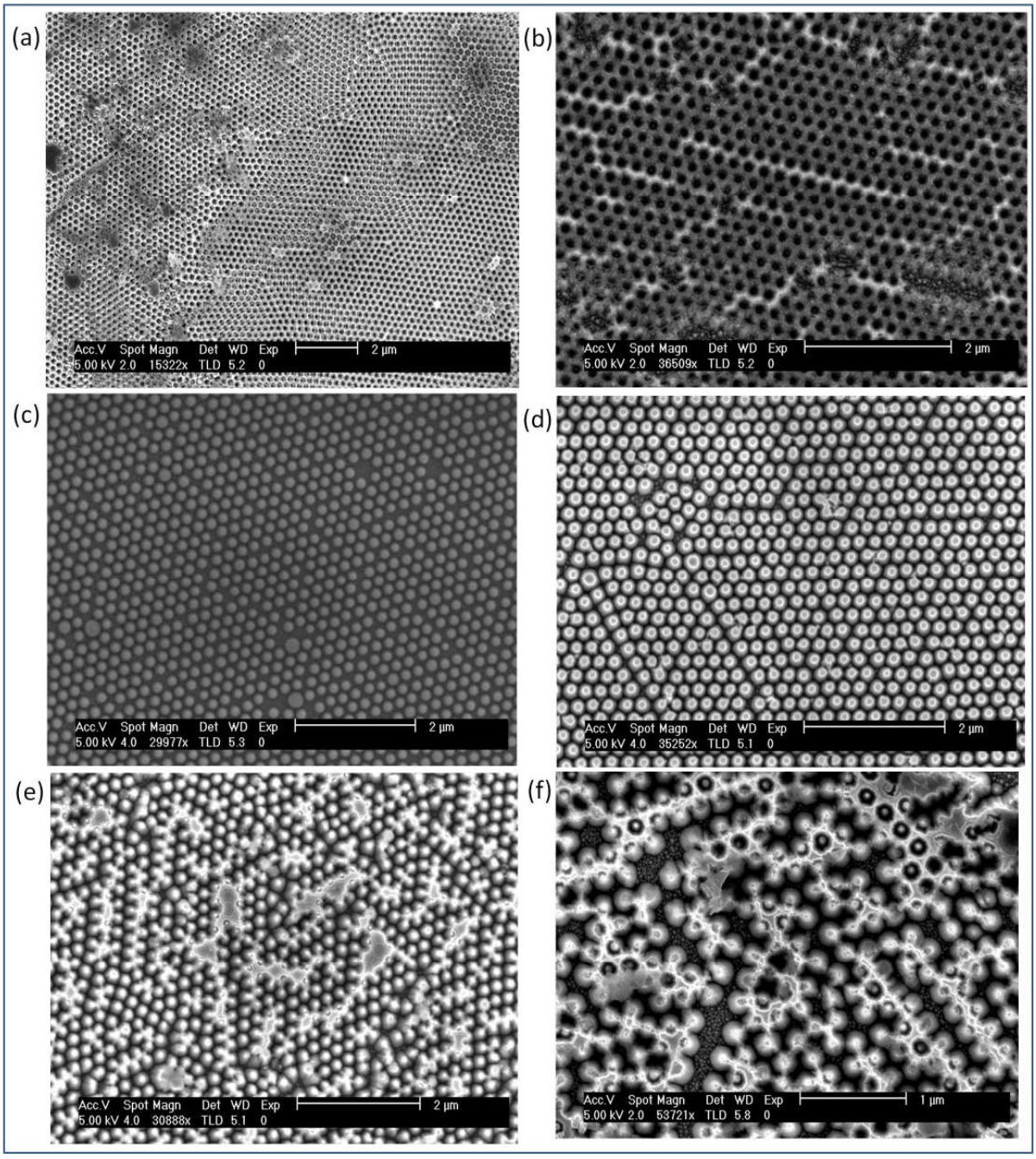

Figure 3.34. The surface morphologies corresponding to the voltammograms presented in Figure 3.33. (a) and (b) are nanowells (a) and (b) respectively. (c) and (d) are nanopillars (a) and (b) respectively. (e) and (f) are linked pillars (a) and (b) respectively.

More information about each sample can be found by referring to the corresponding section in the nanopatterning section. Nanowells (a) is shown in Figure 3.18 (b), and nanowells (b) in Figure 3.19 (b). Nanopillars (a) is Figure 3.16 (a), and nanopillars (b) is Figure 3.17 (a). Linked pillars (a) corresponds to Figure 3.18 (a), and linked pillars (b) is Figure 3.16 (c).

The onset potential shifted towards zero for all three morphologies as compared to the blank and randomly patterned MoS_2 indicating a lower overpotential required to reduce protons, and demonstrating the catalytic incentive of nanostructuring. The onset potentials were -0.19 V SHE, and -0.26 V SHE for nanowells (a) and (b) respectively, and -0.18 V SHE, and -0.19 V SHE for nanopillars (a) and (b) respectively. Linked pillars (a) and (b) had onset potentials of -0.19 V and -0.2 V SHE, respectively. Aside from nanowells (b) all the onset potentials were ≈ 0.2 V SHE, which is a commonly used value for proton reduction on structured MoS_2[59,110,123,127,128]. The overpotential required by nanopillars was around 100 mV smaller than the other morphologies, however this discrepancy was not large enough for conclusions to be drawn. The linked morphologies generally outperformed the nanopillars however, as can be seen in section 3.4.

Random etching appeared superior to bulk MoS_2, but inferior to nanopatterned MoS_2 with an onset potential of -0.34 V SHE. The onset potential of the bulk MoS_2 was -0.71 V SHE, meaning that the nanostructuring process has advantageously resulted in the HER initiating at 0.5 V reduced overpotential.

The nanowells had the highest peak currents at -860 μA cm^{-2} and -990 μA cm^{-2} for (a) and (b), respectively. The nanopillars current densities were intermediate at -835 μA cm^{-2} and -789 μA cm^{-2} for (a) and (b), respectively. The linked pillar morphology displayed the lowest current densities at -682 μA cm^{-2} for (a) and -602 μA cm^{-2} for (b). Once again each sample significantly out-performed the bulk MoS_2, which had a current density of -170 μA cm^{-2}, and the randomly etched sample which had a current density of -285 μA cm^{-2}. Indicating an increase in catalytically active $(10\bar{1}0)$ edge sites. This is as expected as in bulk the $(10\bar{1}0)$ edge sites are rare, and by nanopatterning perpendicular to the basal plane a greater number were exposed[59].

While there is a greater discrepancy between the peak current values than for the onset potential, the differences are again too small for firm conclusions to be drawn. Further there was also considerable deviation between samples displaying the same morphology. The peak currents for the morphologies with linkages between features were at slightly lower overpotentials than for the nanopillar morphologies though, and as the linked morphologies also had later onset potentials this indicated that the linkages improved catalysis. However, the difference in onset potentials was too small to discount experimental error. The reaction pathway was determined using Tafel analysis (Figure 3.35). As suspected the Tafel slopes were lower on morphologies with crosslinking (i.e. nanowells and linked pillars) than those without (nanopillars). The nanowell morphologies had the lowest Tafel slope at 203 mV dec^{-1} and 190 mV dec^{-1}, for (a) and (b), respectively. The linked pillars morphologies were intermediate at 216 mV dec^{-1} for (a), and 215 mV dec^{-1}

for (b). The nanopillars displayed the highest Tafel slope at 268 mV dec^{-1} for (a) and 260 mV dec^{-1} for (b).

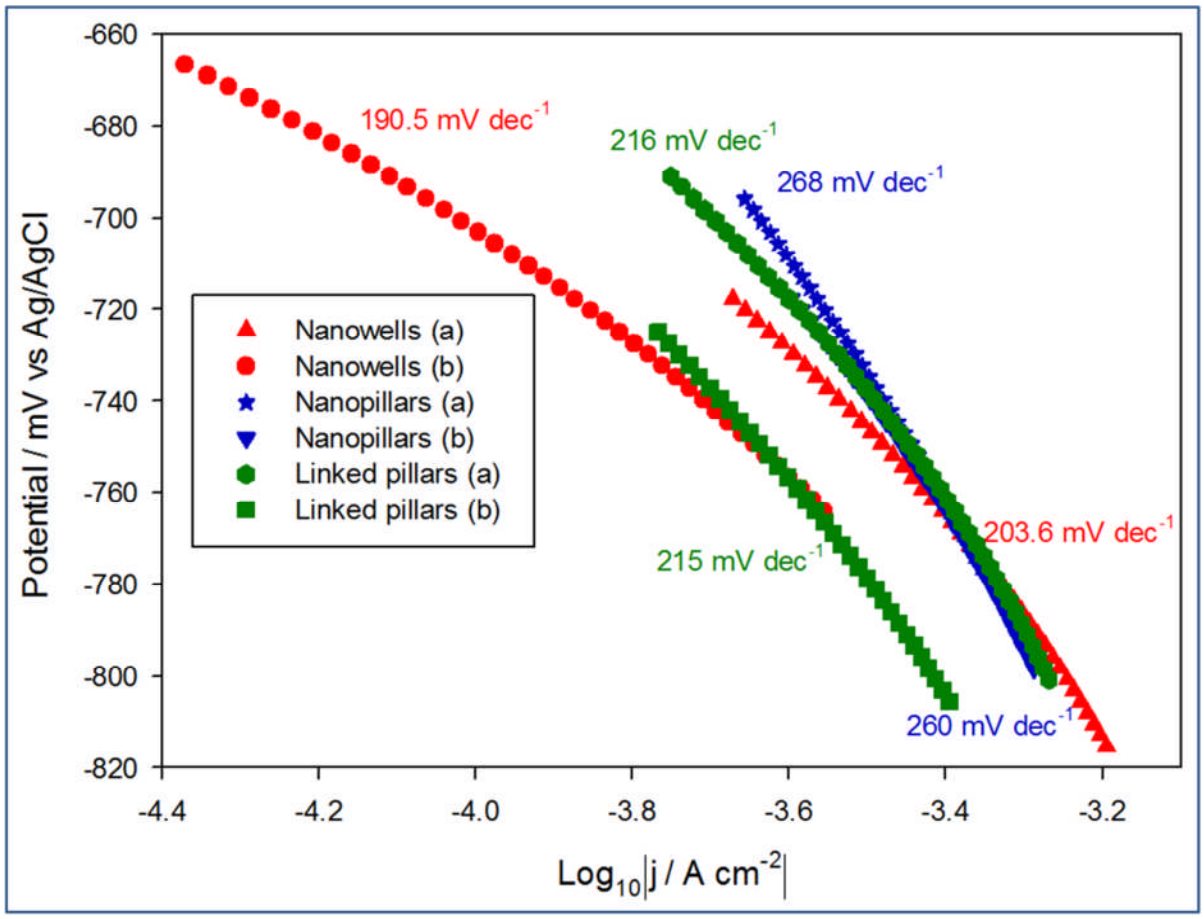

Figure 3.35. Tafel slopes derived from the voltammograms in Figure 3.33. The graph is plotted with the dependent variable on the x-axis as in this configuration the gradient is the Tafel slope.

All of the Tafel slopes were high, the HER on MoS_2 should provide a Tafel slope of 120 mV dec^{-1} [127,128,129]. This can be attributed to the length of time they were exposed to air before testing negatively affecting the MoS_2 by the replacing the sulfur with oxygen, as the catalytically active $(10\bar{1}0)$ edge sites have a high rate of absorption for oxygen[166]. The Tafel

analysis did provide a useful comparison about the relative catalytic properties of the three morphologies produced however. The nanowell morphologies have Tafel slopes ≈20 mV dec^{-1} lower than the linked pillars, and the nanopillars are around 45 mV dec^{-1} higher than the linked pillars. Therefore in terms of reaction pathway the nanowell morphology was superior, followed by the linked pillars, and the nanopillars produced the worst response. As the Tafel slopes were all > 120 mV dec^{-1} the Volmer reaction (Eq. 1.11) was rate limiting, and hence no information on the subsequent reaction step was obtained.

This discrepancy was attributed to the anisotropic properties of MoS_2 created by the different bonds between and across the layers. The covalent bonds across the layers, and Van der Waals bonds between the layers mean charge carriers travel 2200 times faster along the basal plane rather than perpendicularly between the layers[117]. This presents a problem for the HER on MoS_2 as efficient proton reduction requires good conductivity between the catalytically active edge sites and the substrate[116]. In practical terms the energy transfer between the substrate and the edge sites must be faster than the electron-hole recombination time or charge carriers will be lost before reduction can take place[118]. It is also necessary for a kinetically fast HER[52].

The linked structures presented here were advantageous as the charge carriers are able to travel along the layers to the point of least resistance between the edge sites and substrate, and fewer charge carriers were lost to recombination as discussed in Section 1.2.3. Nanowells were the superior morphology due to the charge carriers being able to travel along the entire surface of the crystal in order to reach the path of least resistance. Linked pillars are intermediary, although the Tafel slopes are closer to the nanowell morphologies

than the nanopillars. Linked pillar morphology provided a group of features within which the charge carriers were free to travel. As the Tafel slope was only 20 mV dec^{-1} higher compared to nanowells this suggests that charge carriers did not need to travel far along the basal plan in order to find a significantly less resistive route to the substrate, and thus that even small groups of features are considerably more advantageous than isolated pillars. The nanopillars had the highest Tafel slope by a considerable margin. This was attributed to the charge carriers inability to travel between features to find a more energetically favourable path between the edge sites and substrate, and hence they must travel down the path of least resistance within the individual features.

3.6.1 Electrochemical Modelling

Attempts were made to model the electrochemical measurements presented in Figure 3.33 using DigiElch electrochemical simulation software in order to get a value for k_0 since class IV behaviour is expected. These were unsuccessful as to obtain a close match between the measured and simulated results required treating the area as a variable parameter, suggesting that the surface of these electrodes is heterogeneous with areas of poor or no conductivity.

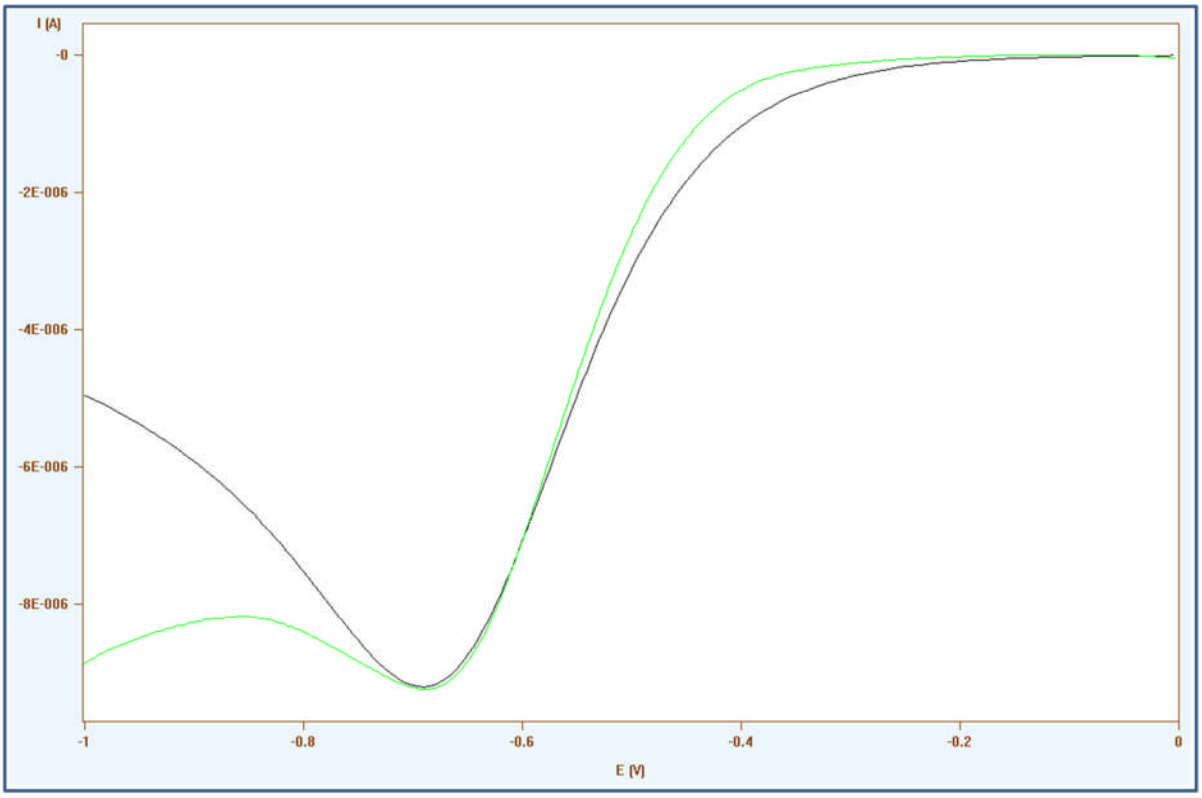

Figure 3.36. An attempt at modelling the voltammogram of Figure 3.33 – Linked pillars (a). It was considered inaccurate as to achieve a fit the modelled area needed to be greater than the geometric area, and all parameters required iterative calculations.

The Linked pillars (a) from Figure 3.33 was modelled in Figure 3.36. The fixed values were an E_0 of -0.159 V, a concentration of 2 mM, and a scan rate of 25 mV s^{-1}. The variables were an α of 0.319, a k_0 of 1.67×10^{-5} cm s^{-1}, and an area of 0.0173 cm^2. Since the measured geometric area was only 0.0135 cm^2 these results were considered inaccurate.

3.7 Freshly Nanostructured Measurements

The Tafel slopes were higher than the 120 mV dec^{-1} expected for the HER on pristine MoS_2 [127,128,129], and this was attributed to the air-exposure between nanostructuring and electrochemical testing. For the purpose of having a set of fresh sample data for comparison two samples were electrochemically tested immediately following the nanostructuring process. To this end the samples were adhered to the substrate, cleaved, and had nanospheres deposited and shrunk the day prior to electrochemical testing. The day of the testing the electrochemical cell was set up and the GC standard checked for accuracy before the SF_6 etch was carried out. The O_2 and SF_6 etches were performed as per Table 3-1, and Table 3-2, respectively. Following the SF_6 etch the samples were electrochemical tested such that a maximum of 4 hours had expired between removal of the sample from the plasma etch chamber and testing. The HER results are presented against the bulk and randomly patterned results in Figure 3.37, and Tafel slopes derived from these results can be seen in Figure 3.38.

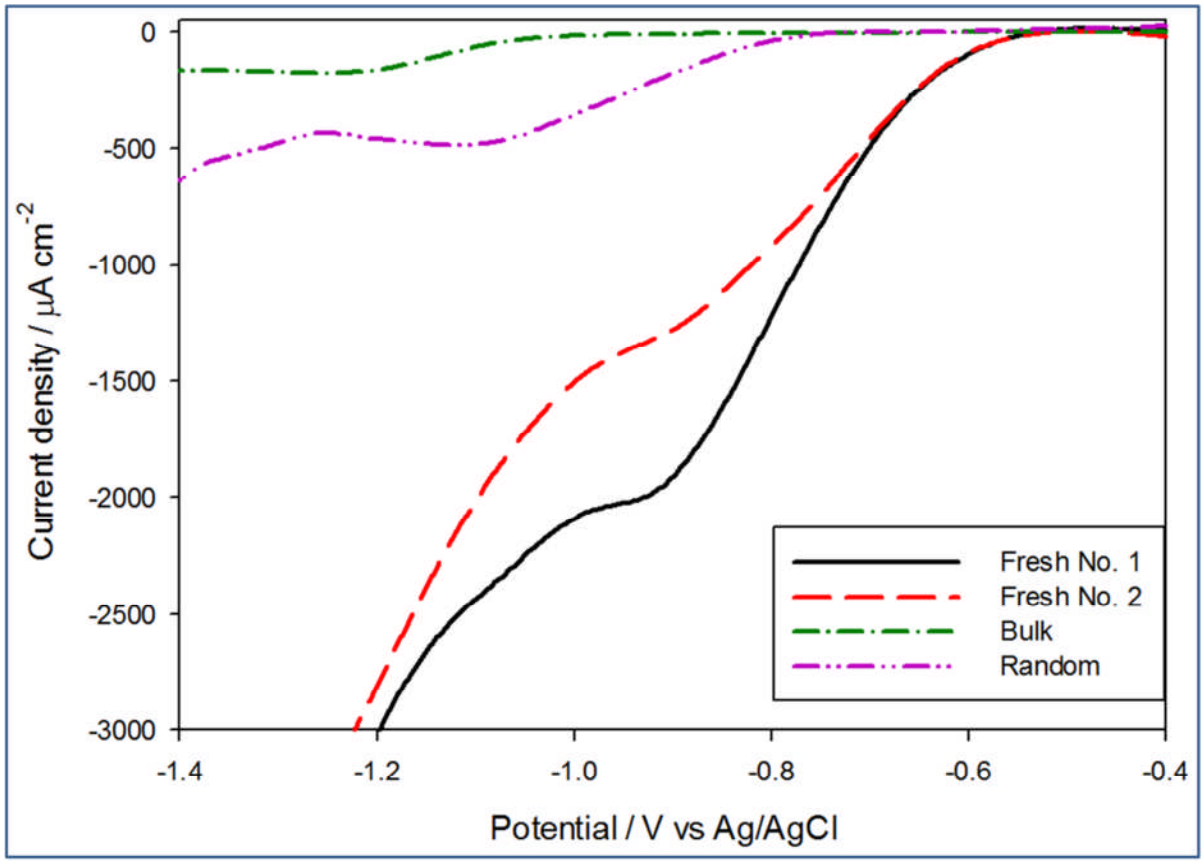

Figure 3.37. Voltammograms obtained from performing H^+ reduction on nanostructured MoS_2 electrodes in 2 mM $HClO_4$ electrolyte at 25 mV s^{-1}.

Both samples had an onset potential of -0.2 V SHE. There was some discrepancy between the peak current results, No. 1 and No. 2 had peak current densities of -2.02 mA cm^{-2} and -1.39 mA cm^{-2}, respectively.

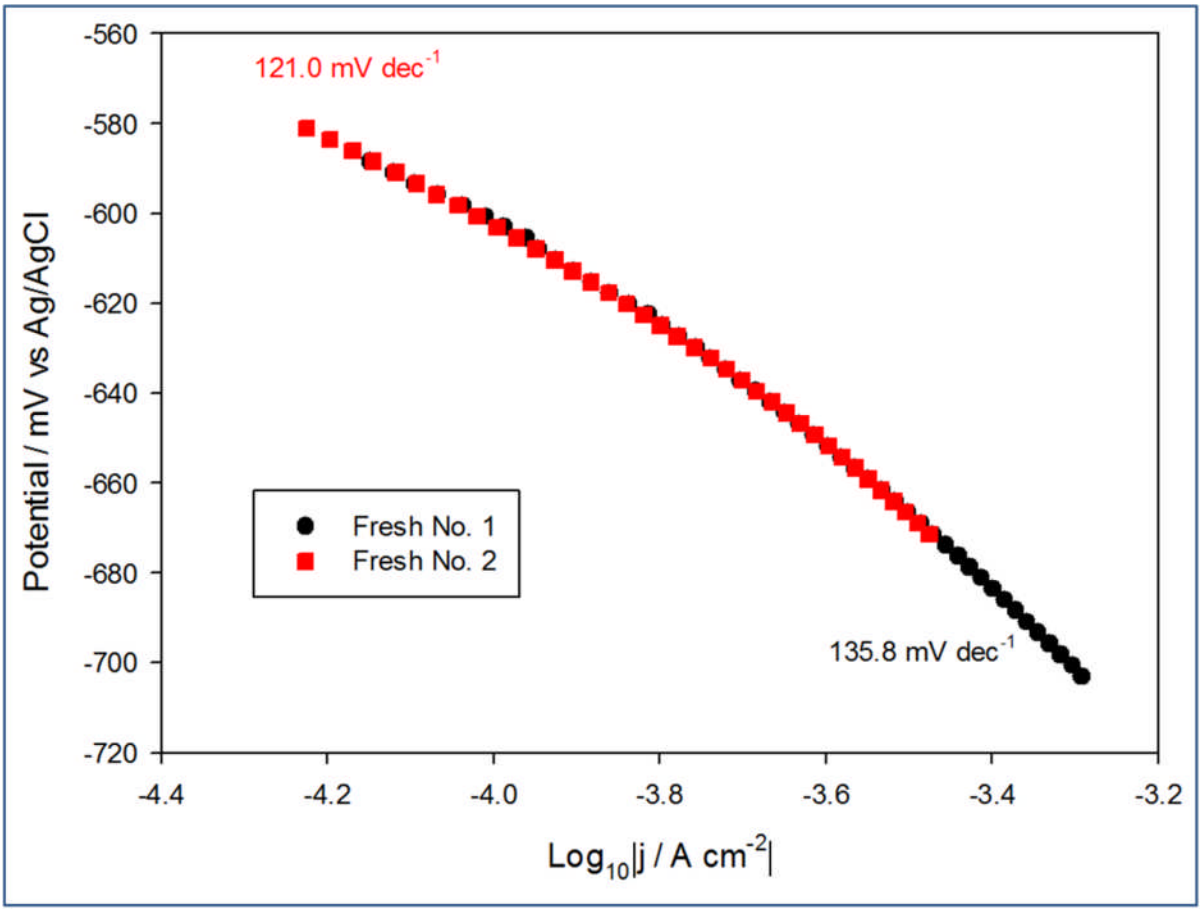

Figure 3.38. Tafel slopes for the nanostructured MoS_2 tested shortly after patterning. The slopes are derived from Figure 3.37.

Sample No. 2 had a Tafel slope close to the established value of 120 mV dec^{-1}, and No. 1 was slightly higher at 135.8 mV dec^{-1}. These samples had Tafel slopes in good agreement with published values on bulk MoS_2, but higher than some values reported for nanostructured MoS_2. Structuring into nanoparticulate MoS_2, 2D MoS_2, and vertically aligned layers; achieved 55 mV dec^{-1},[59] 67 mV dec^{-1}, [123] and 86 mV dec^{-1}, [110] respectively. The higher than expected Tafel slopes were attributed to oxidation of the MoS_2 by the oxygen plasma used to shrink the size of the nanospheres. The oxidation of the surface was expected, but thought to be irrelevant as the basal plane is inert for HER[122,56], and the

edges formed by the structuring were not exposed directly to the oxygen plasma. However given the lacklustre HER results it was believed that some oxygen penetrated within the crystal. This is supported by findings that indicate although the majority of oxidation due to oxygen plasma occurs at the sample surface as the species lack the kinetic energy to penetrate the MoS_2, some of the more reactive species are able to penetrate deeper within the crystal[167,168]. As well as the low proportion of MoS_2 relative to molybdenum oxide species found by XPS analysis (Section 4.2). These more energetic particles can be considered as mostly O^+, O_2^+ and O_2^{2+} ions[169]. These ions freed a number of S and Mo atoms from the lattice, and since the mass of S is considerably smaller than that of Mo, S is relatively easier to displace. The lattice vacancies were predominantly taken up by oxygen due to the excess oxygen supplied by the plasma. The net effect of this process was occupancy of a proportion of S^{2-} sites by O^{2-} ions, resulting in additional defect sites within the MoS_2[169]. These samples confirmed however, that the samples in Section 3.4 were indeed negatively affected by their time in storage as the Tafel slope and onset potential are in reasonable agreement with published values.

4.0 Sulfidation of Air Degraded MoS_2

In the previous chapter MoS_2 electrodes were nanostructured using nanosphere lithography and plasma etching. It was found that the nanostructuring engendered a catalytic effect for the HER, and that exposure to air reduced this catalytic effect. The MoS_2 lost all catalytic property by 28 days after fabrication. In an effort to counter the negative effect extended atmospheric exposure had on the catalytic properties attempts were made to reinvigorate the electrodes by replacing the accumulated oxygen with sulfur. This technique intended to avoid the use of toxic H_2S or vapourised sulfur, which have been previously used as a sulfur sources[170,171]. Instead $Na_2S_2O_3$ was used as the sulfur source, and the sulfidation was accomplished using the air-exposed MoS_2 as a working electrode in an electrochemical set-up. The reasoning for the methodology pursued was derived in part from techniques to synthesise MoS_2, and in part from techniques to remove unwanted sulfur from solutions. Following early successes experiments were undertaken to determine the optimum solution concentration, and electrochemical conditions for the sulfidation with the HER catalytic performance taken as a means of success.

The optimised sulfidation was tested by measuring HER catalytic performance in both light and dark conditions, and found that the sulfidation resulted in a shift of ≈0.05 V towards zero overpotential as well as an increase in peak current. Tafel analysis showed that the sulfidation caused a beneficial shift in reaction pathway with the Tafel slope decreasing from >200 mV dec^{-1} to ≈120 mV dec^{-1}. The chemical composition of a freshly nanostructured sample, an atmospherically exposed sample, and a re-sulfidated sample was measured by XPS. The freshly nanostructured sample had a MoS_2 composition of 56.1

mol. %, this decreased to 45.5 mol. % when left exposed to air for 106 days, and the sulfidation increased the MoS_2 composition to 58.0 mol. %, with the remainder being molybdenum oxides. The decrease in MoS_2 due to air exposure and the increase in MoS_2 caused by sulfidation correlate to the decrease and increase in catalytic performance, respectively.

The effect of the sulfidation on surface morphology was observed by SEM finding that the process can be repeated twice without altering the structures, but that after 8 sulfidations the surface had homogenised.

4.1 $Na_2S_2O_3$ as the Sulfur Source

$Na_2S_2O_3$ has previously been used as a sulfur source in the synthesis of MoS_2 alongside a Mo ion source[172]. It is attractive as a sulfur source as unlike the other commonly used compounds it is a relatively benign chemical in terms of safety[173,174].

This technique drew on methods to synthesise MoS_2 from $Na_2S_2O_3$ and a Mo ion source[172], as well as the sulfidation of other metal ions[175–178]. This method was estimated to work in a similar way to the deposition with Na_2S (i.e an oxidation followed by a reduction), however with the $Na_2S_2O_3$ acid was deemed necessary in order to reduce the $S_2O_3^{2-}$ via[177,179]

$$S_2O_3^{2-}{}_{(aq)} + H^+{}_{(aq)} \rightleftharpoons S_{(s)} + HSO_3^-{}_{(aq)} \qquad \text{(Eq. 4.1)}$$

The oxidation scan was performed in order to fully oxidise the surface of the crystal. It has been found during a technique to synthesise MoS_2 that fully oxidised molybdenum (MoO_4^{2-}) when sulfidised yielded MoS_2[175]. While molybdenum in the 3+ and 4+ oxidation states yielded Mo_2S_3 and Mo_3S_4(Mo_2S_3*MoS), respectively[175]. This oxidation can be achieved by scanning positive in aqueous media[53]. This was confirmed experimentally in Section 4.1.3. A reductive voltage scan was then applied (at a scan rate of 25 mV s^{-1}) to electroreduce the colloidal sulfur onto the electrode (Eq. 4.2)[177].

$$S_{(s)} + 2e^- \rightleftharpoons S^{2-}_{(aq)} \qquad \text{(Eq. 4.2)}$$

As with the Na_2S it was judged that the S^{2-} would displace some of the oxygen on the surface of the atmospherically-aged MoS_2, and reinvigorate the crystal for the HER.

4.1.1 $Na_2S_2O_3$ Sulfur Deposition Methodology

A variety of sulfidation parameters were attempted in order to first determine whether sulidation of air-exposed MoS_2 utilising $Na_2S_2O_3$ was a possibility, and to optimise the reaction once it had been determined it was. The initial experiment was carried out with a degassed 10 mM $Na_2S_2O_3$, 1 mM H_2SO_4, and 0.1 M Na_2SO_4 electrolyte. As the acid was reasoned to begin the reaction by precipitating the sulfur out of solution as per Eq. 4.1 it was not added to the solution until shortly before the sulfidation. The initial test attempted four different potential windows on a single electrode. The H^+ reduction performance of the electrode was tested before sulfidation, and after each sulfidation (Figure 4.1).

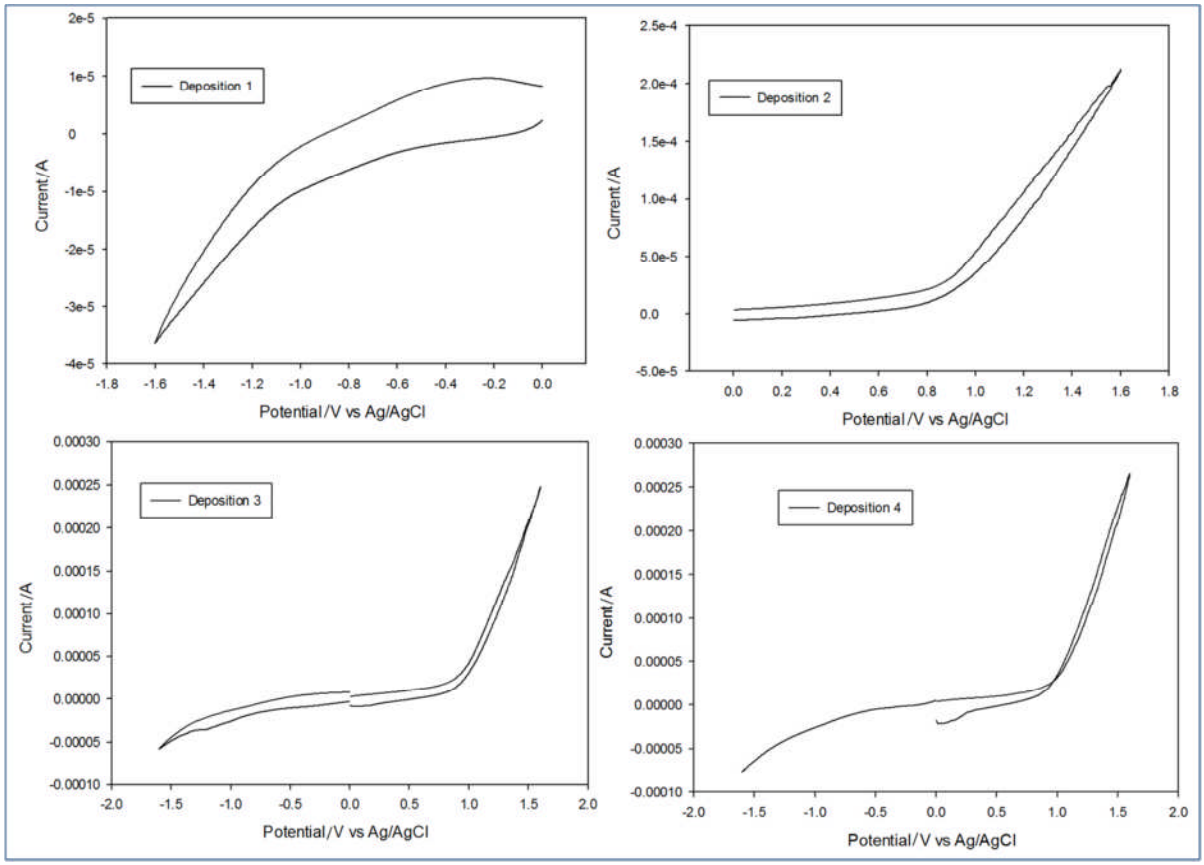

Figure 4.1. Initial sulfur deposition test from 10mM $Na_2S_2O_3$, different deposition potentials were applied with a H^+ reduction test in-between. Deposition 1 applied a cathodic potential from 0 V to -1.6 V Ag/AgCl. Deposition 2 applied an anodic potential from 0 V to +1.6 V Ag/AgCl. Deposition 3 was cycled from 0 V to +1.6 V to -1.6V to 0V Ag/AgCl. Deposition 4 was swept from 0 V to +1.6 V to -1.6V Ag/AgCl.

The first sulfidation applied a cathodic potential from 0 V to -1.6 V Ag/AgCl, the second was anodic from 0 to +1.6 V, the third was anodic from 0 to +1.6 V followed by cathodic from 0 V to -1.6 V Ag/AgCl, and finally the fourth was anodic from 0 to +1.6V followed by cathodic from 0 V to -1.6 V Ag/AgCl with the deposition stopped at -1.6 V without returning to 0 V Ag/AgCl. The post-sulfidation H^+ reduction measurements are compared in Figure 4.2.

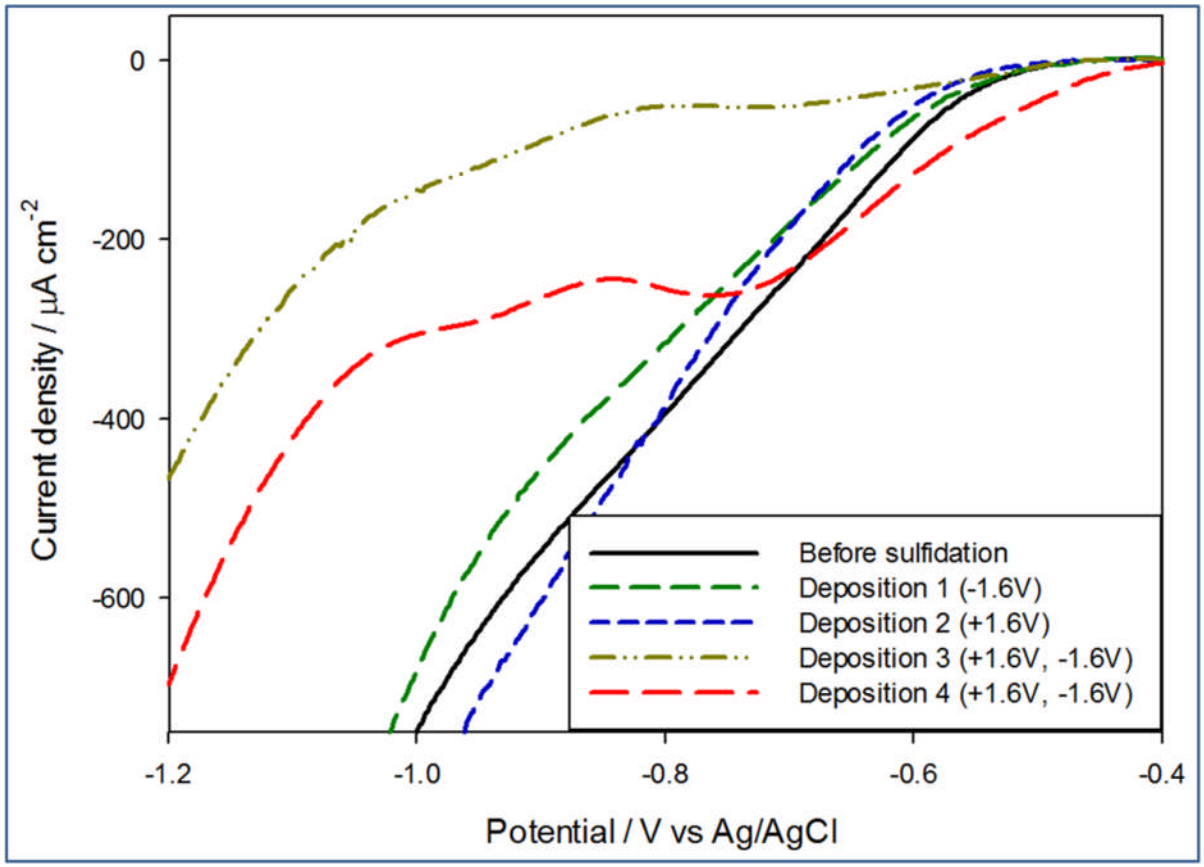

Figure 4.2. H^+ reduction on the MoS_2 treated with $Na_2S_2O_3$ in Figure 4.1. Depositions 1, 2, and 3 lowered the current and increased the onset potential as compared to the before measurement. However deposition 4 showed a beneficial effect to onset potential, and also a more defined peak.

As compared with the before sulfidation measurement depositions 1, 2 and 3 were inferior in terms of both current and onset potential. However, deposition 4 exhibited a lower onset potential of -0.054 V (SHE), compared to -0.17 V (SHE) for the before sulfidation measurement. Also although the sulfidated peak current (-263 µA cm^{-2}) did not increase as compared to before measurement (-291 µA cm^{-2}) the peak did have more definition. In order to establish reproducibility the deposition 4 conditions were repeated with a second

electrode (Figure 4.3). Once again the H^+ reduction performance of the electrode was tested before and after sulfidation.

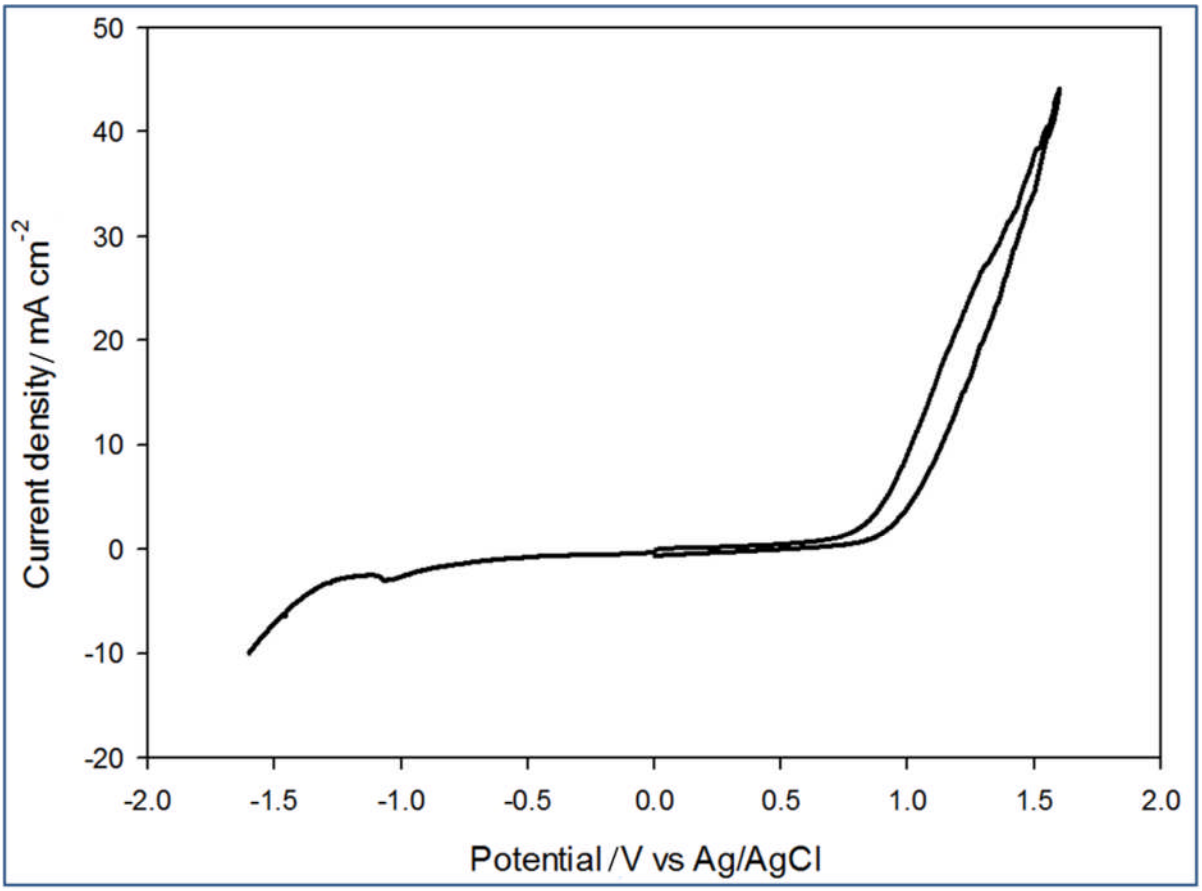

Figure 4.3. The voltammogram of an air-exposed MoS_2 electrode in 10 mM $Na_2S_2O_3$, 1 mM H_2SO_4, and 0.1 M Na_2SO_4 with the potential swept from 0 V to +1.6 V to -1.6 V Ag/AgCl.

This deposition exhibited a reductive peak at ≈-1 V Ag/AgCl similarly to the deposition from Na_2S solution. This peak was absent from the initial deposition test (Figure 4.1), but was present for other $Na_2S_2O_3$ depositions (Figure 4.5, Figure 4.7).

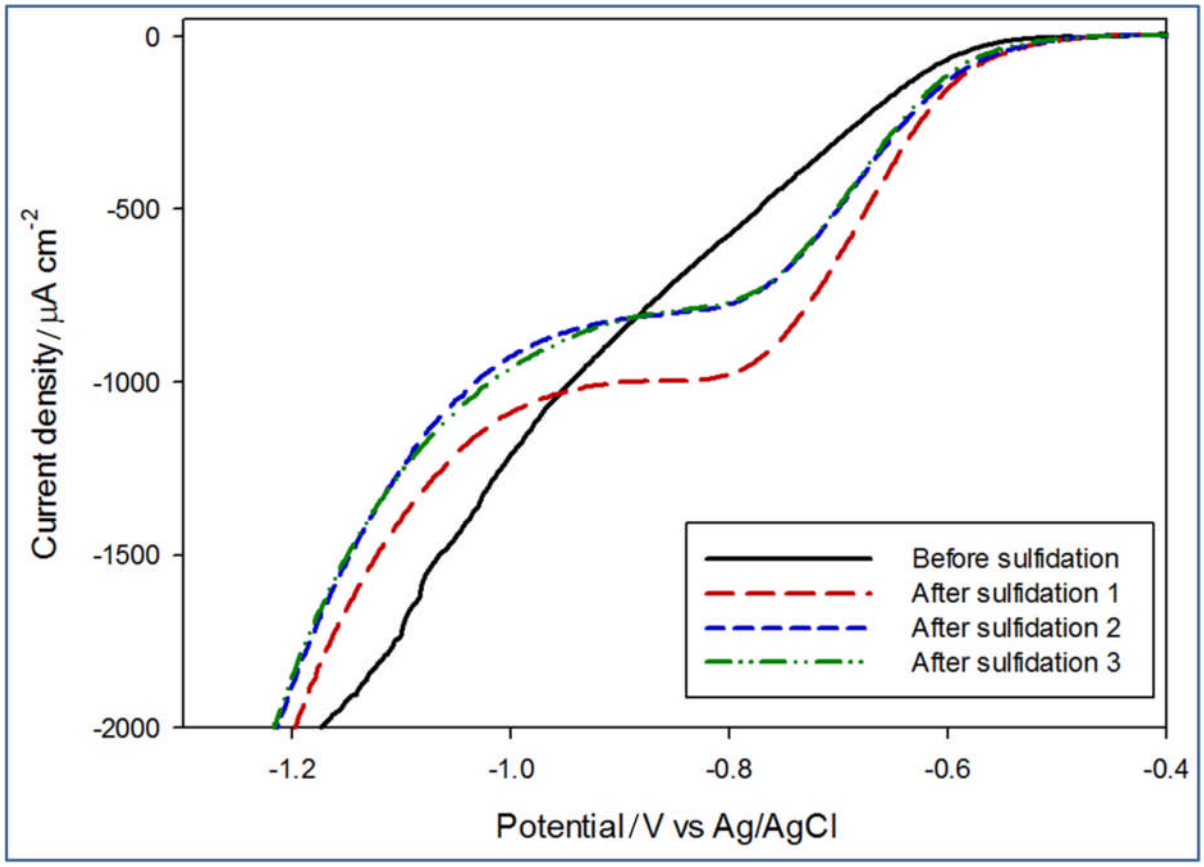

Figure 4.4. H^+ reduction on MoS_2 before and after sulfidation as per Figure 4.3. The sulfidation resulted in an earlier onset potential and higher peak current. These metrics degraded between the 1st and 2nd measurements, but were stable between the 2nd and 3rd.

The second electrode responded more favourably to these deposition parameters than the first, with an increase in peak current from -590 µA cm^{-2} to -1008 µA cm^{-2}, and an earlier onset potential (-0.224 V SHE before, -0.184 V SHE after) than the before measurement. The performance did degrade between the 1st and 2nd post-sulfidation measurements, but was stable between the 2nd and 3rd, with a peak current density of -784 µA cm^{-2}. This test confirmed that applying a potential from 0 V to +1.6 V to -1.6 V Ag/AgCl in 10 mM $Na_2S_2O_3$ engendered a beneficial effect on air-exposed MoS_2 electrodes. As such more experiments

were run to determine the optimum sulfidation conditions from a $Na_2S_2O_3$ electrolyte. Measurements were taken to identify the ideal potential window for the deposition, and the optimum concentration of acid.

4.1.2 Acid Concentration Optimisation

To determine whether equimolar acid would improve the sulfidation an $MoS_xO_{(2-x)}$ electrode was sulfidated in 1 mM H_2SO_4 followed by 10 mM H_2SO_4 combined with 10 mM $Na_2S_2O_3$ and 0.1 M Na_2SO_4, and tested for H^+ reduction capability before and after each sulfidation (Figure 4.5).

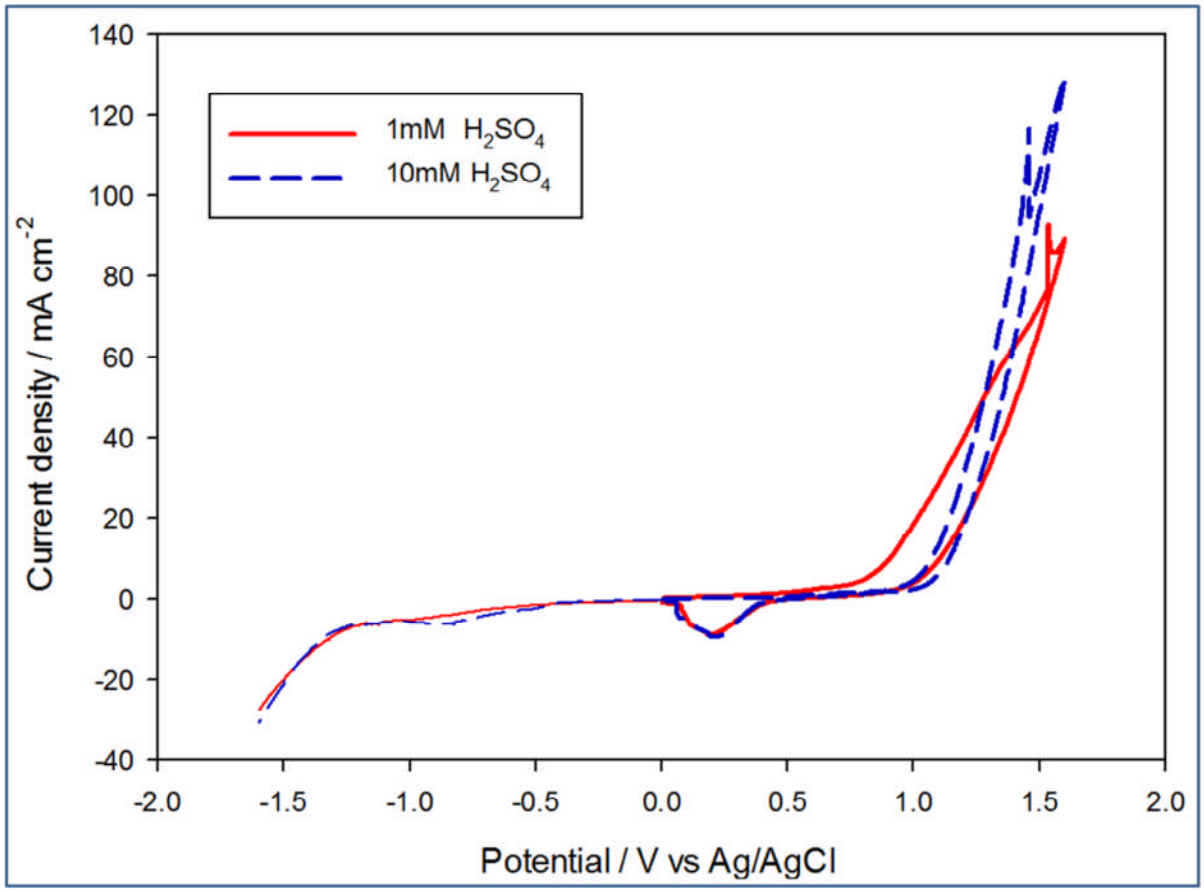

Figure 4.5. The voltammogram for sulfidation using both 1 mM and 10 mM H_2SO_4 in conjunction with 10 mM $Na_2S_2O_3$.

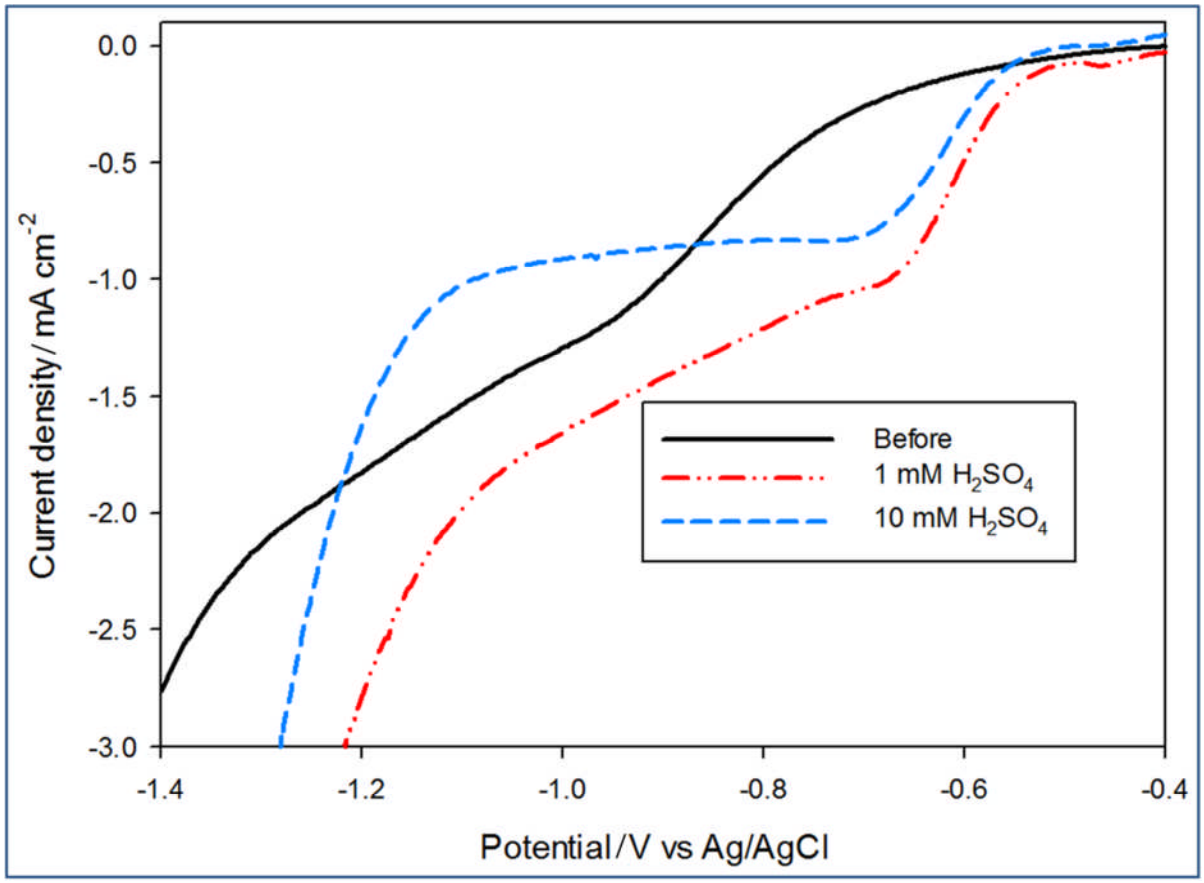

Figure 4.6. H^+ reduction measurements taken before and after sulfidation depicted in Figure 4.5. Both post-sulfidation results were superior to the before measurement, and the 1 mM displayed an earlier onset potential and a higher peak current.

This experiment found that sulfidisation from 1 mM acid results in a better HER catalytic effect on partially oxidised MoS_2. The onset potential was -0.17 V SHE for the 1 mM acid deposition, and -0.21 V SHE for the 10 mM acid deposition. The peak current density was also higher for the lower acid condition at -1.03 mA cm^{-2} versus -0.84 mA cm^{-2}. From this it was concluded that 1 mM acid produced a more greatly enhanced catalytic effect, and as such all subsequent sulfidations were carried out with an electrolyte of 1 mM H_2SO_4, 10 mM $Na_2S_2O_3$, and 0.1 M Na_2SO_4.

4.1.3 Deposition Potential Optimisation

Once the electrolyte had been decided upon, and having confirmed an oxidative followed by a reductive potential results in beneficial sulfidation an experiment was conducted to determine the optimum reductive window for sulfidation, as well as elucidating whether the oxidative sweep alone can be used for sulfidation. Four depositions were carried out at incrementally increasing potential windows with H^+ reduction test undertaken before and in-between each measurement. The first deposition was linear 0 V to +1.6 V Ag/AgCl, and the second cyclic 0 V to +1.6 V Ag/AgCl in order to determine whether the oxidative sweep alone is necessary. Following these the cyclic oxidation was repeated with a subsequent linear reduction to -0.6 V Ag/AgCl, and finally a cyclic oxidation to +1.6 V Ag/AgCl before a reduction to -1.6 V Ag/AgCl.

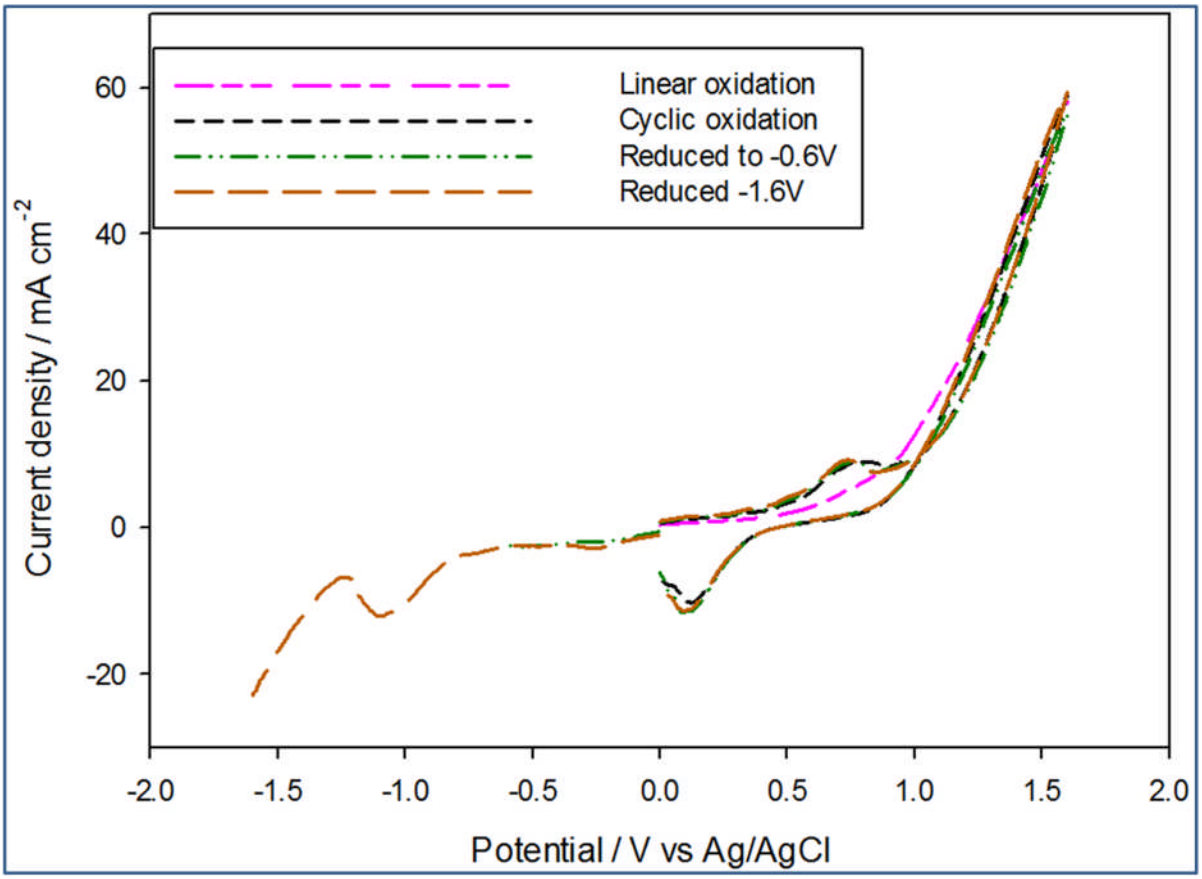

Figure 4.7. Four sulfidations were undertaken to determine whether the oxidative sweep alone is necessary, and what the optimum reductive potential was. Before and between each sulfidation the H^+ reduction ability was tested. Each sulfidation started at 0 V Ag/AgCl and was taken to +1.6 V Ag/AgCl. The linear oxidation was halted at +1.6 V Ag/AgCl while the cyclic swept back to 0V Ag/AgCl. The reductive sweeps had the full cyclic oxidation performed first each time before being swept to -0.6 V Ag/AgCl, and -1.6 V Ag/AgCl.

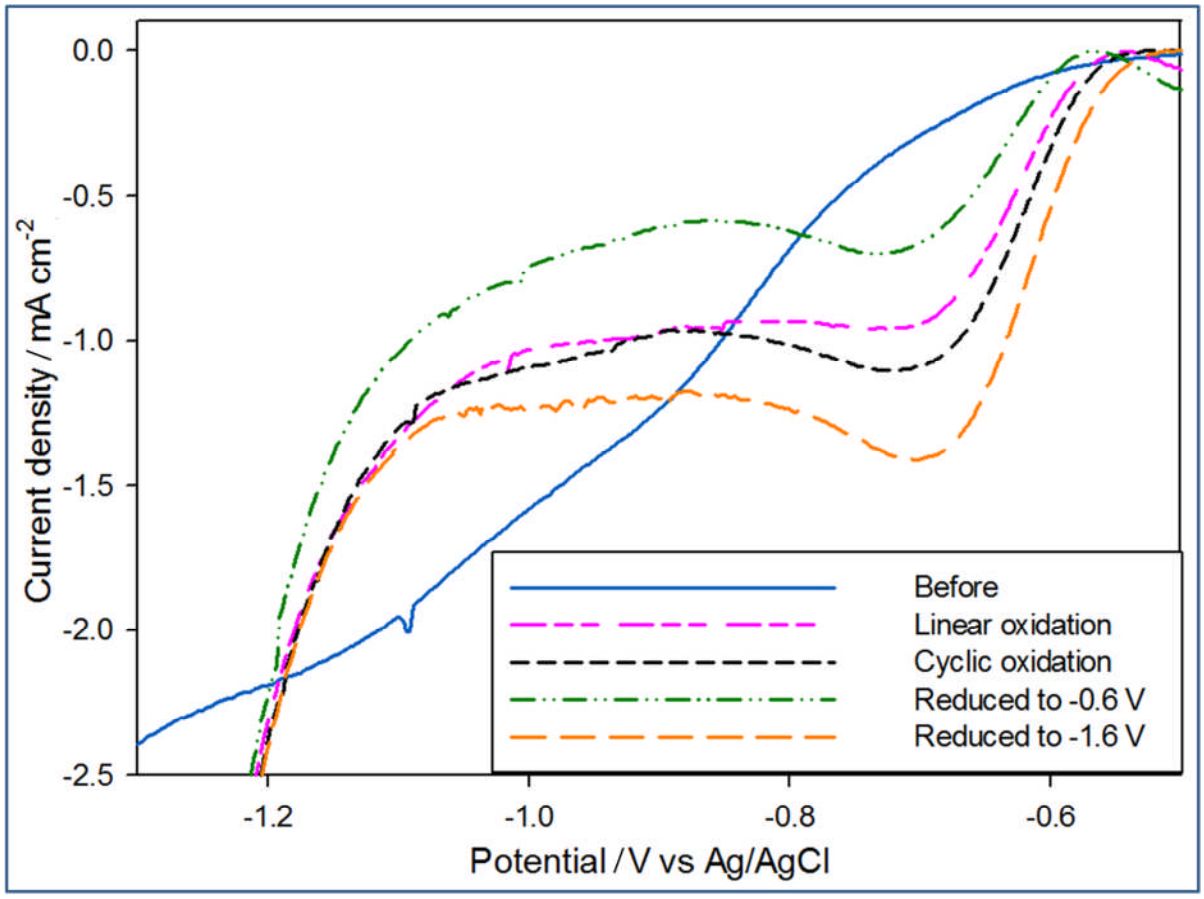

Figure 4.8. In between the sulifidations presented in Figure 4.7 the MoS_2 electrode was tested for H^+ reduction catalysis. The full potential window where the sulfidation was taken from 0 V to +1.6 V to -1.6 V Ag/AgCl yielded the best results. Both cyclic and linear oxidations were shown to have a beneficial effect on the electrodes ability to reduce protons. Although the reduction to -0.6 V Ag/AgCl was superior to the before sulfidation measurement it was detrimental compared to a just oxidative deposition.

All of the sulfidations resulted in a lower onset potential and a higher, better defined peak current. The final measurement utilising the full potential window from 0 V to +1.6 V to -1.6 V Ag/AgCl had the best results with an onset potential of -0.18 V SHE and a peak current density of -1.45 mA cm^{-2}. The solely oxidative scans were intermediary with the cyclic

oxidation resulting in a peak current density of -1.13 mA cm^{-2}, and an onset potential of -0.2 V SHE. The linear oxidation was slightly inferior to this with a peak current of -0.97 mA cm^{-2}, and an onset potential of -0.21 V SHE. The linear reduction to only -0.6 V Ag/AgCl produced inferior results as compared to only performing the cyclic oxidation with a peak current density of -0.72 mA cm^{-2} and a onset of -0.23 V SHE. This result was taken as confirmation that the reductive peak at ≈-1.0 V Ag/AgCl is necessary for the optimum sulfidation by this method, although an oxidative sweep alone did improve the catalytic ability of air-exposed MoS_2.

Once the optimum reductive potential window had been determined a similar experiment was undertaken to obtain the optimum oxidative potential window. A $MoS_xO_{(2-x)}$ electrode was sulfidated at steadily increasing positive potential windows, while the reductive window remained unchanged at -1.6 V Ag/AgCl. The catalytic ability for H^+ reduction was tested before the sulfidation and in-between each sulfidation. The oxidative potential maximum started at +0.3 V Ag/AgCl and was increased in 0.1 V increments up to +1.2V Ag/AgCl, and in 0.2 V increments from then up to +1.6 V Ag/AgCl. A representative selection of these measurements is presented in Figure 4.9.

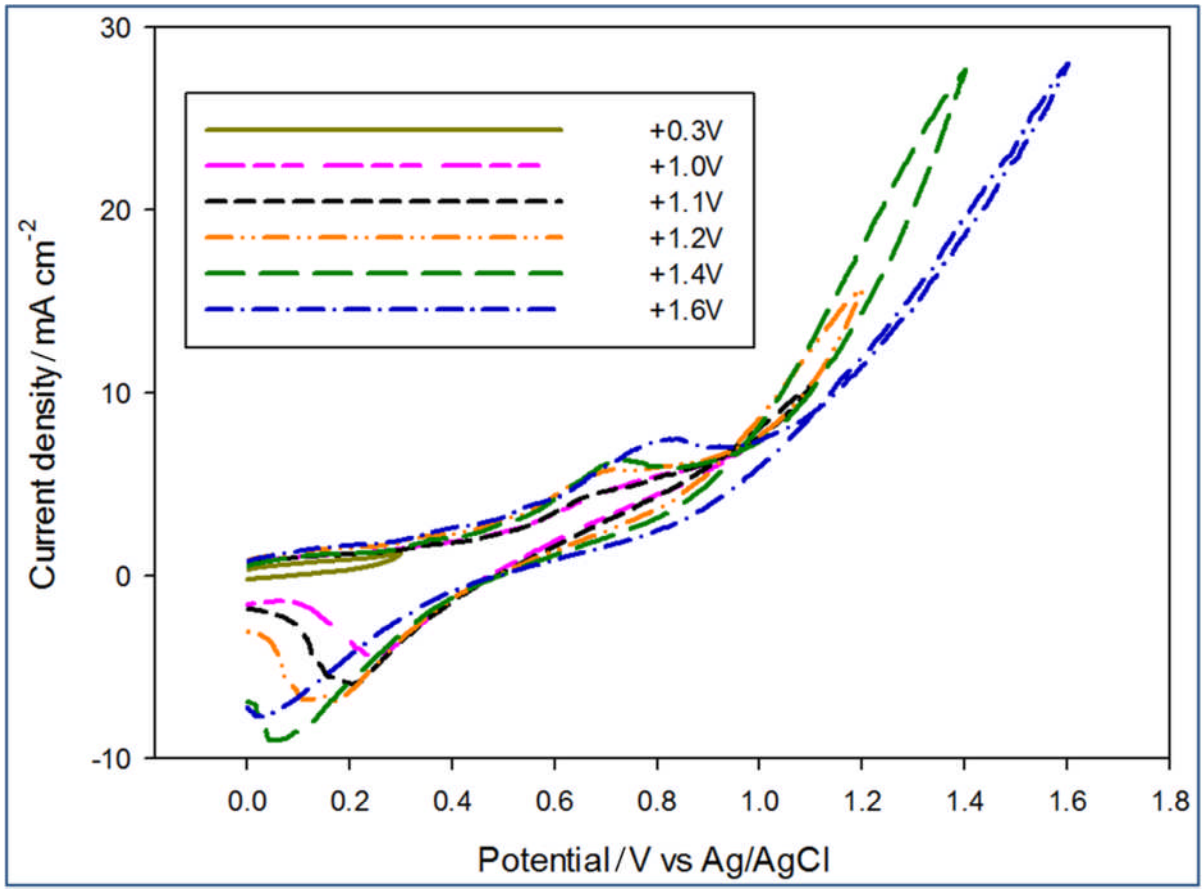

Figure 4.9. Determination of the optimum oxidative potential for sulfidation. The maximum potential was increased in 0.1 V increments to +1.2 V Ag/AgCl, and in 0.2 V increments thereafter. The peaks at ≈+0.8 V Ag/AgCl on the forward scan, and ≈+0.2 V Ag/AgCl on the back scan were common features.

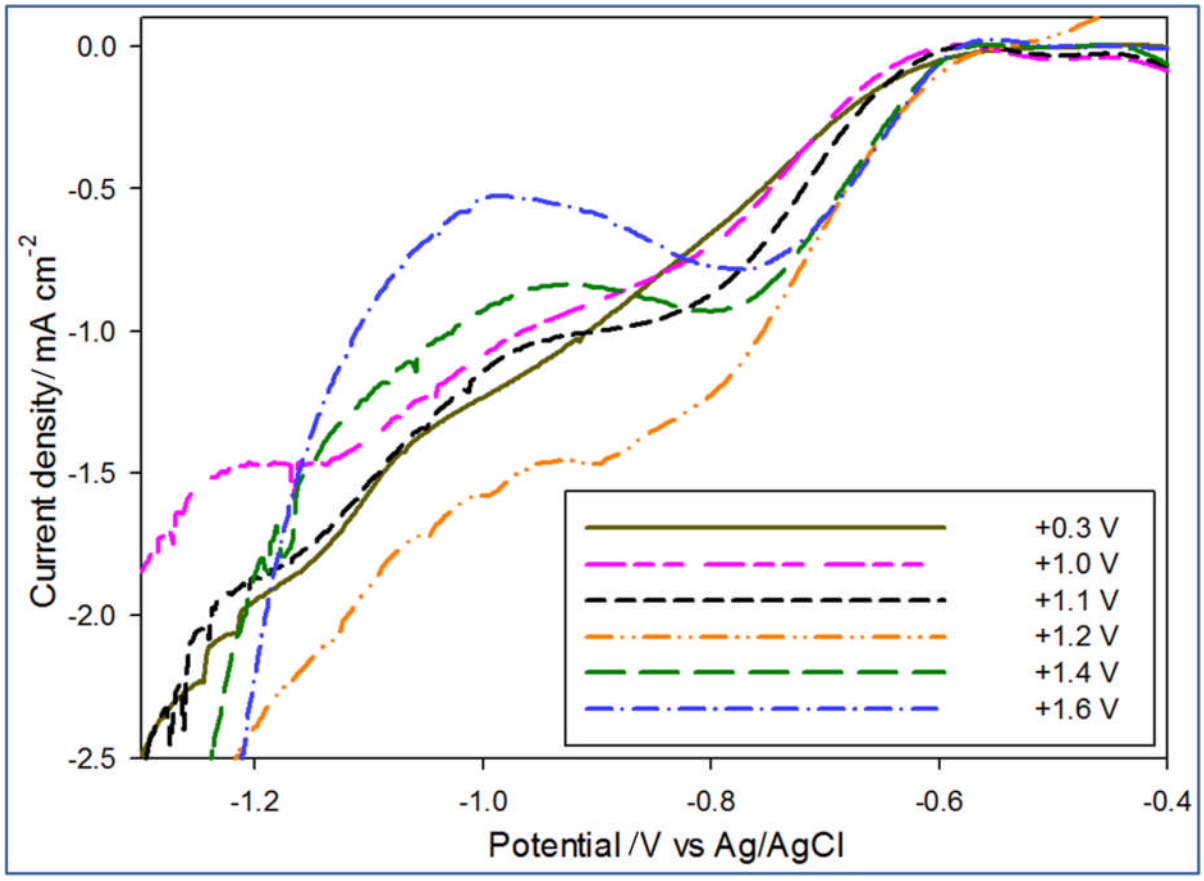

Figure 4.10. H^+ reduction test results produced from incrementally increasing the oxidative potential window during sulfidation. The MoS_2 electrode was cyclically oxidised to the stated potential, then reduced to -1.6 V Ag/AgCl. In between sulfidations these H^+ reduction measurements were taken.

For the H^+ reduction measurements following the +0.3 V to +1.1 V Ag/AgCl deposition windows the onset potential was unchanged at -0.29 V SHE. However, the peak current did increase as the potential window broadened with the +0.3 V measurement yielding an almost linear response with no defined peak current, and +1.0 V and +1.1 V Ag/AgCl having peak current densities of -0.83 mA cm^{-2} and -0.99 mA cm^{-2}, respectively. The +1.0 V deposition peak current density was only 0.07 mA cm^{-2} higher than the result obtained

from the +0.3 V Ag/AgCl deposition window, but had a far more clearly defined proton reduction wave. The peak current of the sulfidation carried out from the +1.1 V Ag/AgCl deposition window had considerably greater definition than the +1.0 V Ag/AgCl sulfidation, from this it was determined that an initial oxidative potential of > +1.0 V Ag/AgCl was necessary for the successful sulfidation of air-exposed MoS_2 via this method.

Increasing the potential to +1.2 V Ag/AgCl caused the H^+ reduction to shift 50 mV to an earlier onset potential of -0.24 V SHE, and increased the peak current density to -1.46 mA cm^{-2}. The sulfidations carried out with a wider deposition window than +1.2 V Ag/AgCl retained the earlier onset potential, but the peak current densities steadily diminished to 0.94 mA cm^{-2} for the +1.4 V Ag/AgCl deposition, and -0.79 mA cm^{-2} for the +1.6 V Ag/AgCl deposition. From these results +1.2 V Ag/AgCl was taken to be the optimum potential for the initial oxidative sweep, and this potential window followed by a reduction to -1.6 V Ag/AgCl was used for subsequent sulfidations.

4.2 XPS Determination of Surface Composition

The change in chemical composition was quantified by XPS analysis in collaboration with the European Bioresearch Institute (EBRI) at Aston University. Three states were investigated: freshly fabricated, air-exposed, and following sulfidation. In order to prevent the samples degrading in air between fabrication and XPS testing the freshly structured and sulfidated samples were fabricated immediately prior to XPS testing. To minimise air-exposure prior to testing the freshly fabricated sample was prepared as far as the

nanosphere shrinking step the day before XPS testing. The SF_6 etch and sulfidation were performed on the morning of the XPS testing so that a maximum of 4 hours expired between the fabrication and the samples entering the XPS vacuum. The degraded sample had been structured 106 days prior.

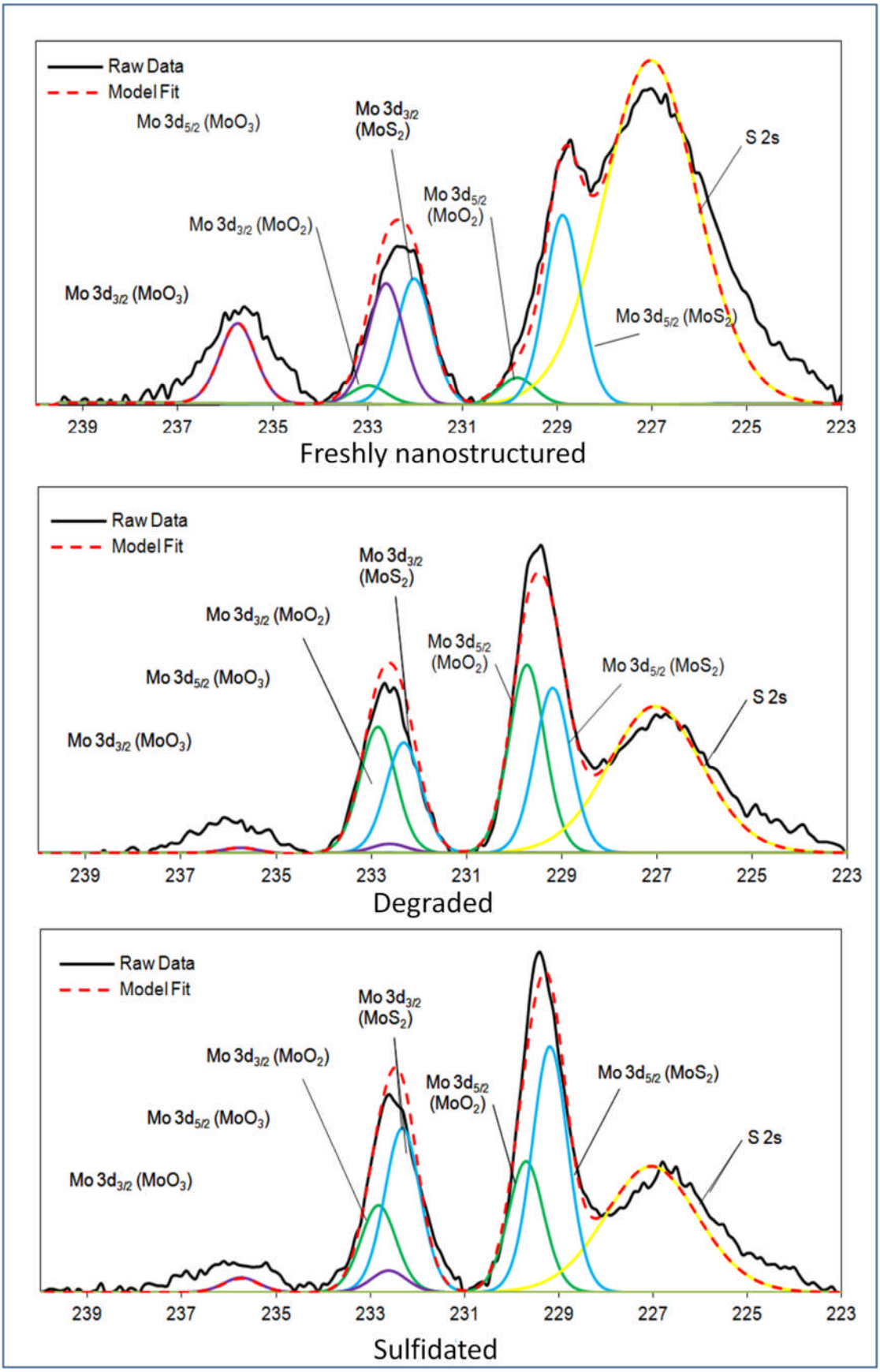
Raw Data
Model Fit
Mo 3d5/2 (MoO3)
Mo 3d3/2 (MoS2)
S 2s
Mo 3d5/2 (MoO2)
Mo 3d3/2 (MoO2)
Mo 3d3/2 (MoO3)
Mo 3d5/2 (MoS2)
239 237 235 233 231 229 227 225 223
Freshly nanostructured
Raw Data
Model Fit
Mo 3d3/2 (MoS2)
Mo 3d3/2 (MoO2)
Mo 3d5/2 (MoO2)
Mo 3d5/2 (MoS2)
Mo 3d5/2 (MoO3)
S 2s
Mo 3d3/2 (MoO3)
239 237 235 233 231 229 227 225 223
Degraded
Raw Data
Model Fit
Mo 3d3/2 (MoS2)
Mo 3d3/2 (MoO2)
Mo 3d5/2 (MoO2)
Mo 3d5/2 (MoS2)
Mo 3d5/2 (MoO3)
S 2s
Mo 3d3/2 (MoO3)
239 237 235 233 231 229 227 225 223
Sulfidated

Figure 4.11. The freshly nanostructured material produced molybdenum species corresponding to MoS_2 (B.E. Mo $3d_{5/2}$ = 229 eV), MoO_2 (B.E. Mo $3d_{5/2}$ = 229.7 eV) and MoO_3 (B.E. Mo $3d_{5/2}$ = 232.5 eV), alongside a strong signal at 227 eV corresponding to sulfur in the metal sulfide form. The degraded sample produced a broadened peak at 229.5 eV, shifted to slightly higher binding energy, indicative of a shift towards a more oxidic Mo species, as well as a decrease in surface sulfur species. Decrease in MoO_3 is clearly evident due to the diminished Mo $3d_{3/2}$ species at 235.6 eV, indicating the sample consists of largely MoO_2. After sulfidation, the major Mo photoelectron peak narrows and returns to a lower binding energy, consistent with the reformation of surface MoS_2 species. The $Mo(O_3)$ 3d peak at 235.6 eV remains in a diminished form, suggesting the sample has returned to a majorly MoS_2 composition[180].

Surface XPS data identified a decrease in the MoS_2 content of the Mo 3d region and concurrent increase in MoO_2 when the sample degraded in air, and that the sulfidation reverses this process (Figure 4.11, Table 4-1) MoO_3, readily identified by a significant Mo $3d_{3/2}$ peaks at 235.6 eV, appears to decrease largely to the Mo(VI) species, of which sulfidation is unable to reoxidise. MoS_2 is identified at a binding energy of 229 eV for the 5/2 peak, with MoO_2 existing at a slightly higher binding energy of 229.7 eV. The broadening and shift to a higher energy of the major Mo $3d_{5/2}$ species could therefore be deconvoluted to probe the chemical composition.

Sample	%MoS_2	% MoO_3	% MoO_2
Freshly fabricated	56.07	35.83	8.10
Air-exposed	45.52	2.51	51.97
Sulfidated	57.99	5.03	36.98

Table 4-1. The molar percentages of MoS_2, MoO_3, and MoO_2 in the electrodes immediately following fabrication, in their air-exposed state, and after sulfidation as determined by XPS analysis.

The sulfidation resulted in a percentage of MoS_2 1.9 % higher than the freshly fabricated sample, and 12.5 % higher than the atmospherically-aged state. The freshly fabricated sample was already significantly oxidised despite the short amount of time since its fabrication, this is attributed to the oxygen plasma oxidising the crystal as discussed in section 3.7.

4.3 Electrochemistry

Once it had been determined that sulfidation from a $Na_2S_2O_3$ solution is viable and results in a beneficial effect on the HER reaction of these atmospherically-degraded MoS_2 samples, and having found an optimised set of conditions for the sulfidation H^+ reduction experiments were performed to observe the magnitude of the effect. These consisted of dark current H^+ reduction measurements to use as a means of comparison with the previous measurements, a degradation study to gain an insight into the rate of atmospheric oxidation of the sulfidised $MoS_xO_{(2-x)}$ and to determine whether the sulfidation is

repeatable, and photoelectrochemical measurements to observe whether these electrodes are applicable as photoelectrodes.

4.3.1 Proton Reduction

Atmospherically-degraded MoS_2 electrodes were tested for their catalytic ability at proton reduction prior to sulfidation. The sulfidation was carried out by the optimum procedure as determined in section 4.1.1. The electrolyte consisted of 10 mM $Na_2S_2O_3$, 1 mM H_2SO_4, and 1 M Na_2SO_4. The sulfidation was performed using a CV scan from 0 V to +1.2 V Ag/AgCl, followed by a linear scan from 0 V to -1.6 V Ag/AgCl. After sulfidation a second series of H^+ reduction measurements were performed and these results are presented in comparison with the freshly prepared samples discussed from section 3.7 in Figure 4.12.

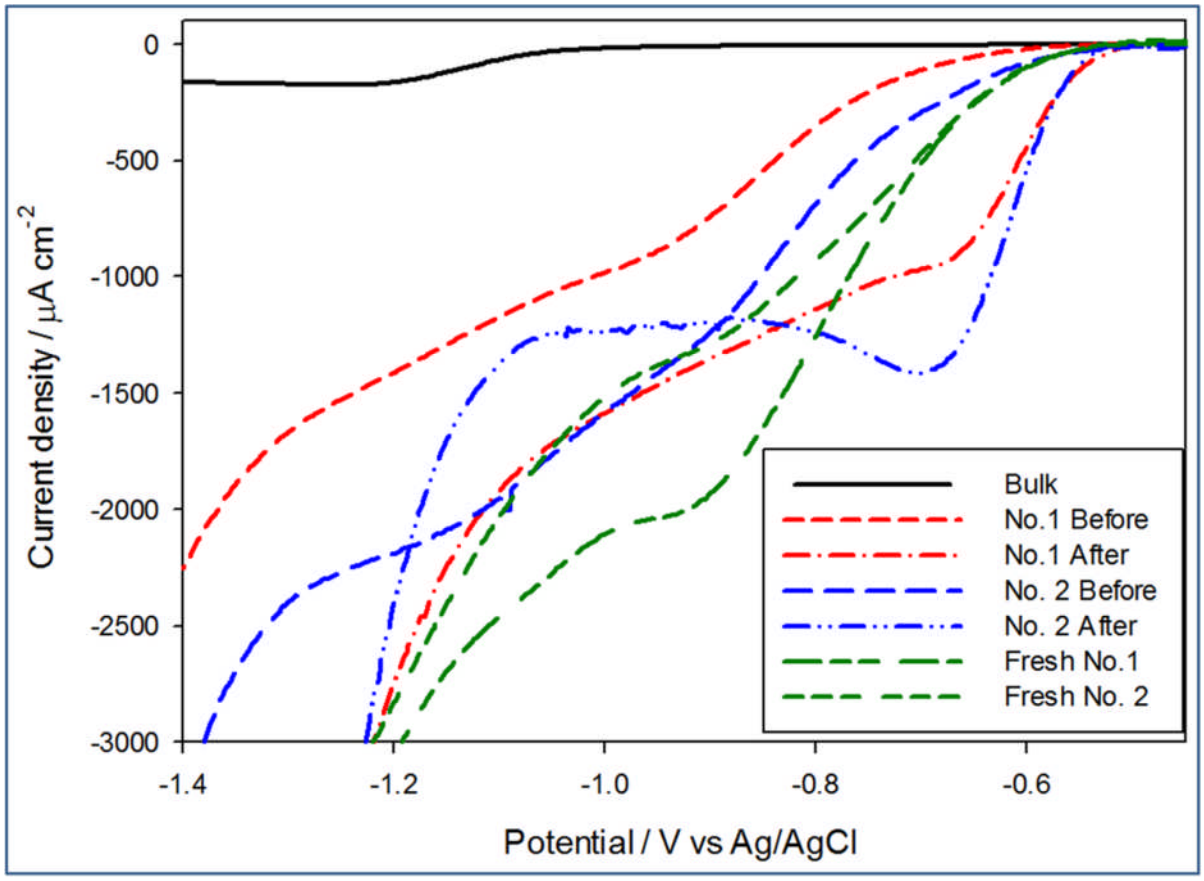

Figure 4.12. Two atmospherically-aged $MoS_xO_{(2-x)}$ electrodes were H^+ reduction tested before and after sulfidation. The results are compared against two freshly fabricated nanostructured MoS_2 samples and bulk MoS_2.

The No. 1 sample had an onset potential of -0.27 V SHE and a peak current density of -963 µA cm^{-2} prior to sulfidation. Following sulfidation the onset potential decreased to -0.17 V SHE and the peak current density increased to -1002.5 µA cm^{-2}. The No. 2 sample also had improvements in terms of onset potential, with the overpotential shifting from -0.22 V SHE to -0.18 V SHE. The peak current was lower at -1424.7 µA cm^{-2} following sulfidation compared to 2159.2 µA cm^{-2} before. However, the peak current following sulfidation was at a significantly lower potential than the before measurement: -0.34 V SHE compared to -

0.81 V SHE. This indicated faster reaction kinetics for the post-sulfidated state which was confirmed by Tafel slopes (Figure 4.13). The onset potentials for the freshly fabricated samples were intermediary to the before and after sulfidation samples at -0.2 V SHE. -0.2 V SHE is a commonly given value for MoS_2, so the freshly prepared samples are in good agreement with previously published values[59,110,127,128,181,]. The air-exposure lead to additional overpotential being required for the HER to initiate, and the sulfidation resulted in an onset potential 0.2 V to 0.3 V earlier than the established values for MoS_2 HER.

The peak current density of Fresh No. 1 was intermediary to both before and after sulfidation measurements at -1276.3 μA cm^{-2}, while Fresh No. 2 had a peak current density higher than the after sulfidation measurements at -2062.0 μA cm^{-2}. However this peak occurred at ca. 0.25 V additional overpotential than the sulfidated samples, once again indicating that the sulfidation resulted in superior reaction kinetics. This reaction pathway was analysed by Tafel slopes in Figure 4.13.

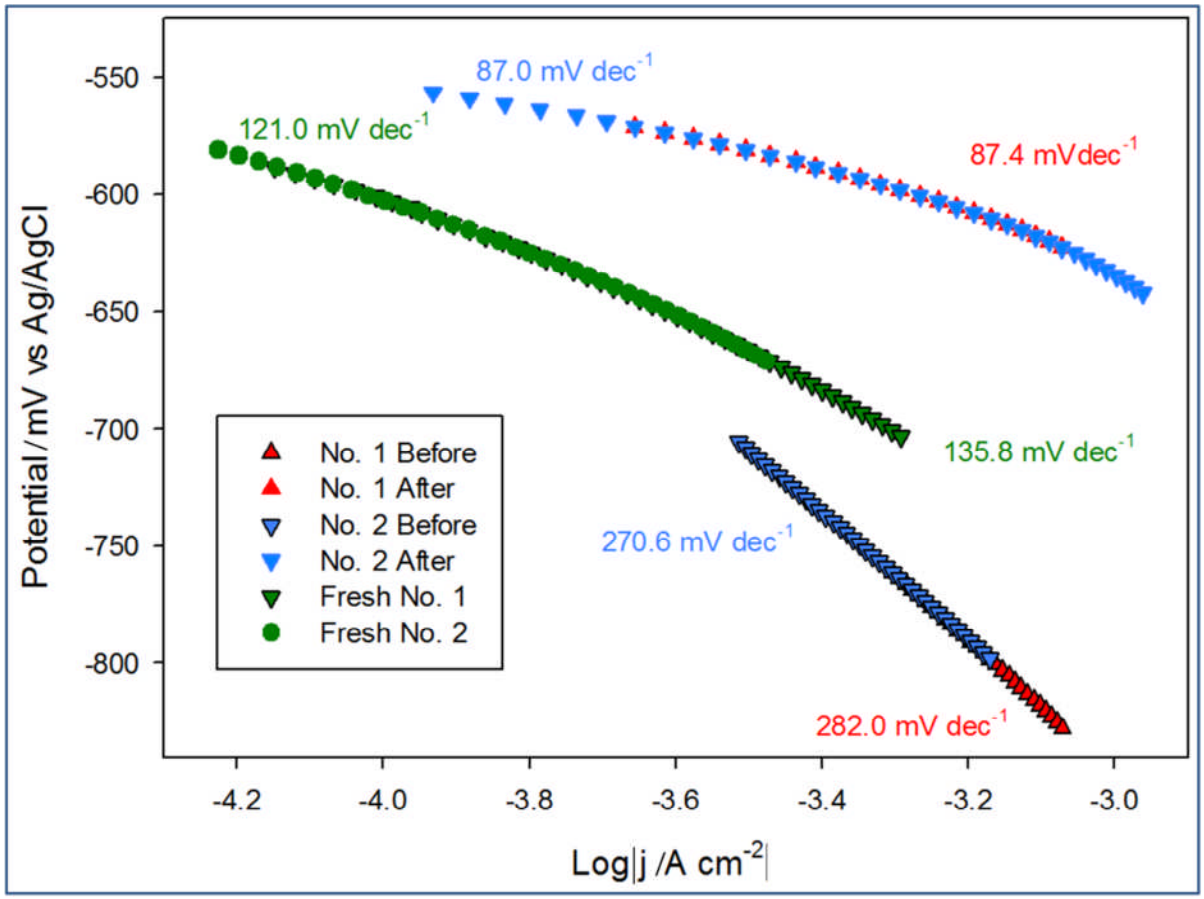

Figure 4.13. Tafel slopes derived from Figure 4.12 as a means of comparison of reaction kinetics between freshly prepared, atmospherically-aged, and sulfidated MoS_2.

Tafel plots were constructed from the voltammetric results in order to calculate the rate determining step and reaction pathway of the HER. Further details can be found in Section 1.2.5. Each of the three cases studied displayed characteristic Tafel responses. The freshly nanopatterned MoS_2 from this work had a slope of ca. 120 mV dec^{-1} indicating the primary discharge step was rate limiting as in the case of bulk MoS_2[127,128,129]. When the samples were exposed to air the Tafel slope rose considerably to 282.0 mV dec^{-1}, and 270.6 mV dec^{-1} for samples No. 1 and No.2, respectively. Sulfidation of the surface improved catalysis to a Tafel slope of ca. 87 mV dec^{-1}, comparable with other structured MoS_2 reports[110,59,123]. This

is consistent with the restoration of catalytically active sulfur atoms on the MoS_2 $(10\bar{1}0)$ edge enabling a faster primary discharge as compared with the air-exposed state[50].

Due to the fast kinetics of the HER on Pt, it is widely considered a benchmark catalyst. The HER on Pt is known to have a slope of 30 mV dec^{-1} and therefore to proceed through the Volmer-Tafel reaction[51,52]. The precise pathway of hydrogen evolution on MoS_2 is still unknown[52]. Bulk MoS_2 has a slope of ≈ 120 mV dec^{-1} which suggests the primary discharge step is rate limiting[127,128,129]. However, MoS_2 has been combined with reduced-graphene oxide (RGO), as well as single-walled carbon nanotubes to achieve Tafel slopes of ≈ 41 mV dec^{-1} indicating a Volmer-Heyrovský reaction[123,52].

Various structuring techniques have been applied to optimise the performance of MoS_2 in the HER. The lowest measured Tafel slope for pure MoS_2 is 49 mV dec^{-1} and was achieved through edge termination and layer expansion[136]. Other structures include nanoparticulate MoS_2, 2D MoS_2, and vertically aligned layers; achieving 55 mV dec^{-1}, [59] 67 mV dec^{-1}, [123] and 86 mV dec^{-1}, [110] respectively. The post-sulfidation Tafel slopes are higher than current state of the art, but still lower than bulk MoS_2. They also show an improvement of nearly 200 mV dec^{-1} against the air-exposed MoS_2, and it may be possible to regenerate the aged structures obtained by other groups through this sulfidation technique.

4.3.2 Degradation

Experiments were conducted to determine whether the sulfidated MoS_2 degraded when exposed to air, and its stability in the acidic electrolyte used for the H^+ reduction measurements. To determine the acid stability an air-exposed MoS_2 was tested for its HER catalytic ability prior to sulifidation. Following sulfidation 20 H^+ reduction tests were performed consecutively, the first, second and twentieth of which are shown in Figure 4.14.

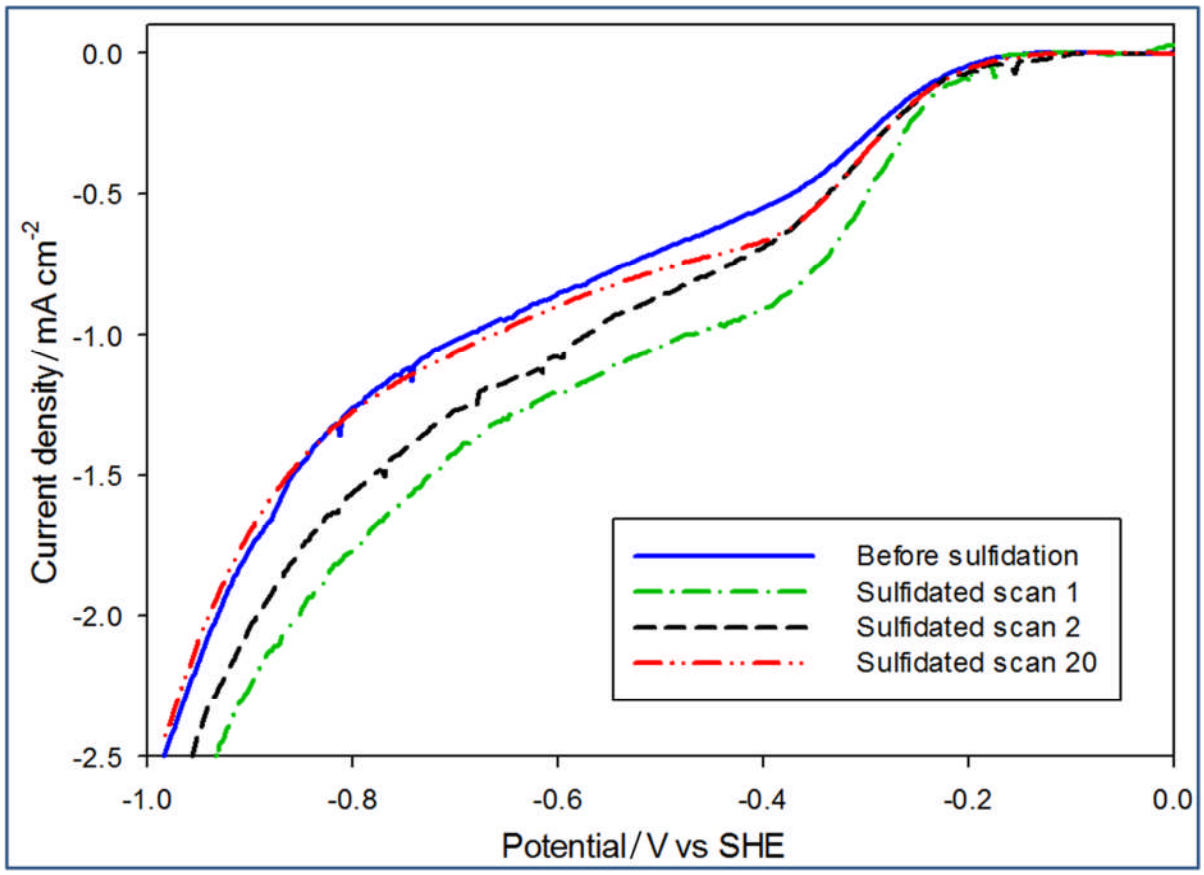

Figure 4.14. To determine the stability of the sulfidated MoS_2 in the acidic electrolyte used for H^+ reduction measurements the catalytic ability was tested prior to sulfidation and 20 times following[180].

It was found that there is a significant degradation in peak current between the first and second measurement, with the peak current density decreasing from -0.98 mA cm^{-2} to -0.65 mA cm^{-2}. However, the onset potential remained unchanged for all the tests at -0.22 V SHE, and the peak current was stable between measurement 2 and measurement 20. It was concluded that following sulfidation a voltammetric sweep is required to stabilise the electrode, but following this the electrode is stable in the 2 mM $HClO_4$ electrolyte. For this reason the voltammogram produced from the H^+ reduction measurements was never used when comparing the catalytic ability of these electrodes in this work.

To determine the effect of atmospheric oxygen on sulfidated MoS_2 a sample was voltammetrically cycled from 0 V Ag/AgCl to -1.6 V in 2 mM $HClO_4$ before and after sulfidation. The sample was left exposed to ambient conditions for three weeks, and it was re-tested for H^+ reduction catalytic ability three times over that time, before being re-sulfidated.

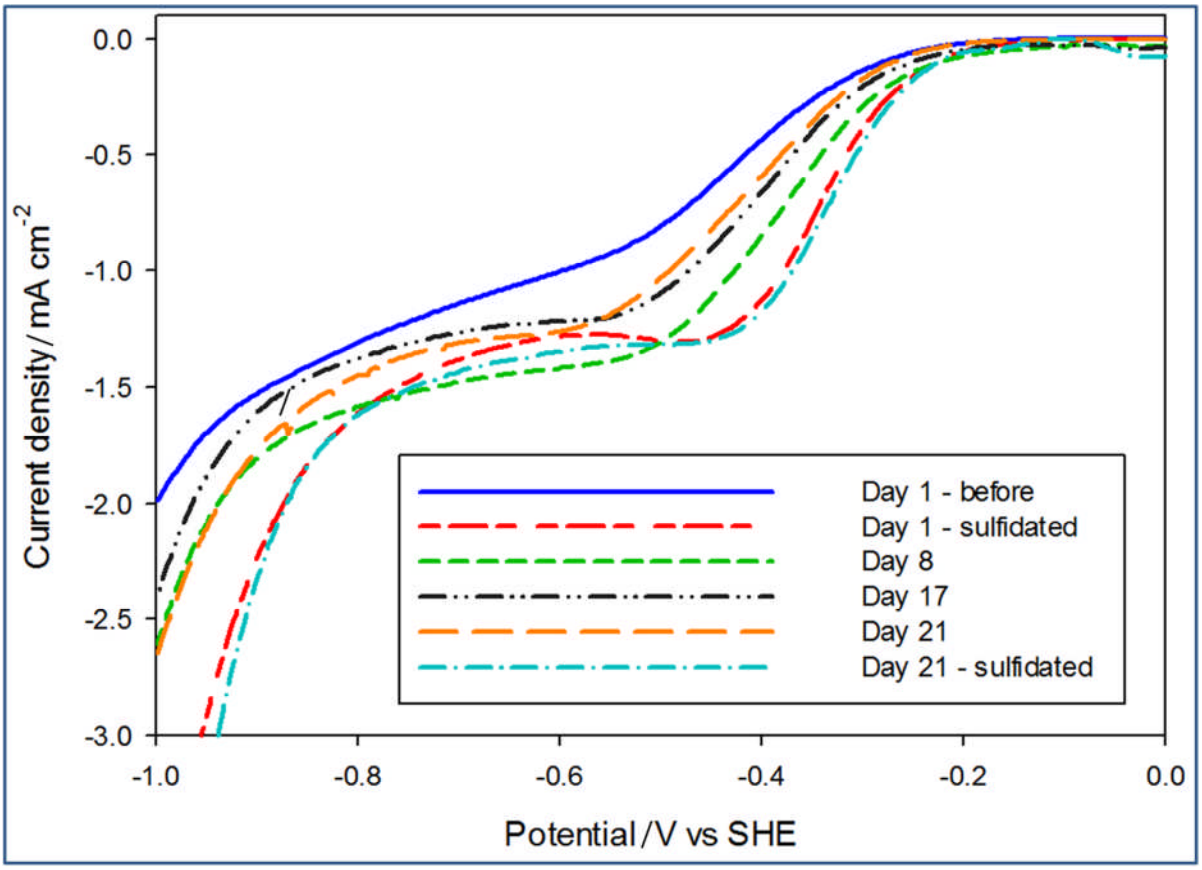

Figure 4.15. As a measurement of the stability of the sulfidated MoS_2 in air a sample H^+ reduction measurements were performed before and after sulfidation and then three times over the next three weeks. The sample was then re-sulfidated[180].

As with previous sulfidations the immediate after measurement was superior to the before measurement, with the peak current density increasing from -0.88 mA cm^{-2} to -1.30 mA cm^{-2}, and the onset potential decreasing from -0.28 V SHE to -0.22 V SHE. The day 8 measurement had a similar onset potential to the post-sulfidation measurement, and a higher peak current density at -1.39 mA cm^{-2}. However, the peak current was at 0.15 V higher overpotential indicating the reaction kinetics had slowed. The Day 17 measurement had the onset potential delayed 0.02 V compared to immediately post-sulfidation and a

reduced peak current density of -1.20 mA cm^{-2}. After three weeks the onset potential was 0.05 V delayed and the peak current was at 0.17 V higher overpotential compared to first post sulfidation measurement. These results showed that the sulfidated MoS_2 is re-oxidised by the atmosphere, and there is a corresponding drop in HER catalytic performance. After the 21 day measurement the sample was re-sulfidated and following this the HER catalytic performance was in close correlation with the day 1 measurement indicating the sulfidation process can be used to repeatedly cycle air-exposed MoS_2 without a permanent decrease in HER catalytic performance.

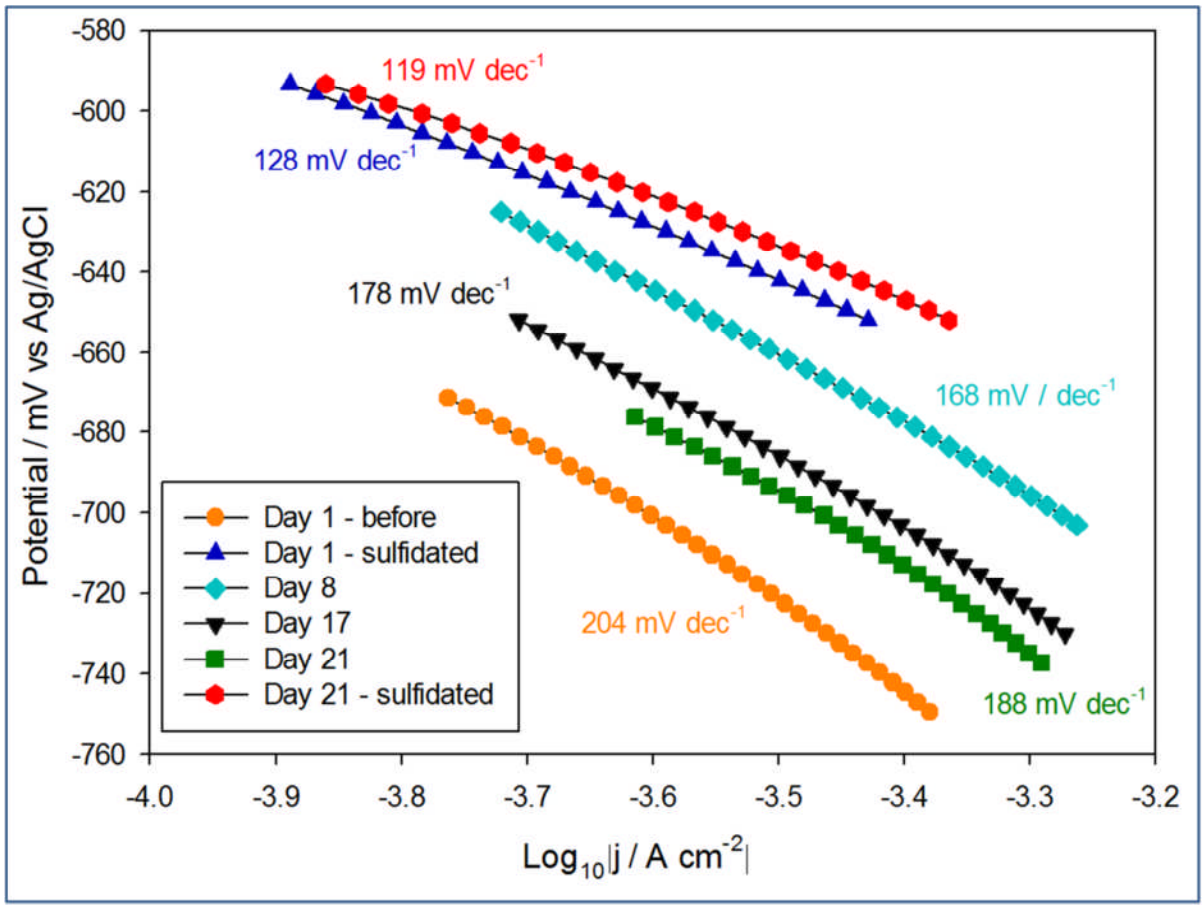

Figure 4.16. Tafel slopes derived from the degradation measurements presented in Figure 4.15[180].

The Tafel slopes confirmed that the efficacy of the MoS_2 for the HER is degraded by exposure to air. After the three weeks the Tafel slope was still lower than in the crystals' (pre-sulfidated) air-exposed state, however both the onset potential and current were inferior to the original before sulfidation H^+ reduction test. The Tafel slope before sulfidation was 204 mV dec^{-1}, and decreased to 128 mV dec^{-1} after the deposition. The slope steadily increased with each subsequent measurement to 188 mV dec^{-1} after the three week period. After the final air-exposed measurement the sulfidation process was repeated and the catalytic ability remeasured. It was found that the performance was in close agreement with the day one sulfidation, with a Tafel slope of 119 mV dec^{-1}.

4.3.3 Photoelectrochemistry

The performance of the sulfidated MoS_2 as a photoelectrode was evaluated using a Hg-Xe lamp positioned to illuminate the crystal with AM 1.5 intensity (1000 W m^{-2}) through a quartz window during the voltammetric measurements. As with previous measurements the HER catalytic performance was measured before (Figure 4.17) and after (Figure 4.18) sulfidation. However, for this experiment the before and after measurements were also performed under dark, light and interrupted light conditions in order to elucidate the effect of the sulfidation on the photoelectrochemical performance of the electrodes.

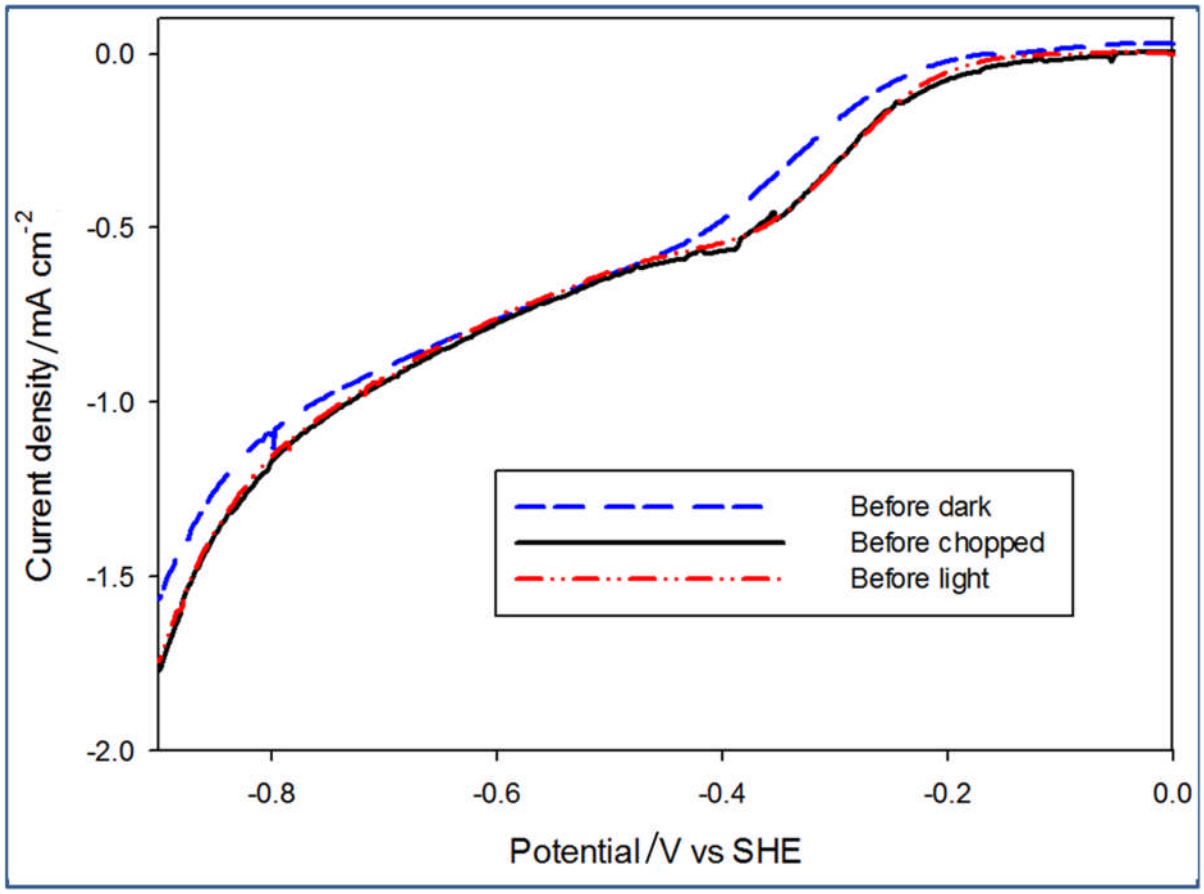

Figure 4.17. H^+ reduction performed on air-exposed $MoS_xO_{(2-x)}$ under dark, light, and interrupted conditions[180].

Before sulfidation the light caused only a slight increase in peak current density from -0.51 mA cm^{-2} to -0.55 mA cm^{-2}, and the interrupted measurements showed peaks and troughs of only ≈ 31 µA cm^{-2}. These measurements indicate that the atmospherically-aged MoS_2 is a poor candidate for photoelectrochemistry as the much of the incident light is not converted into an increased current. As such these degraded electrodes are not capable of spontaneous HER driven by illumination.

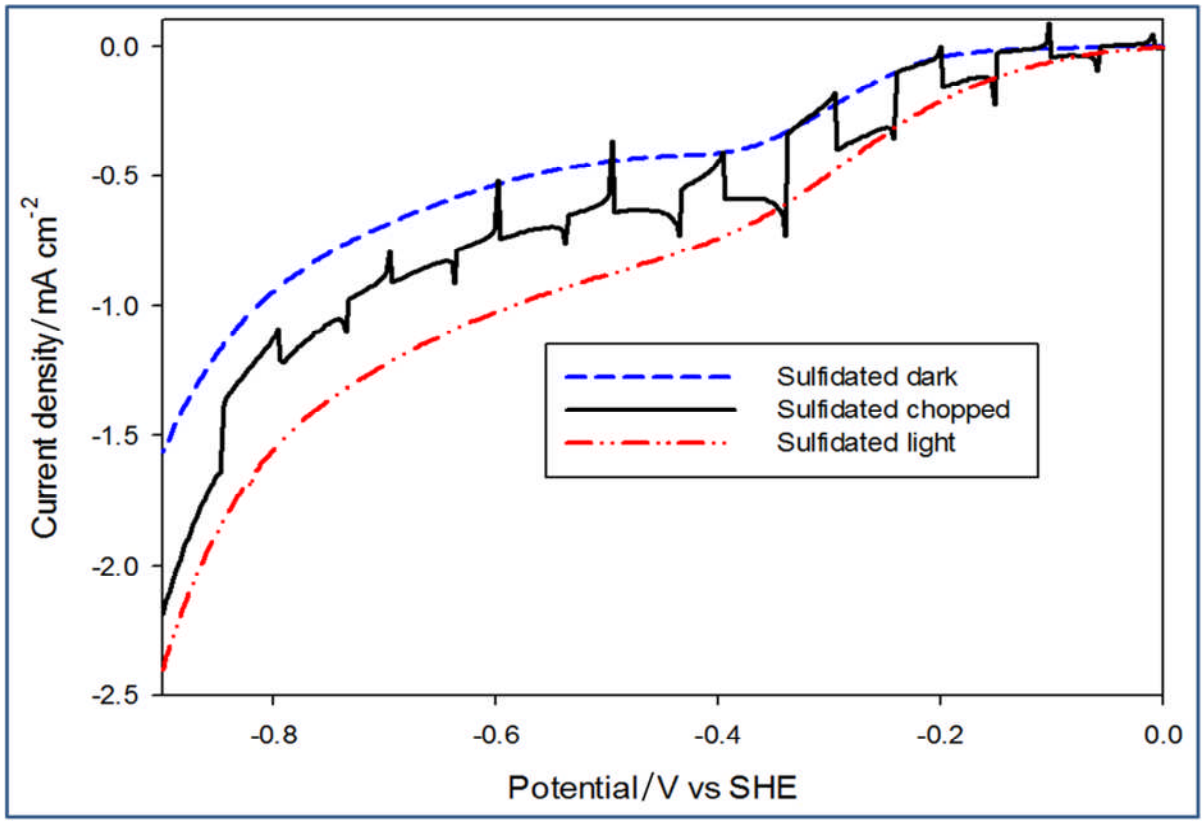

Figure 4.18. H^+ reduction performed on sulfidated MoS_2 under dark, light, and interrupted conditions[180].

Following sulfidation exposure to light led to an increase in peak current from -0.40 mA cm^{-2} to -0.81 mA cm^{-2}, and the difference between the peaks and troughs during the interrupted condition were ≈ 10 times that of the air-exposed state at ≈313 µA cm^{-2}. The onset potential also moved to lower overpotentials at 0.09 V SHE with illumination, and -0.23 V SHE in the dark. This is ascribed to illumination providing additional applied potential as a result of separating charge carriers in the sulfidated MoS_2. This was not observed in the pre-sulfidated state implying that the sulfidation process has altered the material bandgap to a value more applicable for PEC HER[182,183]. These results confirm the efficacy of this technique for the sulfidation of atmospherically-degraded MoS_2 as the air-aged state has

little photoresponse, and following sulfidation illumination caused an increase in peak current and a decrease in the overpotential required to initiate the HER as compared to measurements performed in the dark. Thus showing that ambient conditions prevent these samples functioning as photoelectrodes, and sulfidation restores their ability to convert photons into current.

4.4 Homogenisation of the Surface Morphology

SEM images of the sulfidated surfaces were taken and compared to the images taken following fabrication to elucidate the effect of the sulfidation on the surface morphology (Figure 4.19).

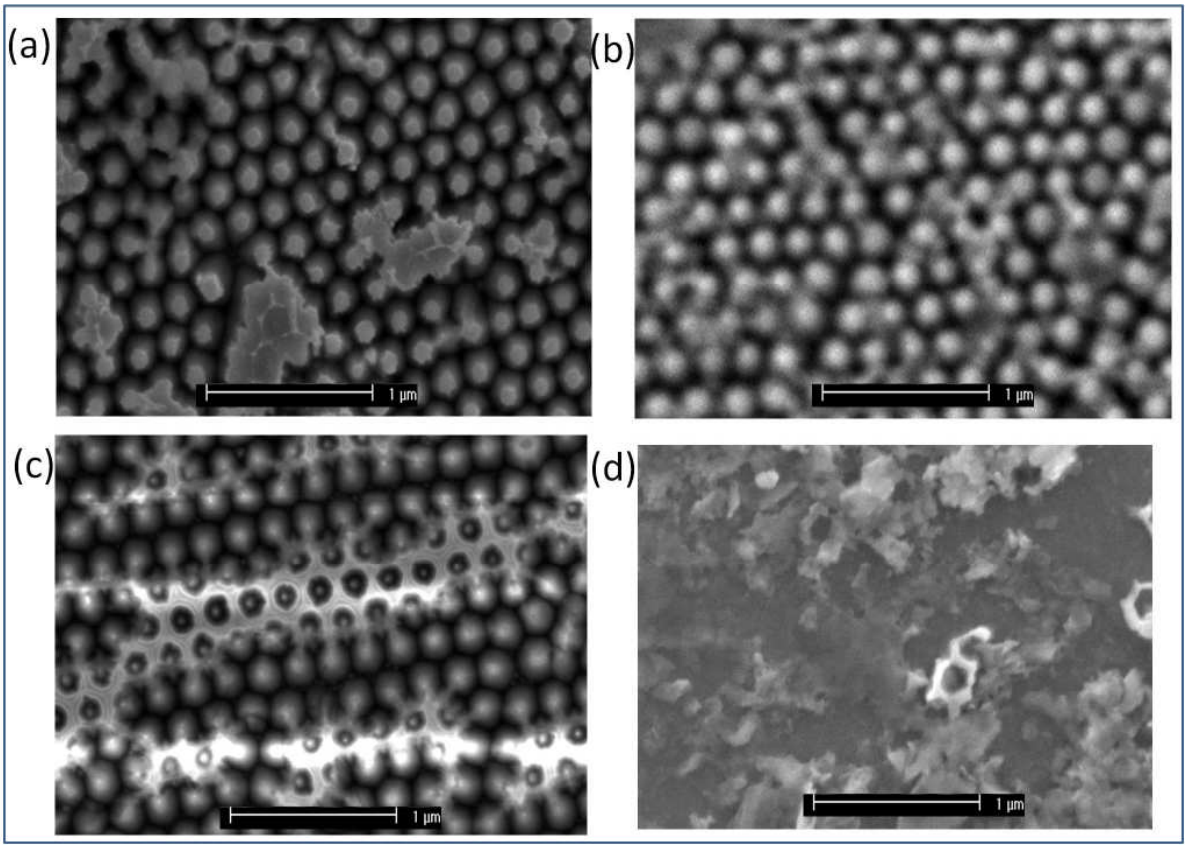

Figure 4.19. SEM images showing the effect of sulfidation on the surface of nanopatterned MoS_2. (a) Sample 1 before sulfidation: the features are individual and distinct, and (b) after 2 sulfidations: the features remain distinct. (c) Sample 2 before sulfidation: the features are individual and distinct, and (d) after 8 sulfidations: the surface has homogenised though some features remain visible[180].

It was found that repeated sulfidations caused a homogenisation of the sample surface. After 2 sulfidations the individual features were still clear and distinct, however after 8 the features were mostly obscured with only some traces remaining showing the pre-sulfidation morphology. It was therefore concluded that although the sulfidation can be used to regenerate atmospherically-aged electrodes (Figure 4.15) repeated sulfidations

cause the nanostructure to lose definition. The filling of gaps between the pillars, which builds up over repeated sulfidations, could explain the lowering of current observed (Figure 4.12) as fewer catalytically active edge sites are available, provided that sufficient active sites are lost over a diffusionally-relevant area to effect a change in diffusional character of the nano-array from Case IV[87]. However, this homogenisation requires multiple sulfidations, and the remaining edge sites appear to have improved catalytic properties as evidenced by the faster reaction kinetics and earlier onset potentials. Indicating this method would be well suited to robust morphologies, or electrodes that do not require multiple re-use.

5.0 Deposition Solvent Composition Effect on the PEC Properties of $ZnFe_2O_4$

This chapter details experiments to determine the effect of the properties of the deposition solvent on the final morphology of electrodes deposited by AACVD. Ethanol and methanol were used as deposition solvents as the physical properties that determine the aerosol droplet size are similar, but they have dissimilar enthalpies of combustion. Thereby the enthalpy of combustion was isolated as the variable under investigation. Eleven deposition solutions were used varying 10 vol. % increments from pure methanol to pure ethanol.

The surfaces of the electrodes were imaged by SEM and a drastic, sequential shift in morphologies was observed. Electrodes deposited using predominantly methanol as the solvent were compact and blocky. On the other hand predominantly ethanol deposited electrodes had textured nanostructures with small features. This was taken as evidence that the nucleation pathway shifted from heterogeneous to homogeneous as the percentage of ethanol in the solvent increased. The shift in pathway was ascribed to the more exothermic enthalpy of ethanol as compared to methanol providing additional energy to aid in the decomposition of the precursor during the vapour phase.

The photoanodic properties of the electrodes were tested by the OER in 1 M NaOH under illumination and in the dark. The quantum efficiency was also measured by IPCE analysis. It was expected that the electrodes PEC performance would be proportional to the percentage ethanol in the solvent, as a higher percentage ethanol encouraged homogenous nucleation and thus less compact morphologies. The decreased feature size in the

homogenously deposited morphology resulted in a shorter path length for the photogenerated charge carriers, and hence reduced recombination with the electrode. The j-V and IPCE measurements supported this hypothesis as the photocurrent density, and conversion efficiency increased with percentage ethanol in the deposition solvent.

5.1 Electrode Deposition

$ZnFe_2O_4$ films were deposited onto FTO glass by AACVD as described in Section 2.1.6. In brief the $ZnFe_2O_4$ precursor solution ($[Fe_2(acac)_4(dmaeH)_2][ZnCl_4]$) was mixed with a vapourisable and combustible solvent. An ultrasonic humidifier was used to convert the precursor solution and solvent into an aerosol which was carried into a heated deposition chamber by a flow of air. Once transferred from the humidifier to the deposition chamber the aerosol was blown onto a FTO substrate positioned perpendicularly to the air flow. Other AACVD depositions have utilised set-ups with the substrate parallel to the air flow, however the parallel set-up often results in an uneven deposition as the flow direction results in a thickness gradient[184,185]. The perpendicular arrangement produces a more even film by transporting the material undergoing deposition to a point several centimetres above the substrate. The material then expands in a cone so as to be wider than the substrate, thereby depositing over the substrate evenly[185]. Once within the deposition chamber an increase in temperature causes the precursor to decompose into $ZnFe_2O_4$, which forms a layer on the FTO substrate[186].

The nanostructure formed by the $ZnFe_2O_4$ on the FTO substrate is determined by the precursor decomposition pathway. In a heterogeneous process the precursor-aerosol mixture impacts the heated substrate surface and the decomposition to the product occurs in contact with the substrate. In this case the thin film is produced by this adsorption and decomposition of precursor on the substrate surface[83,84]. The alternative is a homogeneous process where the decomposition occurs in the vapour-phase so that the product is formed before impacting the substrate. Homogenous deposition is associated with less compact, higher surface area nanostructures[83].

The decomposition pathway can be shifted toward homogeneous by using a reactive carrier aerosol which exothermally oxidises when heated. The oxidation of the solvent generates steep local temperature gradients that encourage vapour-phase decomposition and particle formation. Within the high-temperature deposition chamber the carrier aerosol droplets ignite and react exothermically. This additional energy input results in the vapourization and condensation of nanoscale particles within the thermal boundary region of the reacting droplets. The formation and growth of the nanoscale particles occurs entirely within the thermal boundary region of individual droplets. Following homogenous combustion the synthesised $ZnFe_2O_4$ nanoparticles descend from the gaseous state onto the substrate surface resulting in the thin, nanostructured films[83].

AACVD in practice follows either a homogenous, heterogeneous, or a combination of both pathways. As the physical properties of the solvent (such as droplet diameter, density, and enthalpy of combustion) influence the deposition pathway and hence the morphology of the deposited film the selection of an appropriate solvent is non-trivial[82]. To assess the

effect of the solvent on deposition pathway $ZnFe_2O_4$ thin films were deposited from solvent solutions consisting of pure ethanol and pure methanol as well as mixtures of both in 10% by volume increments. Therefore in total eleven different solvent compositions were used to deposit $ZnFe_2O_4$ thin films, and the surface morphology and photoelectrochemical properties of each were measured as a means of comparison.

5.2 XRD Identification

As the $ZnFe_2O_4$ was synthesised in-situ it was necessary to determine that the desired compound had been successfully deposited. As such following deposition a selection of films were analysed, a typical diffraction pattern is presented in Figure 5.1.

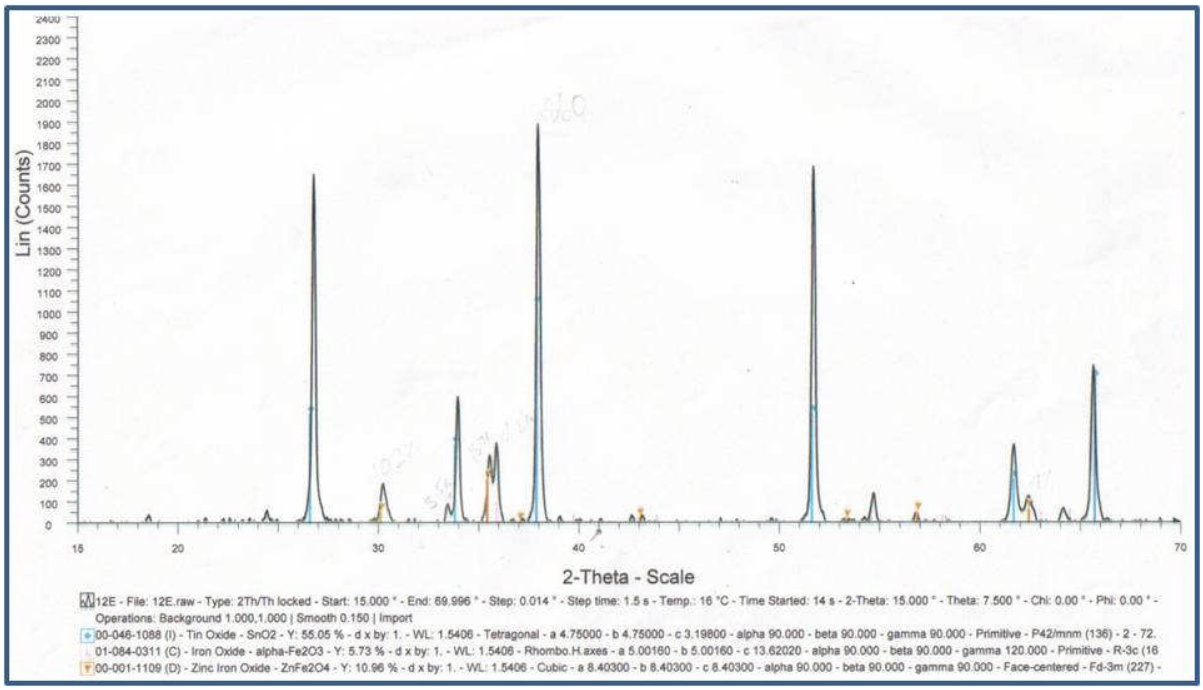

Figure 5.1. An XRD diffraction pattern of the thin film deposited by AACVD from a $[Fe_2(acac)_4(dmaeH)_2][ZnCl_4]$ precursor. The spectra confirmed that the film was comprised of $ZnFe_2O_4$, although it showed that α-Fe_2O_3 was also present in the film.

The XRD diffraction pattern identified that the film was comprised of a mixture of $ZnFe_2O_4$ and α-Fe_2O_3. The presence of the α-Fe_2O_3 showed that the precursor does not always decompose to the bimetallic oxide, sometimes favouring the simpler metal oxide. The presence of the SnO_2 is due to the FTO substrate.

5.3 Aerosol Physical Properties

As the morphology of the deposited materials is influenced by the solvent physical properties appropriate solvent choice can be used to bias towards a desired texture[187,188].

To this end the aerosol droplet size and enthalpy of combustion of the ethanol / methanol mixtures was calculated.

5.3.1 Aerosol Droplet Size

The aerosol droplet size and distribution is influenced by the physical properties of the solvent such as surface tension, density, and viscosity. The aerosol droplet size of the ethanol/methanol compositions was calculated by Eq. 5.1[189].

$$\boldsymbol{d_a = \left(\frac{\pi\sigma}{\rho f^2}\right)^{1/3}} \qquad \text{(Eq. 5.1)}$$

Where d_a is the aerosol droplet diameter, σ is the surface liquid tension, ρ is the liquid density, and f is the frequency of the ultrasonic oscillator. The densities of methanol and ethanol were measured using a density flask of volume 10.175 ml and found to be 797.6 kg m^{-3} and 791.7 kg m^{-3}, respectively. These values were slightly higher than that of the pure methanol (786 kg m^{-3}) and ethanol (784 kg m^{-3})[190,191]. The difference between the measured and literature values could be due to the water impurities in the solvents used.

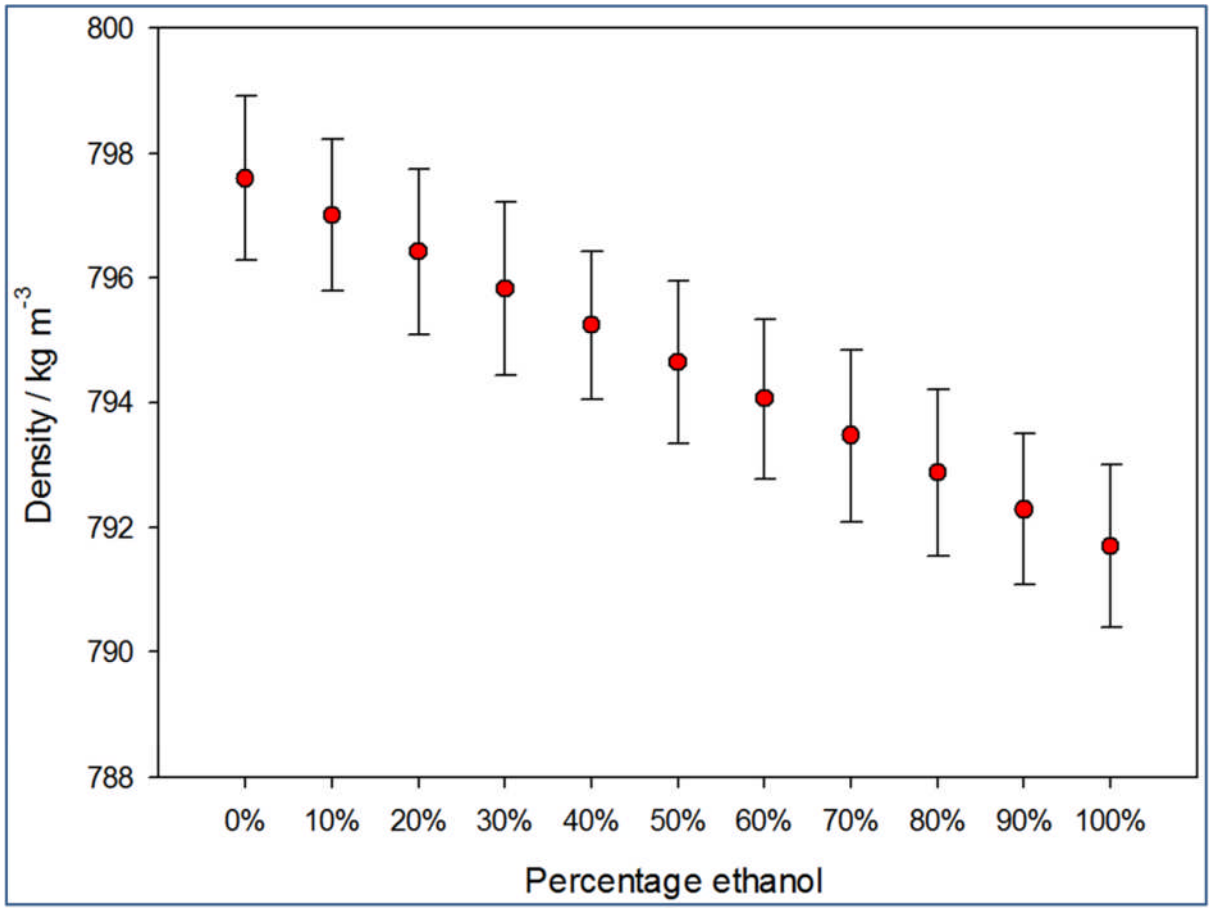

Figure 5.2. The density of the deposition solution vs percentage of ethanol. The solution was pure ethanol and methanol and so the percentage methanol was the inverse of the percentage ethanol[68].

The surface tension of the deposition solvents was measured using a Du Nouy tensiometer as per Section 2.3.10[157]. The surface tension of methanol and ethanol was found to be 22.12 mN m^{-1} and 21.88 mN m^{-1}, respectively. These two values are in line with the reported ones of 22.95 mN m^{-1} and 22.31 mN m^{-1} respectively[192]. The frequency of the ultrasonic oscillator was a constant 40 kHz.

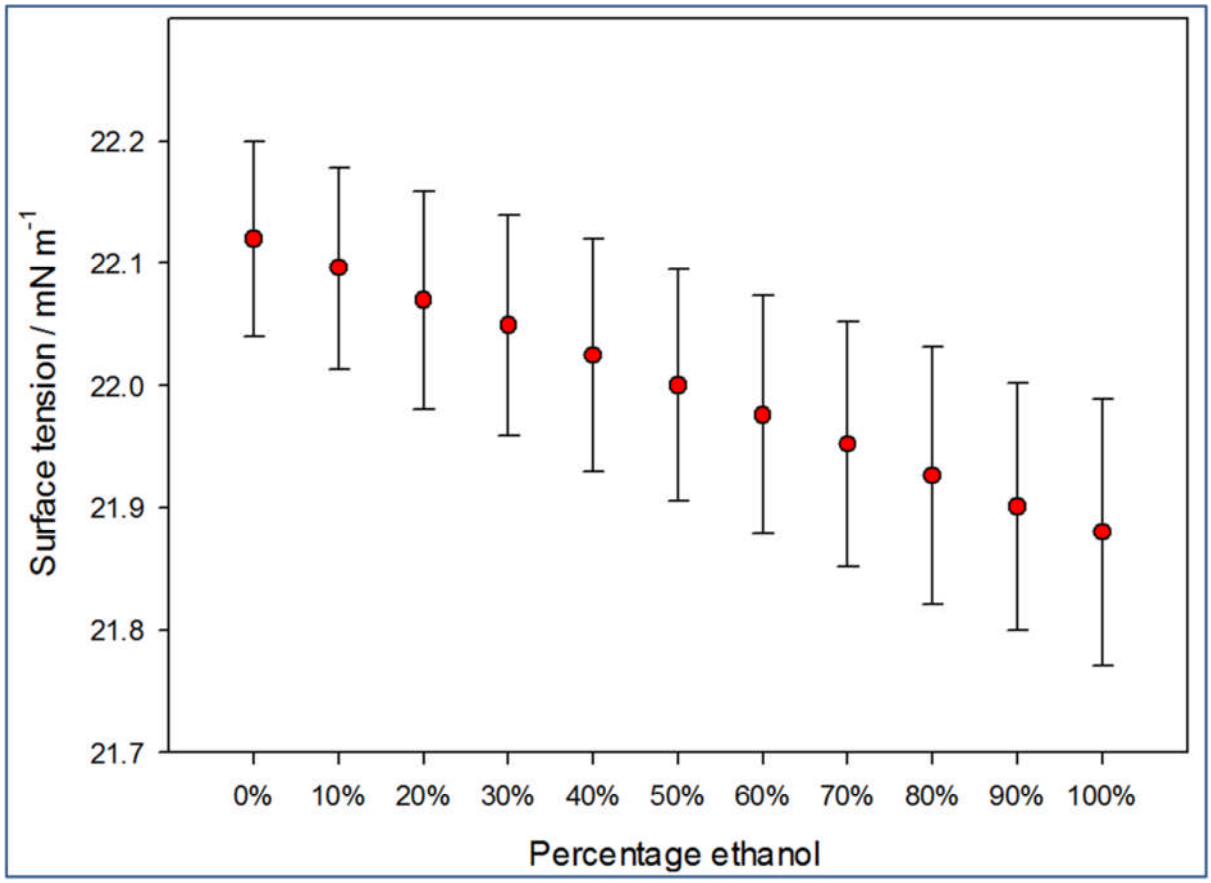

Figure 5.3. The surface tension of the deposition solution vs percentage of ethanol. The solution was pure ethanol and methanol and so the percentage methanol was the inverse of the percentage ethanol[68].

Having calculated the surface liquid tension and density of the methanol / ethanol solutions the aerosol droplet diameter could be calculated according to Eq. 5.1. The diameter of the pure ethanol aerosol droplets was calculated as 37.90 µm, and pure methanol was 37.86 µm (Figure 5.4).

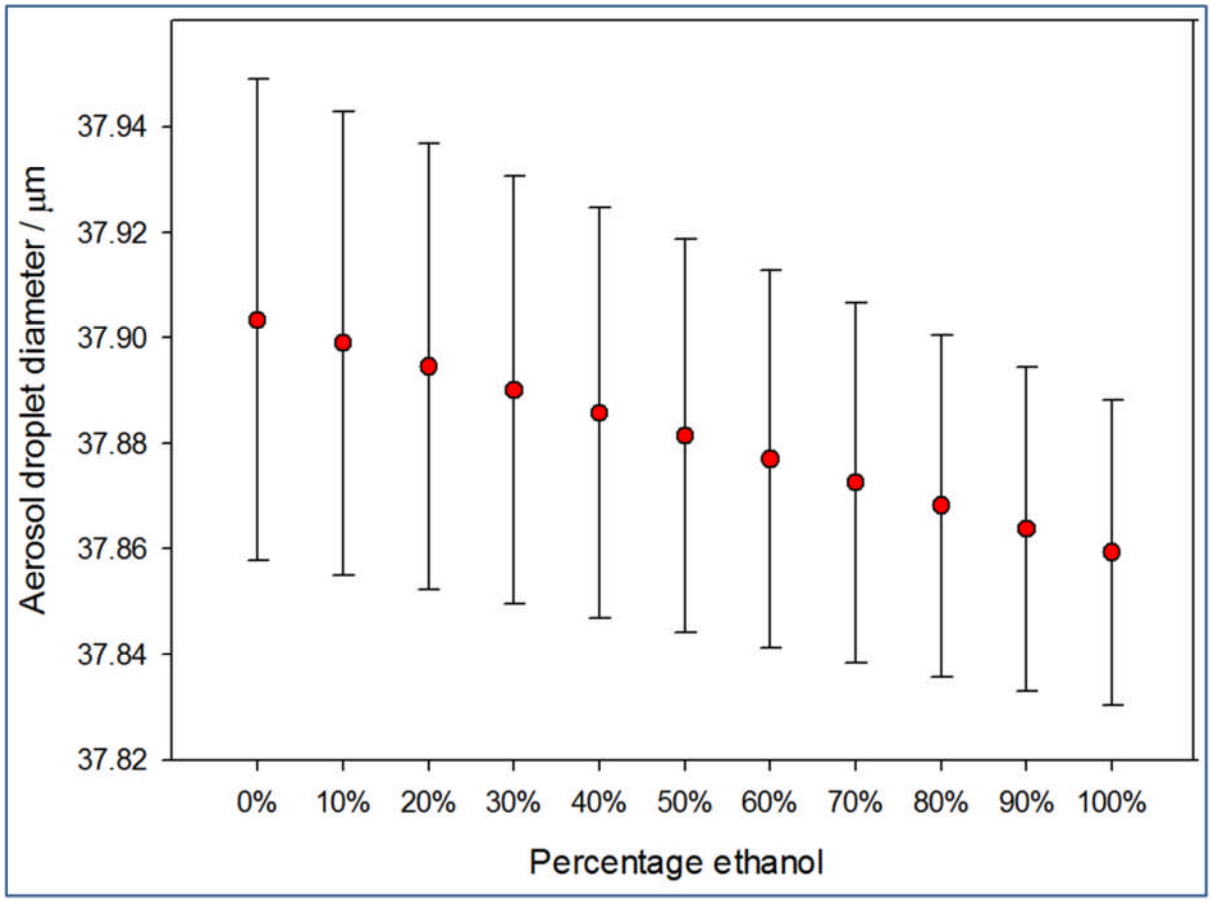

Figure 5.4. The aerosol droplet diameter against percentage ethanol of the deposition solvent used for the AACVD of $ZnFe_2O_4$. The diameter differed by only 0.04 µm between the pure solutions[68].

As shown in Figure 5.4 the aerosol droplet size decreased with an increase in ethanol content in the deposition solution, however the decrease of estimated aerosol droplet size was very small at 0.04 µm. This measured difference was considered insignificant and therefore another factor must dominate the change in morphology of the $ZnFe_2O_4$ films wrought by systematically shifting the solvent between ethanol and methanol.

5.3.2 Solvent Enthalpy of Combustion

Given the small difference between solvents in terms of aerosol droplet diameter the shift in morphology was ascribed to the enthalpy of combustion of the solvent (ΔH_c). The enthalpy of combustion is another key parameter to AACVD as the additional energy provided by a highly exothermic enthalpy of combustion can shift the nucleation from a heterogeneous to homogeneous process[88]. The nucleation pathway is a determining factor in the final morphology of the deposited material in an AACVD process. As such, by altering the chemical kinetics and thermodynamics of the processes occurring in the deposition chamber the enthalpy of combustion of the solvent was in part responsible for the composition of the deposited material[193].

The enthalpies of combustion of the 100% conditions were calculated using the enthalpies of formation (ΔH_f) of ethanol, methanol, carbon dioxide and water according to Eq. 5.2.

$$\Delta H_{c\ (reaction)} = \Sigma \Delta H_{f\ (products)} - \Sigma \Delta H_{f\ (reactants)} \qquad \text{(Eq. 5.2)}$$

The enthalpies of formation used are given in

Table 5-1[194].

	Enthalpy of formation / kJ mol^{-1}
Methanol	-201.0
Ethanol	-235.3
CO_2	-393.5
H_2O	-241.8

Table 5-1. The enthalpies of formation used to calculate the enthalpies of combustion of methanol and ethanol[194].

The enthalpy of combustion of ethanol (-1277.17 kJ mol^{-1}) was found to be nearly twice that of the methanol (-676.15 kJ mol^{-1}). The calculated enthalpies of combustions for each of the ethanol / methanol mixtures are provided in Figure 5.5.

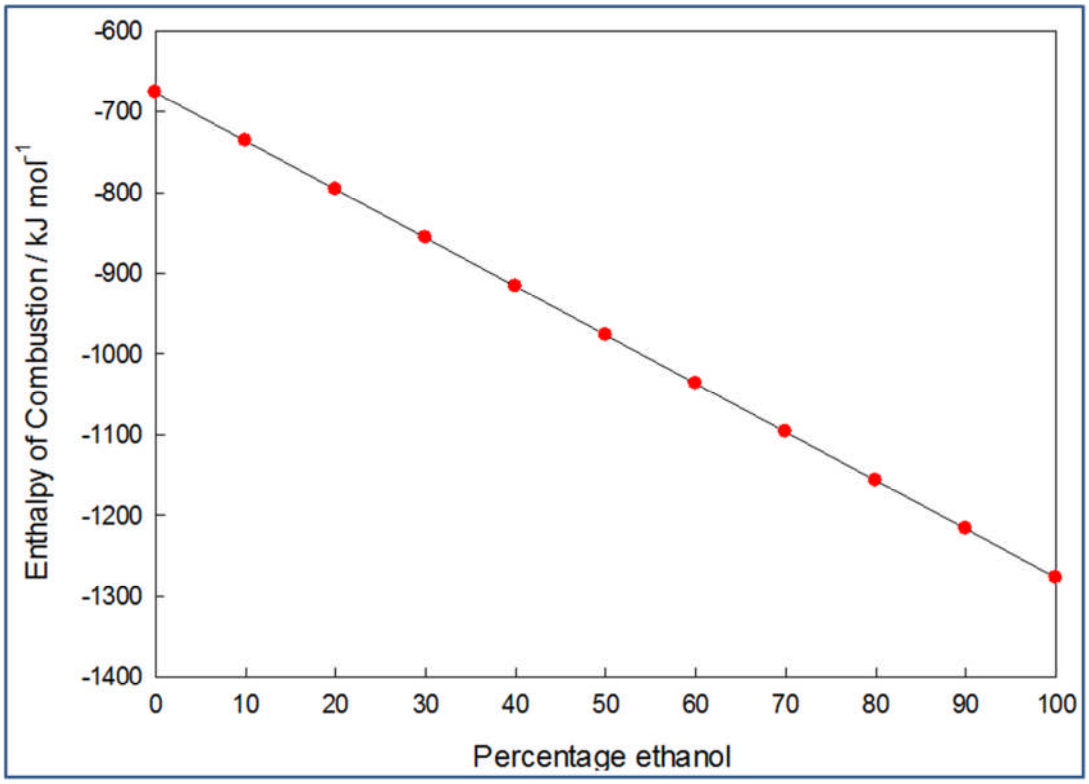

Figure 5.5. The calculated enthalpies of combustion for pure ethanol, pure methanol, and the mixtures of the two which were used as deposition solvents for the AACVD of $ZnFe_2O_4$. The enthalpy of combustion of pure ethanol is nearly twice as exothermic as that of pure methanol[68].

5.4 The Influence of Solvent on Surface Morphology

The eleven thin films deposited at 10 % (by volume) increments between pure ethanol and pure methanol were imaged by SEM to examine the effect of solvent choice on solvent morphology (Figure 5.6).

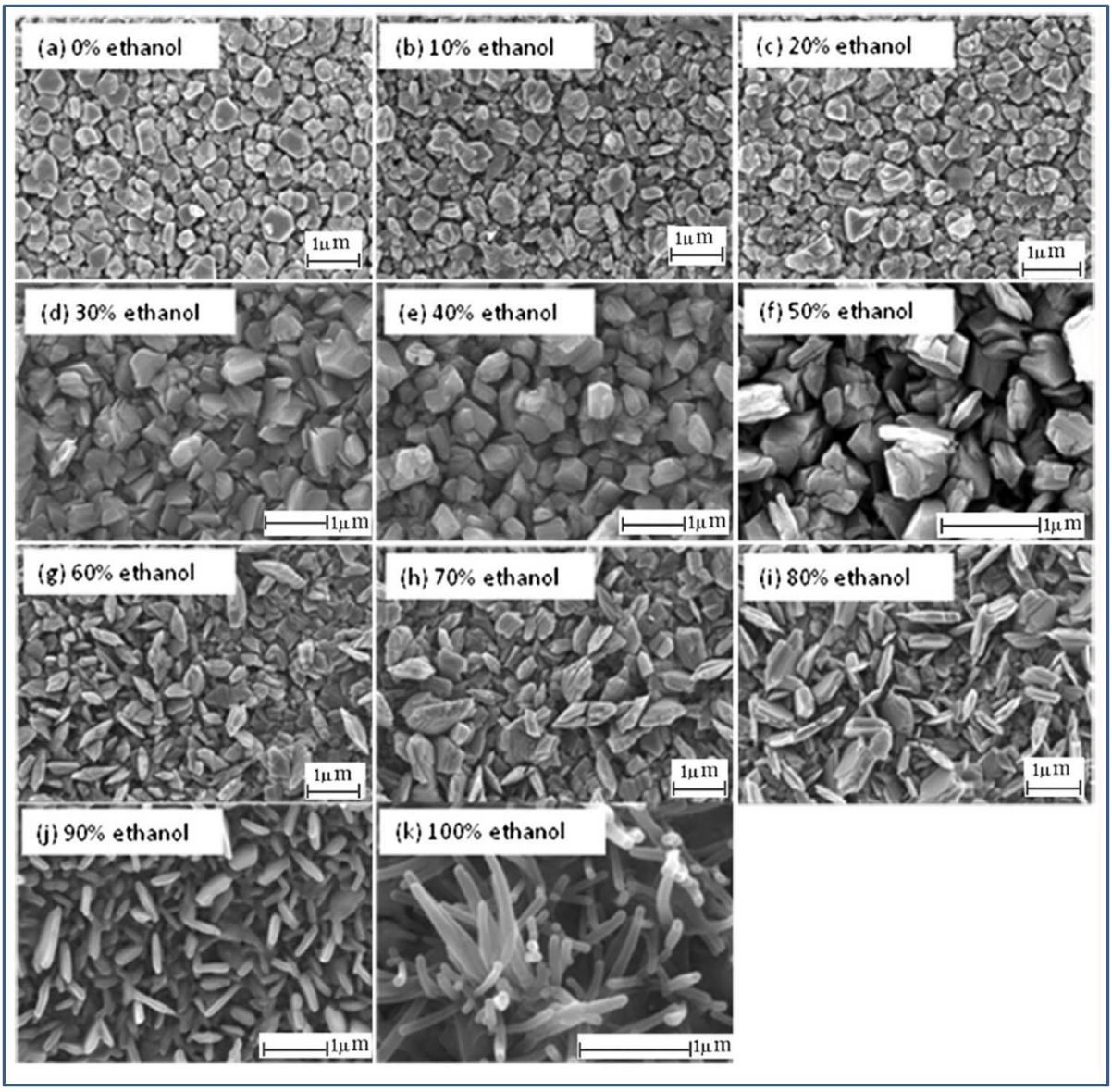

Figure 5.6. SEM images of $ZnFe_2O_4$ deposited by AACVD with the solvent composition changing from 0 % ethanol to 100 % ethanol in 10 % (by volume) increments. The increase in ethanol corresponds to a morphology shift from relatively compact to more textured[68].

The electrode morphologies shown in Figure 5.6 demonstrate that as the vol. % of ethanol is gradually increased in the deposition solution the surface morphology systematically changed from a compact structure to a relatively textured one. The more compact

electrodes are attributed to a heterogeneous nucleation pathway[83]. The most pronounced change in morphology occurred when the vol. % of ethanol was increased from 50 % to 60 %. Prior to this point the films had a blocky compact morphology, at >60 vol.% ethanol in the deposition solution a blade-like structure formed instead. At 80 vol. % ethanol the electrode morphology showed early signs of the rod-like features apparent at the higher ethanol percentages. These features developed to vertically oriented rod-like structures at 90 volume % ethanol in the deposition solution, and at 100 volume % ethanol as the deposition solvent the morphology had fully shifted to nanorods. The nanorods were over 1 µm in length and were randomly orientated on the FTO substrate surface.

Figure 5.6 confirmed that the solvent selection has a pronounced effect on the nanostructure of the deposited films. By plotting feature size in the deposited film against the metrics determined in section 5.3 it can be seen that the features shrink considerably between 50 and 70 vol. % ethanol (Figure 5.7). The average feature size was defined as the average radius of the individual features. In the case of nanorod morphology (present only in the 100 vol. % ethanol deposition) the average radius of the cross-section of the nanorods was taken as the feature size.

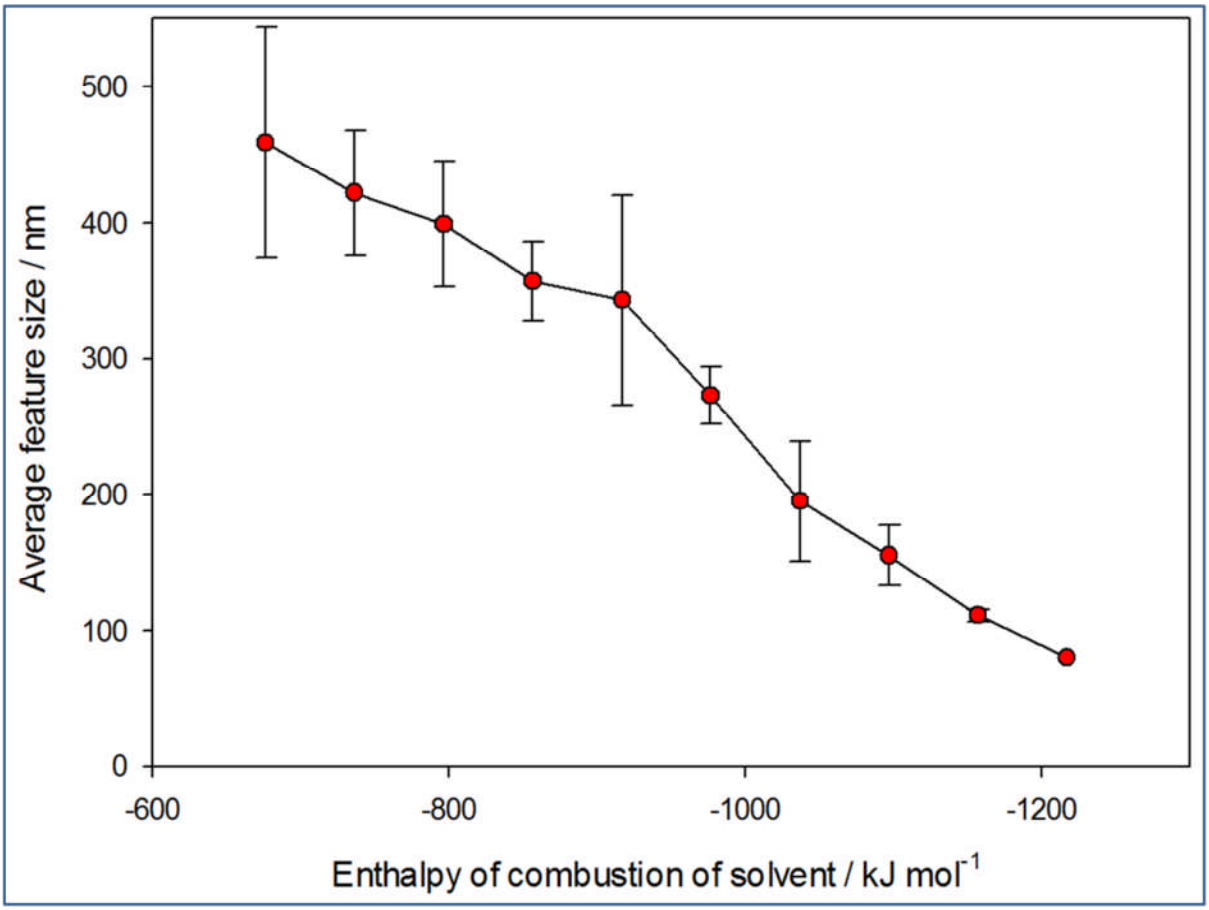

Figure 5.7. Average feature size of the deposited films against the enthalpy of combustion of the solvent used during deposition. The decrease in average feature size corresponds to a more exothermic enthalpy of combustion of solvent, which was the result of a higher volume of ethanol[68].

The sharp decrease in feature size that begins at 50 vol. % ethanol is attributed to the deposition pathway starting to shift from heterogeneous to homogeneous as the proportion of ethanol increases. The examination of the solvent physical properties determined that the aerosol droplet size differed only 0.04 µm between the different solutions, as such the drastic change in morphologies between 100 vol. % methanol and 100 vol. % ethanol solvents is not attributed to this factor. However, the enthalpy of

combustion of ethanol was almost twice that of methanol and the additional energy ethanol provided during the precursor decomposition was deemed responsible for the shift in deposition pathway. Figure 5.8 shows a schematic representation of how the solvent enthalpy of combustion influences nucleation during the AACVD process.

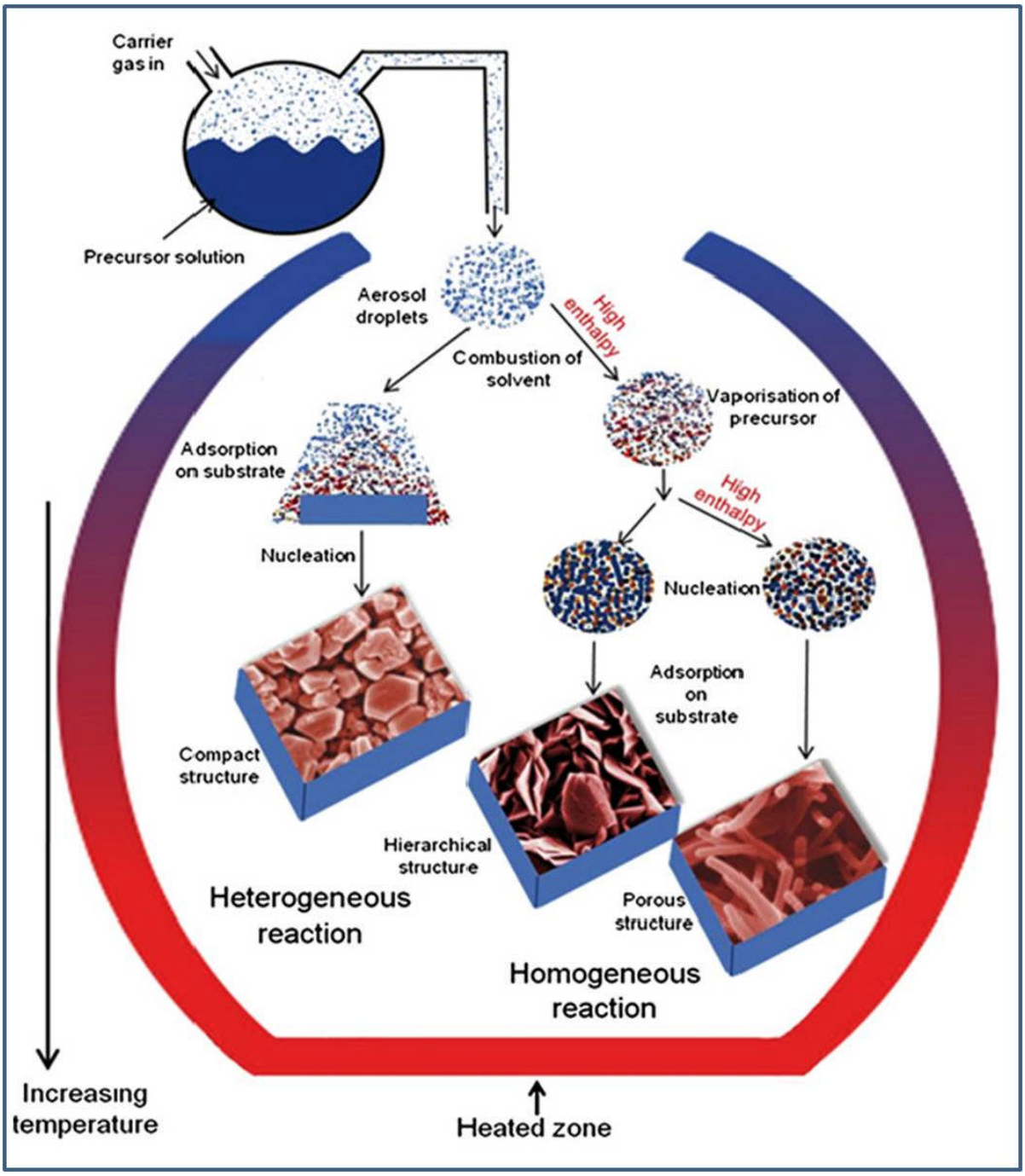

Figure 5.8. A schematic representation of the conditions that resulted in homogeneous or heterogeneous reaction pathways during the deposition of $ZnFe_2O_4$ electrodes by AACVD[68].

As depicted in Figure 5.8 preparation of $ZnFe_2O_4$ electrodes consisted of precursor solution which was converted to aerosol by placing a round-bottomed flask in a humidifier. Air was

used as a carrier gas to transport the vapourised precursor solution to the deposition chamber. A hotplate beneath the deposition chamber established a temperature gradient from the substrate surface to the gas phase with the aerosol travelling from cool to hot. The distance between the delivery tube and substrate was maintained at 10 cm, and the temperature was recorded as increasing from 65°C at the end of delivery tube to 450°C at the substrate surface. The aerosol droplets underwent the processes of evaporation, drying, solute precipitation, thermolysis and decomposition to the product after exiting the deposition tube. If this entire process was accomplished prior to impacting the substrate the nucleation was termed homogenous, however if one or more steps occured in contact with the substrate it was heterogeneous[83,185]. Homogenous deposition is known to favour the porous, high surface area nanostructures preferable for photocatalysis, while heterogenous deposition tends to results in more compact morphologies[83,185].

The nucleation pathway is in part subject to the aerosol droplet size and enthalpy of combustion. The aerosol droplet size has been deemed irrelevant in this study due to the insignificant difference between the solvent mixtures, as such the changes to surface morphology evidenced in Figure 5.6 are attributed to the differing enthalpies of combustion of the solvents.

In the heterogenous nucleation pathway depicted in Figure 5.8 the decomposition of precursor does not begin until the precursor solution has been adsorbed on the substrate, resulting in a compact morphology similar to the ones obtained from depositions carried out with higher percentages of methanol. This is ascribed to the lower enthalpy of combustion of methanol. In contrast when ethanol is used as the deposition solvent the

relatively high enthalpy of combustion caused the aerosol droplets to undergo evaporation, vaporization, precipitation and thermolysis in the gas phase between exiting the deposition tube and encountering the substrate. This is attributed to the mechanisms of heat and mass transfer inside the droplets and the surrounding gas[88,193]. As a result of combustion and the decomposition that occur at the droplet level primary particles arise through the thermally induced processes of nuclei formation, collision and coalescence. The primary particles undergo growth and aggregation in the gas phase to form secondary particles[195]. The secondary particle size and size distribution are mainly influenced by the properties of the aerosol droplets. The distribution of secondary particles is not expected to vary significantly in this study as solvents were selected with small discrepancy in aerosol droplet size, as such the enthalpy of combustion is isolated as the variable under investigation. The primary particles and secondary particles adsorb onto the substrate surface producing highly textured nanostructured electrodes with high internal surface area[195]. The formation of $ZnFe_2O_4$ nanorods (Figure 5.6 k) when ethanol was used as the deposition solvent provides evidence that the homogeneous deposition process occurred at 100 vol. % ethanol.

The deposition process shown in Figure 5.6 gradually shifts from heterogeneous to homogenous as the vol. % of ethanol is systematically increased in the deposition solution. It was reasoned that with ethanol as the deposition solvent the aerosol droplets decomposed close to the end of the delivery tube due to relatively more exothermic enthalpy of combustion, resulting in finer nanoscale particles than with methanol as deposition solvent. When the ethanol deposited particles subsequently transfer onto the substrate surface the additional energy and smaller particle size resulted in the nanorod like

morphology[195]. The SEM topographic studies (Figure 5.6) and feature size analysis (Figure 5.7) suggest that the deposition pathway gradually shifted from a heterogeneously predominant to a homogeneous predominant process with the increase of volume % of ethanol in the deposition solution. This is attributed to the considerably more exothermic enthalpy of combustion of ethanol (-1277.17 kJ mol^{-1}) relative to that of methanol (-676.15 kJ mol^{-1}). A solvent possessing a more exothermic enthalpy of combustion provides more thermal energy for precursor decomposition and therefore aids the precursor in fully decomposing in the gaseous phase. It has previously been reported that precursor that fully decomposed before encountering the substrate is able to form highly textured electrodes whereas a precursor that decomposes through a heterogeneous route produces relatively compact electrodes[83,185]. The highly textured electrodes are expected to better perform photocatalytic water oxidation (OER) as they have higher rates of light absorption, better separation of charge carriers, and a higher surface area for the reaction[97,99,196].

5.5 Influence of Solvent Composition on PEC Properties

The poor photogenerated charge carrier collection and slow interfacial charge transfer reactions at the semiconductor/electrolyte interface inhibit many semiconductor photoanodes, including $ZnFe_2O_4$, ability to oxidise water[43]. The short diffusion length of photogenerated holes combined with brief lifetimes results in a significant amount of photogenerated holes being lost via bulk recombination[97,98]. Many holes that avoid recombination in the space charge region and are transferred to the

semiconductor/electrolyte interface are then lost by surface recombination with electrons[97,98]. As a result oxygen evolution is orders of magnitude slower than the average hole lifetime. The OER happens on a timeframe of ≈ 0.1 – 10 s^{-1}, while the lifetime of holes has been measured as 10 ps in hematite electrodes[48,49]. A nanostructured morphology improves the hole collection at the semiconductor/electrolyte interface by reducing the individual feature size to be comparable to the space charge width as well as increasing the surface area available for light harvesting[99]. When the electrode texture is altered in such a way the bulk recombination is reduced and the hole collection efficiency under illumination is increased[99].

The SEM analysis (Figure 5.6) found compactness of the electrode was proportional to percentage methanol in the deposition solvent. As such it was expected that the electrodes deposited with high proportions of ethanol would yield better photocatalytic results.

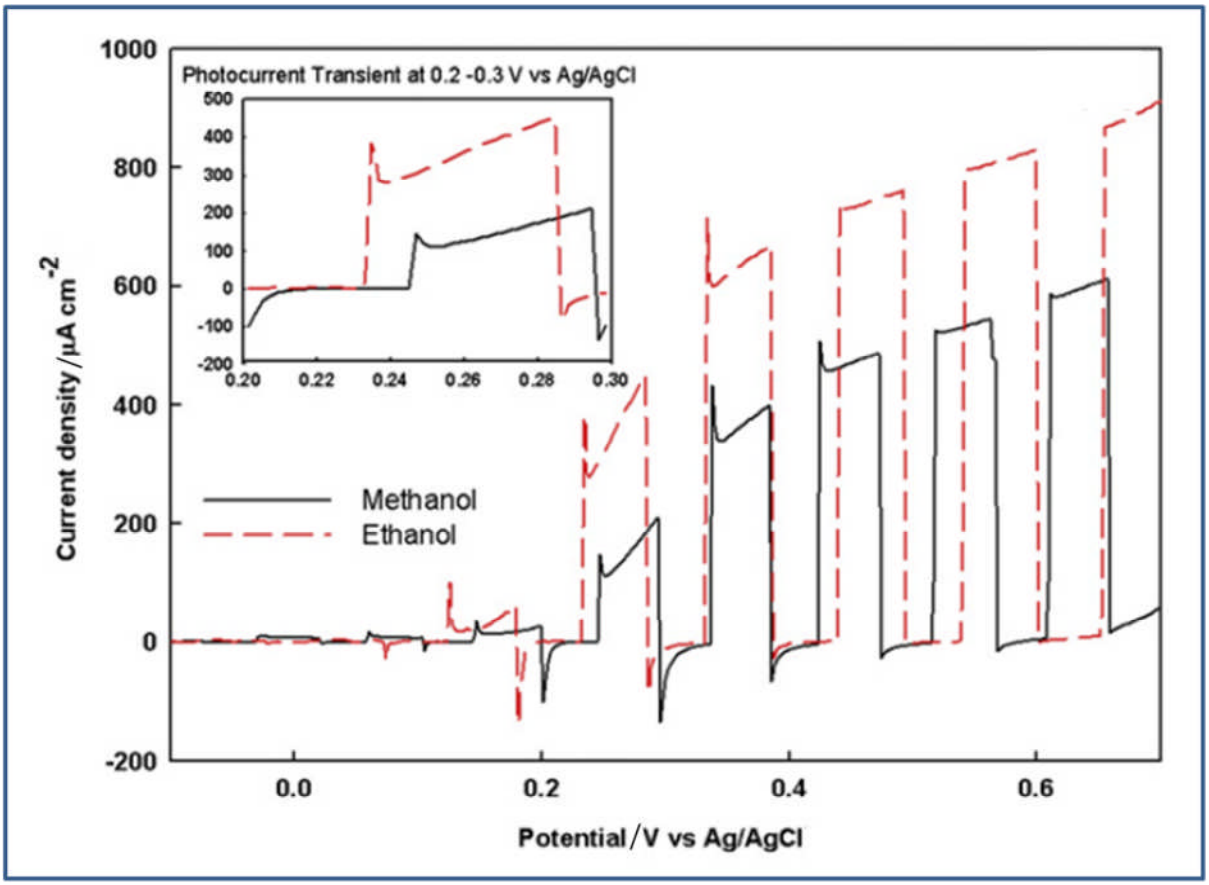

Figure 5.9. A photocurrent density comparison of the films deposited using pure ethanol and pure methanol as the deposition solvents. The light was interrupted during measurement to observe the difference between light and dark current[68].

Figure 5.9 confirmed this to be the case by taking j-V measurements of the electrodes deposited with pure ethanol and pure methanol as solvent between -0.4 V and +0.7 V Ag/AgCl in 1 M NaOH electrolyte. These are used for comparison as they produced the least and most compact electrodes, respectively. It was found that the photocurrent density of the ethanol deposited electrode was triple that of the methanol deposited electrode at 0.25 V vs Ag/AgCl, with photocurrent densities of 344.4 µA cm^{-2} and 104.2 µA cm^{-2}, respectively. This potential was used for the comparison of photocurrent densities as it

correlates to 1.27 V SHE, taking into account the 0.826 V Nernstian shift due to the pH 14 electrolyte and 0.197 V correction for the Sat. KCl Ag/AgCl reference electrode. As the standard oxidation potential of water is given as 1.23 V SHE taking the photocurrent densities at 1.27 V SHE enables a comparison of the currents achieved by the electrodes at a small (0.04 V) overpotential.

The more textured ethanol deposited electrode showed a consistently higher photocurrent density than that of the electrode deposited with methanol, however both showed the characteristics peaks and troughs associated with electron-hole recombination[196]. The sharp rise caused by illumination is a result of defect sites that allow the generation of photoinduced charge carriers at an energy lower than the bandgap of the semiconductor, however these sites also act as centres for electron-hole recombination. As such the peak is followed by decay to steady-state[197–199].

Although all electrodes suffered from recombination a decrease in individual feature size correlated to an increase in photocurrent at 1.27 V SHE (Figure 5.10).

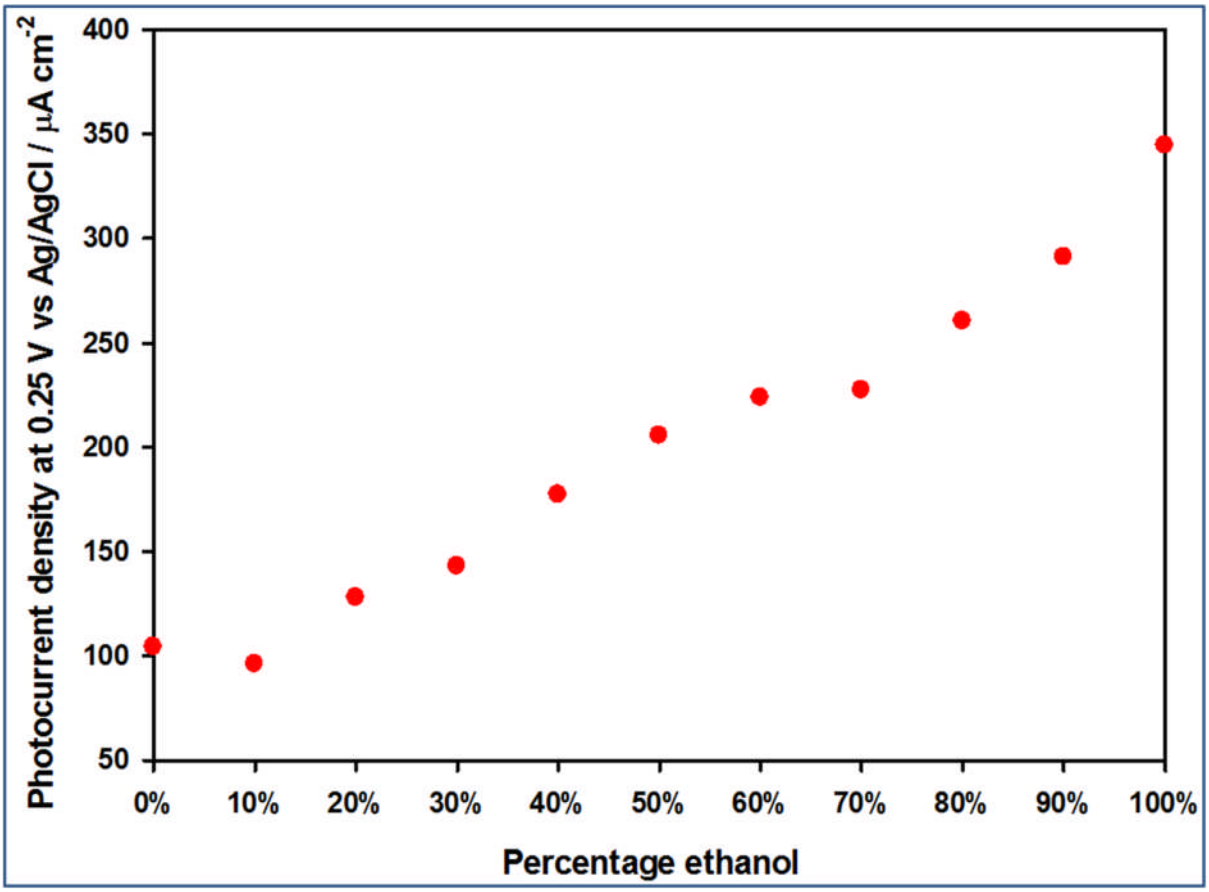

Figure 5.10. The photocurrent density of the $ZnFe_2O_4$ electrodes at 1.27 V SHE against the potential ethanol in the deposition solvent. It has been established that an increase in percentage ethanol corresponds to a decrease feature size in the nanostructure[68].

The photocurrent density followed the expected trend with higher photocurrents correlating to a higher percentage ethanol in the deposition solvent. As was observed in Figure 5.7 a higher percentage ethanol resulted in a reduced feature size in the nanostructure, and the smaller feature size was expected to result in higher light harvesting efficiency, and better collection of charge carriers. The only exception was the electrode deposited with 10 vol. % ethanol as this had a photocurrent of 96.0 μA cm^{-2}, 8.2 μA cm^{-2} lower than the electrode deposited with pure methanol as the solvent (104 μA cm^{-2}). Figure

5.6 shows that both these films were compact in morphology and so it was concluded that 10 vol. % ethanol is not enough to shift the deposition pathway from heterogeneous to homogeneous nucleation. The photocurrent density increased rapidly between 70 vol. % (227.3 μA cm^{-2}) and 80 vol. % (260.5 μA cm^{-2}) and for each deposition thereafter indicating that at 80 vol. % ethanol homogeneous nucleation starts to dominate the deposition process. This is supported by the SEM images (Figure 5.6) as at 80 vol. % the blade morphology has begun to show signs of developing into nanorods.

The incident photon conversion efficiency (IPCE) was measured for five electrodes to compare their quantum efficiency. The electrodes were in a 3-electrode cell with 1 M NaOH electrolyte connected to a potentiostat. During the measurement the potential was held steady at 1.27 V SHE and the electrode was illuminated with monochromated light in 5 nm intervals between 320 nm and 800 nm. The photocurrent response was recorded and the IPCE calculated as per Eq. 2.2 (Figure 5.11).

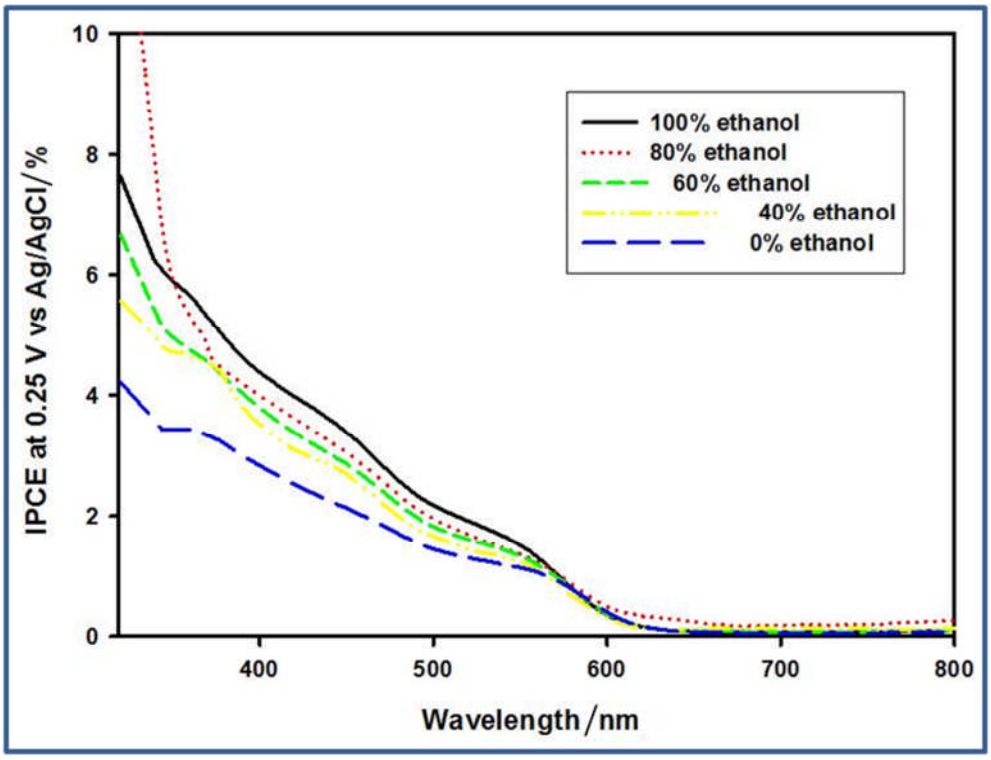

Figure 5.11. IPCE measurements for five electrodes deposited with solvent systematically altered between pure methanol and pure ethanol. A higher proportion ethanol in the deposition solvent correlated to a higher conversion efficiency.

The IPCE results were in agreement with the j-V measurements. Increased percentage of ethanol correlated with more efficient photon conversion from 320 nm to 570 nm with the exception of the 80 vol. % ethanol electrode which outperformed the 100 vol. % ethanol electrode between 320 and 353 nm. Between 570 nm and 617 nm all of the samples had similar conversion efficiencies and between 617 nm and 800 nm the conversion efficiency was <0.1 % and considered negligible. Once again a more compact nanostructure is associated with poorer photoelectrochemical performance.

These results reveal that the $ZnFe_2O_4$ electrodes absorb and convert purple, blue and green light to photogenerated charge carriers. However yellow light has a poor conversion rate and red light is not converted, likely due to not possessing enough energy to promote an electron through the 1.9 eV forbidden zone of $ZnFe_2O_4$[200]. According to Eq. 1.1 the 1.9 eV bandgap should absorb up to 653 nm, as these electrodes do not function at that wavelength the bandgap can be estimated to be wider. Taking 617 nm as the highest wavelength that is converted to photocurrent gives a rough estimate of 2.01 eV as the bandgap of these electrodes. This is around 0.5 eV wider than the ideal which is defined as being wide enough to provide an overpotential above 1.23 eV to ensure efficient water splitting, without being so wide as to invalidate a significant proportion of the visible spectrum[13].

6.0 Conclusion

Nanostructured MoS_2 and $ZnFe_2O_4$ were synthesised and tested as catalytic water splitting photoelectrodes. MoS_2 was top-down nanopatterned from a bulk crystal using a combination of nanosphere lithography and plasma etching. The nanospheres were deposited onto the surface of the MoS_2 by a modified Langmuir-Blodgett method. This consisted of nanospheres being formed into a self-assembled monolayer on the water-air interface of a dish containing a MoS_2 crystal. The level of the water was then lowered until the nanospheres were deposited onto the surface of the MoS_2. Following this the nanospheres were size controlled using O_2 plasma, and a combination of SF_6 etchant, and C_4F_8 passivation agent was used to inscribe the pattern into the MoS_2.

Attempts were made to exercise control over the final morphology through altering the flow rate or etch length of the three etchant gases. These were unsuccessful, with systematic alterations having no reproducible effect on the nanostructure of the MoS_2. However, the degree of close packing of the nanospheres on the surface of the MoS_2 did correlate to three distinct morphologies. When nanospheres were deposited with interstices between them they were shrank symmetrically by the O_2 etch, and nanopillars were etched into the MoS_2. However, the nanospheres could be deposited so close packed they squashed into hexagons, and when this resist was subjected to O_2 plasma a nanomesh was formed. This imprinted a nanowell pattern into the MoS_2. The third morphology was a hybrid between the two and resulted from having areas of both configurations of nanospheres. These samples resembled nanopillars but with linkages between the individual features.

Once nanopatterned the MoS_2 was tested as a photocathode for the HER in acidic electrolyte, with the catalytic performance measured by Tafel analysis. It was found that the morphologies with linkages between features had improved catalysis than those without. Nanowells had a Tafel slope of 191 mV dec^{-1}, linked pillars 215 mV dec^{-1}, and nanopillars 260 mV dec^{-1}. This was reasoned to be a result of the anisotropic properties of MoS_2 which derive from its layered structure. Additional linkages enabled charge carries to travel along the covalently bonded plane to the point of least resistance between the van der Waals bonded vertical layers. Unfortunately precise control of the nanosphere deposition was difficult to establish, and reproducibly selecting for one morphology over another was not achieved. The Tafel slopes were also higher than the reported 120 mV dec^{-1} for MoS_2 HER, and this was attributed to atmospheric oxygen displacing sulfur in the crystal to form $MoS_xO_{(2-x)}$. A sample that was electrochemically tested immediately following patterning was found to have a Tafel slope of 120 mV dec^{-1}.

In the next chapter a new technique to electrochemically sulfidate the air degraded $MoS_xO_{(2-x)}$ electrodes was developed. The challenge was to do so without the use of established, toxic, sulfidation agents H_2S and vaporised sulfur. A technique utilising relatively benign $Na_2S_2O_3$ was developed. As a measure of success the HER reaction was performed before and after each sulfidation. Experiments were undertaken to establish the optimum deposition potential window and electrolyte. It was found that an electrolyte of 10 mM $Na_2S_2O_3$, 1 mM H_2SO_4, 0.1 M Na_2SO_4 produced the greatest beneficial effect on HER catalysis, and the most advantageous deposition potential window was 0 V to +1.2 V to -1.6 V Ag/AgCl. The oxidation step was to fully oxidise the surface of the MoS_2 and the

subsequent reduction deposited sulfur onto the crystal. The chemical composition before and after was verified by XPS analysis finding that air-exposure caused a 15 % decrease in MoS_2, and sulfidation returned the surface to a pre-sulfidation MoS_2 composition.

The optimum sulfidation condition was tested by both electrochemistry and photoelectrochemistry. The electrochemistry found following sulfidation the overpotential required to initiate the reaction decreased from -0.27 V SHE to -0.17 V SHE, and the Tafel slope decreased from 282 mV dec^{-1} to 87 mV dec^{-1}. Ageing studies found that the sulfidated samples are stable in the acidic electrolyte, and indicated that, following re-exposure to air, the sulfidation may be repeated with no subsequent loss in performance. Although repeated sulfidation did homogenise the nanostructure. The PEC measurements showed that prior to sulfidation there was little difference between light and dark current measurements. However after sulfidation light exposure caused an increase in peak current density from -0.40 mA cm^{-2} to -0.81 mA cm^{-2}, confirming that the sulfidation restored the photocatalytic properties of the MoS_2.

The $ZnFe_2O_4$ electrodes were deposited by bottom-up AACVD from a precursor molecule that decomposed on heating to the product. In order to determine the deposition solvents effect on the final nanostructure the solvent composition was systematically altered between methanol and ethanol. It was found that $ZnFe_2O_4$ electrodes deposited from predominantly methanol solvent had compact morphologies, while the electrodes deposited from predominantly ethanol solvent had high surface area rod-like structures. This change in electrode texture was due to shift in precursor nucleation shifting from heterogeneous to homogeneous as the percentage of ethanol increased. The more

exothermic enthalpy of combustion of ethanol was deemed responsible as in the heated deposition chamber the solvent combusted and the additional energy provided from the ethanolic solvent enabled precursor nucleation in the vapour phase. The energy provided by methanol combusting was insufficient to promote homogenous nucleation, and hence the precursor decomposed on the substrate. The heterogenous nucleation pathway created high surface area, small feature sized electrodes, while the homogeneous nucleated resulted in compact morphologies.

The photocurrent density for the OER increased due to this shift with 100 % methanol deposition giving a photocurrent density of 104 μA cm^{-2}, while 100 % ethanol deposition gave a photocurrent density of 344 μA cm^{-2}. This was attributed to less charge-carrier recombination in the smaller feature sized electrodes due to the charge carriers having a shorter mean path length, which reduced the distance needed to travel to the reactive site decreased the chance of recombination before the charge carriers could be collected.

The continuation of the MoS_2 work would require a change in either the etching technique or the material studied. The patterned crystals had poorer than expected proton reduction characteristics, and this is attributed to the O_2 plasma used to shrink the nanospheres. It is believed the highly excited species penetrate deep within the crystal and cause defects. An alternative, non-damaging, way to control the naospheres size would be needed for this technique to be applicable for MoS_2. Alternatively this novel approach to generating nanowells could be applied to metal oxide semiconductors, which would not be damaged in the same way.

7.0 References

1 N. Abas, A. Kalair and N. Khan, *Futures*, 2015, **69**, 31–49.

2 M. Grätzel, *Inorg. Chem.*, 2005, **44**, 6841–6851.

3 *Int. Energy Agency*, 2015, **Key World** , Y4.

4 C. Perpiña Castillo, F. Batista e Silva and C. Lavalle, *Energy Policy*, 2016, **88**, 86–99.

5 H. J. Snaith, *J. Phys. Chem. Lett*, 2013, **4**, 3623−3630.

6 A. Einstein, *Ann. Phys.*, 1905, **17**, 132 – 148.

7 J. Nelson, *Phys. Sol. Cells*, 2003, **Imperial C**.

8 A. H. Taylor and G. P. Kerr, *J. Opt. Soc. Am.*, 1941, **31**, 3–8.

9 A. J. Bard, A. B. Bocarsly, F. R. F. Fan, E. G. Walton and M. S. Wrighton, *J. Am. Chem. Soc.*, 1980, **102**, 3671–3677.

10 S. Dayal, N. Kopidakis, D. C. Olson, D. S. Ginley and G. Rumbles, *Nano Lett.*, 2010, **10**, 239–242.

11 N. Greenham, X. Peng and A. Alivisatos, *Phys. Rev. B*, 1996, **54**, 17628–17637.

12 D. G. Nocera and M. P. Nash, *PNAS*, 2007, **104**, 20142.

13 M. Grätzel, *Nature*, 2001, **414**.

14 Y. Tachibana, L. Vayssieres and J. R. Durrant, *Nat. Photonics*, 2012, **6**, 511–518.

15 O. Khaselev, *Sci.*, 1998, **280**, 425–427.

16 A. Bard and M. A. Fox, *Acc. Chem. Res.*, 1995, **28**, 141–145.

17 M. G. Walter, E. L. Warren, J. R. McKone, S. W. Boettcher, Q. Mi, E. Santori and N. S. Lewis, *Chem. Rev.*, 2010, **110**, 6446–6473.

18 K. Onda, T. Kyakuno, K. Hattori and K. Ito, *J. Power Sources*, 2004, **132**, 64–70.

19 J. Turner, *Sci.*, 1999, **285**, 687–9.

20 J. R. Bolton, S. J. Strickler and J. S. Connolly, *Nature*, 1985, **316**, 495–500.

21 R. van de Krol, Y. Q. Liang and J. Schoonman, *J. Mater. Chem.*, 2008, **18**, 2311–2320.

22 A. A. Isse and A. Gennaro, *J. Phys. Chem. B*, 2010, **114**, 7894–7899.

23 H. Reiss and A. Heller, *J. Phys. Chem.*, 1985, **89**, 4207–4213.

24 M. Archer and A. Nozik, *Nanostructured PEC Syst. Sol. Phot. Convers.*, 2008, **Imperial C**.

25 A. Kudo and Y. Miseki, *Chem. Soc. Rev.*, 2009, **38**, 253–278.

26 J. Pan, Z. Wang, Q. Chen, J. Hu and J. Wang, *Nanoscale*, 2014, **6**, 13565–71.

27 J. Li and N. Wu, *Catal. Sci. Technol.*, 2015, **5**, 1360–1384.

28 K. Keis, C. Bauer, G. Boschloo, A. Hagfeldt, K. Westermark, H. Rensmo and H. Siegbahn, *J. Photochem. Photobiol. A Chem.*, 2002, **148**, 57–64.

29 C. X. Kronawitter, L. Vayssieres, S. Shen, L. Guo, D. A. Wheeler, J. Z. Zhang, B. R. Antoun and S. S. Mao, *Energy Environ. Sci.*, 2011, **4**, 3889.

30 S. Södergren, A. Hagfeldt and S. Lindquist, *J. Phys. Chem.*, 1994, **98**, 5552–5556.

31 A. Heller, *Acc. Chem. Res.*, 1981, **14**, 154–162.

32 A. J. Nozik, *Ann. Rev. Phys. Chem.*, 1978, **29**, 189–222.

33 N. S. Lewis, *Acc. Chem. Res.*, 1990, **23**, 176–183.

34 N. S. Lewis, *J. Electrochem. Soc.*, 1984, **131**, 2496.

35 H. Döscher, J. F. Geisz, T. G. Deutsch and J. A. Turner, *Energy Environ. Sci.*, 2014, **7**, 2951–2956.

36 Y. Zhang, H. Wang, Z. Liu, B. Zou, C. Y. Duan, T. Yang, X. J. Zhang, C. J. Zheng and X. H. Zhang, *Appl. Phys. Lett.*, 2013, **102**, 4.

37 Z. Zhang and P. Wang, *Energy Environ. Sci.*, 2012, **5**, 6506.

38 A. C. C. Tseung and S. Jasem, *Electrochim. Acta*, 1977, **22**, 31–34.

39 Y. Matsumoto and E. Sato, *Mater. Chem. Phys.*, 1986, **14**, 397–426.

40 M. Ni, M. K. H. Leung, D. Y. C. Leung and K. Sumathy, *Renew. Sustain. Energy Rev.*,

2007, **11**, 401–425.

41 C. Santato, M. Ulmann and J. Augustynski, *J. Phys. Chem. B*, 2001, **105**, 936–940.

42 S. D. Tilley, M. Cornuz, K. Sivula and M. Gr??tzel, *Angew. Chemie - Int. Ed.*, 2010, **49**, 6405–6408.

43 R. Dillert, D. H. Taffa, M. Wark, T. Bredow and D. W. Bahnemann, *APL Mater.*, 2015, **3**, 104001.

44 Y. Yang, H. Fei, G. Ruan, L. Li, G. Wang, N. D. Kim and J. M. Tour, *ACS Appl. Mater. Interfaces*, 2015, **7**, 20607–20611.

45 H. Dau, C. Limberg, T. Reier, M. Risch, S. Roggan and P. Strasser, *ChemCatChem*, 2010, **2**, 724–761.

46 I. Cesar, A. Kay, J. A. G. Martinez and M. Grätzel, *J. Am. Chem. Soc.*, 2006, **128**, 4582–4583.

47 C. Miao, S. Ji, G. Xu, G. Liu, L. Zhang and C. Ye, *ACS Appl. Mater. Interfaces*, 2012, **4**, 4428–4433.

48 F. Le Formal, S. R. Pendlebury, M. Cornuz, S. D. Tilley, M. Grätzel and J. R. Durrant, *J. Am. Chem. Soc.*, 2014, **136**, 2564–74.

49 K. Sivula, B. Florian, L. Formal and M. Gra, *Adv. Funct. Mater.*, 2010, 1099–1107.

50 A. B. Laursen, S. Kegnæs, S. Dahl and I. Chorkendorff, *Energy Environ. Sci.*, 2012, **5**,

5577–5591.

51 B. E. Conway and B. V. Tilak, *Electrochim. Acta*, 2002, **47**, 3571–3594.

52 Y. Li, H. Wang, L. Xie, Y. Liang, G. Hong and H. Dai, *JACS*, 2011, **133**, 7296–7299.

53 S. J. Rowley-Neale, D. A. C. Brownson, G. C. Smith, D. A. G. Sawtell, P. J. Kelly and C. E. Banks, *Nanoscale*, 2015, **7**, 18152–18168.

54 D. Voiry, M. Salehi, R. Silva, T. Fujita, M. Chen, T. Asefa, V. B. Shenoy, G. Eda and M. Chhowalla, *Nano Lett.*, 2013, **13**, 6222–7.

55 R. Guidelli, R. G. Compton, J. M. Feliu, E. Gileadi, J. Lipkowski, W. Schmickler and S. Trasatti, *Pure Appl. Chem.*, 2014, **86**, 245–258.

56 C. Tsai, F. Abild-Pedersen and J. K. Norskov, *Nano Lett.*, 2014, **14**, 1381–1387.

57 B. Hinnemann, P. G. Moses, J. Bonde, K. P. Jorgensen, J. H. Nielsen, S. Horch, I. Chorkendorff and J. K. Nørskov, *J. Am. Chem. Soc.*, 2005, **127**, 5308–5309.

58 A. B. Laursen, A. So, F. Dionigi, H. Fanchiu, C. Miller, O. L. Trinhammer, J. Rossmeisl and S. Dahl, *J. Chem. Educ.*, 2012, **89**, 1595–1599.

59 T. F. Jaramillo, K. P. Jørgensen, J. Bonde, J. H. Nielsen, S. Horch and I. Chorkendorff, *Science*, 2007, **317**, 100–102.

60 R. G. Compton and C. E. Banks, *Underst. Voltammetry*, 2007, **Imperial C**.

61 R. N. Kadam, R. S. Shendge and V. V. Pande, *Brazillian J. Pharm. Sci.*, 2015, **51**, 255 – 263.

62 J. Kibsgaard, Z. Chen, B. N. Reinecke and T. F. Jaramillo, *Nat. Mater.*, 2012, **11**, 963–969.

63 M. J. Cuddy, K. P. Arkill, Z. W. Wang, H. P. Komsa, A. V. Krasheninnikov and R. E. Palmer, *Nanoscale*, 2014, **6**, 12463–12469.

64 M. M. Mdeleni, T. Hyeon and K. S. Suslick, *J. Am. Chem. Soc.*, 1998, **120**, 6189–6190.

65 F. Foroutan, J. V. Jokerst, S. S. Gambhir, O. Vermesh, H. W. Kim and J. C. Knowles, *ACS Nano*, 2015, **9**, 1868–1877.

66 P. Colson, C. Henrist and R. Cloots, *J. Nanomater.*, 2013, **2013**.

67 J. M. Lehn, *Angew. Chem. Int. Ed. Engl.*, 1990, **29**, 1304–1319.

68 A. A. Tahir, H. A. Burch, K. G. U. Wijayantha and B. G. Pollet, *Int. J. Hydrogen Energy*, 2013, **38**, 4315–4323.

69 A. Biswas, I. S. Bayer, A. S. Biris, T. Wang, E. Dervishi and F. Faupel, *Adv. Colloid Interface Sci.*, 2012, **170**, 2–27.

70 C. L. Cheung, R. J. Nikolić, C. E. Reinhardt and T. F. Wang, *Nanotechnology*, 2006, **17**, 1339–1343.

71 T. G. Pedersen, S. Xiao, J. Zi and N. A. Mortensen, *Nano Lett.*, 2014, **14**, 2907 – 2913.

72 E. M. Hicks, X. Zhang, S. Zou, O. Lyandres, K. G. Spears, G. C. Schatz and R. P. Van Duyne, *J. Phys. Chem. B*, 2005, **109**, 22351–22358.

73 L. Ji, Y. Chang, B. Fowler, Y. Chen, T. Tsai, K. Chang, M. Chen, T. Chang, S. M. Sze, E. T. Yu and J. C. Lee, *Nano lett.*, 2014, **14**, 813 – 818.

74 N. Marquestaut, A. Martin, D. Talaga, L. Servant, S. Ravaine, S. Reculusa, D. M. Bassani, E. Gillies and F. Lagugné-Labarthet, *Langmuir*, 2008, **24**, 11313–11321.

75 S. Acharya, J. P. Hill and K. Ariga, *Adv. Mater.*, 2009, **21**, 2959–2981.

76 C. C. Ho, P. Y. Chen, K. H. Lin, W. T. Juan and W. L. Lee, *ACS Appl. Mater. Interfaces*, 2011, **3**, 204–208.

77 A. S. Hall, S. A. Friesen and T. E. Mallouk, *Nano lett*, 2013, **13**, 2623–2627.

78 Y. Haidar, A. Pateau, A. Rhallabi, M. C. Fernandez, A. Mokrani, F. Taher, F. Roqueta and M. Boufnichel, *Plasma Sources Sci. Technol.*, 2014, **23**, 065037.

79 A. Frommhold, R. E. Palmer and A. P. G. Robinson, *J. Micro/Nanolithography, MEMS, MOEMS*, 2013, **12**, 033003.

80 D. J. Lewis, A. A. Tedstone, X. L. Zhong, E. A. Lewis, A. Rooney, N. Savjani, J. R. Brent, S. J. Haigh, M. G. Burke, C. A. Muryn, J. M. Raftery, C. Warrens, K. West, S. Gaemers and P. O'Brien, *Chem. Mater.*, 2015, **27**, 1367–1374.

81 D. J. Lewis and P. O'Brien, *Chem. Commun.*, 2014, **50**, 6319–21.

82 M. A. Ehsan, H. N. Ming, M. Misran, Z. Arifin, E. R. T. Tiekink, A. P. Safwan, M. Ebadi, W. J. Basirun and M. Mazhar, *Chem. Vap. Depos.*, 2012, **18**, 191–200.

83 A. A. Tahir, M. A. Ehsan, M. Mazhar, K. G. U. Wijayantha, M. Zeller and A. D. Hunter, *Chem. Mater.*, 2010, **22**, 5084–5092.

84 J. J. Helble, *J. Aerosol Sci.*, 1998, **29**, 721–736.

85 A. Szymczyk, C. Labbez, P. Fievet, A. Vidonne, A. Foissy and J. Pagetti, *Adv. Colloid Interface Sci.*, 2003, **103**, 77–94.

86 N. Godino, X. Borrise, F. X. Muñoz, F. J. Del Campo and R. G. Compton, *J. Phys. Chem. C*, 2009, **113**, 11119–11125.

87 T. J. Davies and R. G. Compton, *J. Electroanal. Chem.*, 2005, **585**, 63–82.

88 A. A. Tahir and K. G. U. Wijayantha, *J. Photochem. Photobiol. A Chem.*, 2010, **216**, 119–125.

89 A. A. Tahir, K. G. U. Wijayantha, M. Mazhar and V. McKee, *Thin Solid Films*, 2010, **518**, 3664–3668.

90 J. Li, Z. Liu and Z. Zhu, *Appl. Surf. Sci.*, 2014, **320**, 146–153.

91 J. Y. Kim, G. Magesh, D. H. Youn, J.-W. Jang, J. Kubota, K. Domen and J. S. Lee, *Sci. Rep.*, 2013, **3**, 2681.

92 Y. Matsumoto, *J. Solid State Chem.*, 1996, **126**, 227–234.

93 R. van de Krol, Y. Liang, J. Schoonman, R. Van De Krol, Y. Liang and J. Schoonman, *J. Mater. Chem.*, 2008, **18**, 2311.

94 M. K. Roy and H. C. Verma, *J. Magn. Magn. Mater.*, 2006, **306**, 98–102.

95 M. Sultan and R. Singh, *J. Phys. D. Appl. Phys.*, 2009, **42**, 115306.

96 A. Sheikh, A. Yengantiwar, M. Deo, S. Kelkar and S. Ogale, *Small*, 2013, **9**, 2091–2096.

97 K. G. Upul Wijayantha, S. Saremi-Yarahmadi and L. M. Peter, *Phys. Chem. Chem. Phys.*, 2011, **13**, 5264.

98 W. J. Albery and P. N. Bartlett, *J. Electrochem. Soc.*, 1983, **130**, 1699–1706.

99 Q. Zhang and G. Cao, *Nano Today*, 2011, **6**, 91–109.

100 J. S. Jang, S. J. Hong, J. S. Lee, P. H. Borse, O.-S. Jung, T. E. Hong, E. D. Jeong, M. S. Won and H. G. Kim, *J. Korean Phys. Soc.*, 2009, **54**, 204.

101 P. H. Borse, J. . Jang, S. J. Hong, J. . Lee, J. H. Jung, T. E. Hong, C. W. Ahn, E. D. Jeong, K. S. Hong, J. H. Yoon and H. G. Kim, *J. Korean Phys. Soc.*, 2009, **55**, 1472.

102 G. Y. Zhang, Y. Q. Sun, D. Z. Gao and Y. Y. Xu, *Mater. Res. Bull.*, 2010, **45**, 755–760.

103 S. W. Cao, Y. J. Zhu, G. F. Cheng and Y. H. Huang, *J. Hazard. Mater.*, 2009, **171**, 431–435.

104 H. Lv, L. Ma, P. Zeng, D. Ke and T. Peng, *J. Mater. Chem.*, 2010, **20**, 3665.

105 S. Boumaza, A. Boudjemaa, A. Bouguelia, R. Bouarab and M. Trari, *Appl. Energy*, 2010, **87**, 2230–2236.

106 X. Cao, L. Gu, X. Lan, C. Zhao, D. Yao and W. Sheng, *Mater. Chem. Phys.*, 2007, **106**, 175–180.

107 E. Casbeer, V. K. Sharma and X. Z. Li, *Sep. Purif. Technol.*, 2012, **87**, 1–14.

108 R. Chianelli, *J. Catal.*, 1984, **86**, 226–230.

109 N. Liu, X. Wang, W. Xu, H. Hu, J. Liang and J. Qiu, *Fuel*, 2014, **119**, 163–169.

110 D. Kong, H. Wang, J. J. Cha, M. Pasta, K. J. Koski, J. Yao and Y. Cui, *Nano Lett.*, 2013, **13**, 1341–1347.

111 S. M. Muzakkir and H. Hirani, *Int. J. Mod. Eng. Res.*, 2014, **4**, 46–49.

112 B. Radisavljevic, A. Radenovic, J. Brivio, V. Giacometti and A. Kis, *Nat. Nanotechnol.*, 2011, **6**, 147–50.

113 R. Ganatra and Q. Zhang, *ACS Nano*, 2014, **8**, 4074–4099.

114 O. Lopez-Sanchez, D. Lembke, M. Kayci, A. Radenovic and A. Kis, *Nat. Nanotechnol.*, 2013, **8**, 497–501.

115 C. Ataca and S. Ciraci, *J. Phys. Chem. C*, 2012, **116**, 8983 – 8999.

116 Z. Chen, D. Cummins, B. N. Reinecke, E. Clark, M. K. Sunkara and T. F. Jaramillo, *Nano*

lett, 2011, **11**, 4168–4175.

117 J. D. Benck, T. R. Hellstern, J. Kibsgaard, P. Chakthranont and T. F. Jaramillo, *ACS Catal.*, 2014, **4**, 3957–3971.

118 J. P. Wilcoxon, P. P. Newcomer and G. A. Samara, *J. Appl. Phys.*, 1997, **81**, 7934.

119 A. Ambrosi and M. Pumera, *ChemComm*, 2015, **51**, 8450–8453.

120 A. Splendiani, L. Sun, Y. Zhang, T. Li, J. Kim, C. Chim, G. Galli and F. Wang, *Nano lett.*, 2010, **10**, 1271–1275.

121 M. Acerce, D. Voiry and M. Chhowalla, *Nat. Nanotechnol.*, 2015, **10**, 313–318.

122 Y. Huang, R. J. Nielsen, W. A. Goddard and M. P. Soriaga, *J. Am. Chem. Soc.*, 2015, **137**, 6692–6698.

123 Y. Cai, X. Yang, T. Liang, L. Dai, L. Ma, G. Huang, W. Chen, H. Chen, H. Su and M. Xu, *Nanotechnology*, 2014, **25**, 465401.

124 V. V. Ivanovskaya, A. Zobelli, A. Gloter, N. Brun, V. Serin and C. Colliex, *Phys. Rev. B*, 2008, **78**, 134104.

125 L. M. Peter and K. G. Upul Wijayantha, *ChemPhysChem*, 2014, **15**, 1983–1995.

126 Y. Zhao, Y. Zhang, Z. Yang, Y. Yan and K. Sun, *Sci. Technol. Adv. Mater.*, 2013, **14**, 043501.

127 H. Wang, C. Tsai, D. Kong, K. Chan, F. Abild-Pedersen, J. K. Nørskov and Y. Cui, *Nano Res.*, 2015, **8**, 566–575.

128 M. A. Lukowski, A. S. Daniel, F. Meng, A. Forticaux, L. Li and S. Jin, *J. Am. Chem. Soc.*, 2013, **135**, 10274–10277.

129 Y. Shi, J. Wang, C. Wang, T. T. Zhai, W. J. Bao, J. J. Xu, X. Xia and H.-Y. Chen, *J. Am. Chem. Soc.*, 2015, **137**, 7365–7370.

130 C. G. Morales-Guio, L.-A. Stern and X. Hu, *Chem. Soc. Rev.*, 2014, **43**, 6555–69.

131 J. Xie, J. Zhang, S. Li, F. Grote, X. Zhang, H. Zhang, R. Wang, Y. Lei, B. Pan and Y. Xie, *J. Am. Chem. Soc.*, 2013, **135**, 17881–17888.

132 J. H. Lee, W. S. Jang, S. W. Han and H. K. Baik, *Langmuir*, 2014, **30**, 9866–9873.

133 V. Subramanian, E. Wolf and P. V Kamat, *J. Phys. Chem. B*, 2001, **105**, 11439–11446.

134 A. E. Russell, *Faraday Discuss.*, 2009, **140**, 9–10.

135 D. Wang, X. Zhang, Y. Shen and Z. Wu, *RSC Adv.*, 2016, **6**, 16656–16661.

136 M.-R. Gao, M. K. Y. Chan and Y. Sun, *Nat. Commun.*, 2015, **6**, 7493.

137 H. E. Zittel and F. J. Miller, *Anal. Chem.*, 1965, **37**, 200–203.

138 *Next Gener. Plasma Syst.*, 2010, **Oxford Ins**.

139 J. Harry, *Introd. to Plasma Technol.*, 2010, **Wiley-VCH**, 77.

140 A. Picard, G. Turban and B. Grolleau, *J. Phys. D Appl.*, 1986, **991**.

141 F. J. Millero, T. Plese and M. Fernandez, *Limnol. Oceanogr.*, 1988, **33**, 269–274.

142 Y. C. Hsieh, S. D. Senanayake, Y. Zhang, W. Xu and D. E. Polyansky, *ACS Catal.*, 2015, **5**, 5349–5356.

143 K. L. Cheng, *Microchem. J.*, 1998, **59**, 457–461.

144 X. Chen, S. Shen, L. Guo and S. S. Mao, *Chem. Rev. (Washington, DC, United States)*, 2010, **110**, 6503–6570.

145 C. A. Gueymard, D. Myers and K. Emery, *Sol. Energy*, 2002, **73**, 443–467.

146 A. A. Tahir, K. G. U. Wijayantha, S. Saremi-Yarahmadi, M. Mazhar and V. McKee, *Chem. Mater.*, 2009, **21**, 3763–3772.

147 M. Zhang, L. Yuan, X. Wang, H. Fan, X. Wang, X. Wu, H. Wang and Y. Qian, *J. Solid State Chem.*, 2008, **181**, 294–297.

148 J. Goldstein, E. Newbury, P. Echlin and D. Joy, *Scanning electron microscopy and x-ray analysis*, Springer, 1992.

149 L. Reimer, *Meas. Sci. Technol.*, 2000, **11**, 1826.

150 H. Seiler, *J. Appl. Phys.*, 1983, **54**, R1.

151 J. W. Niemantsverdriet, *Spectroscopy in Catalysis*, Wiley-VCH, 2007.

152 R. Egerton, *Physical Principles of Electron Microscopy: An Introduction to TEM, SEM, and AEM*, Springer, 2005.

153 D. Briggs and M. Seah, *Practical surface analysis by Auger and X-ray photoelectron spectroscopy*, Wiley, 1983.

154 S. D. Techane, L. J. Gamble and D. G. Castner, *Biointerphases*, 1970, **17**, 98.

155 J. F. Watts, *Vacuum*, 1994, **45**, 653–671.

156 J. S. Rees and P. H. Jacobsen, *Dent. Mater.*, 1989, **5**, 41–4.

157 W. Harkins and H. Jordan, *Jacs*, 1930, **52**, 1751–1772.

158 V. Lotito and T. Zambelli, *J. Colloid Interface Sci.*, 2015, **447**, 202–210.

159 E. J. Plichta, M. A. Hendrickson and S. Mukerjee, *J. Phys. Chem. C*, 2009, **113**, 20127 – 20134.

160 S. H. Lee and J. C. Rasaiah, *J. Chem. Phys.*, 2011, **135**, 124505.

161 E. O. Barnes, X. Chen, P. Li and R. G. Compton, *J. Electroanal. Chem.*, 2014, **720-721**, 92–100.

162 M. C. Lux-steiner, E. Bucher, L. Scandella, A. Schumacher and R. Prim, *Appl. Surf. Sci.*, 1993, **66**, 465–472.

163 I. Electroanal and U. Milano, *J. Electroanal. Chem.*, 1993, **321**, 353–376.

164 F. G. Will and C. A. Knorr, *Electrochem*, 1969, **62**, 258–259.

165 M. Hayes and A. T. Kuhn, *Appl. Surf. Sci.*, 1980, **6**, 1.

166 S. M. Davis and J. C. Carver, *Appl. Surf. Sci.*, 1984, **20**, 193–198.

167 J. R. Lince, M. R. Hilton and A. S. Bommannavar, *Surf. Coatings Technol.*, 1990, **43-44**, 640–651.

168 H.-X. You, N. M.D. Brown and K. F. Al-Assadi, *Surf. Sci. Lett.*, 1993, **284**, A286.

169 N. M. D. Brown, N. Cui and A. Mckinley, *Appl. Surf. Sci.*, 1998, **134**, 11–21.

170 T. Weber, J. C. Muijsers, J. H. M. C. van Wolput, C. P. J. Verhagen and J. W. Niemantsverdriet, *J. Phys. Chem.*, 1996, **100**, 14144–14150.

171 H. Nolan, N. McEvoy, M. O'Brien, N. C. Berner, C. Yim, T. Hallam, A. R. McDonald and G. S. Duesberg, *Nanoscale*, 2014, **6**, 8185–91.

172 R. S. Patil, *Thin Solid Films*, 1999, **340**, 11–12.

173 M. Shea, J. Koziol and S. Howell, *Clin. Pharmacol. Ther.*, 1984, **35**, 419–425.

174 R. Goel, S. M. Cleary, C. Horton, S. Kirmani, I. Abramson, C. Kelly and S. B. Howell, *J. Natl. Cancer Inst.*, 1989, **81**, 1552–60.

175 E. Shembel, R. Apostolova, I. Kirsanova and V. Tysyachny, *J. Solid State Electrochem.*, 2008, **12**, 1151–1157.

176 S. Nakamura and A. Yamamoto, *Sol. Energy Mater. Sol. Cells*, 2001, **65**, 79–85.

177 T. Yukawa, K. Kuwabara and K. Koumoto, *Thin Solid Films*, 1996, **286**, 151–153.

178 M. Pac, X. Han and M. Tao, *ECS Trans.*, 2011, **41**, 157–166.

179 K. LaMer and A. Kenyon, *J. Colloid. Sci*, 1947, **2**, 257–264.

180 H. A. Burch, M. Isaacs, K. Wilson, R. E. Palmer and N. V. Rees, *RSC Adv.*, 2016, **6**, 26689 – 26695.

181 Y. Cai, Y. Xu, X. Wang and K. Hu, *Asian J. Chem.*, 2012, **24**, 4065–4067.

182 D. E. Scaife, *Sol. Energy*, 1980, **25**, 41–54.

183 Z. Chen, T. F. Jaramillo, T. G. Deutsch, A. Kleiman-Shwarsctein, A. J. Forman, N. Gaillard, R. Garland, K. Takanabe, C. Heske, M. Sunkara, E. W. McFarland, K. Domen, E. L. Miller, J. a. Turner and H. N. Dinh, *J. Mater. Res.*, 2010, **25**, 3–16.

184 G. Shaw, I. P. Parkin, K. F. E. Pratt and D. E. Williams, *J. Mater. Chem.*, 2005, **15**, 149–154.

185 X. Hou and K. L. Choy, *Chem. Vap. Depos.*, 2006, **12**, 583–596.

186 S. Saremi-Yarahmadi, A. A. Tahir, B. Vaidhyanathan and K. G. U. Wijayantha, *Mater. Lett.*, 2009, **63**, 523–526.

187 K. Okuyama and I. Wuled Lenggoro, *Chem. Eng. Sci.*, 2003, **58**, 537–547.

188 G. L. Messing, S.-C. Zhang and G. V. Jayanthi, *J. Am. Ceram. Soc.*, 1993, **76**, 2707–2726.

189 V. Jokanović, D. Janaćković and D. Uskoković, *Ultrason. Sonochem.*, 1999, **6**, 157–169.

190 P. S. Nikam, L. N. Shirsat, M. Hasan, P. Chemistry, M. S. G. College and M. Camp, *Engineering*, 1998, **9568**, 732–737.

191 L. Albuquerque, C. Ventura and R. Gonçalves, *J. Chem. Eng. Data*, 1996, **41**, 685–688.

192 G. Vasquez, E. Alvarez and J. M. Navaza, *J. Chem. Eng. Data*, 1995, **40**, 611–614.

193 J. D. Desai, H. M. Pathan, S. K. Min, K. D. Jung and O. S. Joo, *Appl. Surf. Sci.*, 2006, **252**, 2251–2258.

194 *CRC handbook of chemistry and physics*, CRC Press, Cleveland, OH, 44th edn., 1963.

195 O. Milosevic, L. Mancic, M. E. Rabanal, L. S. Gomez and K. Marinkovic, *KONA Powder Part. J.*, 2009, **27**, 84–106.

196 L. Peter, K. Wijayantha and A. Tahir, *Faraday Discuss.*, 2012, **155**, 309 – 322.

197 L. Peter, *Chem. Rev.*, 1990, **90**, 753–769.

198 L. L. M. Abrantes and L. M. L. Peter, *J. Electroanal. Chem. Interfacial Electrochem.*, 1983, **150**, 593–601.

199 R. Beranek and H. Kisch, *Electrochem. commun.*, 2007, **9**, 761–766.

200 Y. Fu and X. Wang, *Ind. Eng. Chem. Res.*, 2011, **50**, 7210–7218.